Exploring different facets of magnetic skyrmion nucleation and dynamics in ultra-thin films

Roméo Juge

Université Grenoble Alpes

THÈSE

Pour obtenir le grade de

DOCTEUR DE L'UNIVERSITE GRENOBLE ALPES

Spécialité : Physique de la Matière Condensée et du Rayonnement

Arrêté ministériel : 25 mai 2016

Présentée par

Roméo Juge

Thèse dirigée par **Gilles Gaudin,** Directeur de recherche, CNRS
et co-dirigée par **Olivier Boulle,** Chargé de recherche, CNRS

préparée au sein du **Laboratoire Spintronique et Technologie des Composants (SPINTEC)**

dans **l'École Doctorale de Physique**

Nucléation et dynamique de skyrmions magnétiques dans des films ultra-minces

Exploring different facets of magnetic skyrmion nucleation and dynamics in ultra-thin films

Thèse soutenue publiquement le **29 janvier 2020**,
devant le jury composé de :

Monsieur André Thiaville
Directeur de recherche, CNRS, C2N, Palaiseau, Rapporteur **Monsieur Joo-Von Kim**
Chargé de recherche, CNRS, C2N, Palaiseau, Rapporteur **Monsieur Dafiné Ravelosona**
Directeur de recherche, CNRS, C2N, Palaiseau, Président **Monsieur Laurent Ranno**
Maître de conférences, UGA, Institut Néel, Grenoble, Examinateur **Madame Claire Baraduc**
Ingénieure de recherche, CEA, SPINTEC, Grenoble, Invitée

N'a de convictions que celui qui n'a rien approfondi.
Emile Cioran, *De l'inconvénient d'être né*, Gallimard (1973)

Remerciements

Trois ans et une bonne centaine de pages plus tard... La préparation de cette thèse aura été le théâtre de nombreuses rencontres, qui auront contribué à bien des égards à en faire une expérience riche et inoubliable. C'est donc naturellement que cette monographie s'ouvre sur les remerciements qui, je l'espère, expriment aussi fidèlement que possible ma reconnaissance envers tous ceux à qui je dois une partie, petite ou grande, du chemin parcouru.

Mes premiers remerciements vont à mes deux encadrants, Olivier et Gilles. Vous avez été présents tout au long de ma thèse... Olivier, ta confiance dans tout ce que j'entreprenais, ta curiosité intellectuelle, ton enthousiasme et ta promptitude à constamment explorer de nouvelles idées ont certainement rendu ces trois ans riches et stimulants. Malgré le travail titanesque que tu t'es vu imposé dans cette course effrénée aux petits skyrmions, tu as toujours su garder un pied (parfois deux) dans mon monde, jonglant entre temps de faisceau, salle blanche, rapports, réunions et conférences aux quatre coins de la planète... Mais surtout, merci d'avoir rendu possible tout le travail effectué pendant ces trois ans. Je devrais en toute honnêteté te nommer dans beaucoup des paragraphes qui suivent... Gilles, alors même que tu avais toi aussi mille choses à faire, tu as toujours pris le temps de répondre à mes questions, qu'elles requièrent ta compréhension approfondie de la physique, ton esprit critique, ta capacité à peser le pour et le contre, ou encore ta fine connaissance des rouages administratifs du CEA ; et ce avec une pertinence parfois déconcertante... Pire encore, tu le faisais avec calme, gentillesse et entrain ! Et bien sûr, je n'oublie pas toutes les *e-beams*, parfois parfaitement planifiées, souvent sous la contrainte du temps et de la nécessité — d'aucuns diraient à l'arrache, mais toujours terminées avant notre départ au synchrotron.

Je remercie l'ensemble des membres du jury, André, Joo-Von, Dafiné, Laurent et Claire, d'avoir pris le temps de relire avec tant d'attention les pages qui suivent, ainsi que pour nos échanges lors de la soutenance.

Assurément, un étudiant qui étudie, des encadrants qui encadrent, des rapporteurs qui rapportent et des examinateurs qui examinent c'est bien, mais ça ne suffit pas à faire une thèse. Il aura fallu la participation de nombreuses personnes avec qui j'ai eu la chance de collaborer, à commencer par l'équipe des post-docs : Soong-Geun, Gaurav et Qiang. Bien que vous ne vous soyez pas tous côtoyés, turnover infernal de la recherche oblige, j'ai eu le plaisir de travailler avec chacun d'entre vous. Merci de m'avoir épaulé en salle blanche quand le temps ne jouait pas en notre faveur. Merci Gaurav de m'avoir fait profiter de ton expertise du MFM (et accessoirement d'avoir pris une des plus belles images de ma thèse). Mais surtout, merci pour votre présence et votre aide au synchrotron. C'était bien agréable — et indispensable — de vous avoir avec nous, à toute heure du jour et de la nuit. Tout comme nos acolytes préférés de l'Institut Néel d'ailleurs. Merci beaucoup Jan pour ton aide et ta compagnie au synchrotron. C'est à toi qu'on doit l'observation de notre premier déplacement de skyrmion. Je me souviens de ce matin où, légèrement exaspéré par ces skyrmions qui refusaient obstinément de bouger, tu montas le courant au maximum, nous débloquant (littéralement) la situation ! Merci à toi aussi Dayane de nous avoir prêté main forte dans notre tour d'Europe des synchrotrons, et d'en avoir égayé les jours et les nuits de ta bonne humeur communicative.

Je tiens maintenant à remercier chaleureusement tous les spécialistes de la microscopie à rayons X, sans qui la plupart des images présentées dans les pages qui suivent (et les études qui en découlent) n'auraient pu voir le jour. Merci Andrea, Onur et Francesca de m'avoir fait découvrir le monde du synchrotron à Elettra. Malgré une première expérience (scientifique) un peu désastreuse —

compensée en partie par les fameuses pizzas et *gelate*, vous m'avez donné envie d'y revenir ! On pouvait toujours compter sur vous, bien souvent jusqu'à une heure avancée de la nuit... Merci Lucia et Michael pour tous les moments passés à Alba. Merci de m'avoir appris une foule de choses indispensables sur le PEEM mais aussi pour tout l'à-côté. Vous avez fait des *beamtimes* une expérience (scientifique autant qu'humaine) des plus enrichissantes dont je garderai toujours un excellent souvenir. Merci Jordi de nous avoir fait profiter de ta paillasse parfaitement ordonnée et de m'avoir aidé quand je m'arrachais les cheveux sur la micro-soudeuse. Merci Rachid, Brice et Adrien pour toutes les manip' à Soleil (et pour les changements impromptus apportés à votre setup). C'est grâce à vous et à votre expertise du STXM qu'on a pu observer nos premiers skyrmions antiferro ! Enfin, merci Francesco d'avoir assuré à toi tout seul un temps de faisceau à Diamond.

Au bourdonnement du synchrotron se substituait le reste du temps celui de la salle blanche, des machines et des couloirs de Spintec. J'ai eu la chance de travailler avec beaucoup de personnes pendant ces trois ans... Je veux remercier tout particulièrement Liliana pour les simulations « désordonnées », pour toutes les fois où je t'ai demandé d'en lancer « une dernière, juste pour vérifier un truc » et plus généralement pour t'être toujours enquise de l'avancement de mes travaux. Tu avais toujours un petit mot bienveillant quand je passais devant ton bureau... Je remercie sincèrement toutes les personnes avec qui j'ai eu l'occasion de collaborer : Mohamed et Yves du LSPM pour les mesures BLS (bien que nous ayons échangé e-mails et échantillons, je n'ai jamais eu la chance de vous rencontrer...) ; Mamour, Dominique et Dafiné du C2N pour les expériences d'irradiation ; Jay et Mihai de Spintec pour les mesures de SOT ; Stefania et José de l'Institut Néel pour les mesures de vitesses de paroi ; et Olivier et Kyongmo de Spintec pour les mesures FMR. Vous m'avez permis d'apprendre tout un tas de choses et d'étoffer considérablement mes résultats ! J'ai aussi passé beaucoup de temps à l'Institut Néel en l'agréable compagnie de Stefania et Jan. Merci à tous les deux de m'avoir laissé utiliser vos manip' quand j'en avais besoin. Un grand merci à Stéphane, fervent défenseur du copier-coller à la souris et du *scrolling* (j'aurai quand même réussi à te faire utiliser les raccourcis clavier une fois en trois ans), pour les innombrables échantillons déposés, les discussion scientifiques et techniques et toutes celles « annexes » qui venaient souvent s'y greffer. Enfin, je tiens à remercier Catherine, Rachel et Sabrina pour m'avoir rendu la vie si facile au labo et aidé à préparer mes incessants déplacements.

Merci à tous les thésards, post-docs et permanents de Spintec qui ont été si agréables à découvrir puis fréquenter au quotidien, au labo comme en-dehors, pendant les pauses-café, déjeuners, conférences et soirées plus ou moins arrosées. Merci Marco, Jay, Arnaud, Caro, Dai, Laurent, Cécile, Daniel & Daniel, Michael, Steven, Aurélien, Léa, Álvaro, Sabrina, Luis, Haozhe, Mathieu, Chandra, Jyotirmoy, Svetlana, Paul, Thomas et bien d'autres encore... Mention spéciale à la bande des « cosmopolites », Dali, Guillaume, Jude et Paulo, et à toutes les discussions politiquement incorrectes qui animaient bon nombre de nos soirées. Plus généralement, merci à toute l'équipe de Spintec pour la bonne ambiance qui y règne (*keep it up!*).

Un immense merci aux trois joyeux drilles avec qui j'ai eu la chance — ou la malchance, il faudrait leur demander — de vivre ces dernières années. Véritables compagnons de fortune et d'infortune, au gré des joies et des affres de la thèse, j'ai nommé Pape, Romy et Luca ! Sans oublier tous ceux qui défilent souvent chez nous : Edouard, Maria, Ioanna, Seb et Jov pour ne citer qu'eux...

Merci à ma famille, venue me soutenir (sans mauvais jeu de mot) le jour J, et en particulier à mes parents, qui ont fourni le gros du boulot : vingt-six ans à me supporter, ce n'est pas rien...

Merci à vous tous qui êtes venus assister à ma soutenance, merci pour vos mots que j'ai pris plaisir à lire et bien sûr pour les super cadeaux ! J'aurai une pensée pour vous avant de sauter en parachute (en espérant que j'y survive...).

Merci à toi qui lis ces lignes et qui peut-être, si le cœur t'en dit, parcourras quelques pages parmi celles qui suivent.

Enfin c'est à toi, Titiksha, que j'adresse mes derniers remerciements, ainsi qu'au hasard pour avoir arrangé, pour mon plus grand bonheur, cette rencontre fortuite. Merci pour ta constance, ton inconditionnel soutien, ton optimisme inébranlable et ta patience à toute épreuve. Merci d'être là, tout simplement, dans *toutes* les facettes de ma vie.

Résumé

Les skyrmions magnétiques sont des enroulements chiraux de l'aimantation que l'on peut visualiser comme de minuscules domaines magnétiques circulaires délimités par des parois de domaine chirales. En raison de leur taille potentiellement nanométrique et car on leur prédit un déplacement efficace sous courant, les skyrmions magnétiques sont devenus des candidats prometteurs pour transporter l'information dans des mémoires et des dispositifs logiques non-volatiles et à forte densité de stockage. Ils ont récemment été observés à température ambiante dans des empilements du type métal lourd/ferromagnétique/non-magnétique, franchissant une étape importante en vue de développer des dispositifs utilisant des skyrmions. Suivant ces premières observations, l'objectif de cette thèse est d'étudier certaines propriétés clés des skyrmions que sont leur nucléation, leur stabilité et leur déplacement sous courant ; toutes à température ambiante. Les premiers résultats présentés portent sur la nucléation de skyrmions dans des films ultra-minces (pour une épaisseur de ferromagnétique de l'ordre de 1 nm) réalisée par ingénierie des propriétés magnétiques aux interfaces ainsi que de la géométrie des échantillons. La nucléation de skyrmions dans des films ultra-minces étendus, en géométrie confinée, dans des films polarisés par échange inter-couche puis dans des motifs définis par irradiation d'ions est présentée. La deuxième partie de ce travail concerne l'étude de la dynamique des skyrmions magnétiques sous courant. Dans un film ultra-mince de composition Pt/Co/MgO, on mesure des vitesses atteignant 100 m s^{-1}, pour des skyrmions de l'ordre de 100 nm. Cette étude met également en lumière l'effet Hall de skyrmion, signature de leur topologie, qui décrit la déviation de la trajectoire d'un skyrmion par rapport à celle dictée par le courant. Nous trouvons que cette déviation dépend nettement de la vitesse des skyrmions, contrairement à ce que prédisent les modèles existants. En combinant modèle analytique et simulations micromagnétiques, s'appuyant sur une caractérisation poussée des propriétés du film, nous trouvons que cette dépendance avec la vitesse peut être entièrement attribuée à des effets de piégeage qui entravent le déplacement des skyrmions. Enfin, la dernière partie de ce travail porte sur l'étude expérimentale de multi-couches antiferromagnétiques synthétiques, caractérisées par un moment magnétique net nul. Dans ces systèmes, on s'attend à ce que le déplacement des skyrmions s'effectue dans la direction du courant — sans effet Hall de skyrmion, une condition requise pour les applications. L'optimisation de multi-couches spécifiques permet l'observation, en microscopie à rayons X, de skyrmions antiferromagnétiques synthétiques de l'ordre de 100 nm. Puisque leur nucléation est délicate, un dispositif est par la suite conçu pour injecter localement du courant électrique à travers des pointes lithographiées. Ce dispositif permet de créer et de supprimer des skyrmions de manière contrôlée, en utilisant uniquement du courant, rapprochant ces skyrmions un peu plus des applications.

Abstract

Magnetic skyrmions are chiral magnetisation windings that can be pictured as minuscule, circular magnetic domains bounded by chiral domain walls. Owing to their potential nanometre size and predicted efficient current-driven motion, magnetic skyrmions hold great promise as future information carriers in high-density, non-volatile memory and logic applications. Their recent observation at room temperature in material stacks consisting of heavy metal/ferromagnet/non-magnet has lifted an important bottleneck towards the practical realisation of skyrmion-based devices. Following these early observations, the objective of this work is to tackle certain key attributes of magnetic skyrmions that are their nucleation, stability and current-driven motion; all at room temperature. The first results presented in this thesis deal with the stabilisation and nucleation of skyrmions in ultra-thin films (for a ferromagnet thickness around 1 nm) by engineering of the interfacial magnetic properties and the geometry. The nucleation of skyrmions in extended films, confined geometries, exchange-biased films and ion-irradiated films are presented. The second part of this work concerns the current-driven dynamics of magnetic skyrmions. In an ultra-thin Pt/Co/MgO film, we measure velocities up to 100 m s^{-1} for skyrmion sizes in the range of 100 nm. This study further highlights the skyrmion Hall effect, a hallmark of the skyrmion topology, which describes the deflection of a skyrmion trajectory from that imposed by the current. The angle of deflection is found to be dependent on the skyrmion velocity, in contrast with existing models. Combining analytical modelling and micromagnetic simulations, based on a thorough characterisation of the film properties, we find that this dependence on the velocity can be entirely attributed to pinning effects hindering the skyrmion motion. Finally, in the last part of this work, we investigate experimentally synthetic antiferromagnetic multilayers with vanishing magnetic moment. In such systems, magnetic skyrmions are expected to be driven along the current direction — without skyrmion Hall effect, a prerequisite for applications. By optimising specific multilayers and using element-sensitive X-ray microscopy, we observe synthetic antiferromagnetic skyrmions at room temperature with sizes in the range of 100 nm. As their nucleation is somewhat challenging, a device is then designed to locally inject current through patterned tips. This allows to create and delete skyrmions in a controlled fashion using solely current, bringing them one step closer to applications.

Table of Contents

List of Abbreviations

AF	Antiferromagnet(ic)
BL	Bias layer
BLS	Brillouin light scattering
DL	Damping-like
DMI	Dzyaloshinskii-Moriya interaction
FL	Field-like
DW	Domain wall
FIB	Focused ion beam
FM	Ferromagnet(ic)
FMR	Ferromagnetic resonance
HM	Heavy metal
ID	Irradiation dose
IP	In plane
LLG	Landau-Lifshitz-Gilbert
MFM	Magnetic force microscopy
MOKE	Magneto-optical Kerr effect
NM	Non-magnet(ic)
OOP	Out of plane
PMA	Perpendicular magnetic anisotropy
RKKY	Ruderman-Kittel-Kasuya-Yosida
RT	Room temperature
SAF	Synthetic antiferromagnet(ic)
SEM	Scanning electron microscopy
SHE	Spin Hall effect
SIA	Structural inversion asymmetry
SkHA	Skyrmion Hall angle
SkHE	Skyrmion Hall effect
SOC	Spin-orbit coupling
SOT	Spin-orbit torque
SQUID	Superconducting quantum interference device
STT	Spin-transfer torque
STXM	Scanning transmission X-ray microscopy
VSM	Vibrating sample magnetometry
XMCD	X-ray magnetic circular dichroism
X-PEEM	X-ray photo-emission electron microscopy

List of Symbols

A	Exchange constant	J m^{-1}
C	Magnetic field per unit current density	T A^{-1} m^2
D	Dzyaloshinskii-Moriya interaction constant	J m^{-2}
$\boldsymbol{\mathcal{D}}$	Dissipation matrix	kg s^{-1}
$\boldsymbol{F}$	Force	kg m s^{-2} (N)
$\boldsymbol{G}$	Gyrotropic vector	kg s^{-1}
$\boldsymbol{H}$	Magnetic field	A m^{-1}
J	Current density	A m^{-2}
K_{eff}	Effective anisotropy constant	J m^{-3}
K_u	Uniaxial anisotropy constant	J m^{-3}
$\boldsymbol{m}$	Reduced magnetisation vector	
M_s	Saturation magnetisation	A m^{-1}
N_{sk}	Topological charge	
p	Skyrmion core polarity number	
R	Skyrmion radius	m
t_X	Thickness of material X	m
$\boldsymbol{T}$	Reduced torque	s^{-1}
$\hat{\boldsymbol{u}}$	Unit vector	
W	Winding number	
α	Magnetic damping	
γ	Gyromagnetic ratio	Hz T^{-1}
Δ	Domain wall width	m
Θ_{SkH}	Skyrmion Hall angle	
μ_0	Vacuum magnetic permeability	$4\pi \times 10^{-7}$ T A^{-1} m
σ_{DW}	Domain wall energy	J m^{-2}

Introduction

Information storage and handling continuously demands faster, denser, non-volatile and low-power-consuming technologies, which have been fuelling research beyond the conventional semiconductor technologies. In this context, spintronics, which utilises both electronic and spin degrees of freedom, has provided some novel concepts to ameliorate the erstwhile state of the art.

A major breakthrough came with the discovery of the giant magneto-resistance (GMR) effect in late 1980's [1,2]. The GMR refers to a significant change of the resistance of two ferromagnetic (FM) layers separated by a metallic spacer, depending on their relative magnetisation orientation (parallel or anti-parallel). This discovery notably led to a soaring increase in the storage capacity of hard disk drives (HDDs), which revolutionised information storage.

Later on, the tunnel magneto-resistance (TMR) effect [3,4], in the case of two FM layers separated by an insulator, also known as a magnetic tunnel junction (MTJ), was found to be an order of magnitude larger than the GMR, improving the reading power consumption in present-day HDDs. During this period a new memory concept emerged: known as magnetic random access memory (MRAM), it combines the short access time of semiconductor-based RAMs with the non-volatility of magnetic memories. MRAMs essentially consist of a reference (pinned) layer and a free layer separated by an insulating spacer, in which the parallel/anti-parallel magnetisation orientation corresponds to a 0/1 bit. While TMR provides the reading part, several writing mechanisms were explored to achieve fast, reliable and low-power switching of the free layer. These included local magnetic fields applied via current lines (Oersted fields) until new current-induced mechanisms emerged. Spin-transfer torque (STT) is one such method which utilises the reference layer as a spin-polariser for the electrical current flowing through the MTJ [5,6]. This spin-polarised current then switches the free layer magnetisation via spin angular momentum transfer.

More recently, a new mechanism, the so-called spin-orbit torque (SOT), was discovered in systems with structural inversion asymmetry using large-spin-orbit-coupling (SOC) materials such as a heavy metal (HM), adjacent to a FM [7]. In such systems, when a charge current flows in the HM, a spin accumulation is generated at the HM/FM interface by SOC-related mechanisms, either in the bulk of the HM (spin Hall effect) or at the interface (Rashba effect). This results in a torque exerted on the FM layer magnetisation and subsequently switches it. This type of switching was proven to be more efficient and hence lower power consuming than the conventional STTs. It therefore triggered the idea of SOT-MRAM, combining the advantages of low energy writing and high endurance by separating the read and the write paths, as opposed to STT-MRAM.

In parallel emerged an alternative idea to manipulate information using magnetic domains in domain wall (DW) racetrack memories [8]. Here an information bit is no longer localised in an MRAM cell but is mobile in a nanowire consisting of a chain of $\uparrow$ and $\downarrow$ domains separated by DWs. Building three-dimensional nanowires arrays with integrated reading and writing elements would allow to achieve even higher storage density. Nevertheless, this concept faces drawbacks of limited speed as it relies on STTs to displace the DWs.

In systems with structural inversion asymmetry (SIA), a new interaction was unveiled: the Dzyaloshinskii-Moriya interaction (DMI). The DMI imposes a chiral configuration on the DW, *i.e.* a fixed direction of rotation of the magnetisation from $\uparrow$ to $\downarrow$. When combined with SOTs, it was shown to lead to extraordinarily high DW speeds, promising even faster manipulation of information.

In recent years, a new protagonist entered the game of spintronics: the magnetic skyrmion. A magnetic skyrmion is a chiral, localised whirling of the magnetisation stabilised by the DMI. In simpler words, it consists of a small magnetic domain enclosed by a chiral DW. The potential nanometre size of magnetic skyrmions, their expected efficient current-induced manipulation by SOTs and high stability have made them promising candidates to store and manipulate information in so-called skyrmion racetrack memory, heir of the DW racetrack memory [9]. While theoretically discussed thirty years ago, they were only recently observed at low temperature first in 2009 in bulk materials, and shortly after in 2011 in systems with SIA. An important breakthrough came with their observation at room temperature (RT) in 2015 and 2016, which has made skyrmionics a 'hot' topic in magnetism since then. This is well reflected by the number of publications and citations of articles containing the words 'magnetic' and 'skyrmion' shown in Fig. I.1 for the past two decades.

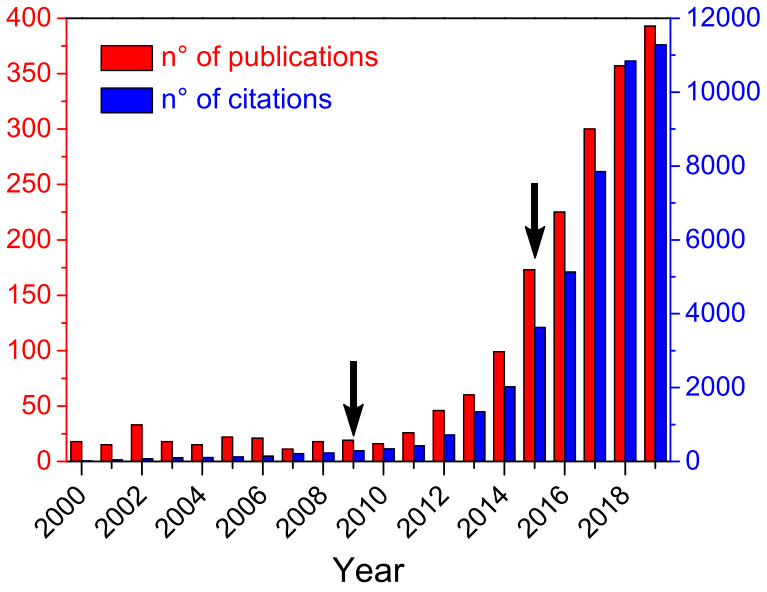

Fig. I.1: Magnetic skyrmions: a 'hot' topic | Number of publications (red) including the words 'magnetic' and 'skyrmion' and number of citations (blue) of these articles over the last twenty years. The two arrows indicate the first observations of magnetic skyrmions at low temperature in bulk materials (2009) and in systems with structural inversion asymmetry at room temperature (2015) *(source: Web of Science)*.

At the beginning of this thesis, in 2016, we are in what one may call the 'boom' of room-temperature skyrmionics. Following these early observations, there are many challenges that lie on the way to skyrmion-based devices. These include their controlled nucleation, stability, scalability and current-driven motion. The observation of magnetic skyrmions at RT in Pt/Co/MgO in 2016 at Spintec provided the starting point of my PhD. In this context, the primary objectives of this work were to study the skyrmion nucleation and stabilisation as well as their current-driven dynamics. Different mechanisms to nucleate and stabilise skyrmions were explored in Pt/Co/MgO-based systems through engineering of the interfacial magnetic properties and geometries. In parallel, the current-driven skyrmion dynamics was studied in the same system. This study notably highlighted the skyrmion Hall effect, a signature of the skyrmion topology, that imposes a deflection of the skyrmion in a direction perpendicular to the applied current. As this effect is detrimental for future applications, it would need to be suppressed. For this purpose, the last part of this work is dedicated to the study of synthetic antiferromagnetic (SAF) skyrmions which are foreseen to resolve this issue. The outline of this manuscript is given below.

Outline This thesis is divided into six main chapters, a conclusion chapter and an appendix. A list of the abbreviations and symbols used is provided. All links (figures, equations, chapter and section names, footnotes, references) are click-able. The manuscript is organised as follows:

Chapter 1: Essential notions on interfacial magnetism and domain walls | This chapter is meant to introduce the basic concepts required to understand the results of this thesis. The magnetic energies at play in magnetic materials and in particular in ultra-thin HM/FM/NM films (*i.e.* for FM thickness of 1 nm or less) are first recalled. Further, essential notions on DW statics and dynamics driven by an external magnetic field and an electrical current are provided.

Chapter 2: Magnetic skyrmions: properties and dynamics | This chapter is entirely dedicated to magnetic skyrmions in ultra-thin HM/FM/NM films with perpendicular magnetic anisotropy. It aims to provide a clear definition of what a magnetic skyrmion is and some key elements to understand their stability and current-driven motion. It draws on the state of the art of the research in the field of skyrmionics (including results published during my thesis).

Chapter 3: Experimental techniques | This chapter presents the different experimental techniques of magnetic characterisation and microscopy used during my thesis. A particular attention is drawn to X-ray microscopy techniques to interpret the images presented in the following chapters. The nanofabrication process used to make the different devices studied is also detailed.

Chapter 4: Skyrmion nucleation in ultra-thin films | This chapter presents different approaches investigated during my PhD to tackle certain key aspects regarding the skyrmion nucleation and stability in ultra-thin FM films at RT. It consists mainly of the study of skyrmion nucleation in extended films, confined geometries, exchange-biased films and He^+-irradiated films.

Chapter 5: Current-driven skyrmion dynamics in ultra-thin films | This chapter presents the study of the current-driven motion of magnetic skyrmions in an ultra-thin Pt/Co/MgO film at RT. The experimental results, including the observation of the current-driven skyrmion motion and characterisation of the magnetic film properties, are first presented. These results are then discussed and interpreted in the light of the Thiele model and micromagnetic simulations.

Chapter 6: Skyrmions in synthetic antiferromagnets | Here, the optimisation of SAF multilayers is first detailed, followed by the observation of SAF skyrmions using element-sensitive X-ray microscopy. Finally, an approach to locally nucleate skyrmions by injection of ns current pulses is presented.

Chapter 7: Summary and perspectives | Here, the main results of this thesis presented in the three previous chapters are briefly summarised, highlighting the future prospects of this work.

Appendix: Forces of the Thiele equation | This chapter details the different steps to calculate the skyrmion velocity and skyrmion Hall angle using Thiele's approach to model the current-driven skyrmion dynamics.

Chapter 1

Essential notions on interfacial magnetism and domain walls

This chapter is meant to introduce the basic concepts required to understand the results of this thesis. First, an overview of the different magnetic energies and interfacial properties is provided. Then, focusing the discussion on ultra-thin films exhibiting perpendicular magnetic anisotropy (PMA) and structural inversion asymmetry (SIA), we explore their role in determining the stable magnetic configuration; in particular the formation of domain walls (DWs). Finally, as an introduction to the case of magnetic skyrmions, discussed in the next chapter, an insight into the mechanisms governing the dynamics of domain walls is given.

1.1 Overview of magnetic energies in thin films

1.1.1 Introduction: magnetic order and micromagnetism

In a magnetic material, each atom at site i carries a net magnetic moment, also referred to as atomic spin or simply as spin, $\boldsymbol{S_i}$.[1] The volume density of magnetic moments defines the magnetisation, $\boldsymbol{M}$ (in A m^{-1}). The saturation magnetisation, M_s, is the maximum magnetisation available in the system when all the magnetic moments are collinear.

A ferromagnet (FM) is a material exhibiting a net magnetisation below the ordering temperature, T_c, called the Curie temperature, such that $M_s(T < T_c) > 0$. Above T_c the thermal fluctuations outweigh the interaction between magnetic moments, resulting in a net cancellation of the magnetisation ($M_s(T > T_c) = 0$), which defines the paramagnetic state. In contrast, an antiferromagnet (AF) is a material exhibiting a zero net magnetisation as a result of the anti-parallel alignment of neighbouring magnetic moments. The AF state is again dependent on temperature and exists below an ordering temperature, T_N, called the Néel temperature. For $T > T_N$, the AF order is broken by the thermal fluctuations, leading to the paramagnetic state. Finally, if the magnetisation of a system with AF order is not fully compensated, owing to the different magnitudes of the AF-coupled magnetic moments, the system is referred to as ferrimagnetic.

The magnetisation of non-atomically-small systems is usually handled in the framework of micromagnetism. This model, originally developed by Brown [10], is based on a continuum approximation: since the length scale of the variation of the atomic magnetic moments direction, typically the exchange length $4-10$ nm, is much larger than the inter-atomic distances, typically $0.2-0.3$ nm, their discrete nature can be overlooked and the magnetisation can be described by a continuous function, $\boldsymbol{M}(\boldsymbol{r})$, of the spatial coordinate $\boldsymbol{r}$. In addition, for a given material and at a given temperature, T, the norm of the magnetisation is constant and equal to the saturation magnetisation, $M_s(T)$, in a uniformly magnetised part of the system (*i.e.* a magnetic domain). It is therefore suitable to define the reduced magnetisation vector, $\boldsymbol{m}(\boldsymbol{r}) = \boldsymbol{M}(\boldsymbol{r})/M_s(T)$, a continuously varying unit vector indicating the local direction of the magnetisation.

[1] To avoid confusion, it will be specified in the following when referring to the spin of electrons.

1.1.2 Zeeman energy

The Zeeman energy is related to the interaction of magnetic moments with an external magnetic field. Its density (in J m^{-3}) is given by

$$\varepsilon_Z = -\mu_0 M_s \boldsymbol{m} \cdot \boldsymbol{H}_{ext} \tag{1.1}$$

with μ_0 the vacuum permeability, M_s the saturation magnetisation, $\boldsymbol{m}$ the reduced magnetisation vector and $\boldsymbol{H}_{ext}$ the external magnetic field. It promotes the alignment of the magnetisation along the external field. Note that all the magnetic energy contributions described hereafter can be associated with an effective magnetic field such that each term can be written as in eq. (1.1).

1.1.3 Symmetric exchange interaction

The symmetric exchange interaction, first introduced by Heinsenberg in the 1920's, promotes the alignment of two neighbouring magnetic moments $\boldsymbol{S}_i$ and $\boldsymbol{S}_j$. This short-range interaction originates from the Coulomb repulsion between electrons of atoms on sites i and j and is spin-dependent because of the Pauli exclusion principle. Using an atomistic description, the Hamiltonian takes the following form:

$$\mathcal{H}_{ex} = -\sum_{i<j} J_{ij} \boldsymbol{S}_i \cdot \boldsymbol{S}_j \tag{1.2}$$

Here, J_{ij} (in J) is the exchange integral between two neighbouring atoms i and j and the sum is over all neighbouring atoms. Considering only the nearest neighbours and an isotropic material, one has $J_{ij} = J$ for all pairs of nearest neighbours i and j. The sign of J then determines the magnetic ordering: when $J > 0$, the FM state is energetically favoured (all the spins parallel) while the AF state (neighbouring spins anti-parallel and zero net magnetisation) is favoured when $J < 0$. Note that in certain alloys where an AF coupling exists, *e.g.* Co_xTb_{1-x}, Co_xGd_{1-x}, a net magnetisation can exist if the magnetic moments of the two sub-lattices do not compensate: these materials are referred to as ferrimagnets. In the continuum approximation used in micromagnetism, the energy density associated with the exchange interaction can be written as follows:

$$\varepsilon_{ex} = A \left((\boldsymbol{\nabla} m_x)^2 + (\boldsymbol{\nabla} m_y)^2 + (\boldsymbol{\nabla} m_z)^2 \right) \tag{1.3}$$

with A the exchange constant[1] (in J m^{-1}) given by $A \approx JS^2 n/a$, with a the lattice parameter and n the number of atoms per unit cell [11]. A is typically in the range $10 - 30$ pJ m^{-1} for FM transition metals (Co, Fe, Ni).

1.1.4 Dipolar energy

Each magnetic moment inside a magnetic body generates a magnetic stray field, called dipolar field or magneto-static field, and written $\boldsymbol{H}_d$. This field interacts with all the other magnetic moments composing the magnetic body. The dipolar energy density thus takes the form of a Zeeman-type energy (see eq. (1.1)):

$$\varepsilon_d = -\frac{\mu_0 M_s}{2} \boldsymbol{m} \cdot \boldsymbol{H}_d \tag{1.4}$$

Here the 1/2 factor is introduced not to count twice the interaction between two magnetic moments. The dipolar energy can further be obtained by integrating over the volume of the magnetic body considered. The dipolar interactions depend on the relative orientation of the magnetic moments and on the distance r between them as $1/r^3$. This long-range and fundamentally non-local character makes it difficult to calculate analytically ε_d; it is often required to evaluate it numerically. A way to handle this interaction is to introduce the concept of magnetic charges. Writing the

[1] or exchange stiffness

second Maxwell equation in the absence of external field yields $\boldsymbol{\nabla} \cdot \boldsymbol{B} = \mu_0 \boldsymbol{\nabla} \cdot (\boldsymbol{H}_d + \boldsymbol{M}) = \boldsymbol{0}$, and hence $\boldsymbol{\nabla} \cdot \boldsymbol{H}_d = -\boldsymbol{\nabla} \cdot \boldsymbol{M}$. Note that only the part of the dipolar field occurring inside the magnetic body, the so-called demagnetising field, is considered. From this equation, it is possible to define magnetic volume charges as $\rho_M = \boldsymbol{\nabla} \cdot \boldsymbol{M}$, by analogy with electrostatic charges. Furthermore, it appears that the magnetisation at the edges goes abruptly from a finite value, M_s, to zero. This singularity can be lifted by introducing surface magnetic charges: $\sigma_M = \boldsymbol{M} \cdot \hat{\boldsymbol{n}}$, with $\hat{\boldsymbol{n}}$ the unit vector normal to the surface of the. When considering only the dipolar interaction, the ground state is then given by the magnetic configuration that minimises the volume and magnetic surface charges. As a result, the shape of the magnetic body strongly influences the dipolar energy, giving rise to a shape anisotropy.

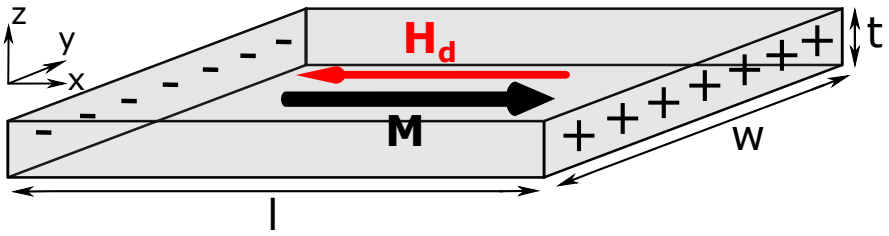

Fig. 1.1: Demagnetising field inside a uniformly magnetised thin film | $\boldsymbol{M}$ denotes the magnetisation, $\boldsymbol{H}_d$ the demagnetising field and the $+/-$ symbols indicate the magnetic surface charges created by the uniform magnetisation. In the case of a thin film with $l > w \gg t$, the magnetisation aligns preferentially with the length of the film as this configuration minimises magnetic surface charges.

To illustrate this, let us consider the case of a uniformly magnetised thin film with length l, width w and thickness t such that $l > w \gg t$, as illustrated in Fig. 1.1. The demagnetising field can be expressed simply in terms of the demagnetising coefficients N_i as:

$$H_{d,i} = -N_i M_i \tag{1.5}$$

with $i = x, y, z$ and $N_x + N_y + N_z = 1$. For the thin film considered, one has $N_x < N_y \ll N_z$, hence $N_z \approx 1$ [12]. Therefore, in the absence of any other anisotropy, the magnetisation would spontaneously align along the length of the sample. This can be seen in Fig. 1.1: if the magnetisation aligned along the y- or the z-axis, the amount of surface charges would increase, thus increasing the demagnetising energy. Therefore, any deviation from the x-axis would constitute a cost in dipolar energy, which introduces a shape anisotropy in the system. If the two lateral dimensions are identical, it defines an easy plane for the magnetisation. Assuming that the magnetisation is uniform and subtends an angle θ with the film normal, eq. (1.5) yields $\boldsymbol{H}_d = -\boldsymbol{M}_z$. The dipolar energy density (eq. (1.4)) thus reads

$$\varepsilon_d = \frac{\mu_0 M_s^2}{2} \cos^2\theta = K_d \cos^2\theta \tag{1.6}$$

where K_d is the shape anisotropy constant (in J m^{-3}). This shape anisotropy tends to bring the magnetisation in the plane of the film. K_d is a measure of the maximum energy density that may be connected with demagnetising fields.

1.1.5 Spin-orbit coupling

In magnetic materials, and in particular in multi-layered films, the spin-orbit coupling (SOC) is the source of a multitude of emergent phenomena such as the perpendicular magnetic anisotropy, the spin Hall effect, the Rashba-Edelstein effect and the Dzyaloshinskii-Moriya interaction [13]. The SOC describes the relativistic interaction between the electron spin and orbital angular momenta. Let us consider a semi-classical picture of an electron orbiting around the nucleus of an atom. In

the nucleus rest frame, the electron moves at a velocity $\boldsymbol{v}$ in an electric field $\boldsymbol{E}$ generated by the nucleus. In its rest frame, the electron experiences a magnetic field that can be written as

$$\boldsymbol{B}_{SO} = \frac{1}{c^2}\boldsymbol{E} \times \boldsymbol{v} \tag{1.7}$$

where c is the speed of light. This leads to a Zeeman-type interaction between the intrinsic magnetic moment of the electron, $\boldsymbol{\sigma}$, and this magnetic field, given by the following Hamiltonian:

$$\mathcal{H}_{SO} = -\boldsymbol{\sigma} \cdot \boldsymbol{B}_{SO} = \lambda_{SO}\boldsymbol{L} \cdot \boldsymbol{S} \tag{1.8}$$

Here, $\boldsymbol{L}$ and $\boldsymbol{S}$ are respectively the electron orbital and spin angular momenta and λ_{SO} is a constant. This energy is thus greatly dependent on the local electric field $\boldsymbol{E}$ which can arise from the same ion or from a neighbouring ion in the material, in the bulk or at an interface. In addition, one can show that λ_{SO} scales as Z^4, with Z the atomic number [14]. This explains why the SOC is strong in heavy elements such as Pt, Ta, W and Ir.

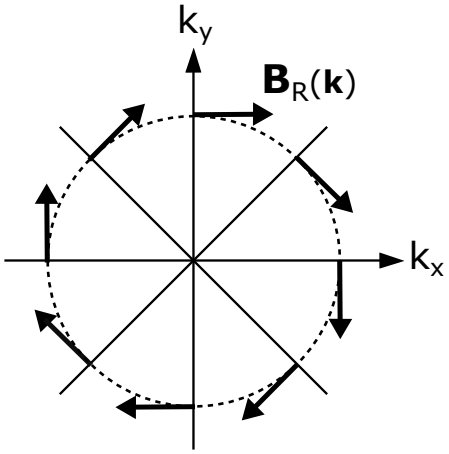

Fig. 1.2: Orientation of the Rashba field in the momentum space | The Rashba field $\boldsymbol{B}_R(\boldsymbol{k})$ (black arrows) of eq. (1.9) is orthogonal to the momentum $\boldsymbol{k}$ of the electron at the interface. In this picture, $\hat{\boldsymbol{z}}$ is the normal to the interface.

In systems with structural inversion asymmetry (SIA), *e.g.* a stack A/B/C composed of three different materials,[1] a particular SOC-related phenomenon takes place at the interface: the Rashba SOC [15,16]. Due to SIA, an asymmetric potential exists at the interface, which generates an electric field, $\boldsymbol{E} = E\hat{\boldsymbol{z}}$, $\hat{\boldsymbol{z}}$ being the interface normal. The itinerant electrons moving in this electric field experience a momentum-dependent effective magnetic field, $\boldsymbol{B}_R(\boldsymbol{k})$, referred to as Rashba field. The interaction between the electron spin magnetic moment and the Rashba field is given by the following Hamiltonian [17]:

$$\mathcal{H}_R = -\boldsymbol{\sigma} \cdot \boldsymbol{B}_R(\boldsymbol{k}) = \alpha_R \boldsymbol{\sigma} \cdot (\boldsymbol{k} \times \hat{\boldsymbol{z}}) \tag{1.9}$$

where $\alpha_R \propto E$ is the Rashba coefficient ($\sim$ 0.1 eV nm) and $\boldsymbol{k}$ the electron momentum (*i.e.* its wave vector). As depicted in Fig. 1.2, the Rashba field is always orthogonal to the electron momentum. This means that electrons with different $\boldsymbol{k}$-vectors experience different $\boldsymbol{B}_R$ and precess around it. In the following, we discuss two major implications of the Rashba SOC on the Dzyaloshinkii-Moriya interaction and the current-induced spin-orbit torques, in §1.1.7 and §1.3.3.2 respectively.

[1] A/B/C means that A is the bottom layer (first deposited) and C the top layer. This convention will be used throughout this thesis.

1.1.6 Magnetic anisotropy

1.1.6.1 Magneto-crystalline anisotropy

The exchange interaction predicts the spontaneous magnetisation but cannot account for other properties of magnetic materials such as the hysteresis phenomenon. In real systems, the spins tend to align along specific crystallographic directions that are not necessarily the direction given by the shape anisotropy: this contribution is referred to as magneto-crystalline anisotropy (MCA). The MCA is linked to the crystal field, that is the static electric field produced by the surrounding charge distribution of the crystal. Due to the SOC, the spins prefer to align along certain crystallographic directions that minimise the SOC energy (see eq. (1.8)). One type of MCA is the uniaxial anisotropy, which is present for example in hexagonal, tetragonal and rhombohedral structures. In this case, the MCA energy density has the following form (in the second-order approximation):

$$\varepsilon_{MC} = K_1 \sin^2 \alpha \tag{1.10}$$

K_1 is the volume uniaxial anisotropy constant (in J m^{-3}) and α the angle between the spin (or the magnetisation vector in a micromagnetic picture) and the high-symmetry axis of the crystal (*e.g.* the c axis for the hexagonal structure). This axis, along which the spins preferentially align, is referred to as easy axis, while any crystallographic axis perpendicular to it is called a hard axis. Note that only the second-order term is considered: for large positive K_1 values, this approximation is valid and one has indeed a uniaxial anisotropy. However, for negative K_1, the system exhibits an easy plane, perpendicular to the high-symmetry axis, and higher-order terms need to be taken into account.

1.1.6.2 Interface-induced magnetic anisotropy

In multi-layered films, the broken symmetry at interfaces can generate an additional anisotropy. First predicted by Néel in 1953 [18], it is described by a uniaxial anisotropy energy [19]:

$$\varepsilon_S = \frac{K_s}{t} \sin^2 \theta \tag{1.11}$$

where K_s is the surface anisotropy constant (in J m^{-2}), t the magnetic film thickness and θ the angle between the magnetisation and the film normal. This contribution tends to bring the magnetisation in the out-of-plane (OOP) direction, hence the convention $K_s > 0$. Note that K_s contains the contributions from the two interfaces. This term introduces an easy axis, perpendicular to the film plane, and adds up to the aforementioned bulk MCA as well as to the shape anisotropy. The total anisotropy of the system is thus usually described by an effective anisotropy constant: $K_{eff} = K_1 + K_s/t - \mu_0 M_s^2/2$. In ultra-thin films, the volume contribution to the anisotropy is in most cases dominated by the shape anisotropy.[1] The effective anisotropy constant then simplifies into:

$$K_{eff} = \frac{K_s}{t} - \frac{\mu_0 M_s^2}{2} \tag{1.12}$$

The quantity $K_u = K_s/t$ (in J m^{-3}) is referred to as uniaxial anisotropy constant such that $K_{eff} = K_u - K_d$. Therefore, if the interface anisotropy outweighs the shape anisotropy, *i.e.* $K_{eff} > 0$, it promotes an OOP easy axis, giving rise to perpendicular magnetic anisotropy (PMA). From eq. (1.12), it is hence possible to define a critical FM thickness t_c above which the magnetisation preferentially lies in the film plane. It defines the spin reorientation transition between PMA and in-plane (IP) anisotropy; typically, $t_c \sim 1$ nm for Pt/Co-based systems. Fig. 1.3.a displays schematically the variation of the quantity $K_{eff}t$ with the magnetic film thickness t [20]. The slope at large t provides the volume contribution (largely the shape anisotropy) while the intercept provides the interface contribution. For very small thicknesses (typically $0.2 - 0.3$ nm), the Curie

[1] Except in the case of epitaxial films where it is usually of the same order as the MCA.

temperature and thus M_s decrease due to intermixing of the FM with the adjacent layers, resulting in a deviation from linearity.

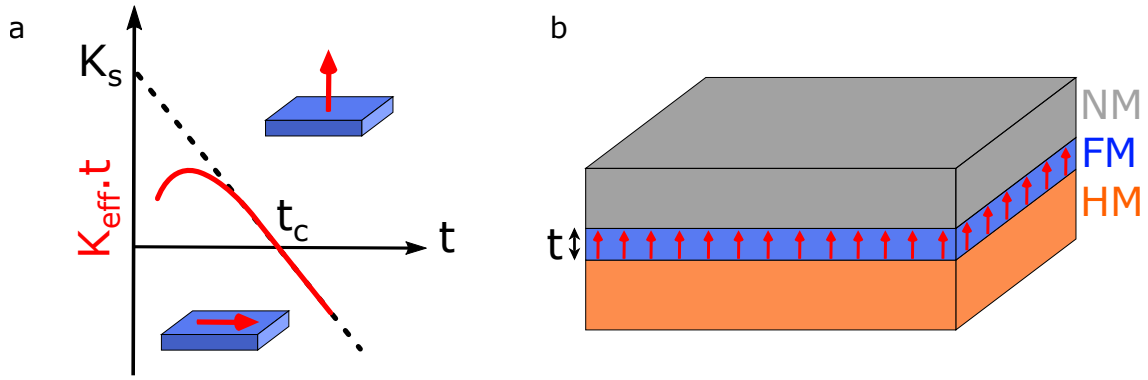

Fig. 1.3: Perpendicular magnetic anisotropy | **a.** Evolution of the effective anisotropy constant with the FM film thickness t. For Pt/Co/MgO, the critical thickness is $t_c \approx 1$ nm. **b.** A typical PMA stack composed of a heavy metal (HM), a ferromagnet (FM) and a non-magnetic (NM) layer, for example an oxide or another HM.

A typical PMA stack is represented in Fig. 1.3.b. It is composed of a HM (Pt, Ta, W, Pd), an ultra-thin ($t \approx 1$ nm) FM (Co, CoFeB) and a NM layer; the latter can either be an oxide (AlO_x, MgO) or another HM. In this type of stack, both interfaces contribute to the PMA.

At the HM/FM interface, the PMA is attributed to the hybridisation of the $5d$ orbitals of the HM and the $3d$ orbitals of the FM, which modifies the crystal field at the interface. In the case of the Pt/Co interface, due to the large SOC of the Pt, this leads to an enhancement of the OOP Co magnetic moment and results in an induced Pt magnetic moment that aligns parallel to the Co moment [21,22].

Let us consider the case of a HM/FM/Ox stack, for instance Pt/Co/MgO which has been used in this thesis to study the stability and dynamics of magnetic skyrmions. The FM/Ox interface also contributes to the PMA [23]. Here, the SOC is much weaker and the PMA stems from the hybridisation of the $3d$ orbitals of the FM and the $2p$ orbitals of the oxygen [24]. The PMA is thus greatly dependent on the oxidation state at the interface and is therefore sensistive to oxygen migration, for example upon annealing [25,26].

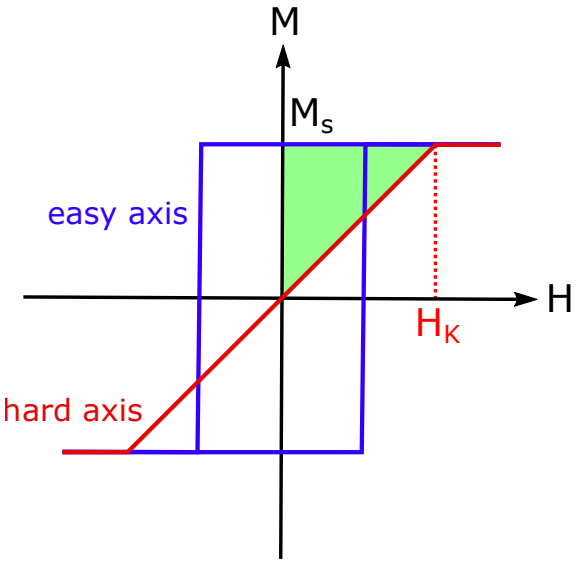

Fig. 1.4: Determination of the effective anisotropy | Schematic representation of the easy-axis and hard-axis hysteresis loops for a FM film with large PMA. H_K is referred to as the anisotropy field.

Experimentally, the effective anisotropy can be determined from the hard-axis hysteresis loop. It is represented schematically in Fig. 1.4 (in red) in the case of a sample exhibiting a large PMA ($M = M_s$ in the OOP direction at zero field). K_{eff} is the energy barrier that needs to be overcome to bring the magnetisation in the film plane. The energy density needed to change the magnetisation by an amount dM is given by $\varepsilon = \mu_0 H dM$, where H is the external magnetic field. Graphically, this energy is given by the area comprised between the easy- and hard-axis loops (in green). When $H = H_K$, with H_K the so-called anisotropy field, the magnetisation is completely saturated in the plane, hence $K_{eff} = \mu_0 H_K M_s/2$.

1.1.7 Dzyaloshinskii-Moriya interaction

The Dzyaloshinskii-Moriya interaction (DMI) is an antisymmetric exchange interaction. It is a key element in the stabilisation of chiral magnetic textures such as chiral domain walls and magnetic skyrmions. It was first proposed by Dzyaloshinskii in 1958 [27] to explain the weak yet non-zero spontaneous magnetisation observed in certain AF materials. He understood that there was a direct link between the symmetry of the crystal and the magnetic configuration. Shortly after, in 1960, Moriya demonstrated how to calculate this additional exchange by taking into account the SOC in a crystal lacking inversion symmetry [28,29]. The DMI Hamiltonian has the following form:

$$\mathcal{H}_{DMI} = -\sum_{i<j} \boldsymbol{d}_{ij} \cdot (\boldsymbol{S}_i \times \boldsymbol{S}_j) \tag{1.13}$$

with $\boldsymbol{d}_{ij}$ the DMI vector whose direction depends on the crystal symmetry and whose amplitude is proportional to the SOC. The DMI energy is minimum when the two spins $\boldsymbol{S}_i$ and $\boldsymbol{S}_j$ are perpendicular to each other and when the cross product $\boldsymbol{S}_i \times \boldsymbol{S}_j$ is parallel to $\boldsymbol{d}_{ij}$. The DMI hence favours non-collinear spin textures with a preferred sense of rotation such as chiral domain walls, spin spirals and magnetic skyrmions. This preferred sense of rotation, given by the sign of $\boldsymbol{d}_{ij}$, defines the spin texture chirality. It can be seen that — in the absence of any other interaction — the DMI and the exchange interaction act on the same length scale and compete directly to determine the type of magnetic texture, collinear or non-collinear.

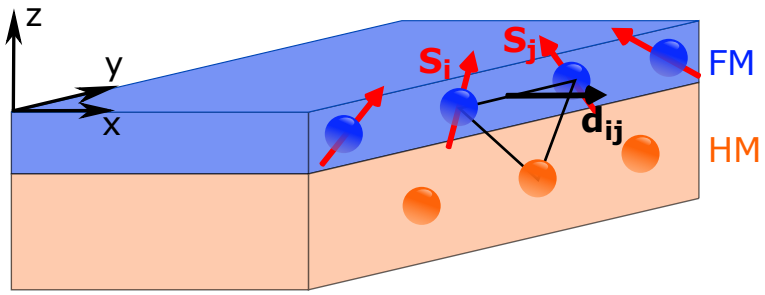

Fig. 1.5: Dzyaloshinskii-Moriya interaction at the HM/FM interface | Schematic representation of the DMI at the interface between a HM and a FM as described by the 3-site mechanism proposed by Fert and Levy [30,31].

The DMI can exist in crystals lacking inversion symmetry, like B20 crystallographic structures (*e.g.* MnSi, FeGe), and is referred to as bulk DMI. It was notably in MnSi that magnetic skyrmions were first observed in 2009 [32].

In addition, the DMI can arise at interfaces in systems exhibiting SIA. SIA naturally exists in multilayers where the FM layer is sandwiched between two different materials. The resulting DMI is hence referred to as interfacial DMI [30,33,34]. This interfacial DMI has been predicted by Fert and Levy to arise from a 3-site mechanism between two neighbouring spins of the FM $\boldsymbol{S}_i$ and $\boldsymbol{S}_j$ and a non-magnetic ion with a large SOC (*e.g.* a HM) [30,31]. It is illustrated in Fig. 1.5: in this case, the DMI vector is given by $\boldsymbol{d}_{ij} = d\,(\hat{\boldsymbol{r}}_{ij} \times \hat{\boldsymbol{z}})$ where $\hat{\boldsymbol{z}}$ is the unit vector perpendicular to the film plane and $\hat{\boldsymbol{r}}_{ij}$ is the unit vector connecting the two spins and pointing towards $\boldsymbol{S}_j$ [9,31]. The sign of d hence defines the favoured direction of rotation: $d > 0$ promotes left-handed (anticlockwise) rotation

of spins ↑↖←↙↓ while $d < 0$ promotes right-handed (clockwise) rotation of spins ↑↗→↘↓.[1] In addition, the DMI depends by definition on the stacking order. For example, Co on Pt favours a left-handed chirality while Pt on Co favours a right-handed chirality. Consequently, the DMI vanishes for a Pt/Co/Pt film and in general for symmetric stacks. Note however that for polycrystalline films, because of the different growth conditions, the two interfaces may not be identical and a small DMI can be measured [35]. Similarly, the DMI can be artificially enhanced by combining interfaces with opposite DMI signs [36] such as Pt/Co and Ru/Co into Pt/Co/Ru [37,38].

The DMI is usually handled in the continuum approximation. From eq. (1.13), one can express the DMI energy density [39]:

$$\varepsilon_{DMI} = D\left((\boldsymbol{m}\cdot\boldsymbol{\nabla})\, m_z - m_z \boldsymbol{\nabla}\cdot\boldsymbol{m}\right) \tag{1.14}$$

with D (in J m^{-2}) the micromagnetic DMI constant. Similarly to the exchange constant A (see §1.1.3), the DMI constant can be expressed as $D \sim d/at$ where d is the amplitude of the DMI vector, a the lattice parameter of the FM and t the magnetic film thickness [40,41]. D is typically in the order of $1-2$ mJ m^{-2} for Pt/Co. Then, the associated effective magnetic field is [42]:

$$\boldsymbol{H}_{DMI} = -\frac{2D}{\mu_0 M_s}\left(\boldsymbol{\nabla} m_z - (\boldsymbol{m}\cdot\boldsymbol{\nabla})\,\hat{\boldsymbol{z}}\right) \tag{1.15}$$

In an ultra-thin film exhibiting PMA, this magnetic field exists only inside DWs: it is oriented in the film plane and perpendicular to the DW. As detailed hereafter (§1.2), $\boldsymbol{H}_{DMI}$ favours the formation of Néel DWs over Bloch DWs which would otherwise minimise the DW dipolar energy.

Different methods are used to measure the DMI. A first approach consists in measuring the effective DMI magnetic field by propagating DWs with an easy-axis OOP field in the presence of an IP field [35,43,44]. The external field for which the DW velocity is zero provides a measurement of H_{DMI} and hence of D. Moreover, it was shown that the DMI can be extracted from spin-wave spectroscopy techniques such as Brillouin light spectroscopy (BLS) [41,45,46] as it will be presented in §5.3.2.

Furthermore, the DMI can also exist in the absence of HM or large-SOC material. To explain this, a mechanism based on the Rashba SOC was proposed [47]. As explained in §1.1.5, the itinerant electrons at an inversion-asymmetric interface experience a momentum-dependent magnetic field, the Rashba field $\boldsymbol{B}_R$. The precession of the electron spins around $\boldsymbol{B}_R$ results, through $s-d$ exchange coupling with the local magnetic moments, in the canting of the magnetisation in a specific direction. The direction of the canting is dictated by the direction of the Rashba field. This effect is hence referred to as Rashba DMI with the associated DMI constant: $D_R = 4\alpha_R m_e A/\hbar^2$ [47]. This Rashba DMI can notably explain the DMI arising at a FM/Ox interface, *e.g.* Co/MgO or Fe/MgO [36], and can account for the large DMI measured in Pt/Co/AlO$_x$ [41] and Pt/Co/MgO [48], systems that combine a HM/FM and a FM/Ox interface. Finally, it can also explain the voltage-induced tuning of DMI measured experimentally [49].

To summarise, for both mechanisms, the DMI is of interfacial origin and requires the presence of SIA. As predicted by *ab initio* calculations, the sign and amplitude of the DMI for a given set of materials is largely determined by the atoms right at the interface [36,40]. Being of interfacial origin, it follows an inverse-dependence with the FM film thickness t [41,50] such that an interfacial DMI parameter D_s can be defined by $D = D_s/t$. D_s is in the order of 1 pJ m^{-1}, that is one order of magnitude smaller than the exchange constant. Note however that the interfacial DMI also depends on the thickness of the adjacent HM layer in a HM/FM stack [51,52]. For example, Kim *et al.* [51] found that in a sputtered Pt(t_{Pt})/Co(1.6nm)/AlO$_x$(2nm) film, the DMI increases monotonically with the Pt thickness, up to $t_{Pt} \approx 2.5$ nm where it saturates. One possible explanation is the improvement of the interface quality and the promotion of the (111) texturing of the Pt as it is made thicker. In this work, all the stack studied are Pt/Co-based and exploit the large DMI present at the Pt/Co interface.

[1] Note that this sign convention can be different in the literature as it depends on the definition of $\mathcal{H}_{DMI}$ and $\boldsymbol{d}_{ij}$. For consistency, we will use the same throughout this work. In addition, only the denomination left/right-handed will be used in the following.

1.1.8 Interlayer exchange coupling: artificial magnetic order

In the above sections, we saw the different energies at play inside a magnetic material: the Zeeman, exchange, dipolar, anisotropy and DMI energies. In particular, we saw that the exchange interaction is responsible for the magnetic ordering, FM or AF. In magnetic multilayers, magnetic order can be induced artificially by an indirect exchange interaction mediated by a non-magnetic metallic spacer, the so-called Ruderman-Kittel-Kasuya-Yosida (RKKY) interaction [53,54]. In a $FM_1/NM/FM_2$ stack, the magnetic ions in one FM layer spin-polarise the conduction electrons in their neighbourhood, which then mediate the interaction with the magnetic ions in the other FM layer through the NM spacer, resulting in an indirect exchange coupling. This coupling between the two FM layers, FM_1 and FM_2, can be FM or AF depending on the NM spacer thickness. The RKKY energy density can be written as $\varepsilon_{RKKY} = -J_{12}\,(\boldsymbol{m}_1 \cdot \boldsymbol{m}_2)$ (in J m^{-2}), with $\boldsymbol{m}_1$ and $\boldsymbol{m}_2$ the magnetisation in FM_1 and in FM_2 respectively. The interlayer exchange constant has the following form [55]:

$$J_{12} \propto \frac{1}{t_{NM}^2} \sin\left(2k_F t_{NM} + \Phi\right) \tag{1.16}$$

where t_{NM} is the NM layer thickness, k_F the Fermi wave vector and Φ a constant. When $J_{12} > 0$ ($J_{12} < 0$), a FM (AF) coupling is promoted. This has a damped oscillatory nature as a function of t_{NM}, as shown in Fig. 1.6. This interaction is notably utilised to build synthetic AFs (SAFs), which consist of two AF-coupled FM layers. SAFs are used to build magnetic tunnel junctions, magnetic sensors and can also be employed to stabilise skyrmions as it will be explained in Chapter 6

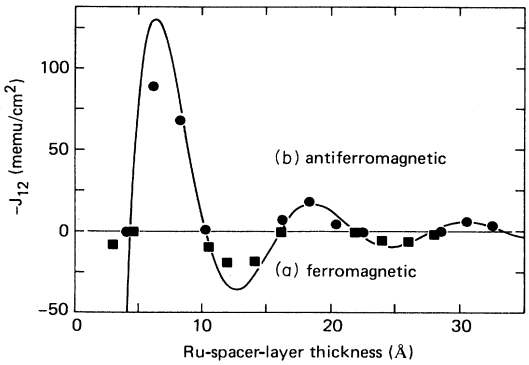

Fig. 1.6: Ruderman-Kittel-Kasuya-Yosida interaction | RKKY exchange constant measured in a CoNi/Ru/CoNi film as a function of the Ru spacer thickness. The solid line is a fit using eq. (1.16). Adapted from ref. [55]

1.2 Domains and domain walls in films with PMA

In the previous section, we saw an overview of the magnetic energies that determine the stable magnetic configuration. In the following, we focus only on ultra-thin films with PMA. Before discussing in details the particular case of magnetic skyrmions in Chapter 2, we describe the case of magnetic domains and domain walls.

Let us first consider a system with PMA, exchange and dipolar interactions only. If the film is uniformly magnetised OOP, magnetic charges appear at the opposite edges (see Fig. 1.1), increasing the total demagnetising energy. In order to minimise this energy, the magnetic texture divides into domains with opposite magnetisation directions (↑ / ↓). The small region separating two domains is called a domain wall (DW). The magnetisation inside a DW can rotate in different ways, the two limiting cases being the so-called Bloch and Néel DW schematically represented in Fig. 1.7. In a Bloch DW, the magnetisation rotates in DW plane (yz plane in Fig. 1.7) while it rotates perpendicular to the DW plane (xz plane) in a Néel DW. The configuration that minimises the

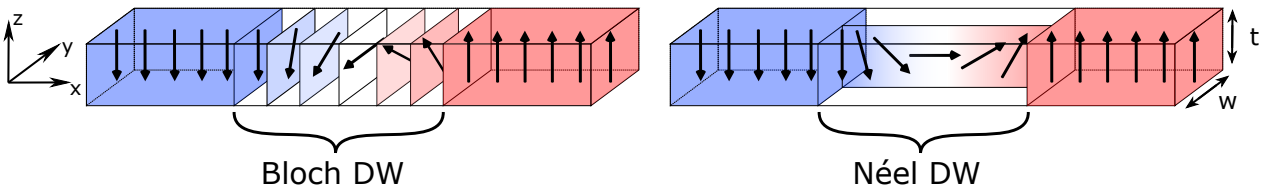

Fig. 1.7: Bloch and Néel domain walls | Schematic representation of a Bloch DW and a Néel DW in an ultra-thin film of thickness t and width w exhibiting PMA.

magneto-static energy is the Bloch DW. Indeed, it prevents the additional creation of magnetic charges since $\boldsymbol{\nabla} \cdot \boldsymbol{m} = \partial m_x / \partial x = 0$, whereas $\boldsymbol{\nabla} \cdot \boldsymbol{m} \neq 0$ in a Néel DW. Therefore, the Bloch DW is energetically favoured. Nonetheless, as the stripe is made narrower ($w \to 0$ in Fig.1.7), the surface demagnetising energy of the Bloch DW increases (due to surface charges in the y direction), which can lead to a reorientation from Bloch to Néel is w if small enough, typically $w < 100$ nm [56]. We will not consider this particular case in the following.

The formation of a DW is energetically expensive: it results from a competition between the exchange and anisotropy energies on the one hand and the demagnetising energy on the other hand. The DW energy σ_{DW}, that is the energy per unit area of the DW (in J m^{-2}) is $\sigma_{DW} = 4\sqrt{AK_{eff}}$ [57]. The energy competition also determines the equilibrium width of the DW, which is given by the Bloch width parameter Δ [57]:

$$\Delta = \sqrt{\frac{A}{K_{eff}}} \tag{1.17}$$

Let us now add the DMI to the problem. As explained previously in §1.1.7, the DMI is equivalent to an effective magnetic field that exists inside the DW and oriented perpendicular to it. If large enough, the DMI can outweigh the gain in dipolar energy that constitutes the Bloch DW and can promote a Néel DW. This is emphasised in Fig. 1.8.a. The DMI hence reduces the DW energy such that [58]:

$$\sigma_{DW} = 4\sqrt{AK_{eff}} \pm \pi D \tag{1.18}$$

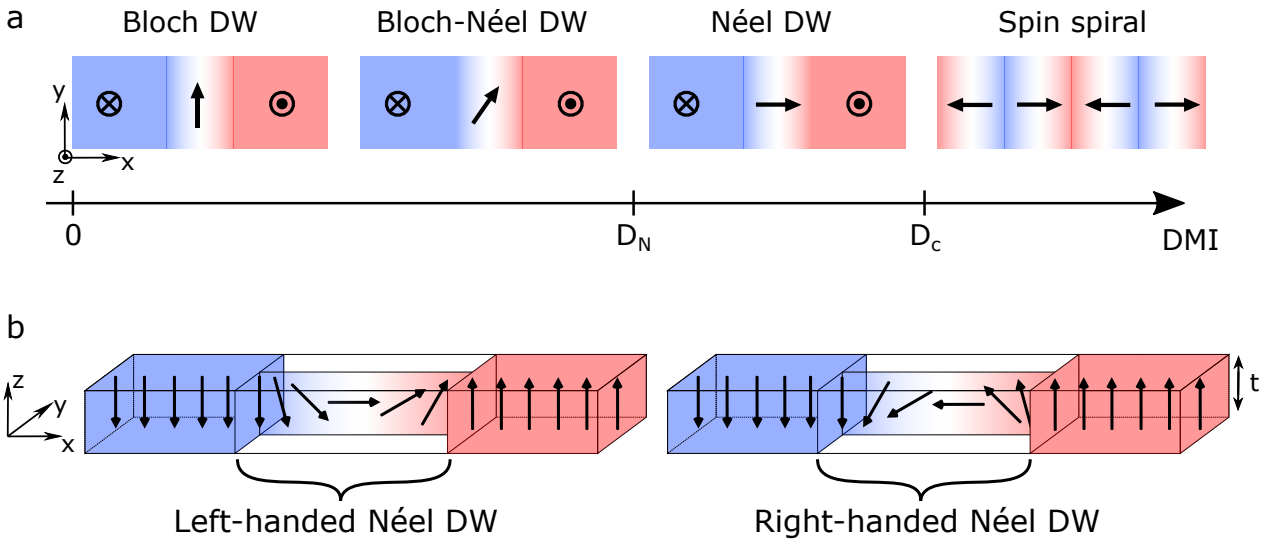

Fig. 1.8: Chiral Néel DW in the presence of DMI | **a.** Transition from Bloch to Néel DW with increasing DMI. When $D_N < D < D_c$, a pure Néel DW is stabilised. When $D > D_c$, the DW energy (eq. (1.18)) becomes negative and a spin spiral is stabilised, that is the magnetisation rotates continuously. **b.** In a left-handed (right-handed) Néel DW, promoted by $D > 0$ ($D < 0$), the magnetisation rotates anticlockwise (clockwise) when moving from left to right across the DW.

Here, the ± sign indicates that one chirality is favoured over the other. More precisely, as previously explained in §1.1.7, $D > 0$ ($D < 0$) promotes a left-handed (right-handed) chirality, as represented in Fig. 1.8.b. Therefore, in addition to determining the orientation (Bloch/Néel), the DMI also fixes the direction of rotation of the spins inside the DW. The resulting DMI-stabilised Néel DW is then referred to as homochiral. In the absence of DMI, both chiralities are equiprobable and the DW is referred to as achiral. Different thresholds can be distinguished (see Fig. 1.8.a): D_N (~ 0.1 mJ m^{-2}) such that for $D_N < D$ a pure Néel DW is stabilised; and D_c such that for $D_N < D_c < D$, the DW energy becomes negative. When $\sigma_{DW} < 0$, the magnetisation rotates continuously with a given sense of rotation and describe a homochiral spin spiral. This critical DMI D_c can be obtain from eq. (1.18): $D_c = 4\sqrt{AK_{eff}}/\pi$. Note finally that the DW width (eq. (1.17)) is expected to be independent of the DMI [58].

1.3 Magnetisation dynamics: the case of DWs in films with PMA

The present section focuses on certain key aspects of the magnetisation dynamics and draws on the example of DWs as an introduction to the case of magnetic skyrmions. The dynamics of DWs driven by an external field is first described, followed by their current-driven dynamics and its underlying mechanisms.

1.3.1 The Landau-Lifshitz-Gilbert equation

The spatial and temporal evolution of the magnetisation is described by the Landau-Lifshitz-Gilbert (LLG) equation [59,60]:

$$\frac{\partial \boldsymbol{m}}{\partial t} = -\gamma_0 \left(\boldsymbol{m} \times \boldsymbol{H}_{eff}\right) + \alpha \left(\boldsymbol{m} \times \frac{\partial \boldsymbol{m}}{\partial t}\right) \tag{1.19}$$

Here, $\gamma_0 = \mu_0 \gamma$ with $\gamma = g|e|/2m_e$ the gyromagnetic ratio. g is the Landé factor[1] ($g \approx 2$), e the electron charge and m_e the electron mass. $\boldsymbol{H}_{eff}$ is the effective magnetic field that includes all the micromagnetic energies (exchange, anisotropy, magneto-static, external field and DMI) as well as any other effective field that may be interacting with the magnetisation. Finally, $\alpha > 0$ is the magnetic damping parameter.

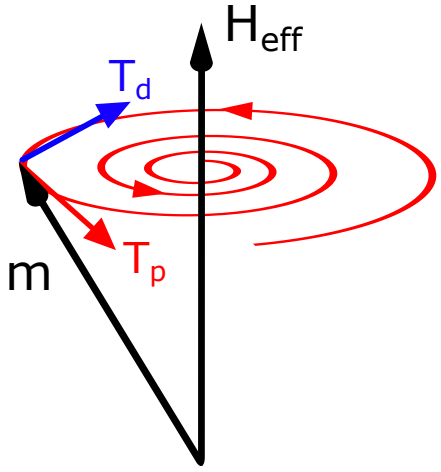

Fig. 1.9: Magnetisation dynamics described by the LLG equation | The first term on the right-hand side of eq. (1.19), $\boldsymbol{T}_p$, describes a precession of the magnetisation $\boldsymbol{m}$ around the effective magnetic field $\boldsymbol{H}_{eff}$. The second term, $\boldsymbol{T}_d$, is the damping torque that tends to align $\boldsymbol{m}$ with $\boldsymbol{H}_{eff}$.

The right-hand side of the LLG equation is the sum of two torques, $\partial \boldsymbol{m}/\partial t = \boldsymbol{T}_p + \boldsymbol{T}_d$. They are represented in Fig. 1.9: the first term, $\boldsymbol{T}_p$, is a conservative torque that describes the precession

[1] or g-factor

of the magnetisation around $\boldsymbol{H}_{eff}$. The second, $\boldsymbol{T}_d$, is a damping term. It tends to align the magnetisation with $\boldsymbol{H}_{eff}$ by describing a spiral around it. Without this term, the magnetisation would precess endlessly. The damping describes the dissipation of magnetic energy within the lattice of the system and encompasses many mechanisms, both intrinsic or extrinsic to the system [61].

1.3.2 Field-driven domain wall dynamics

In magnetic materials, the magnetisation reversal driven by an external magnetic field can occur though domain nucleation and DW propagation. When an external field $\boldsymbol{H}_{ext}$ is applied, two torques are exerted on the magnetisation: $\boldsymbol{T}_{p,H_{ext}} = -\gamma_0 (\boldsymbol{m} \times \boldsymbol{H}_{ext})$ and $\boldsymbol{T}_{d,H_{ext}} = \alpha (\boldsymbol{m} \times \partial \boldsymbol{m}/\partial t) \approx -\gamma_0 \alpha (\boldsymbol{m} \times (\boldsymbol{m} \times \boldsymbol{H}_{ext}))$ (if $\alpha^2 \ll 1$). These two terms are represented in Fig. 1.10 in the case of a film exhibiting PMA and Néel DWs and for a field applied along the easy axis. For simplicity, the torques have been represented only in the centre of the DWs. The green arrows indicate the direction of DW motion, which results in the expansion of the domain with magnetisation parallel to the field.

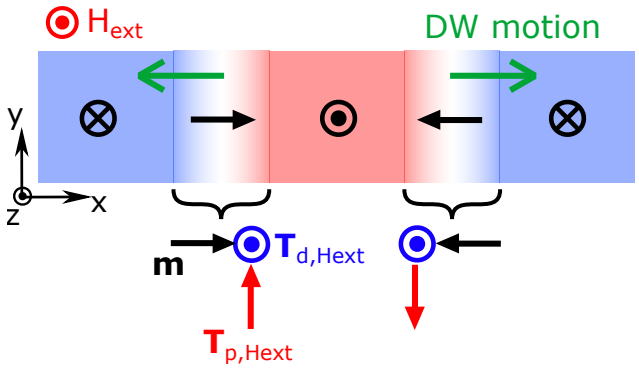

Fig. 1.10: Field-driven domain wall dynamics | Direction of DW motion (green arrows) under an external magnetic field $\boldsymbol{H}_{ext}$ applied along the easy axis for a film exhibiting PMA and Néel DWs. The two torques of the LLG equation (eq. (1.19)) due to the external field are represented in the centre of the DW.

The dynamics of DWs driven by an external magnetic field applied along the easy axis was first described by Walker in 1974 [62]. In this model, the DW dynamics is divided into two regimes: a steady-state regime at low field, and a precessional regime at high field, represented in Fig. 1.11.a.

In the absence of DMI, hence for a Bloch DW, the torque $\boldsymbol{T}_p$ due to the external field rotates the magnetisation in the xy plane. This creates magnetic charges at the DW edges and produces a demagnetising field perpendicular to the DW. The resulting torque pulls the magnetisation OOP, leading to the displacement of the DW. The damping torque opposes $\boldsymbol{T}_p$ such that, at equilibrium, they compensate, hence resulting in a steady motion of the DW with an equilibrium angle in the xy plane. This regime is characterised by a large and constant DW mobility, $\mu_{DW} = \partial v/\partial H_{ext}$. Increasing the external field further rotates the magnetisation in the xy plane, hence increasing the demagnetising field. Above a certain critical field H_W, called the Walker field, the damping torque no longer compensates the precessional torque and the magnetisation starts to precess in the xy plane. This phenomenon is referred to as Walker breakdown. When further increasing the external field, the DW enters the precessional regime: the magnetisation at the centre of the DW undergoes back and forth displacements, resulting in a smaller mobility [63].

In the presence of DMI, the DW is pinned in the Néel configuration (Fig. 1.10) by the DMI effective field which opposes the magnetisation precession. As shown by Thiaville *et al.* [58], the Walker breakdown is pushed towards higher fields, extending the steady-state regime (see Fig. 1.11.b). Hence, much larger velocities can be reached using asymmetric trilayers with large DMI such as Pt/Co/AlO_x [64,65] or Pt/Co/GdO_x [65] than with symmetric stacks exhibiting zero or weak DMI like Pt/Co/Pt [65,66].

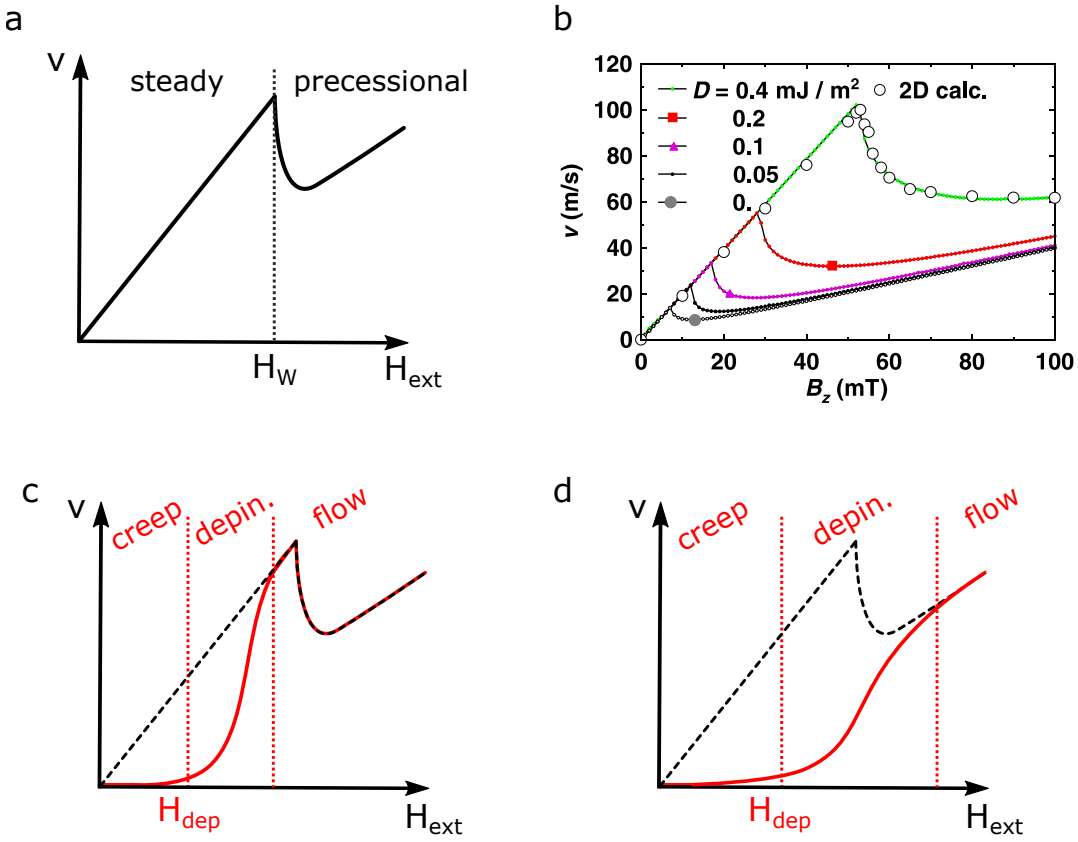

Fig. 1.11: Velocity of a DW driven by an external magnetic field | **a.** Schematic diagram showing the DW velocity as a function of the external magnetic field applied along the easy axis, as depicted in Fig. 1.10. The dynamics exhibits two regimes, a steady-state regime and a precessional regime separated by the Walker breakdown for $H_{ext} = H_W$. **b.** DW velocity obtained from micromagnetic simulations and analytical calculations for different DMI values. Adapted from ref. [58]. **c,d.** In real systems, defects and imperfections introduce different thermally-activated regimes: the creep, depinning and flow regimes. The depinning field H_{dep} separates the creep and depinning regimes. The measured flow regime can be either **c.** the steady-state regime or **d.** the precessional regime.

However, this model is only valid for ideal systems. In real systems, material defects and thermal activation play a major role in the DW dynamics. In particular, material defects are a source of pinning for DWs. Pinning introduces different thermally-activated regimes in the dynamics [66–68], represented in Fig. 1.11.c and 1.11.d. At low external field, the DW dynamics occurs by successive deformation of the DW lines between pinning sites, resulting in small velocities: this is the creep regime. Above a certain critical field H_{dep} called depinning field, the dynamics enters the depinning regime. In this regime, the DW motion proceeds by thermally-activated jumps between pinning sites. Upon further increasing the driving force, the DW mobility eventually reaches a constant value, characterised by a linear velocity as predicted theoretically: this is the flow regime. Note that the Walker breakdown can be hidden by the creep and depinning regimes (Fig. 1.11.d) in which case the flow regime observed is the precessional regime [66].

1.3.3 Current-driven domain wall dynamics

In order to describe the current-driven dynamics of magnetic skyrmions, we shall first introduce that of DWs and some of its underlying mechanisms. To this end, the case of an ultra-thin HM/FM/NM film is considered. To drive magnetic textures, two main mechanisms have been widely studied in recent years: spin-transfer torque (STT) [69] and spin-orbit torque (SOT) [7]. The former describes the transfer of angular momentum between the spins of the conduction electrons within the magnetic layer and the local magnetic moments. The latter also describes a transfer of angular

momentum from the electron spins to the local magnetic moments. However, the spin polarisation originates from the injection of spin currents through an interface which are generated by SOC-related phenomena. While both of these effects can exist, in ultra-thin HM/FM-based stacks, the SOTs are expected to dominate and to be more efficient at driving DWs and magnetic skyrmions than the STTs [70,71]. For this reason, we will not dwell at length on the STT and focus on the more efficient SOT driving scheme.

1.3.3.1 Spin transfer torques

When a current flows in a FM metal, it gets spin-polarised along the magnetisation direction due to the different scattering rates of ↑-spin and ↓-spin conduction electrons. When conduction electrons flow from one magnetic domain to another with a different magnetisation orientation — hence crossing a DW — their spin rotates. Since the $s-d$ exchange interaction conserves the spin, this variation of spin angular momentum is transferred to the local magnetisation, resulting in a torque on the DW internal magnetisation; the so-called STT. This torque is the sum of two terms: an adiabatic and a non-adiabatic torque.

The adiabatic describes a situation where the spins of the conduction electrons follow perfectly the local magnetic moments inside the DW. This torque tends to align the magnetic moments with the spins of the conduction electrons and has the following form [72]: $\boldsymbol{T}_{ad} = -(\boldsymbol{u}\cdot\boldsymbol{\nabla})\,\boldsymbol{m}$, where $\boldsymbol{u} = (g\mu_B P/2eM_s)\,\boldsymbol{J}$ with $P > 0$ the spin-polarisation of the current and $\boldsymbol{J}$ the current density (oriented against the electron flow). It results in a DW motion along the electron flow.

The non-adiabatic torque had to be introduced [73,74] to account for the measured DW velocities which were much smaller than the one predicted using solely the adiabatic term [75,76]. It takes the following form [72]: $\boldsymbol{T}_{non-ad} = \beta\boldsymbol{m}\times((\boldsymbol{u}\cdot\boldsymbol{\nabla})\,\boldsymbol{m})$, with β is a dimensionless coefficient that quantifies its strength. This term, analogous to a dissipative torque, was attributed to spin-relaxation phenomena inside the DW [77]. To summarise, we can write the LLG equation (eq. (1.19)) including the STT terms [72]:

$$\frac{\partial\boldsymbol{m}}{\partial t} = -\gamma_0\,(\boldsymbol{m}\times\boldsymbol{H}_{eff}) + \alpha\left(\boldsymbol{m}\times\frac{\partial\boldsymbol{m}}{\partial t}\right) - (\boldsymbol{u}\cdot\boldsymbol{\nabla})\,\boldsymbol{m} + \beta\boldsymbol{m}\times((\boldsymbol{u}\cdot\boldsymbol{\nabla})\,\boldsymbol{m}) \tag{1.20}$$

The STT induces a DW motion against the current direction (*i.e.* along the electron flow). One can show that the DW undergoes an instability analogous to the Walker breakdown for a critical u value, u_W. For $u < u_W$, the DW velocity increases linearly as $v = (\beta/\alpha)\,u$. When $u > u_W$, the magnetisation inside the DW starts to precess, which is reflected either by a drop in the DW

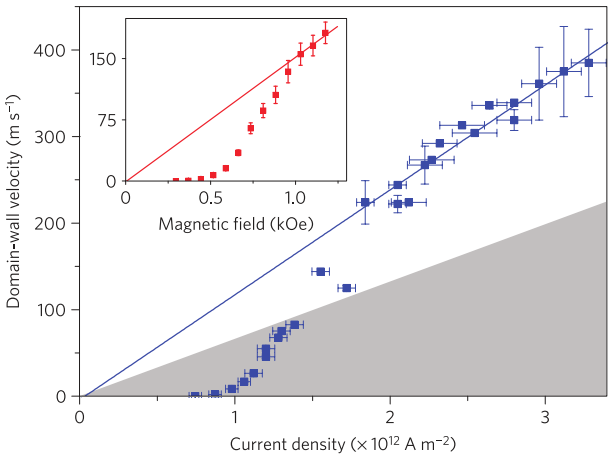

Fig. 1.12: Current-driven DW dynamics in Pt/Co/AlO$_x$ | DW velocity as a function of the current density measured in a Pt(3)/Co(0.6)/AlO$_x$(2) film (thicknesses in nm) at RT. The observed direction of motion is against the electron flow. The inset shows the DW velocity as a function of the external OOP magnetic field. Adapted from ref. [64].

velocity if $\beta > \alpha$, or by an increase of the DW velocity if $\beta < \alpha$ [72]. In addition, similarly to the field-driven DW motion, a critical depinning current density, u_c, needs to be reached to set the DW in motion. Therefore, significant efforts have been concentrated on reducing u_c and optimising the β/α ratio to increase the efficiency, particularly interesting for the development of applications like DW racetrack memories [8]. DW velocities up to 120 m s^{-1} have notably been reported in NiFe films [78].

More recently, much larger DW velocities were reported in perpendicularly magnetised films with SIA, without any Walker breakdown signature. For instance Pt/Co/AlO$_x$ [64], Pt/CoFe/MgO [79], Ta/CoFe/MgO [79] and Pt/Co/Ni/Co/TaN [80]. Fig. 1.12 shows the results obtained by Miron *et al.* [64]: the authors measured DW velocities up to 350 m s^{-1} in a Pt(3)/Co(0.6)/AlO$_x$(2) film (thicknesses in nm). The measured current-driven DW velocity exhibits a very similar evolution to that driven by a field with a pinning and a depinning regime (inset of Fig. 1.12). The shaded area delimits the maximum velocity that can be obtained with STTs. Here, neither the large velocities nor the direction of motion, against the electron flow, could be completely explained with the conventional STTs. An additional mechanism was introduced: SOTs.

1.3.3.2 Spin-orbit torques

In the case of STTs, the electrical current gets naturally spin-polarised within the magnetic material due to the different scattering rates for ↑-spin and ↓-spin electrons. In the case of SOTs, obtained in systems with SIA, the spin current is generated by the conversion of orbital angular momentum into spin angular momentum via the SOC, either in the bulk of the HM layer or at the HM/FM interface. Two main effects have been proposed to explain the generation of SOTs: the spin Hall effect (SHE) [81–83] and the Rashba-Edelstein or inverse spin-galvanic effect[1] [17,84]. Similarly to the STT, which contain two terms acting in two perpendicular directions, the SOT can be decomposed into two orthogonal components: the damping-like (DL) and field-like (FL) SOT, $\boldsymbol{T}_{DL}$ and $\boldsymbol{T}_{FL}$. They take the following general form [7]: $\boldsymbol{T}_{DL} \sim \boldsymbol{m} \times (\boldsymbol{m} \times \boldsymbol{\xi})$ and $\boldsymbol{T}_{FL} \sim \boldsymbol{m} \times \boldsymbol{\xi}$, with $\boldsymbol{\xi}$ a unit vector that depends on the charge-to-spin conversion mechanism. These torques, by definition perpendicular to the magnetisation, can be expressed in terms of their effective magnetic fields, $\boldsymbol{H}_{DL}$ and $\boldsymbol{H}_{FL}$ respectively, such that: $\boldsymbol{T}_{DL(FL)} = -\gamma_0 \left(\boldsymbol{m} \times \boldsymbol{H}_{DL(FL)} \right)$. The DL-SOT effective field depends on the magnetisation direction whereas the FL-SOT is equivalent to a magnetic field applied perpendicular to the current direction, hence their respective designation. The general LLG equation (eq. (1.19)) including the SOTs thus reads:

$$\frac{\partial \boldsymbol{m}}{\partial t} = -\gamma_0 \left(\boldsymbol{m} \times \boldsymbol{H}_{eff} \right) + \alpha \left(\boldsymbol{m} \times \frac{\partial \boldsymbol{m}}{\partial t} \right) - \gamma_0 \left(\boldsymbol{m} \times \boldsymbol{H}_{DL} \right) - \gamma_0 \left(\boldsymbol{m} \times \boldsymbol{H}_{FL} \right) \tag{1.21}$$

In general in HM/FM/NM systems, both the SHE and the Rashba-Edelstein effect can produce simultaneously a DL-SOT and a FL-SOT. This complex interplay has been fostering an ongoing debate on the origin of the SOTs in different systems [7]. Nonetheless, in HM/FM/NM systems, and in particular in Pt/Co-based films, studied in this thesis, the SHE is expected to provide a stronger contribution to the DL-SOT while the Rashba effect is expected to provide a stronger contribution to the FL-SOT.

Let us first describe the DL-SOT produced by SHE and its implication on the current-driven DW dynamics, which is our main interest in this section. The mechanism is represented schematically in Fig. 1.13.a and 1.13.b: when a charge current $\boldsymbol{J}$ flows in the HM layer, the SOC induces a deflection of the conduction electrons according to their spin: electrons with opposite spins are deviated in opposite directions. This produces a pure spin current, $\boldsymbol{J}_S$, flowing perpendicular to the charge current. Note that no charge is transported in a pure spin current; it can be seen as the superimposition of two equal electron flows propagating in opposite directions, each flow carrying opposite spins. This spin current reads $\boldsymbol{J}_S \sim \hat{\boldsymbol{s}} \times \boldsymbol{J}$, where $\hat{\boldsymbol{s}}$ is the spin polarisation direction. For a spin polarisation along $-\hat{\boldsymbol{y}}$ and a charge current flowing along $+\hat{\boldsymbol{x}}$, the spin current propagates

[1] referred to simply as Rashba effect in the following

along $+\hat{\boldsymbol{z}}$, *i.e.* from the HM bulk towards the HM/FM interface. The transfer of spin angular momentum to the local magnetic moments located close to the interface results in a torque on the magnetisation with the associated effective field as follows [85]:

$$\boldsymbol{H}_{DL} = H_{DL}^{0}\left(\left(\hat{\boldsymbol{z}} \times \hat{\boldsymbol{j}}\right) \times \boldsymbol{m}\right) \tag{1.22}$$

Here, $\hat{\boldsymbol{j}}$ is the unit vector in the direction of the current such that $\boldsymbol{J} = J\hat{\boldsymbol{j}}$, and $H_{DL}^{0} \propto \Theta_{SH} J$ where Θ_{SH} is the so-called spin Hall angle (SHA) [7]. The SHA, expressed as the ratio J_S/J of the spin current to the charge current, quantifies the charge-to-spin conversion efficiency in the HM. In particular, one can show that $H_{DL}^{0} = \hbar\Theta_{SH} J/(2|e|M_s t)$, with t the FM film thickness [85]. Note that the measured SHA often differs from the intrinsic SHA of the bulk HM due to additional effects lowering the efficiency such as dissipation of the spin current in the HM or reflection at the HM/FM interface which can make its evaluation difficult [7]. In addition, its sign and its amplitude depend on the combination of HM and FM materials as well as their respective thicknesses. For instance, $\Theta_{SH} > 0$ (Fig. 1.13.b) for Pt [79,86,87], and $\Theta_{SH} < 0$ (Fig. 1.13.a) for Ta [79,88] and W [89].

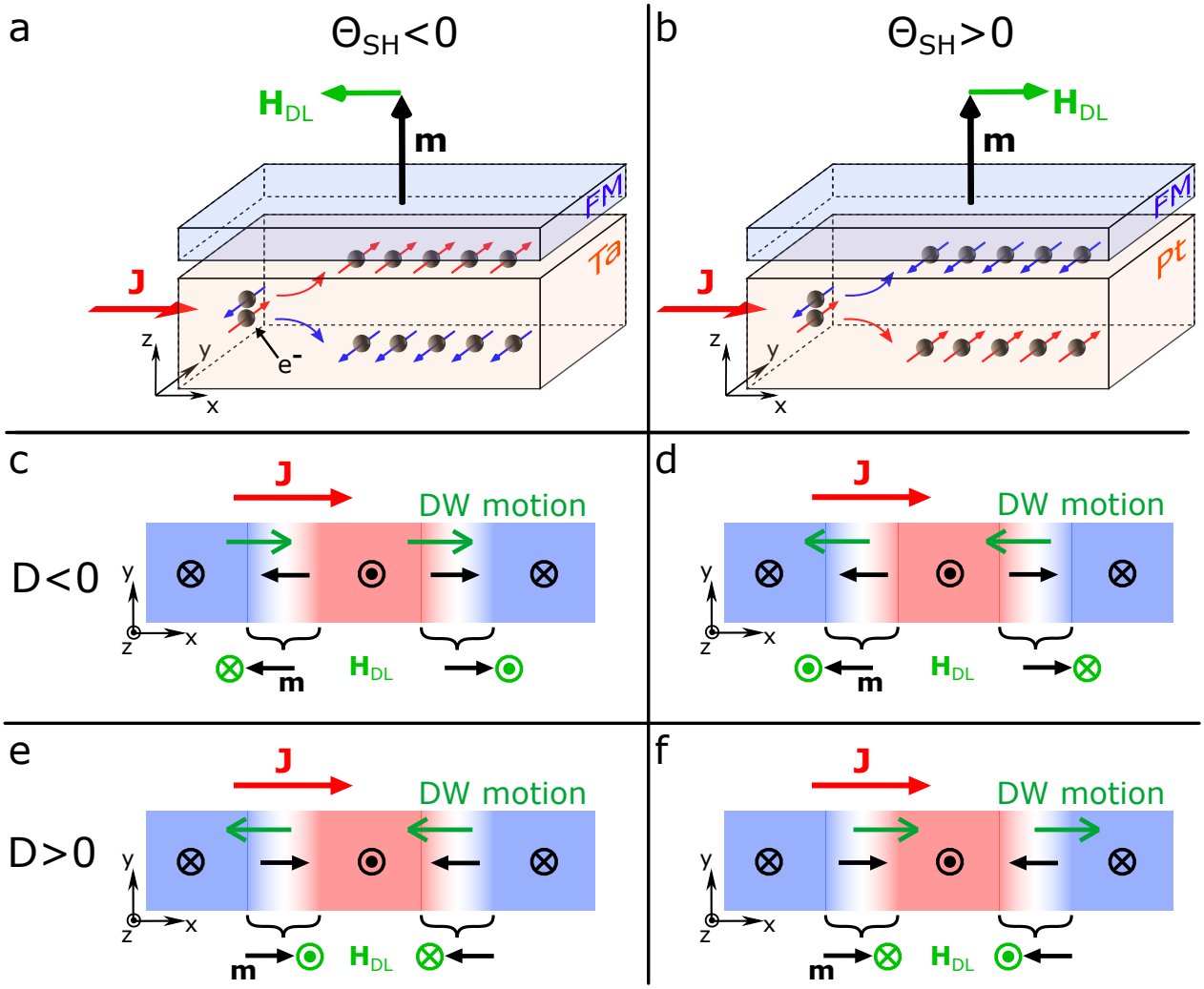

Fig. 1.13: Spin Hall effect and current-driven DW dynamics | **a,b.** Illustration of the SHE for two materials with opposite spin Hall angle Θ_{SH}. **a.** For $\Theta_{SH} < 0$ (*e.g.* Ta), the direction of the spin accumulation at the HM/FM interface when the current flows along $+\hat{\boldsymbol{x}}$ is along $+\hat{\boldsymbol{y}}$. **b.** For $\Theta_{SH} > 0$ (*e.g.* Pt), it is along $-\hat{\boldsymbol{y}}$. $\boldsymbol{H}_{DL}$ is the effective magnetic field associated with the DL-SOT (eq. (1.22)). **c-f.** Direction of motion of Néel DWs with **c,d.** $D < 0$ (right-handed) and **e,f.** $D > 0$ (left-handed). In this thesis, all the systems studied are Pt/Co-based, which corresponds to **f**.

The direction of the DL-SOT hence depends on the sign of the SHA. Considering that it also depends on the direction of the magnetisation, this has major implications when determining the direction of DW motion with respect to the current/electron flow direction. This is illustrated in Fig. 1.13.c-f for different combinations of Θ_{SH} and D. In particular, all the systems studied in this work are Pt/Co-based, which corresponds to $\Theta_{SH} > 0$ and $D > 0$ (left-handed chirality), that is a DW motion along the current direction (Fig. 1.13.f). These diagrams only represent homochiral Néel DWs. Two consecutive Néel DWs with opposite chiralities would move in opposite directions, resulting in the expansion of one domain and the contraction of the other. Furthermore, it can easily been inferred from Fig. 1.13 that for a Bloch DW, $\boldsymbol{m} \perp \hat{\boldsymbol{j}}$ in its centre, and the DL-SOT vanishes, resulting in no DW motion. This model, including both DMI and SHE-induced DL-SOT [58] can notably explain the direction of DW motion as well as the large velocities observed experimentally in stacks with SIA [64,79,80].

Let us now consider the FL-SOT and focus on the Rashba effect. This effect describes the electrical generation of a spin density when a current flows in a system lacking inversion symmetry. In a HM/FM/NM stack, the lack of inversion symmetry originates from the interfaces (SIA). As described earlier in §1.1.5, the electrons at the interface experience a Rashba field, $\boldsymbol{B}_R$, perpendicular to their direction of motion. When a current flows in the stack, the spins of the conduction electrons interact with $\boldsymbol{B}_R$ and align parallel to it, thus generating a non-equilibrium spin density. This spin density results — via $s-d$ exchange interaction — in a torque on the magnetisation [17,90,91]. It was shown that this torque has a FL symmetry with the associated effective magnetic field as follows [17]:

$$\boldsymbol{H}_{FL} = H_{FL}^{0} \left(\hat{\boldsymbol{z}} \times \hat{\boldsymbol{j}} \right) \tag{1.23}$$

Here $H_{FL}^{0} \propto \alpha_R J$, with α_R the Rashba coefficient introduced earlier (§1.1.5). This FL-SOT is equivalent to the action of a magnetic field perpendicular to the current direction whose amplitude is proportional to the injected current density. The effect of the FL-SOT on the current-driven dynamics of magnetic skyrmions will be discussed in §5.5.

Finally, different techniques exist to measure SOTs in magnetic multilayers: spin-torque ferromagnetic resonance [92], magneto-optical Kerr effect [93] and harmonic Hall voltage measurements [87,94]. The harmonic Hall voltage measurement technique was used in this thesis to measure the SOTs in a Pt/Co/MgO film to model the skyrmion dynamics (see §5.3.5).

1.4 Conclusions

In this chapter, we first saw an overview of the different energy contributions that determine the stable magnetic configuration in perpendicularly magnetised ultra-thin films with SIA, in particular the role of the DMI in the stabilisation of homochiral Néel DWs. Focusing the discussion on these Néel DWs, we then gave the principal mechanisms governing their current-driven dynamics, in particular the SOTs. As it will be detailed in the next chapter, a magnetic skyrmion can be seen as a small domain enclosed by a chiral DW. The present notions can hence be naturally extended to the case of magnetic skyrmions.

Chapter 2

Magnetic skyrmions: properties and dynamics

This chapter describes in detail magnetic skyrmions in systems with SIA and tackles certain key aspects regarding their stability, nucleation and current-driven dynamics.

2.1 Definitions and topology

Magnetic skyrmions are non-collinear spin textures pictured as localised whirlings of the magnetisation (see Fig. 2.1) [39,95,96]. They are named after the physicist Tony Skyrme who proposed in the 1960's a quantum field theory to describe interacting elementary particles as topological defects in a vector field [97]. In magnetic materials, a skyrmion can be described as a small, two-dimensional, circular magnetic domain enclosed by a chiral DW. This means that the magnetisation undergoes a continuous 360° rotation in one and only one direction when moving outwards from the skyrmion centre (Fig. 2.1). The swirling structure of a skyrmion is characterised by a topological charge (or skyrmion number), N_{sk}, defined by [98,99]:

$$N_{sk} = \frac{1}{4\pi} \iint dxdy\, \boldsymbol{m} \cdot \left(\frac{\partial \boldsymbol{m}}{\partial x} \times \frac{\partial \boldsymbol{m}}{\partial y} \right) \tag{2.1}$$

where $\boldsymbol{m}$ is the reduced magnetisation vector and the integration is performed over the whole 2D space.

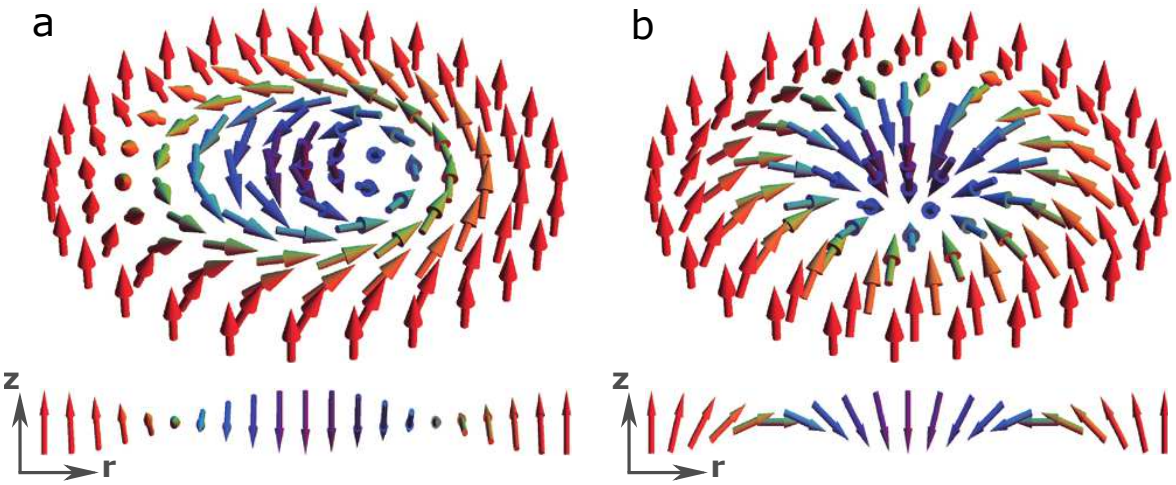

Fig. 2.1: Spin texture of a magnetic skyrmion | **a.** A Bloch skyrmion with core polarity number $p = -1$, winding number $W = 1$ and helicity $\Psi = \pi/2$ (right-handed). **b.** A Néel skyrmion with $p = -1$, $W = 1$ and $\Psi = \pi$ (right-handed). Ψ is defined in Fig. 2.2. A cut along the radial direction is represented below each skyrmion. Adapted from ref. [100].

It can already be pointed out that $N_{sk} = 0$ for the FM saturated state where all the spins are collinear since $\partial \boldsymbol{m}/\partial x = \partial \boldsymbol{m}/\partial y = \mathbf{0}$. To calculate the topological charge of a single skyrmion in an otherwise uniformly magnetised background, it is suitable to use a polar coordinate system, (r, φ), such that $x = r\cos\varphi$ and $y = r\sin\varphi$. The reduced magnetisation vector is contained within a unit sphere, described by the coordinates $(1, \Phi(\varphi), \theta(r))$, such that $\boldsymbol{m} = (m_x, m_y, m_z) = (\cos\Phi\sin\theta, \sin\Phi\sin\theta, \cos\theta)$. The different angles are defined in Fig. 2.2. Here, θ is a function of r only since the skyrmion exhibits a rotational (cylindrical) symmetry. Furthermore, Φ is assumed to be independent of the radial coordinate r for the present calculation. Although this is in general not true, especially for a large skyrmion exhibiting an extended plateau — $|m_z| = 1$ — in its centre, it does not change the result since the skyrmion core does not contribute to the topological charge. Eq. (2.1) can then be rewritten as follows:

$$N_{sk} = \frac{1}{4\pi}\int_0^{+\infty} dr \int_0^{2\pi} d\varphi \left(\sin\theta \frac{\partial\theta}{\partial r}\frac{\partial\Phi}{\partial\varphi}\right) = \frac{1}{4\pi}\left[-\cos\theta(r)\right]_0^{+\infty}\left[\Phi(\varphi)\right]_0^{2\pi} = p \cdot W \tag{2.2}$$

In eq. (2.2), p is the skyrmion core polarity number and W the winding number[1] given by:

$$p = \frac{1}{2}\left[m_z(0) - m_z(+\infty)\right] = \pm 1 \tag{2.3}$$

$$W = \frac{1}{2\pi}\left[\Phi(\varphi)\right]_0^{2\pi} \tag{2.4}$$

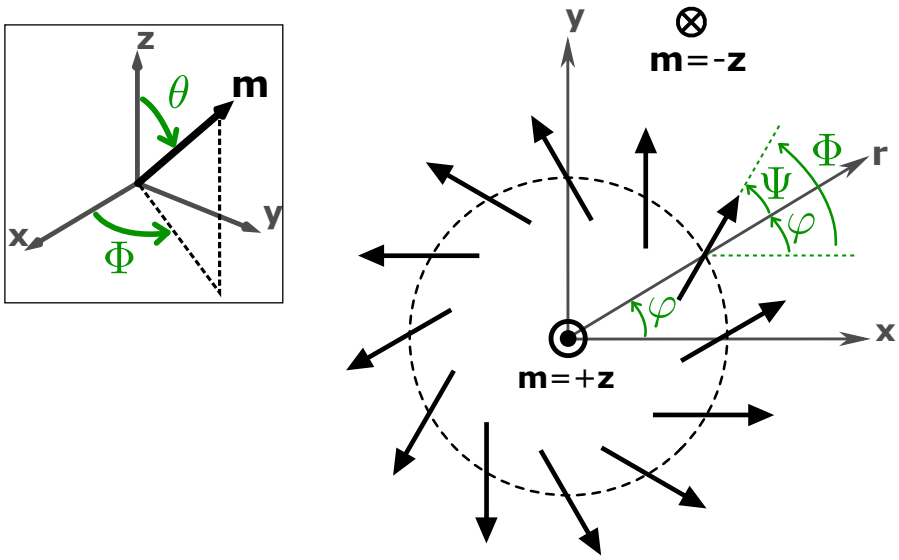

Fig. 2.2: Schematics of a magnetic skyrmion | Definition of the polar coordinates, (r, φ), and the spherical coordinates for the magnetisation $\boldsymbol{m}$, $(1, \Phi, \theta)$. The thick black arrows indicate the direction of the magnetisation in the region where $m_z = 0$. This skyrmion is characterised by a core polarity number $p = +1$, a winding number $W = +1$ and a helicity $0 < \Psi < \pi/2$.

Therefore $p = +1$ ($p = -1$) for a skyrmion core with magnetisation $m_z = +1$ ($m_z = -1$). The winding number counts how many times the magnetisation wraps the unit sphere. In other words, it counts by what angle Φ the magnetisation has rotated upon performing a complete, 2π rotation around the skyrmion core, from $\varphi = 0$ to $\varphi = 2\pi$. A magnetic skyrmion is characterised by a winding number $W = 1$ while a spin texture with $W = -1$ is referred to as an antiskyrmion [99], represented in Fig. 2.3. After performing a 2π rotation around the antiskyrmion core, the magnetisation has rotated by -2π, hence $W = -1$. Thus, the topological charge of a skyrmion is quantised and determined only by its core polarity: $N_{sk} = p = \pm 1$ ($N_{sk} = -p$ for an antiskyrmion). Note that a non-circular domain enclosed by a chiral DW also has a topological charge of ± 1 as it

[1] also referred to as vorticity number or simply vorticity

can be transformed continuously into a circular domain. It can hence still be referred to as a skyrmion from this point of view. Furthermore, because of its peculiar topology, a skyrmion (or an antiskyrmion) cannot be easily 'unwound' by continuous transformations. This means that one cannot go continuously from the skyrmion state to a state with a different N_{sk} (*e.g.* the uniform FM state with $N_{sk} = 0$) without having to overcome a large energy barrier. This property of magnetic skyrmions has often been referred to as topological protection. Nevertheless this description is valid for a continuously varying vector field $\boldsymbol{m}$. In real magnetic systems, the magnetic moments are located on discrete atomic sites and this topological protection derived from continuity arguments is not observed...

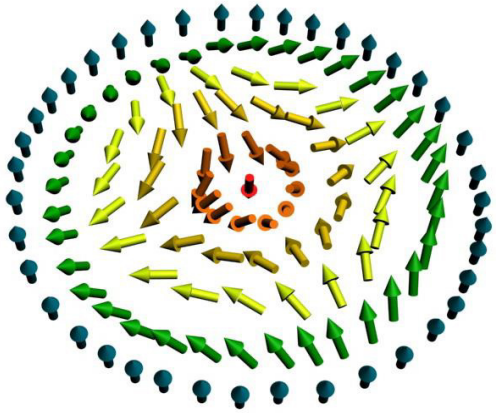

Fig. 2.3: Spin texture of a magnetic antiskyrmion | An antiskyrmion is characterised by a winding number $W = -1$. This particular antiskyrmion has a core polarity $p = -1$ hence its topological charge is $N_{sk} = +1$. Adapted from ref. [101].

A classification of magnetic skyrmions can be established based on their helicity number, that is the angle Ψ between the magnetisation and the radial axis, defined by the relation $\Phi(\varphi) = W\varphi + \Psi$. The limiting cases are the so-called Bloch skyrmion (Fig. 2.1.a) and Néel skyrmion (Fig. 2.1.b), characterised respectively by $\Psi = \pi/2$ or $3\pi/2$ and $\Psi = 0$ or π, named by analogy with the Bloch and Néel DWs. Intermediate helicities define composite Bloch-Néel skyrmions such as the one drawn in Fig. 2.2. Each skyrmion type (Bloch and Néel) can exhibit two different polarities ($p = \pm 1$) and two different chiralities (left- and right-handedness), which we define here as the direction of rotation of the magnetisation when propagating along the radial direction, and from left to right. For instance, the two skyrmions of Fig. 2.1 exhibit a right-handed chirality.[1]

Both Bloch and Néel skyrmions can be realised in magnetic materials as detailed hereafter. Their presence originates in most cases from the DMI and the stabilisation of either type skyrmion depends on the the symmetry of the DMI, that is the orientation of the $\boldsymbol{d}_{ij}$ vector introduced earlier in §1.1.7: when $\boldsymbol{d}_{ij} \parallel \boldsymbol{r}_{ij}$, Bloch skyrmions are favoured, while Néel skyrmions are promoted when $\boldsymbol{d}_{ij} \perp \boldsymbol{r}_{ij}$. The chirality is selected by the sign of the DMI, *i.e.* by the direction of the $\boldsymbol{d}_{ij}$ vector for a given orientation.

2.2 Observations of magnetic skyrmions

Although the idea of magnetic skyrmions dates back to the early 1990's [39,95,96], they were only recently observed in 2009 [32]. Magnetic skyrmions were first reported in bulk non-centrosymmetric single-crystals (or chiral magnets) such as MnSi [32], $Fe_{1-x}Co_xSi$ [102,103], FeGe [104] and Cu_2OSeO_3 [105]. They were observed in the form of Bloch skyrmion lattices, in the presence of an external magnetic field and below RT, with sizes in the order of 20-90 nm (see Fig. 2.4.a). In these chiral

[1] Taking a cut of a Néel skyrmion with $p = -1$ along the radial direction, the magnetisation rotates according to ↑↗→↘↓↙←↖↑ for a right-handed skyrmion and ↑↖←↙↓↘→↗↑ for a left-handed skyrmion.

magnets, the presence of Bloch magnetic skyrmions is attributed to a bulk DMI, originating from the absence of inversion symmetry of the crystal structure.

They were later observed in ultra-thin epitaxial films composed of an atomically-thin FM grown on a single-crystal HM substrate, such as Ir(111)/Fe [106] and Ir(111)/Fe/Pd (Fig. 2.4.b) [107,108]. In these systems, the combination of interface-driven PMA and DMI leads to the stabilisation of Néel skyrmions. Ultra-small skyrmions counting only a few atomic magnetic moments, down to ≈ 2 nm, were observed [108]. However, their stabilisation required large external magnetic fields (1-3 T) as well as cryogenic temperatures ($T < 10$ K) as these films are paramagnetic at RT.

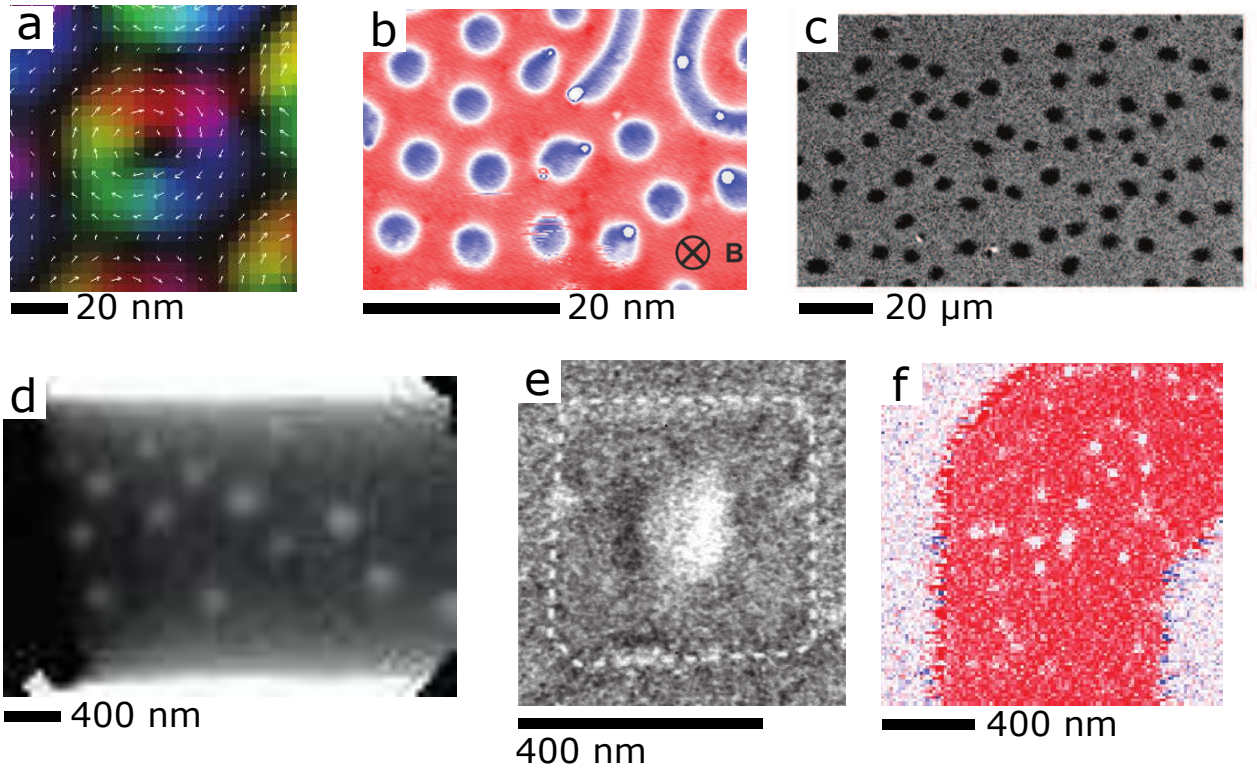

Fig. 2.4: Observations of magnetic skyrmions | **a.** Bloch skyrmion lattice in a 50-nm-thick FeGe plate ($\mu_0 H_z = 0.1$ T, $T = 260$ K) observed by LTEM. **b.** Néel skyrmions observed in an epitaxial Ir(111)/Fe/Pd film ($\mu_0 H_z = 1.5$ T, $T = 2.2$ K) by SP-STM. **c-f.** Magnetic skyrmions in sputtered HM/FM/NM stacks observed at room temperature in **c.** $Ta/Fe_{60}Co_{20}B_{20}/TaO_x$ by polar MOKE microscopy ($\mu_0 H_z = 0.5$ mT), **d.** $[Pt/Co_{60}Fe_{20}B_{20}/MgO]_{15}$ by STXM ($\mu_0 H_z \sim 10$ mT), **e.** Pt/Co/MgO in a square dot by X-PEEM ($\mu_0 H_z = 0$) and **f.** $[Ir/Co/Pt]_{10}$ by STXM ($\mu_0 H_z = 68$ mT). Adapted from ref. **a.** [104], **b.** [108], **c.** [109], **d.** [110], **e.** [48] and **f.** [111].

Very recently, an important breakthrough was made with the observation of magnetic skyrmions at RT, in sputtered HM/FM(t_{FM})/NM stacks with $t_{FM} \sim 1$ nm, exploiting here also the interface-induced PMA and DMI, favouring the formation of Néel skyrmions. Most of the observations were reported in typical PMA systems where chiral Néel DWs had been evidenced. These stacks are typically composed of one or several repetitions of the HM/FM/NM trilayer: $Ta/FeCoB/TaO_x$ (Fig. 2.4.c) [109], $[Pt/Co/Ta]_{15}$ [110], $[Pt/CoFeB/MgO]_{15}$ (Fig. 2.4.d) [110], Pt/Co/MgO (Fig 2.4.e) [48], $[Ir/Co/Pt]_{10}$ (Fig. 2.4.f) [111], $[Ir/Fe/Co/Pt]_{20}$ [112], $[W/FeCoB/MgO]_{15}$ [113].[1] Here, as for DWs introduced earlier (§1.2), the skyrmion chirality depends on the sign of the DMI: $D > 0$ ($D < 0$) promotes left-handed (right-handed) Néel skyrmions. Skyrmion sizes ranging from a few 10 nm [111] to several µm [109] were reported in these systems. It should be pointed out that large µm-sized skyrmions are often referred to as skyrmionic bubbles. This is because they are mainly stabilised by dipolar interactions rather than by DMI for more compact skyrmions, which has been

[1] A more extensive report on the state of the art of the observations of skyrmions in sputtered films can be found in the most recent reviews published on the topic [114–116].

fuelling an ongoing debate [117,118]. However, in the presence of a large enough DMI ($D > D_N$), both 'types' of skyrmions share the same topology ($|N_{sk}| = 1$) and some of its resultant properties. Consequently, the skyrmionic bubbles are fundamentally distinct from the 'conventional' magnetic bubbles, widely studied in the 1970's [57]. Magnetic bubbles are cylindrical magnetic domains, also observed in perpendicularly magnetised FM films, but they are solely stabilised by dipolar interactions. In the absence of any chiral interaction imposing a well-defined chirality such as the DMI (whether of bulk or interfacial origin), these bubbles might present complex, non-uniform topologies and chiralities, with arbitrary winding numbers [57,119,120].

Regarding the detection and observation of skyrmions, a broad range of experimental techniques has been employed. The early observations of skyrmion lattices in chiral magnets were done in the reciprocal space using neutron scattering [32,102], and later using real-space techniques such as Lorentz transmission electron microscopy (LTEM) (Fig. 2.4.a) [103–105]. LTEM utilises the deflection of electrons by the local magnetisation to image magnetic textures with a high resolution, and allows to determine their chirality. The observation of ultra-small skyrmions in epitaxial systems was achieved using an ultra-high-resolution microscopy technique, namely spin-polarised scanning tunnelling microscopy (SP-STM) (Fig. 2.4.b) [106–108]. In sputtered films, the intermediate skyrmion sizes, their stability at RT combined with the fact that the films can be grown on different substrates[1] have allowed to employ a large variety of microscopy techniques: magneto-optical Kerr effect (MOKE) microscopy [109] (2.4.c), most suitable to observe µm-sized spin textures, scanning transmission X-ray microscopy (STXM) (Fig. 2.4.d and 2.4.f) [110,111], X-ray photo-emission electron microscopy (X-PEEM) (Fig.2.4.e) [48], magnetic force microscopy (MFM) [121] and LTEM [122]. In this thesis, we employed X-PEEM, STXM and MFM to image magnetic skyrmions. The principle of these techniques will be explained later in §3.3. Finally, apart from imaging techniques, skyrmions were also detected by extraordinary Hall effect measurements [123,124] and their signature was recently detected in a magnetic tunnel junction by tunnel magneto-resistance measurements [125].

2.3 Motivations: potential skyrmion-based applications

One of the the reasons why magnetic skyrmions are being extensively studied, besides their fundamental interest, is their potential for applications. Their unique topological properties and very small size confer them particle-like properties. In particular, the possibility to displace magnetic skyrmions with an electrical current has opened a new paradigm to manoeuvre the magnetisation at the nanoscale. Following the early observations of skyrmion lattices in chiral magnets, their current-driven motion, driven by STT, was demonstrated. It revealed very low depinning current densities, four to five orders of magnitude below those required to move DWs [126,127]. From the promise of a compact, potentially nm-sized magnetic object, [108] with a foreseen efficient current-induced manipulation, has emerged the idea of utilising skyrmions in technologies [9]. The most prominent skyrmion-based application is the so-called skyrmion racetrack memory in which the information is encoded on a chain of individual skyrmions; the presence/absence of a skyrmion coding for a 1/0 bit [9,70,71,128].

Among the different classes of materials hosting skyrmions, the sputtered HM/FM/NM films are those which — so far — combine the most interesting features for applications: (i) skyrmions are stable at RT, a prerequisite for using them in any kind of technology;[2] (ii) sputtering deposition is a versatile tool that allows to deposit a large variety of materials on different substrates with a high deposition rate, hence easily integrable with standard spintronic technologies unlike epitaxial films; (iii) the current-induced SOTs constitute a more efficient mechanism than the STTs to manipulate magnetic skyrmions [70,71]. In the following, only the case of thin films with PMA and interfacial DMI will be considered.

[1] They are usually grown on Si substrates and can be grown on membranes for transmission microscopy experiments.

[2] Note that skyrmion lattices have been recently observed near and above RT in the chiral magnet $Co_xZn_yMn_z$ [129–131].

In this context, the concept of skyrmion racetrack memory shares certain similarities with the previously proposed DW racetrack memory where the information is encoded on a chain of domains with opposite magnetisation [8,132]. In both cases, the information bit (0/1) is encoded on the magnetisation orientation (↓/↑) and the magnetic texture (DW or skyrmion) is driven by an electrical current. In the case of skyrmion racetrack memory, the spacing between two skyrmions can be as small as their diameter [70,133] and the skyrmions can be compressed by reducing the track width [114] as it will be shown experimentally in §4.3.2. Finally, although the driving mechanism is the same, there are substantial differences between the SOT-driven dynamics of DWs and skyrmions. Notably, as explained hereafter in §2.5, the peculiar topology of magnetic skyrmions causes their deflection from the trajectory imposed by the current, an effect referred to as skyrmion Hall effect.

From the concept of racetrack emerged the idea of performing logic operations with skyrmions. Concepts of AND and OR skyrmion-based logic gates were notably proposed [134]. Beyond the racetrack and skyrmion-shift operations, other applications exploiting the dynamical skyrmion breathing modes [135] have been put forward for the development of skyrmion-based microwave detectors [136] and nano-oscillators [137]. Finally, applications in probabilistic computing are also foreseen [138,139].[1]

In order to realise skyrmion-based devices, optimising skyrmion stability and their current-driven dynamics is crucial. In the following, we address some of the key features for understanding these aspects.

2.4 Skyrmion stability and nucleation

2.4.1 Balance of energies inside a magnetic skyrmion

The stability of magnetic skyrmions results from a subtle interplay between the different magnetic energies of the system. In order to provide a good representative picture of this balance of energies, we use the analytical model developed by Bernand-Mantel *et al.* [118]. This model incorporates the contributions from the exchange (E_{ex}), effective anisotropy (E_K), DMI (E_{DMI}), long-range dipolar interactions (E_d) and Zeeman (E_Z) energies. All these terms express the energy difference between a single skyrmion with core magnetisation $m_z = -1$ ($p = -1$) and a FM background with uniform magnetisation $m_z = 1$. The total skyrmion energy with respect to the saturated state, E_{sk}, is the sum of all the aforementioned contributions, $E_{sk} = E_{ex} + E_K + E_{DMI} + E_d + E_Z$, and can be written as follows [118]:

$$E_{sk} = \frac{E_0}{\frac{2R}{\pi\Delta} + 1} + 2\pi R t \sigma_{DW} - 2\pi\mu_0 M_s^2 R t^2 I\left(\frac{2R}{t}\right) + 2\pi\mu_0 M_s H_z R^2 t \tag{2.5}$$

Here, t is the FM film thickness, R is the skyrmion radius, $\sigma_{DW} = 4\sqrt{AK_{eff}} - \pi D$ is the DW energy introduced earlier (§1.2), $E_0 = E_{sk}(R = 0) = 8\pi A t$, $H_z > 0$ is the external magnetic field applied in a direction opposite to the skyrmion core magnetisation and $I\,(2R/t)$ is a function of the complete elliptic integrals of the first and second kind. The first two terms on the right-hand side of eq. (2.5) correspond to $E_{ex} + E_K + E_{DMI}$, the third to E_d and the fourth to E_Z. To evaluate numerically these terms, we use a set of parameters corresponding to Pt/Co(0.9nm)/MgO: $A = 16$ pJ m^{-1}, $M_s = 1.42$ MA m^{-1}, $K_{eff} = 7 \times 10^4$ J m^{-3} ($K_u = 1.34 \times 10^6$ J m^{-3}), $D = 1.27$ mJ m^{-2} and $t = 0.9$ nm.[2] The different energies are plotted as a function of the skyrmion radius in Fig. 2.5.a-c for different external fields $\mu_0 H_z$. The total energy for the different field values is plotted in Fig. 2.5.d. All the energies are normalised by $E_{RT} = k_B T$ with $T = 298$ K.

It shows that all the energies evolve monotonically with the skyrmion radius and that their sum results in the formation of an energy minimum, defining the equilibrium skyrmion radius R_{eq} (black dots in Fig. 2.5.d). A criterion can be established to distinguish magnetic skyrmions from

[1] More details on the envisaged skyrmion-based applications can be found in different reviews [114–116,140].
[2] The determination of these parameters is detailed in §5.3.

skyrmionic bubbles, based on the sign of the slope $\partial E_{sk}/\partial R$ when $R \to 0$. Skyrmionic bubbles are characterised by $\partial E_{sk}/\partial R > 0$ while magnetic skyrmions are characterised by $\partial E_{sk}/\partial R < 0$ (as in Fig. 2.5). This shall allow to compress magnetic skyrmions to much smaller radii upon applying an external magnetic field [118]. Note that this model is valid only for large skyrmion-bubbles with $R \gg \Delta$. Nevertheless, the role of each interaction can be analysed qualitatively from these plots. The aim here is to provide some basis of understanding and to draw a guideline for the results presented in the following chapters.

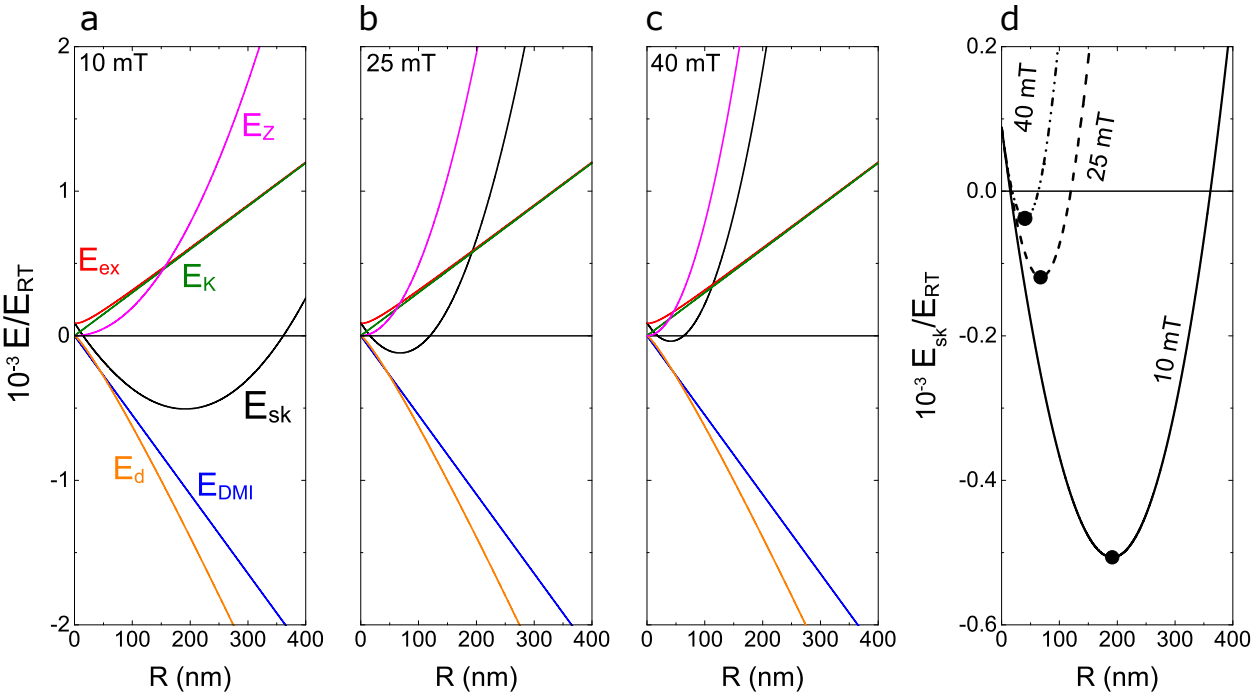

Fig. 2.5: Competing energies inside a magnetic skyrmion | a-c. Energies of an isolated magnetic skyrmion in a uniform FM background as a function of the skyrmion radius R calculated from eq. (2.5); exchange E_{ex} (red), anisotropy E_K (green), DMI E_{DMI} (blue), dipolar E_d (orange), Zeeman (external field) E_Z (magenta) and total skyrmion energy E_{sk} (black) for different applied magnetic fields. **d.** Total skyrmion energy for these three values of the applied field. The black dots indicate the equilibrium skyrmion radius R_{eq}. The energies are normalised by $E_{RT} = k_B T$ with $T = 298$ K.

First of all, increasing the external field results in the compression of the skyrmion and in a shallower energy minimum, indicating the existence of a critical radius below which the skyrmion is not thermally stable. This stability can be defined by the annihilation barrier, $E_a = E_0 - E_{sk}(R_{eq})$, that is the energy required to annihilate a skyrmion, which exhibits a non-trivial dependence on the different micromagnetic parameters; RT applications requiring typically $E_a/E_{RT} > 50$. Note that at $H_z = 0$, no minimum is observed for E_{sk}, highlighting the necessity to apply an external field to stabilise skyrmions.

Then, it appears that E_{ex} and E_K promote smaller R_{eq} and smaller E_a, while E_{DMI} promotes larger R_{eq} and larger E_a. This can be understood from the contribution of A, K_{eff} and D to the DW energy σ_{DW}: larger A and K_{eff} result in a larger DW energy, hence promoting shorter DWs, and therefore smaller skyrmions. Likewise, a larger D results in a smaller DW energy, hence promoting larger skyrmions. This is true if all the other terms — in particular H_z — are kept constant. Indeed, if decreasing K_{eff} and increasing D promotes larger R_{eq}, it also enhances the skyrmion stability by shifting the energy minimum downwards. To better visualise this, we plot in Fig. 2.6 different diagrams showing the variation of R_{eq}, E_a and the ratio E_a/R_{eq} as a function of different parameters: $(D, \mu_0 H_z)$ and $(K_{eff}, \mu_0 H_z)$.

Let us first look at the influence of the DMI (Fig. 2.6.a-c), which is varied in the range $D = 0-2$ mJ m^{-2}, typical for HM/FM-based films. Upon increasing D, at constant field, we see that both the equilibrium skyrmion size (Fig. 2.6.a) and the annihilation barrier (Fig. 2.6.b) increase. A good figure of merit to evaluate the impact of D on the skyrmion stability can be obtained from the annihilation barrier to equilibrium radius ratio, E_a/R_{eq}, given in Fig. 2.6.c. This plot reveals that E_a/R_{eq} greatly increases with increasing D. Hence, for identical skyrmion sizes, the DMI enhances the thermal skyrmion stability. Smaller skyrmions can therefore be stabilised in systems with a larger DMI, provided that a larger external field is applied.

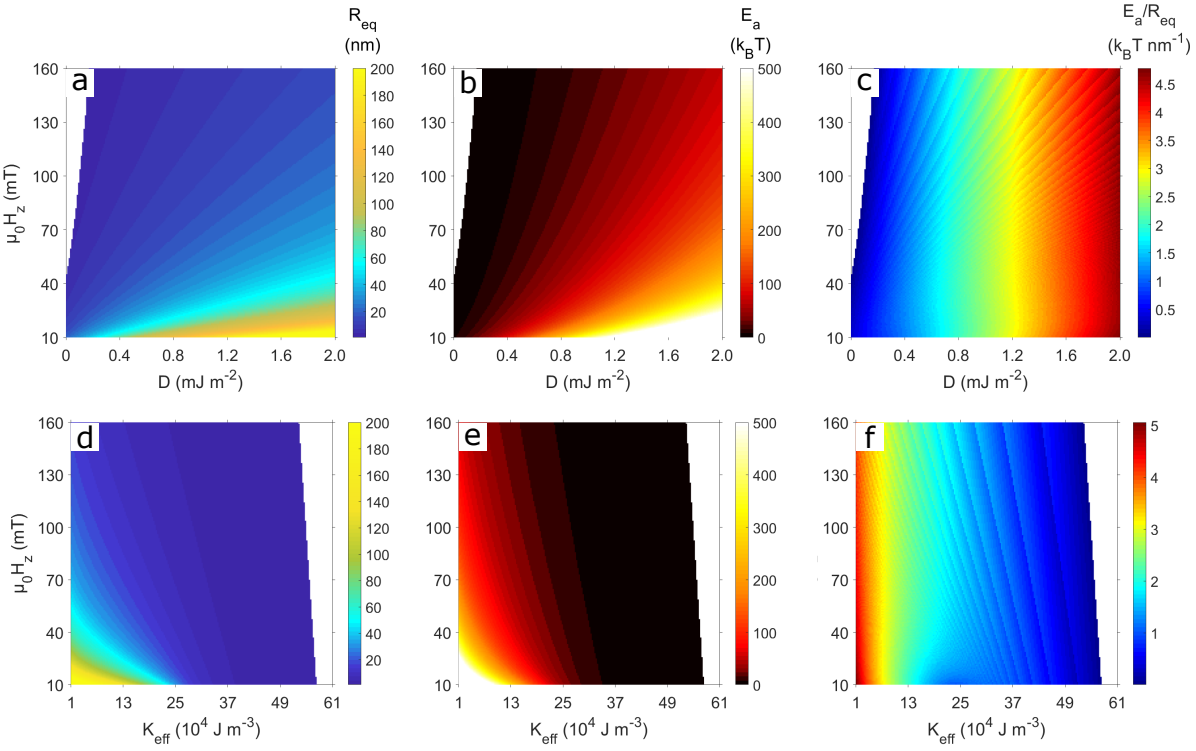

Fig. 2.6: Influence of the DMI and the effective anisotropy on the skyrmion size and stability | **a-c.** $(D, \mu_0 H_z)$ diagrams showing **a.** the equilibrium skyrmion radius R_{eq}, **b.** the annihilation barrier $E_a = E_0 - E_{sk}$ and **c.** the ratio E_a/R_{eq}. **d-f.** $(K_{eff}, \mu_0 H_z)$ diagrams. All diagrams were calculated from eq. (2.5) using the following parameters: $A = 16$ pJ m^{-1}, $M_s = 1.42$ MA m^{-1}, $t = 0.9$ nm with **a-c.** $K_{eff} = 7 \times 10^4$ J m^{-3} and **d-f.** $D = 1.27$ mJ m^{-2}.

A similar analysis can be performed for the effective anisotropy K_{eff} (see Fig. 2.6.d-f), which is varied in the range $K_{eff} = 1 \times 10^4 - 61 \times 10^4$ J m^{-3} (for $D = 1.27$ mJ m^{-2}). The lower limit corresponds to a vanishing PMA, *i.e.* the spin reorientation transition; the higher limit corresponds to the effective anisotropy measured in Pt/Co(0.63nm)/MgO (§5.3). We first notice that no stable solution is found if K_{eff} exceeds a certain value (see the white areas on the diagrams). Then, as discussed previously, decreasing the effective anisotropy promotes larger equilibrium skyrmion sizes (Fig. 2.6.d) as well as larger annihilation barriers (Fig. 2.6.e). Finally, the E_a/R_{eq} diagram (Fig. 2.6.f) reveals here also that reducing the effective anisotropy enhances the thermal skyrmion stability. Note that a similar conclusion can be drawn for the exchange constant A [117].

Lastly, the dipolar interactions E_d also contribute to the stabilisation of magnetic skyrmions by decreasing their total energy ($E_d < 0$). Furthermore, since $E_d \propto M_s^2$, increasing M_s favours larger R_{eq} as well as larger E_a. The precise impact of M_s is nonetheless delicate to quantify in a simple manner as it is involved in all the terms of eq. (2.5). Numerical calculations suggest for instance that reducing drastically M_s to $\sim 10^4$ A m^{-1}, *i.e.* one or two orders of magnitude below the typical M_s of FM, should allow to reach very small skyrmions (below 10 nm), stable at RT [117].

To summarise, low-K_{eff} and high-D HM/FM-based systems appear as good candidates for the observation of stable, small RT skyrmions.

2.4.2 Skyrmions in single- vs multi-layers

The model described above [118], and two-dimensional models in general [117,118], are valid for a FM film with homogeneous magnetisation across its thickness t, which can be assumed if $t < l_{ex}$, where $l_{ex} = \sqrt{2A/(\mu_0 M_s^2)}$ is the so-called exchange length (typically 4-10 nm). This is in most cases verified in ultra-thin HM/FM/NM films since t is usually around 1 nm or less. In multilayers however, *i.e.* $[\text{HM/FM/NM}]_N$ stacks composed of N repetitions of the HM/FM/NM trilayer, although $t < l_{ex}$ within each FM layer, the inter-layer stray fields have a non-negligible influence and tend to favour the formation of flux-closure domains. If large enough, the inter-layer dipolar interactions can outweigh the DMI, resulting in the stabilisation of skyrmion with different helicities in different layers. This effect has been evidenced in several material stacks: $[\text{Pt(3)/Co(1.1)/Ta(4)}]_{10}$ [141], $[\text{Pt(1)/Co(0.8)/Al}_2\text{O}_3\text{(1)}]_{20}$ [142] and $[\text{Ta(3)/FeCoB(1.45)/MgO(2)}]_{16}$ [143] (thicknesses in nm). Fig. 2.7 displays the results of micromagnetic simulations obtained by Li *et al.* [143] for the parameters of $[\text{Ta/FeCoB/MgO}]_{16}$. It shows that the skyrmion helicity in the bottom-most layer corresponds to the one dictated by the DMI. However, the skyrmion helicity evolves from layer to layer due to the dipolar interactions and one goes continuously from a left-handed Néel skyrmion (bottom-most) to a right-handed Néel skyrmion (top-most) via a Bloch skyrmion in an intermediate layer. The position of this Bloch skyrmion within the multilayer depends on the relative strength of the DMI and the dipolar interactions. This effect is all the more important when N, M_s and t are large and when the spacer thickness (*i.e.* the distance separating two FM layers) is small. A homogeneous Néel configuration can hence be stable if the DMI is large enough and/or the inter-layer dipolar interactions are small enough [144,145]. More specifically, recent analytical calculations [144] suggest that for typical D, M_s, t and spacer thickness values, the critical number of layer above which hybrid chiralities are expected is around $N = 10$, which remains in the order or below the common choice of N in experiments [110–113,121,122,146]. Hence, this stray-field-related effect is an additional complexity to consider when working with multilayers.

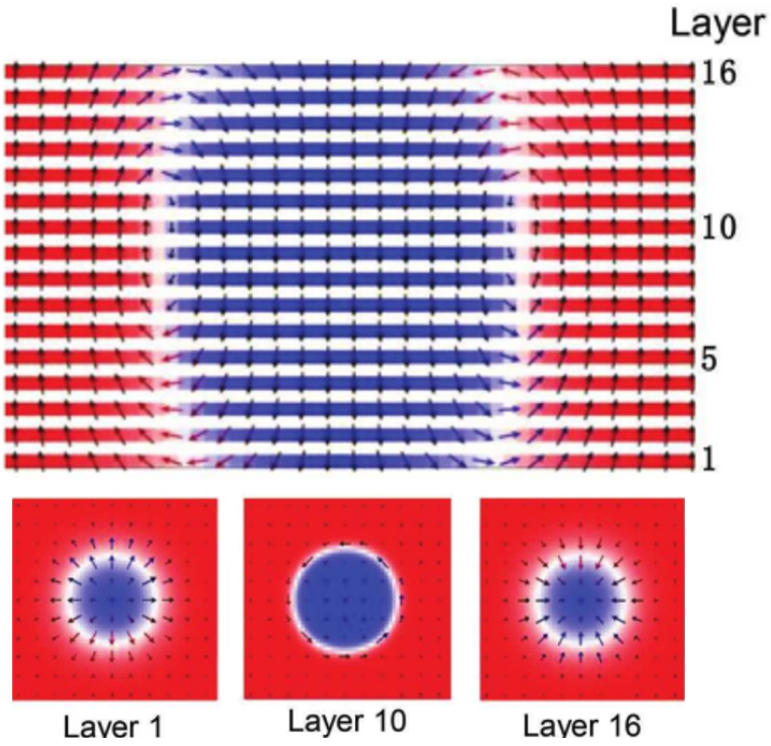

Fig. 2.7: Hyrbid skyrmionic textures in FM multilayers | Simulated skyrmion profile in a $[\text{Ta(3)/FeCoB(1.45)/MgO(2)}]_{16}$ multilayer. The bottom-most and top-most layers host Néel skyrmions with opposite helicities, respectively left- and right-handed. Intermediate layers host skyrmions with composite Bloch-Néel characters and a pure Bloch skyrmion is stabilised in layer 10. Adapted from ref. [143].

2.4.3 Skyrmion nucleation

In order to nucleate skyrmions in physical systems, the strength of the different interactions needs to be engineered to create the appropriate energy minimum. As presented in §2.2, RT skyrmions can be realised in HM/FM/NM stacks. From the analysis of the competing energies inside a magnetic skyrmion (§2.4.1), we saw that materials with low K_{eff} and large D are good candidates for hosting RT skyrmions. So far, Pt/Co-based systems are those which offer the largest DMI magnitudes. This has notably motivated the choice of exploiting the Pt/Co interface — which also provides the PMA — in the different material stacks studied in this thesis. The most easily implementable method to reduce the effective anisotropy in a given material stack is to increase the FM thickness. Lowering the effective anisotropy or increasing the strength of the dipolar interactions, for example by increasing the number of repetitions in a multilayer, leads to the formation of stripe or worm-like domains. In the presence of an OOP external field, this multi-domain state can shrink into individual skyrmions or a skyrmion lattice depending notably on the ratio D/D_c [147]. This was evidenced experimentally in $[\text{Ir/Fe/Co/Pt}]_{20}$ multilayers by varying the Fe/Co thickness ratio [112]: increasing D/D_c leads to a transition from individual skyrmions to a skyrmion lattice in the presence of an external field. Reaching the (meta-)stable skyrmion ground state almost always requires an external field. This remains the most commonly used method to stabilise skyrmions. This, as well as other approaches relying on the tuning of the static properties of the film, will be discussed in more details in Chapter 4, in the light of experiments conducted during this thesis.

Moreover, other stimuli can be used to overcome the energy barrier between a given state, *e.g.* stripe domains, and the more stable skyrmion state such as current-induced (Joule) heating [121,148] or SOTs in constricted tracks [109]. Besides current-induced mechanisms, electric fields can also be employed to tune the skyrmion stability. Electric-field-induced skyrmion nucleation/annihiliation was notably demonstrated for small skyrmions in epitaxial films at low temperature [149] and for µm-sized skyrmionic bubbles in sputtered films at RT [49,150], as a result of a change of the anisotropy and saturation magnetisation [150] and of the interfacial DMI [49].

2.5 Current-driven skyrmion dynamics

An crucial aspect for the development of skyrmion-based devices and for performing of skyrmion-shift operations is their motion. In this section, the principal theoretical elements to describe the current-driven dynamics of magnetic skyrmions are presented. As mentioned earlier, we consider a HM/FM/NM film, with interfacial PMA and DMI. Moreover, we only focus on SOTs which are expected, as for DWs, to provide a more efficient driving mechanism than STTs [70,71]. The SOT-driven dynamics of magnetic skyrmions shares many similarities with that of DWs introduced earlier in §1.3.3.2. Hence, its mechanisms can naturally be extended to magnetic skyrmions. For the present description, we only consider the DL-SOT term. The FL-SOT is omitted for now as it does not impact the skyrmion dynamics in the model described below. Its effect will be discussed later using micromagnetic simulations (§5.5). In this framework, the magnetisation dynamics is described by the following LLG equation (§1.3.3.2):

$$\frac{\partial \boldsymbol{m}}{\partial t} = -\gamma_0 \left(\boldsymbol{m} \times \boldsymbol{H}_{eff}\right) + \alpha \left(\boldsymbol{m} \times \frac{\partial \boldsymbol{m}}{\partial t}\right) - \gamma_0 \left(\boldsymbol{m} \times \boldsymbol{H}_{DL}\right) \tag{2.6}$$

where $\boldsymbol{H}_{DL} = H_{DL}^0 \left(\boldsymbol{m} \times \left(\hat{\boldsymbol{j}} \times \hat{\boldsymbol{z}}\right)\right)$ is the effective field associated with the DL-SOT and $\boldsymbol{J} = J\hat{\boldsymbol{j}}$ is the charge current (opposite to the electron flow). For consistency, we will consider a DL-SOT of the same sign as that of Pt, *i.e.* $H_{DL}^0 > 0$. Defining $\hat{\boldsymbol{j}} = \hat{\boldsymbol{x}}$ leads to $\boldsymbol{H}_{DL} = H_{DL}^0 \left(\hat{\boldsymbol{y}} \times \hat{\boldsymbol{m}}\right)$. A good picture of the SOT-induced skyrmion motion containing the essential physical ingredients necessary to its description is provided by the Thiele equation [151]. In Thiele's formalism, the skyrmion is assumed to be a rigid spin texture so that one may only consider the motion of its centre of mass. Under this assumption, the steady-state skyrmion velocity, $\boldsymbol{v}$, results from an equilibrium between different forces. Its derivation from the LLG equation is detailed in §A.1. It reads:

$$\boldsymbol{F}_{DL} + \boldsymbol{G} \times \boldsymbol{v} - \alpha \boldsymbol{\mathcal{D}} \cdot \boldsymbol{v} = \boldsymbol{0} \tag{2.7}$$

Here, $\boldsymbol{F}_{DL}$ is the force due to the DL-SOT, $\boldsymbol{G}$ the gyrotropic vector and $\boldsymbol{\mathcal{D}}$ the dissipation matrix. They are given respectively by:

$$\boldsymbol{F}_{DL} = \begin{pmatrix} F_{DL,x} \\ F_{DL,y} \\ 0 \end{pmatrix}, F_{DL,i} = -\mu_0 M_s t H_{DL}^0 \iint dxdy \left(m_x \frac{\partial m_z}{\partial x_i} - m_z \frac{\partial m_x}{\partial x_i} \right) \tag{2.8}$$

$$\boldsymbol{G} = \begin{pmatrix} 0 \\ 0 \\ G \end{pmatrix}, G = -\frac{M_s t}{\gamma} \iint dxdy\, \boldsymbol{m} \cdot \left(\frac{\partial \boldsymbol{m}}{\partial x} \times \frac{\partial \boldsymbol{m}}{\partial y} \right) \tag{2.9}$$

$$\boldsymbol{\mathcal{D}} = \begin{pmatrix} \mathcal{D}_{xx} & \mathcal{D}_{xy} \\ \mathcal{D}_{yx} & \mathcal{D}_{yy} \end{pmatrix}, \mathcal{D}_{ij} = \frac{M_s t}{\gamma} \iint dxdy \left(\frac{\partial \boldsymbol{m}}{\partial x_i} \cdot \frac{\partial \boldsymbol{m}}{\partial x_j} \right) \tag{2.10}$$

with $i = x, y$ and t the FM film thickness. Note that the FL-SOT does not generate a force on a rigid skyrmion as its action is equivalent to that of a homogeneous external magnetic field, perpendicular to the current. Assuming further that the skyrmion exhibits a rotational symmetry, one has $(\partial \boldsymbol{m}/\partial x) \perp (\partial \boldsymbol{m}/\partial y)$. Consequently, $\mathcal{D}_{xy} = \mathcal{D}_{yx} = 0$ and $\mathcal{D}_{xx} = \mathcal{D}_{yy} = \mathcal{D}$. Then, noticing that $G = -(M_s t/\gamma) 4\pi N_{sk}$ (see eq. (2.1)), the above equations become:

$$\boldsymbol{F}_{DL} = \begin{pmatrix} F_{DL,x} \\ F_{DL,y} \\ 0 \end{pmatrix}, F_{DL,i} = -\mu_0 M_s t H_{DL}^0 \iint dxdy \left(m_x \frac{\partial m_z}{\partial x_i} - m_z \frac{\partial m_x}{\partial x_i} \right) \tag{2.11}$$

$$\boldsymbol{G} = \begin{pmatrix} 0 \\ 0 \\ G \end{pmatrix}, G = -4\pi \frac{M_s t}{\gamma} N_{sk} = -4\pi \frac{M_s t}{\gamma} p \tag{2.12}$$

$$\boldsymbol{\mathcal{D}} = \begin{pmatrix} \mathcal{D} & 0 \\ 0 & \mathcal{D} \end{pmatrix}, \mathcal{D} = \frac{M_s t}{\gamma} \iint dxdy \left(\frac{\partial \boldsymbol{m}}{\partial x} \right)^2 \tag{2.13}$$

The expressions of the longitudinal (v_x) and transverse (v_y) skyrmion velocity can hence be derived:

$$v_x = \frac{\alpha \mathcal{D} F_{DL,x} - G F_{DL,y}}{G^2 + \alpha^2 \mathcal{D}^2} \tag{2.14}$$

$$v_y = \frac{G F_{DL,x} + \alpha \mathcal{D} F_{DL,y}}{G^2 + \alpha^2 \mathcal{D}^2} \tag{2.15}$$

From Fig. 2.2 and eq. (2.11), it can be inferred that $F_{DL,x} = 0$ for a Bloch skyrmion and $F_{DL,y} = 0$ for a Néel skyrmion. In other words, the DL-SOT drives a Bloch (Néel) skyrmion in a direction perpendicular (parallel) to the current direction. Accordingly, a composite Bloch-Néel skyrmion is driven along an intermediate direction. Néel skyrmions hence present a clear advantage for performing skyrmion-shift operations in tracks. Then, the direction of motion, that is the sign of $F_{DL,x}$ and $F_{DL,y}$, depends on the skyrmion chirality (left/right-handedness). Furthermore, the dissipative force $-\alpha \mathcal{D} \boldsymbol{v}$, proportional to the magnetic damping, is directed against the direction of motion. Finally, the gyrotropic force $\boldsymbol{G} \times \boldsymbol{v}$ describes a deflection of the skyrmion from the direction imposed by the driving force $\boldsymbol{F}_{DL}$: this is the so-called skyrmion Hall effect (SkHE). The SkHE is characterised by the skyrmion Hall angle (SkHA), Θ_{SkH}, defined as the angle between the driving force and the skyrmion motion direction, $\Theta_{SkH} = (\boldsymbol{F}_{DL}, \boldsymbol{v})$. Its expression can be simplified into:

$$\tan \Theta_{SkH} = \frac{G}{\alpha \mathcal{D}} \tag{2.16}$$

Here, it can already be pointed out that the SkHA is independent of the current density or the skyrmion velocity. More specifically, it only depends on the skyrmion core polarity p (and not on its helicity). To better visualise this effect, the direction of motion of magnetic skyrmions with $p = 1$ and different helicities is represented schematically in Fig. 2.8. For each skyrmion, the orientation of $\boldsymbol{F}_{DL}$ and $\boldsymbol{v}$ is represented. For the opposite skyrmion polarity ($p = -1$), $G > 0$, resulting in an opposite SkHA. A parallel can be drawn with the conventional charge Hall effect, which describes the deflection of charged particles (electrons and holes) in a direction transverse to the current flow in the presence of an external magnetic field, as a result of the Lorentz force, $q\,(\boldsymbol{v} \times \boldsymbol{B})$. Particles with opposite charges q are deflected in opposite directions. Likewise, upon reversing the magnetic field direction, the direction of deflection is also reversed. The difference with a skyrmion however is that reversing the magnetic field also reverses its charge N_{sk}.

Note that there is a fundamental difference between magnetic skyrmions and bubbles: magnetic bubbles have arbitrary topological charges, leading to a complex topological-charge-dependent dynamics. On the contrary, all magnetic skyrmions in a given material stack are virtually identical and exhibit the same direction of motion, which constitutes a clear advantage for technological purposes.

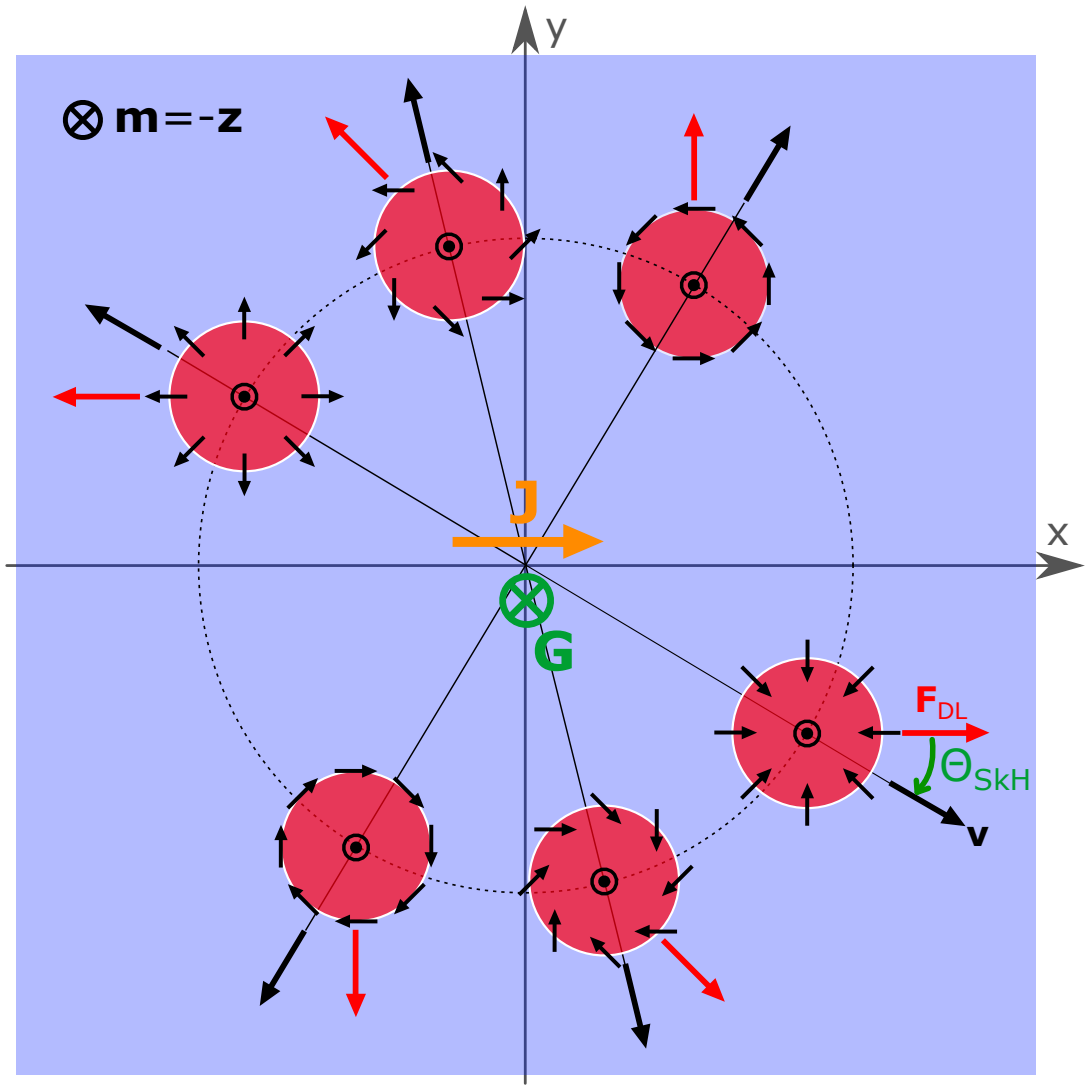

Fig. 2.8: SOT-driven skyrmion motion direction | Direction of motion of magnetic skyrmions with $p = 1$ and different helicities driven by the DL-SOT with the sign according to Pt ($H^0_{DL} > 0$). The charge current $\boldsymbol{J}$ (opposite to the electron flow) flows along $+\hat{\boldsymbol{x}}$ and the gyrotropic vector $\boldsymbol{G}$ points along $-\hat{\boldsymbol{z}}$ for all skyrmions ($p = 1$). The skyrmion Hall angle is defined as the angle between the driving force and the skyrmion motion direction, $\Theta_{SkH} = (\boldsymbol{F}_{DL}, \boldsymbol{v})$.

Let us now focus the discussion on Néel skyrmions only as they are the stable configuration promoted by the interfacial DMI in HM/FM/NM films. As detailed in §A.2, if $R \gg \Delta$, analytical expressions for $F_{DL,x}$ ($F_{DL,y} = 0$) and $\mathcal{D}$ can be derived [152]: $F_{DL,x} = \pm\mu_0 M_s t \pi^2 H^0_{DL} R$ and $\mathcal{D} = \frac{M_s t}{\gamma} 2\pi \frac{R}{\Delta}$. The + (−) sign in the expression of $F_{DL,x}$ stands for a left-handed (right-handed) chirality. We can then derive the skyrmion velocity and the SkHA as follows:

$$v = \sqrt{v_x^2 + v_y^2} = \frac{\gamma\pi}{4} \frac{R}{\sqrt{\left(\frac{\alpha R}{2\Delta}\right)^2 + 1}} C_{DL} J \tag{2.17}$$

$$\tan\Theta_{SkH} = -p\,\frac{2\Delta}{\alpha R} \tag{2.18}$$

Here, we have written $\mu_0 H^0_{DL} = C_{DL} J$, with C_{DL} the effective field per unit current density (in T A^{-1} m^2) associated with the DL-SOT. Note that in this case, because the driving force $\boldsymbol{F}_{DL}$ is along the current, the expression of the SkHA simplifies into $\tan\Theta_{SkH} = v_y/v_x$. From these equations, it appears that smaller skyrmions exhibit smaller velocities, which constitutes an evident downside for applications. This shall be compensated by using low-damping and/or large-SOT materials. Furthermore, although Néel skyrmions are driven along the current direction, in track geometry, the SkHE will always impose a deflection towards one edge of the device. This remains true for curved tracks since the current is always locally parallel to the edges. Micromagnetic studies predicted that the skyrmion should experience a repulsion from the track edge [70,133,153]. This repulsion would counterbalance the SkHE, resulting in a sliding motion along the edge. This would then cancel the transverse skyrmion velocity and enhance its longitudinal velocity; provided that the current density is kept below a certain critical value above which the skyrmion is expelled from the track [154]. However, in experiments [155], a reduced velocity is rather observed for skyrmions 'sliding' along a track edge as compared to skyrmions free from any confining potential. This may be due to edge defects created during the fabrication process [155]. Other proposals have been put forward to inhibit the SkHE. These involve novel chiral magnetic textures like antiskyrmions [156] and AF skyrmions [157].[1] Antiskyrmions were recently observed at RT in bulk tetragonal Heusler compounds [101] and could be stabilised in interfacial systems with anisotropic DMI [160,161]. AF skyrmions may be realised in AF materials, synthetic AF (SAF) or compensated ferrimagnets. Chapter 6 is dedicated to the study of SAF multilayers for the observation and nucleation of skyrmions.

In recent years, mostly during the course of my thesis, intense efforts have been directed towards achieving current-driven skyrmion motion in HM/FM-based systems by several groups, in both single- and multi-layers. The main results are summarised in Fig. 2.9. Overall, the velocity was observed to increase monotonically with the injected current density, and the observed direction of motion was consistent with that expected for Néel skyrmions driven by the SHE-induced DL-SOT, as well as with the skyrmion chirality expected from the sign of the DMI. Velocities ranging from a few m s^{-1}, for ≈ 1-µm-diameter skyrmions in Ta/FeCoB/TaO_x (Fig. 2.9.b) [155], to ≈ 100 m s^{-1} for ≈ 150-nm-diameter skyrmions in $[Pt/CoFeB/MgO]_{15}$ (Fig. 2.9.a) [110], were reported. Furthermore, these measurements have revealed the existence of a critical depinning current density below which no motion is observed. This depinning current densities were found in the order of 10^{10} A m^{-2} for µm-sized skyrmions and in the order of a few 10^{11} A m^{-2} for skyrmion sizes in the 100 nm range. Although larger than those reported for STT-driven skyrmion lattices in chiral magnets ($\sim 10^6$ A m^{-2}) [163], these values remain just below or in the order of those measured for DWs. Regarding the SkHE, two studies [146,155] have revealed that the SkHA depends on the current density (or similarly on the skyrmion velocity), in sharp contrast with the predictions of the model described above. This aspect of the skyrmion dynamics will be addressed in more detail in Chapter 5 in the light of experiments conducted during this thesis.

Finally, it is important to note that the description of the current-driven skyrmion dynamics presented in this section is valid only for a FM film with homogeneous magnetisation across its

[1] As well as more exotic spin textures such as skyrmioniums [158,159].

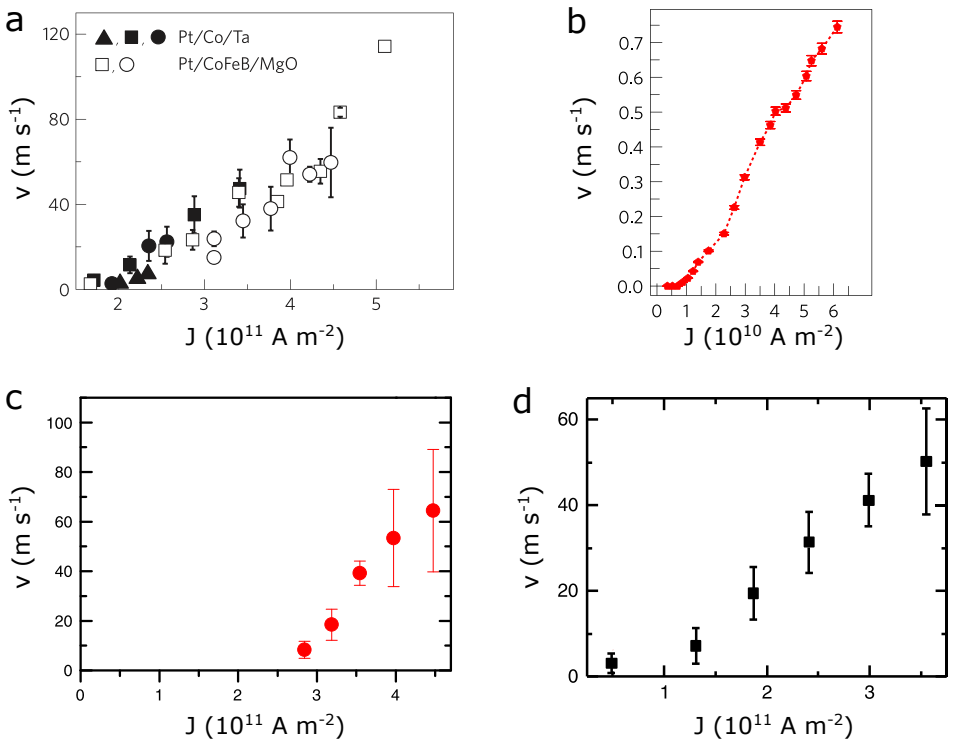

Fig. 2.9: Current-driven skyrmion motion: observations | Skyrmion velocity v as a function of the current density J measured in different material stacks at RT. **a.** $[Pt/Co/Ta]_{15}$ (average skyrmion diameter $d_{sk} \approx 150$ nm) and $[Pt/Co_{60}Fe_{20}B_{20}/MgO]_{15}$ ($d_{sk} \approx 150$ nm). **b.** $Ta/Fe_{60}Co_{20}B_{20}/TaO_x$ ($d_{sk} \approx 1000$ nm). **c.** Pt/Ni/Co/Ni/Au/Ni/Co/Ni/Pt ($d_{sk} \approx 160$ nm). **d.** $[Pt/Fe_{65.6}Gd_{25}Co_{9.4}/MgO]_{20}$ ($d_{sk} \approx 180$ nm). Adapted from ref. **a.** [110], **b.** [155], **c.** [152] and **d.** [162].

thickness. In stray-field-coupled multilayers, the possible presence of layer-dependent skyrmion helicities may lead to layer-dependent SOTs [144]. Indeed, it can be inferred from Fig. 2.7 and 2.8 that different skyrmion helicities result in different DL-SOT-induced directions of motion. Furthermore, as suggested by recent theoretical studies [145,164], the hybrid skyrmions in multilayers may not conserve their topological charge during the motion and therefore loose their skyrmionic character, strongly impeding their motion and limiting their applicability [164]. Lastly, for a given current density, a larger Joule dissipation is also expected in multilayers and in thicker films in general. If we write $P = RI^2$ the dissipated power, since R is inversely proportional to the total thickness of the conductive layer(s) and I is proportional to it, P scales with the total film thickness. Hence, for a multilayer $[HM/FM/NM]_N$, $P \propto N$ so the dissipated power is N times larger than in a single HM/FM/NM layer. These aspects further motivate the choice of using single-layer films to study the skyrmion dynamics.

2.6 Conclusions

In this chapter, we saw that magnetic skyrmions are small magnetic domains enclosed by a chiral DW, characterised by a quantised topological charge, $|N_{sk}| = 1$. Their stability at RT in sputtered films combined with their small size and efficient current-induced manipulation by SOTs make them promising candidates for memory and logic applications. In the following chapters, we address certain key aspects concerning the skyrmion stability and nucleation and their current-driven dynamics. Chapter 4 presents different approaches investigated to stabilise magnetic skyrmions at RT. Chapter 5 is dedicated to the study of their current-driven motion. Chapter 6 presents the results obtained on the optimisation of SAF multilayers, motivated by the foreseen advantages of SAF skyrmions. Before addressing these aspects, Chapter 3 details the different experimental techniques employed during this thesis.

Chapter 3

Experimental techniques

In this chapter, the different experimental techniques used in this thesis are explained. It includes a brief description of the deposition and characterisation tools as well as a more detailed explanation of the X-ray microscopy techniques employed to image magnetic skyrmions. Finally, the nanofabrication steps for the samples observed with X-ray microscopy are detailed.

3.1 Thin film deposition: magnetron sputtering

Magnetron sputtering is a physical vapour deposition technique among the most widely used in the microelectronics industry. Although sputtering often does not result in long-range crystalline order but rather partially-ordered or amorphous layers, unlike epitaxial films, it is compatible with all standard applications and industrial requirements and is fast as well as easily implementable. This has motivated the choice of sputtering to deposit the samples studied in this thesis. The principle is the following: the substrate is placed in a chamber at room temperature and under vacuum (typically 10^{-6} to 10^{-9} mbar) to ensure a good purity of the deposition. A plasma is generated from an inert gas, in our case Ar, by applying a RF electric field between the substrate and the target material to deposit. The Ar^+ ions are then accelerated onto the target, leading to the ejection of a target atom that deposits on the substrate. Then, a magnet located near the target imposes helical trajectories on the electrons of the plasma in the vicinity of the target, leading to an increased number of ionising collisions with the Ar atoms. This further increases the number of Ar^+ ions and subsequently the deposition rate. Typical deposition rates are in the order of 0.05 nm s^{-1}. In addition, the deposition tool is equipped with a treatment chamber where oxidation steps can be performed, for example to form MgO by oxidation of Mg.

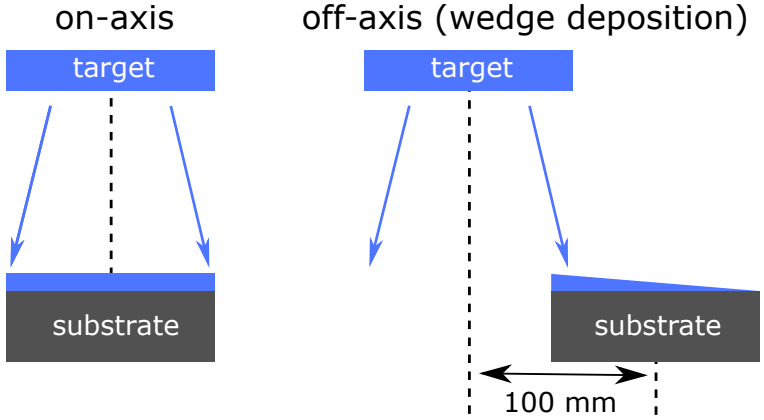

Fig. 3.1: Sputtering geometries | Schematic representation of the two possible deposition geometries. The off-axis geometry allows to deposit the material as a wedge with a thickness variation up to a factor of 2 on a 100 mm wafer.

Two depositions geometries, represented in Fig. 3.1, can be used. In the on-axis geometry, the substrate is placed under the target and set in rotation, ensuring a spatially homogeneous deposition. In the off-axis geometry, the substrate is shifted from the on-axis position and the rotation is stopped. This allows to deposit materials as wedges, *i.e.* with a thickness gradient. For a shift of 100 mm, on a 100 mm wafer, the thickness can be varied up to about a factor of 2 along the wedge. Finally, by rotating the substrate by 90°, we can deposit double wedges, perpendicular to each other, and span a wide range of material properties. For each material, the thickness gradient is calibrated by X-ray reflectivity. Wedges that allow to finely tune the material properties were used extensively all along this thesis as it will be detailed in the following chapters. All the samples studied were deposited on Si/SiO_2 substrates for X-ray photo-electron microscopy and characterisation, and on 100-nm-thick Si_3N_4 membranes for scanning transmission X-ray microscopy. Note that sputtering does not require a specific substrate, as opposed for example to epitaxy, which makes it a very versatile tool.

All the samples were deposited at Spintec by Stéphane Auffret and Miguel Rubio Roy.

3.2 Characterisation techniques

In this section, the magnetic characterisation techniques used during this thesis are briefly presented: magneto-optical Kerr effect (MOKE), vibrating sample magnetometry (VSM) and superconducting quantum interference device (SQUID).

3.2.1 Magneto-optical Kerr effect

The magneto-optical Kerr effect (MOKE) is a powerful tool to measure local changes of the magnetisation. It describes the change in the polarisation of a light that is reflected from a magnetic material [165]. The principle is the following: when a linearly polarised light is reflected from a magnetic material exhibiting a net magnetisation, it acquires an elliptical polarisation (Kerr ellipticity) with a rotated plane of polarisation, *i.e.* the plane containing the incident light and the sample surface normal (Kerr rotation). The magnetisation of a sample can hence be measured by determining the change in the polarisation of the reflected light. This is achieved with a polariser, through which a linearly polarised laser beam can be produced and directed onto the sample, plus an analyser to determine the Kerr rotation.

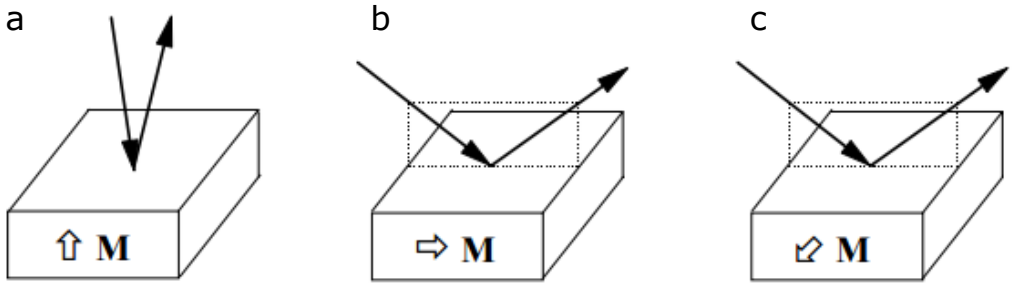

Fig. 3.2: Magneto-optical Kerr effect configurations | **a.** Polar, **b.** longitudinal and **c.** transverse MOKE configurations.

The Kerr rotation depends on the direction of the magnetisation with respect to the incident beam. Three limiting configurations can be distinguished: the polar, longitudinal and transverse MOKE, represented in Fig. 3.2. In the polar configuration, the magnetisation is contained in the plane of incidence and perpendicular to the sample surface. In the longitudinal configuration, the magnetisation is also contained in the plane of incidence but lies in the sample plane. Finally, in the transverse configuration, the magnetisation is normal to the plane of incidence but lies in the

sample plane. Since the laser spot can be focused, it allows to locally measure changes in the sample magnetisation, typically hysteresis loops.

In this thesis, we used the commercial NanoMOKE3® from Durham Magneto Optics (see Fig. 3.3). It consists of a laser source (660 nm), a polariser, an analyser and a detector, as well as an electromagnet and a motorised stage. The laser beam is focused to a $\sim$ 300 µm spot at an angle of 45° with respect to the sample surface. This geometry allows the observation of the three MOKE configurations. In this work, only perpendicularly magnetised samples were studied. For this purpose, the set up was adjusted to measure the polar MOKE. The electromagnet position was also adjusted to produce an OOP magnetic field at the position of the laser spot (up to $\approx$ 200 mT). The motorised stage and the small spot size allow to measure hysteresis loops as a function of the sample position, which is suitable for mapping magnetic properties in wedged films.

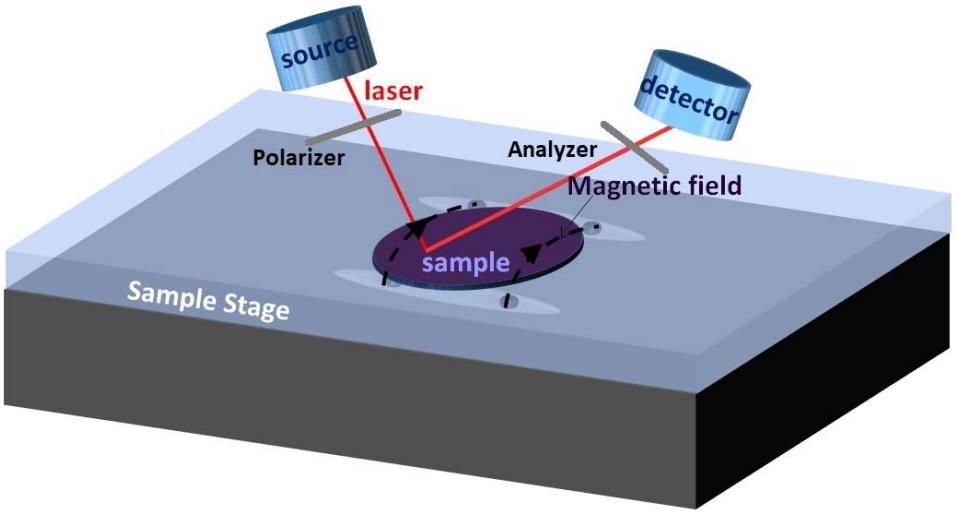

Fig. 3.3: Schematics of the NanoMOKE3® setup | The sample is placed on a motorised stage and the laser spot size is $\sim$ 300 µm. The electromagnet is located below the stage. Adjusting its position allows to apply a (quasi-)pure OOP external magnetic field. *(Courtesy of Titiksha Srivastava [166]).*

3.2.2 Magnetometry techniques

3.2.2.1 Vibrating sample magnetometry

In vibrating sample magnetometry (VSM), the sample is introduced in a constant, uniform magnetic field which induces a magnetisation in the sample. As the sample is vibrated at a certain frequency, it induces perturbations in the external field, perturbation that are then measured by a set of coils (the pick-up coils) arranged around the sample. The measurement principle is based on Faraday's law of electromagnetic induction, which states that a change in the magnetic flux in a circuit produces an electrical current. Hence, using a lock-in technique, the change of the magnetisation of the sample as a function of the applied magnetic field can be extracted. VSM provides a measurement of the magnetic moment in the direction of the applied field, hence OOP and IP hysteresis loops can be measured by changing the orientation of the sample with respect to the applied field.

In this thesis, we used the VSM from MicroSense, at room temperature, which allows to apply magnetic fields up to 1.8 T with a sensitivity in the order of 10^{-6} emu (10^{-9} A m^2). It was typically used to measure hysteresis loops of thin films with a large saturation fields such as SAF multilayers (Chapter 6). It is a fast technique to measure the IP and OOP saturation fields of ultra-thin magnetic films. However, for more precise magnetisation measurements, we used a SQUID as described hereafter.

3.2.2.2 Superconducting quantum interference device

A SQUID is a magnometre used to measure weak magnetic moments within a large range of external magnetic fields and temperatures. A SQUID consists of two Josephson junctions in parallel that form a superconducting loop inside which the magnetic flux is quantised. Any change in this magnetic flux, for example upon passing a magnetised sample through the SQUID, can be measured as an output voltage change. A SQUID hence provides a measurement of the total magnetic moment of the sample in the direction perpendicular to the SQUID.

In this thesis, we used a SQUID from Quantum Design with a electromagnet allowing to apply magnetic fields up to 5 T with a sensitivity in the order of 5×10^{-8} emu (5×10^{-11} A m^2). It was used to measure precisely the magnetisation of ultra-thin Pt/Co/MgO films at room temperature.

3.3 X-ray microscopy techniques

In this section, the principle of the X-ray microscopy techniques used in this thesis is detailed, namely X-ray photo-emission electron microscopy (X-PEEM) and scanning transmission X-ray microscopy (STXM). Both of these techniques utilise the absorption of circularly-polarised X-ray light produced by synchrotron radiation. In X-PEEM, the magnetic texture is imaged using the photo-emitted electrons extracted from the sample surface (*photon-in/electron-out*) while STXM utilises the X-ray light transmitted through the sample (*photon-in/photon-out*).

3.3.1 X-ray magnetic circular dichroism

The X-ray magnetic circular dichroism (XMCD) denotes the difference in the absorption of X-ray photons with circular left (CL) and circular right (CR) polarisation by a magnetic material. The absorption of an X-ray photon induces an electronic transition from a core level to the valence band with a well defined energy. By tuning the energy of the X-ray on a specific absorption edge, one can then probe different elements and magnetic properties in the same sample. Most of the XMCD-based techniques utilise the synchrotron radiation as it produces a monochromatic soft X-ray light with a high brilliance whose polarisation can be tuned (CR, CL, linear). In FM transition metals (Fe, Co, Ni), magnetism stems from the uneven occupation of $3d$ and $4s$ bands by $\uparrow$-spin and $\downarrow$-spin electrons at the Fermi level. The absorption edges exhibiting the largest XMCD are the L_3 and L_2, corresponding respectively to $2p_{3/2} \rightarrow 3d$ and $2p_{1/2} \rightarrow 3d$ electronic transitions. For Co, the L_3 and L_2 energies are respectively 779 eV and 794 eV.

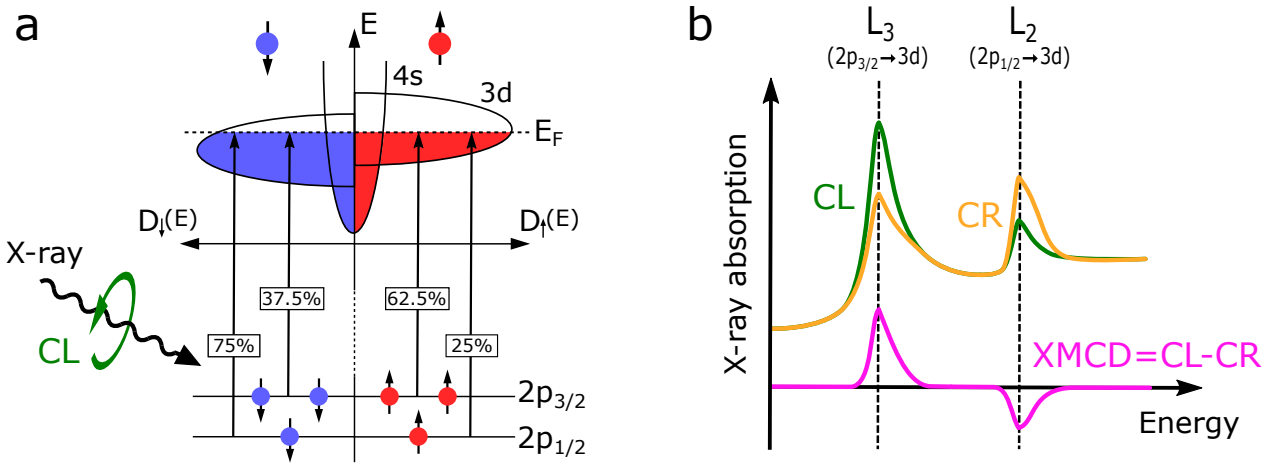

Fig. 3.4: X-ray Magnetic Circular Dichroism (XMCD) | **a.** Electronic transitions induced by the absorption of an X-ray photon with circular left (CL) polarisation at the L_3 ($2p_{3/2} \rightarrow 3d$) and L_2 ($2p_{1/2} \rightarrow 3d$) edges of a FM transition metal. **b.** Typical absorption spectrum and XMCD at the L_3 and L_2 edges of a FM transition metal.

The absorption process is represented schematically in Fig. 3.4.a for a CL-polarised light. A circularly polarised X-ray photon carries an orbital angular momentum that can be transferred to the electron spin angular momentum, via the SOC, following specific selections rules. By tuning the X-ray energy on a specific absorption edge, an electronic transition from a core level to the valence band can be induced. The transition probability depends on the number of empty states at the Fermi level, $D(E_F)$. In FM metals, the density of states at the Fermi level is different for $\uparrow$-spins and $\downarrow$-spins electrons ($D_\uparrow(E_F) \neq D_\downarrow(E_F)$) hence the absorption of CL and CR X-ray photons is different at a given transition. More specifically, it can be shown that at the L_3 (L_2) edge, a CL photon excites 62.5% (25%) of $\uparrow$-spin electrons and 37.5% (75%) of $\downarrow$-spin electrons [167,168]. For the CR polarisation, the photon carries an opposite angular momentum and the absorption probabilities are opposite to those of the CL case. In the example of Fig. 3.4.a, $D_\uparrow(E_F) > D_\downarrow(E_F)$, meaning that more $\uparrow$-spin than $\downarrow$-spin states are available: the absorption is therefore larger for CL photons than for CR photons at the L_3 edge. Accordingly, more CR photons than CL photons are absorbed at the L_2 edge. The absorption is represented in Fig. 3.4.b. The XMCD is calculated as the difference between the absorption of CL and CR photons. Hence, at a given absorption edge, different magnetisation directions will results in different XMCD signals. Accordingly, for a non-magnetic material, since $D_\uparrow(E_F) = D_\downarrow(E_F)$, the absorption of CL and CR X-rays is identical and hence does not produce an XMCD contrast. In the following sections, two techniques that utilise this effect to image magnetic textures are presented. For both techniques, the images were acquired at the L_3 edge of the FM material as it exhibits the largest absorption.

3.3.2 X-ray photo-emission electron microscopy

X-ray photo-emission electron microscopy (X-PEEM) is a hybrid technique that uses the electrons emitted from a sample upon irradiation by X-rays to image its magnetic texture.

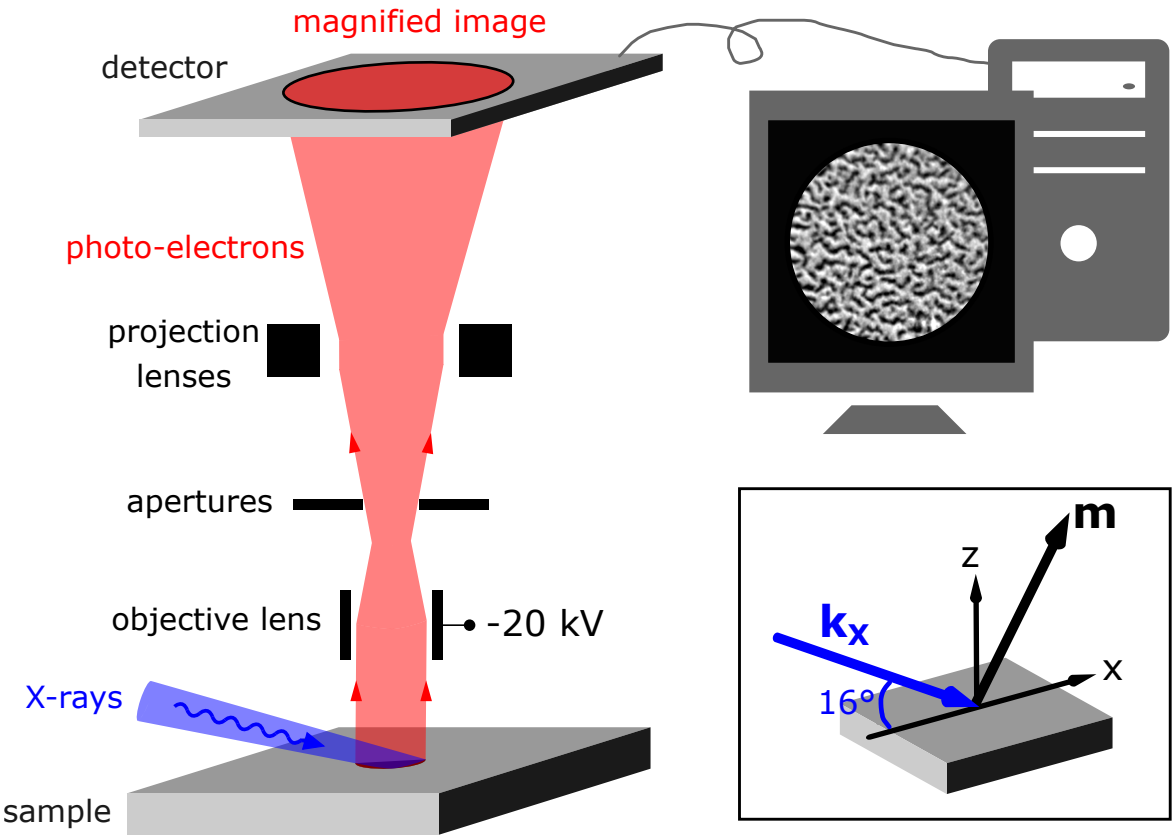

Fig. 3.5: X-ray photo-emission electron microscope | The X-ray beam impinges at a grazing angle of 16° on the sample surface as shown in the inset. The XMCD-PEEM contrast, C, is given by $C \propto \boldsymbol{k}_X \cdot \boldsymbol{m}$.

The principle of the technique is based on the Auger process: when a circularly polarised X-ray photon is resonantly absorbed by the magnetic material, an electron from a core level is excited (*e.g.* $2p_{3/2} \rightarrow 3d$ for the L_3 edge), hence creating an empty state. Electrons from an intermediate state, between the core and the Fermi level, fill this empty core state. As the energy of the process must be conserved, an electron from the intermediate state is excited just above the Fermi level to compensate the decay from the intermediate state to the core level. Finally, if this electron is given enough kinetic energy, upon applying a large voltage, it can be extracted from the sample and collected.

A schematics of the microscope is shown in Fig. 6.5: the sample is placed in ultra-high vacuum ($10^{-8}-10^{-9}$ mbar) and illuminated by the X-ray beam. The photo-electrons emitted are accelerated by the high voltage applied between the sample surface and the objective lens (10 to 20 kV). The accelerated electrons are then processed by the different electron-optic components before reaching an electron-sensitive screen. This is a full-field technique since all the photo-electrons on a given area of the sample are collected simultaneously. In the experiments conducted during this thesis, the sample was placed on a sample-holder with a built-in electromagnet to apply an OOP magnetic field. The sample-holder can be displaced horizontally using piezoelectric motors. In the experiments of current-driven skyrmion dynamics presented in Chapter 5, the sample was stuck with silver paste on a PCB to ensure a common electrical ground, and electrical contacts were realised by micro-bonding.

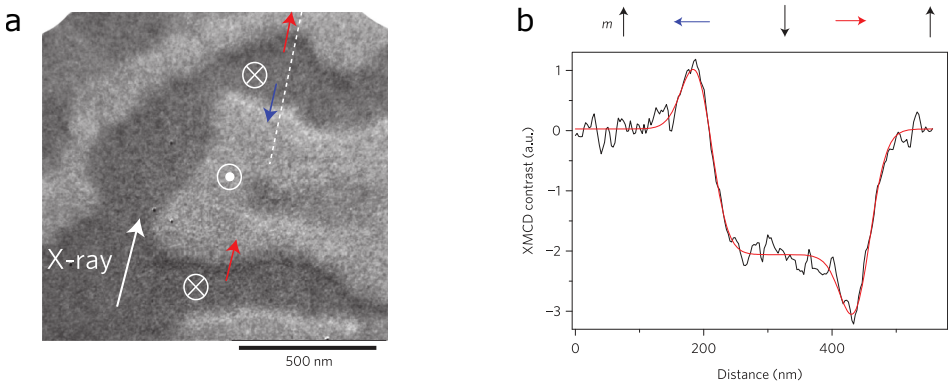

Fig. 3.6: XMCD-PEEM image of Néel DWs | **a.** XMCD-PEEM image of the domain configuration in an ultra-thin Pt/Co/MgO film at RT acquired at the Co L_3 absorption edge. **b.** XMCD contrast along the white dashed line in **a**. The red line is a fit with a 180° DW profile. The XMCD contrast is proportional to the projection of the incident X-ray beam on the magnetisation direction. Hence, the brightest and darkest contrasts in the direction of the beam at the DW indicate a left-handed Néel configuration. Adapted from ref. [48].

Since the absorption of circularly polarised X-rays is spin-dependent (§3.3.1), so is the number of photo-emitted electrons. Furthermore, the absorption is proportional to the projection of the X-ray beam direction on the magnetisation. Consequently, the absorption is maximum (minimum) when the magnetisation and the X-ray beam are parallel (anti-parallel). The imaging process is the following: for each polarisation (CL and CR), the intensity is averaged over typically 60 images. The two resulting images are then subtracted to obtain the XMCD-PEEM image.[1] In the microscope used during this thesis, the SPELEEM III Microscope from Elmitec GmbH, the X-ray beam impinges at a grazing angle of $\alpha = 16°$ on the sample surface (inset of Fig. 6.5). If the beam is contained in the xz plane with $\hat{\boldsymbol{x}}$ in the sample plane and $\hat{\boldsymbol{z}}$ its normal, the XMCD-PEEM contrast is given by $C \propto \boldsymbol{k}_\mathrm{X} \cdot \boldsymbol{m} = -m_z \sin\alpha + m_x \cos\alpha$, $\boldsymbol{k}_\mathrm{X}$ being the X-ray wave vector. Consequently, the contrast is about 3.5 times larger for the IP component of the magnetisation in the direction of the beam (m_x) than for the OOP component (m_z). Similarly, the contrast is zero for the magnetisation component perpendicular to the beam (m_y). This technique is hence of particular interest to image

[1] Note that X-PEEM refers to the microscopy technique and we call X-PEEM image an image acquired with a given polarisation (CL or CR). An XMCD-PEEM image is the subtraction of two X-PEEM images acquired with opposite polarisations.

the internal magnetisation of DWs and skyrmions. Fig. 3.6.a shows an XMCD-PEEM image of the domain configuration in a Pt/Co/MgO sample with PMA at RT, taken from the study of Boulle *et al.* [48]. For DWs perpendicular to the X-ray beam direction, black and white lines can be seen, indicating that the magnetisation is parallel/anti-parallel to the X-ray beam. On the contrary, this effect is not seen for DWs orientated parallel to the beam: this is the signature of a left-handed Néel DW. Fig. 3.6.b displays the measured XMCD contrast in the beam direction. It reveals two peaks at the position of the DWs. Fitting this contrast with the expression of C given above and assuming a 180° Bloch DW profile provides a very good agreement with the experiments.

The X-PEEM experiments were carried out on the SPELEEM III Microscope (Elmitec GmbH) at the following beamlines: CIRCE beamline, Alba synchrotron, Cerdanyolla del Vallès (Barcelona), Spain; Nanospectroscopy beamline, Elettra synchrotron, Basovizza (Trieste), Italy; I06 beamline, Diamond Light Source, Didcot, United Kingdom. These experiments were realised with the support of Lucia Aballe, Michael Foerster and Jordi Prat at the CIRCE beamline; Andrea Locatelli, Tevfik Onur Menteş and Francesca Genuzio at the Nanospectroscopy beamline; Francesco Maccherozzi at the I06 beamline.

3.3.3 Scanning transmission X-ray microscopy

The results presented in Chapter 6 have been obtained by using another X-ray imaging technique, namely scanning transmission X-ray microscopy (STXM).

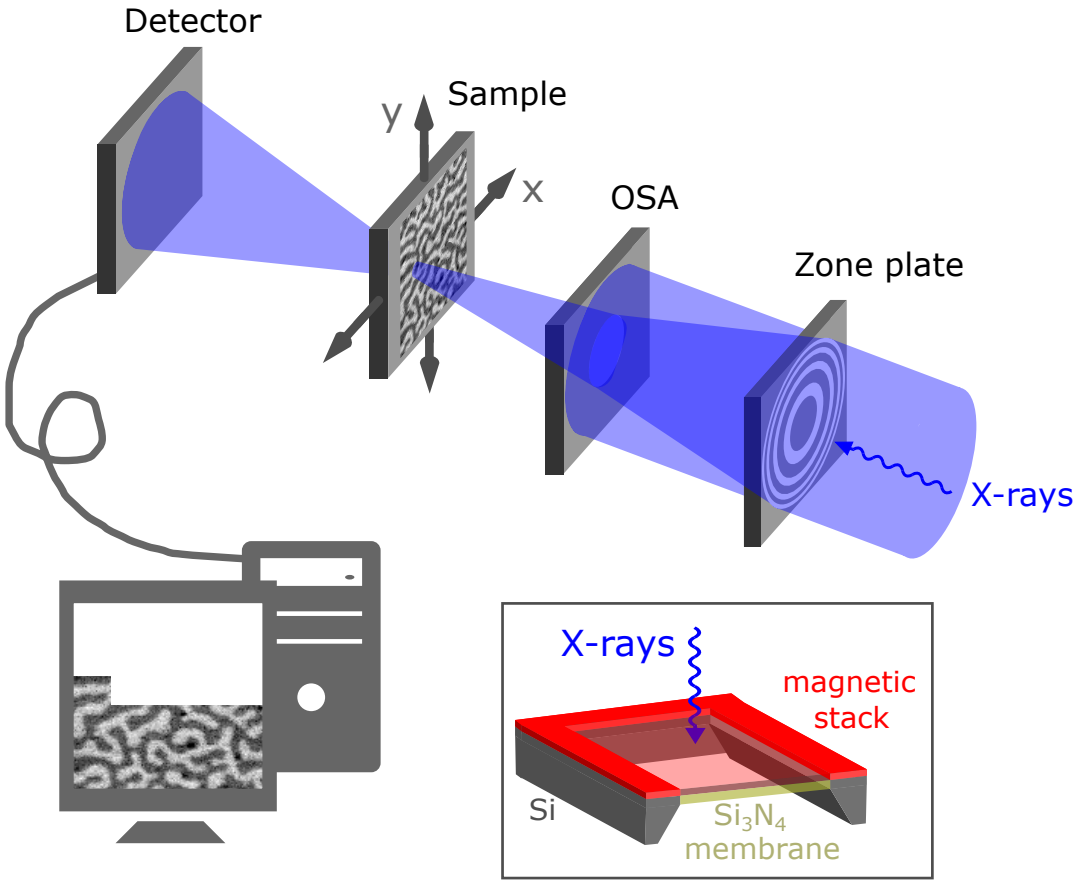

Fig. 3.7: Scanning Transmission X-ray microscope | The circularly polarised X-ray beam is focused through a zone plate and the order selecting aperture (OSA) filters out high-order diffraction modes. The sample is placed in the focus of the zone plate and is scanned laterally using piezoelectric motors. The light transmitted through the sample is collected by the detector and the image is acquired pixel by pixel. The inset shows a schematics of the Si_3N_4 membrane with the magnetic stack deposited on it.

STXM is an all-optical technique that measures the absorption of circularly polarised X-rays by detecting the light transmitted through the sample. For this reason, the magnetic stack needs to be deposited on a membrane transparent to X-rays. In the experiments conducted during this thesis, 100-nm-thick Si_3N_4 membranes, of lateral dimensions 100×100 µm^2 were used (see inset of Fig. 3.7). In addition, only primary vacuum (10^{-3} mbar) may be used.

The principle of the technique is represented in Fig. 3.7: the X-ray beam is transmitted through a zone plate, which consists of alternating transparent and opaque rings of varying period (spacing), decreasing from the inner rings to the outer rings. The resulting diffraction pattern of the transmitted beam is a spot, whose size is determined by the period at the outer-most ring. Hence, the zone plate acts as a focusing lens. Higher diffraction orders are then filtered out by an order selecting aperture (OSA) locating between the zone plate and the sample at a distance of typically 1 mm from the sample. The sample is placed in the focus of the zone plate and is scanned laterally using piezoelectric motors. The transmitted light is collected by the detector and the image is acquired pixel by pixel (scanning). Finally, performing two scans for CL and CR polarisations allows to calculate the XMCD-STXM, exactly like the XMCD-PEEM image.

In the experiments conducted during this thesis, the X-ray beam was perpendicular to the sample surface, such that the observed contrast is proportional to the OOP component of the magnetisation (m_z). STXM is thus perfectly suitable to study perpendicularly magnetised materials. The IP components of the magnetisation may also be measured by tilting the sample with respect to the beam axis, although the tilt angle is limited by the distance between the OSA and the sample, limiting the measurable contrast in the IP direction. In STXM, contrarily to X-PEEM which is a surface-sensitive technique, thicker materials provide a larger X-ray absorption and hence a larger contrast. Accordingly, X-PEEM is more suitable to study ultra-thin magnetic layers while STXM is preferable to study thicker PMA stacks, typically multi-layered films.

The STXM experiments were carried out at the following beamlines: HERMES beamline, SOLEIL synchrotron, Saint-Aubin, France; MAXYMUS beamline, BESSY II, Berlin, Germany. These experiments were realised with the support of Rachid Belkhou, Stefan Stanescu, Brice Sarpi and Adrien Bession at the HERMES beamline; Joachim Gräfe and Markus Weigand at the MAXYMUS beamline.

3.4 Nanofabrication process

In the experiments of skyrmion dynamics and confinement in nanostructures as well as current-induced nucleation in synthetic antiferromagnetic multilayers, the sample were patterned using the process described in Fig. 3.8. The same process was used for samples deposited on Si substrates and on Si_3N_4 membranes, only with additional precautions when working with membranes, as explained below. Here is the detailed fabrication process represented in Fig. 3.8:

- **a.** The stack is deposited by magnetron sputtering (§3.1).
- **b.** Contact pads consisting of Ti(10nm)/Au(100nm)/hard mask are defined by UV lithography and deposited using electron-beam (e-beam) evaporation. The hard mask consists of Pt(5nm)/ Al(t_{Al}) where t_{Al} is adjusted according to the thickness of the stack to be etched. The Pt(5nm) layer needs to be inserted to prevent the formation of a Au_xAl_y alloys that has a poor conductivity.
- **c.** The nanostructures are defined by e-beam lithography. The hard mask consisting of Al(t_{Al}) is deposited by e-beam evaporation.
- **d.** The parts not protected by the mask are etched out by ion-beam etching (IBE). The remaining Al is removed by chemical etching using a dedicated developer (AZ 326 MIF).

- **e.** Injection tips consisting of Ti(10nm)/Au(100nm) are defined by e-beam lithography and deposited by e-beam evaporation. This additional step is realised to perform skyrmion nucleation experiments (Chapter 6).

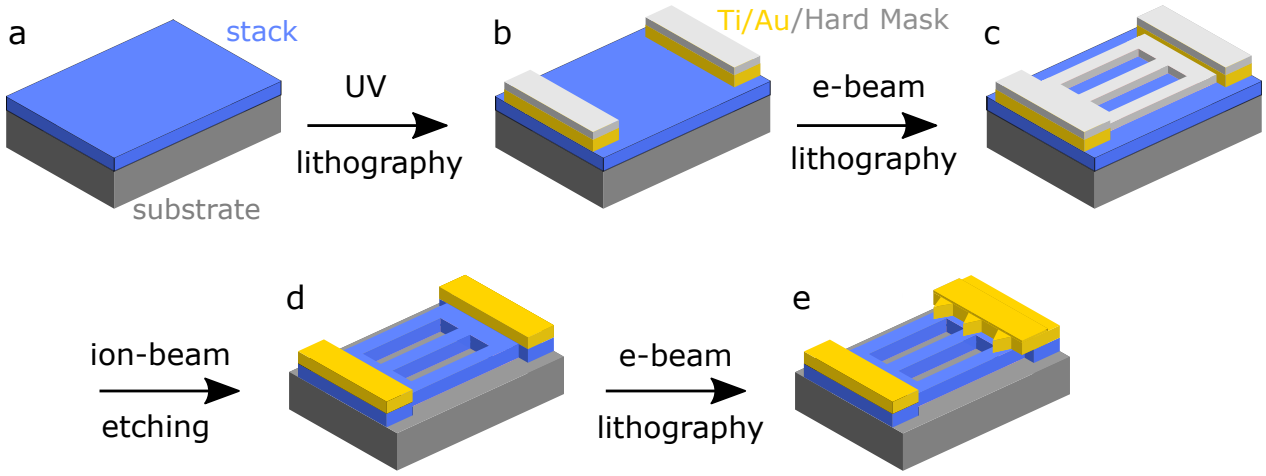

Fig. 3.8: Nanofabrication process | Schematic diagrams of the different steps in the patterning of the nanostructures studied in this thesis. Details about each step is given below.

NOTE: When the process is performed on Si_3N_4 membranes, additional precautions must be taken. In particular, the use of ultrasonics during lift-off steps is to be avoided as it would tear the membrane. For the resist coating and all deposition steps, the membrane must be fixed on a substrate, like a Si wafer, using for example Kapton® tape. Moreover, if the membrane is placed under vacuum, it may be stuck on a Si wafer with PMMA[1] resist. This allows to equalise the pressure on both sides and prevents trapping air beneath the membrane, which might otherwise break it when placed under vacuum. Finally, during IBE steps, over-etching the membrane must also to be avoided since thinning it down would make it even more fragile. This can be achieved by controlling the etching time as well as the hard mask thickness. Apart from these additional precautions, the nanofabrication processes for Si substrates and Si_3N_4 membranes are essentially the same.

The fabrication process was realised by me at the Plateforme Technologique Amont (PTA), in Grenoble, with the support of Gilles Gaudin and Olivier Boulle for e-beam steps.

[1] Poly(methyl methacrylate)

Chapter 4

Skyrmion nucleation in ultra-thin films

This chapter presents different approaches investigated during my PhD to tackle certain key aspects regarding the skyrmion nucleation and stability in ultra-thin FM films. First, the nucleation of skyrmions in extended films is presented. Then in confined geometries where the effect of pinning on the field-dependence of the skyrmion size is discussed. Further, a novel approach to achieve stable zero-field skyrmions in exchange-biased extended films is introduced. Finally, some preliminary results on local writing of skyrmions using He^+ irradiation are put forward. All the experiments were carried out at RT using the Pt/Co/MgO trilayer as a building block.

4.1 Introduction: Pt/Co/MgO system and observation of chiral Néel skyrmions

Most of the experiments conducted during this thesis were performed on an ultra-thin Pt/Co/MgO film. This was motivated by the early observations of magnetic skyrmions at Spintec by Boulle *et al.* [48] using X-PEEM. Fig. 4.1.a shows a XMCD-PEEM image[1] of a magnetic skyrmion in a 420 nm square dot at zero external magnetic field. Fig. 4.1.b shows a line-scan of the contrast in the direction of the X-ray beam.

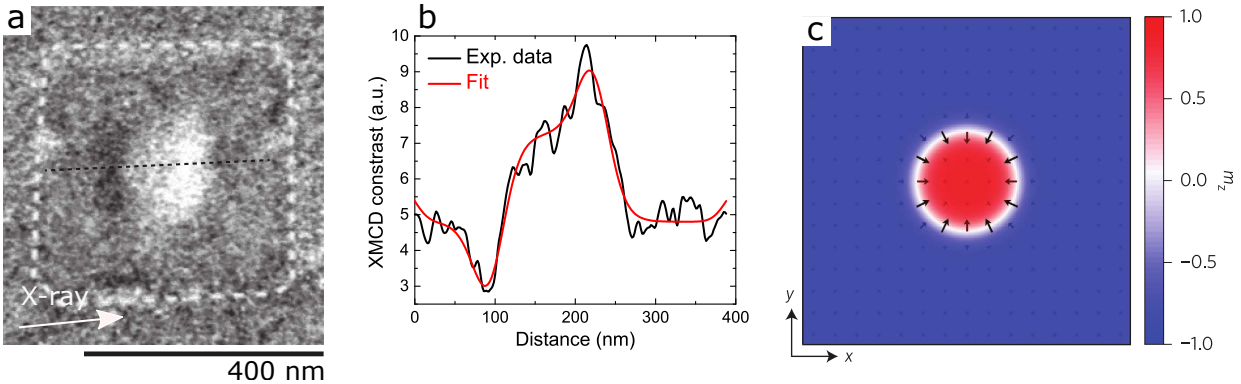

Fig. 4.1: Room-temperature Néel magnetic skyrmion in Pt/Co/MgO | **a.** XMCD-PEEM image showing a magnetic skyrmion in a 420 nm square dot. The direction of the X-ray beam is indicated by the white arrow. **b.** XMCD contrast measured along the black dashed line in **a**. The red line is a fit with a 360° Bloch DW profile.[2] **c.** Micromagnetic simulations using the experimental parameters of **a**. Adapted from ref. [48].

[1] Subtraction of two X-PEEM images acquired with opposite circular X-ray polarisation (§3.3.2).

[2] $m_z = \cos\theta(r)$ with $\theta(r) = -2\arctan\left(\exp\left(\frac{r-R}{\Delta}\right)\right)$ [108]. Note that the DW/skyrmion profile is expected to be independent of the DMI [58] and therefore of its Bloch or Néel character.

As explained earlier in §3.3.2, the XMCD-PEEM contrast is proportional to the projection of the magnetisation on the X-ray beam direction, which impinges the sample surface at a grazing angle of 16°. Hence, following the X-ray beam direction from left to right, one comes across two Néel DWs with opposite magnetisation. The magnetisation hence rotates as follows: ↓↘→↗↑↖←↙↓. The same contrast is obtained by rotating the sample by 90° with respect to the beam. This is exactly the signature of a left-handed Néel skyrmion. The spin texture obtained from micromagnetic simulation is shown in Fig. 4.1.c.

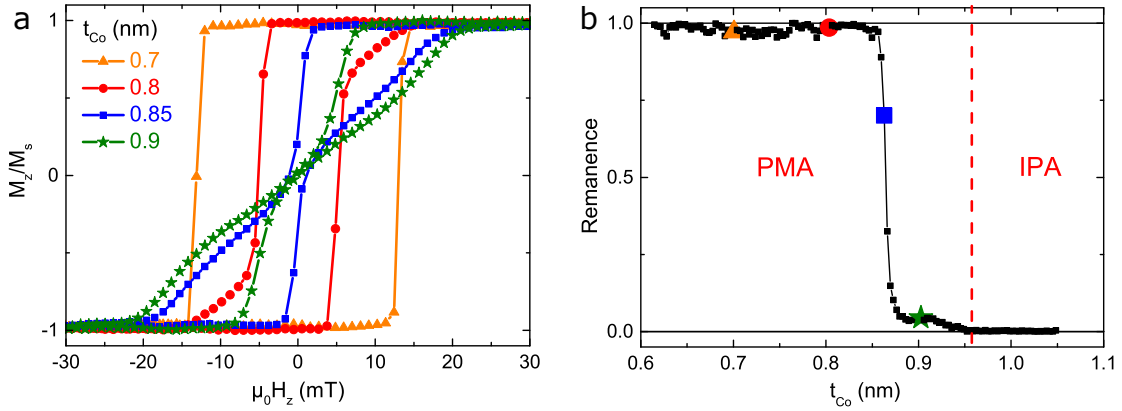

Fig. 4.2: Hysteresis loops for Pt/Co/MgO | The sample consists of Pt/Co(0.6-1.1nm)/MgO and the magnetic field is applied in the OOP direction. **a.** MOKE hysteresis loops measured at different locations on the Co wedge. **b.** Zero-field MOKE signal (remanence) as a function of the Co thickness. The loops in **a** are indicated by the corresponding symbols in **b**.

The complete stack that has been used for the experimental studies presented in this chapter and the next is Ta(3)/Pt(3)/Co(0.6-1.1)/MgO(0.9)/Ta(2) (thicknesses in nm), grown by sputtering on a Si/SiO_2 substrate. This stack contains the essential ingredients required to stabilise magnetic skyrmions: PMA and a strong interfacial DMI [48,169]. The Ta(3) buffer layer is used to promote a good adherence of the layers deposited on SiO_2 and to favour a (111)-oriented textured growth of the Pt(3) [170], resulting in a strong PMA. This Pt layer also allows the injection of spin current via the SHE to exploit SOTs for the skyrmion motion. The top Ta(2) layer serves as a capping layer to protect the MgO from further oxidation. In the experiments presented hereafter, the Co layer was deposited as a wedge (*i.e.* with a thickness gradient). Fig. 4.2.a. displays the hysteresis loops measured at different locations on the wedge. The external magnetic field is applied perpendicular to the film plane. For $t_{Co} = 0.7$ nm, the large PMA leads to a square hysteresis loop, indicating that the sample is fully magnetised at remanence ($H_z = 0$). When increasing the Co thickness, the decrease in the PMA combined with the larger demagnetising field, *i.e.* the diminution of K_{eff}, results in a bended loop, characteristic of a reversal involving multi-domain states. A decrease in the magnetisation at remanence is observed around $t_{Co} = 0.85$ nm, indicating the presence of worm-like domains at zero field. Fig. 4.2.b. displays the normalised remanence, measured from the zero-field MOKE amplitude, as a function of the Co thickness. It shows the decrease in the anisotropy for increasing t_{Co} and the spin reorientation transition — from PMA to IP anisotropy — for $t_{Co} \approx 0.95$ nm. Note that the nominal thickness for which this spin reorientation transition occurs can vary from one deposition to another as all the parameters are dependent on the interface quality. Depositing the Co layer as a wedge allows us to use the Co thickness as a tuning parameter. This way, we select the desired thickness for which the characteristic bended hysteresis loops are observed.

4.2 Skyrmions in extended films

Let us now look at the magnetisation texture close to the spin reorientation transition. Fig. 4.3.a displays the OOP hysteresis loop measured on a Pt/Co/MgO film at a position on the wedge

corresponding to $t_{Co} = 0.96$ nm.[1] Fig. 4.3.b-f show magnetic force microscopy (MFM) images for different external magnetic field values. The first image (Fig. 4.3.b) displays the remanent magnetisation configuration ($H_z = 0$) after OOP saturation with $\mu_0 H_z \approx 100$ mT. It exhibits a labyrinthine worm-domain pattern with zero (or very close to zero) net magnetisation, as indicated by the vanishing Kerr amplitude in the hysteresis loop. In the absence of external field or other stimuli, this is the most stable configuration that minimises notably the demagnetising energy. Then, upon progressively increasing the external field, the worm domains shorten (Fig. 4.3.c) and eventually shrink into isolated skyrmions (Fig. 4.3.d-f), reaching a diameter of $d_{sk} = 65$ nm on average, at $\mu_0 H_z = 18$ mT (Fig. 4.3.e). As explained in §2.4.1, the external field modifies the energy of magnetic skyrmions: it shifts the energy minimum towards smaller sizes and reduces the annihilation barrier. Indeed, increasing the field from $\mu_0 H_z = 14$ mT to $\mu_0 H_z = 26$ mT leads to a compression of the magnetic skyrmions towards smaller sizes. At $\mu_0 H_z = 40$ mT, all the skyrmions have been annihilated. The fact that some skyrmions have disappeared at $\mu_0 H_z = 26$ mT (Fig. 4.3.f) while others have remained stable, indicate that they might have different annihilation barriers, most likely due to material inhomogeneities.

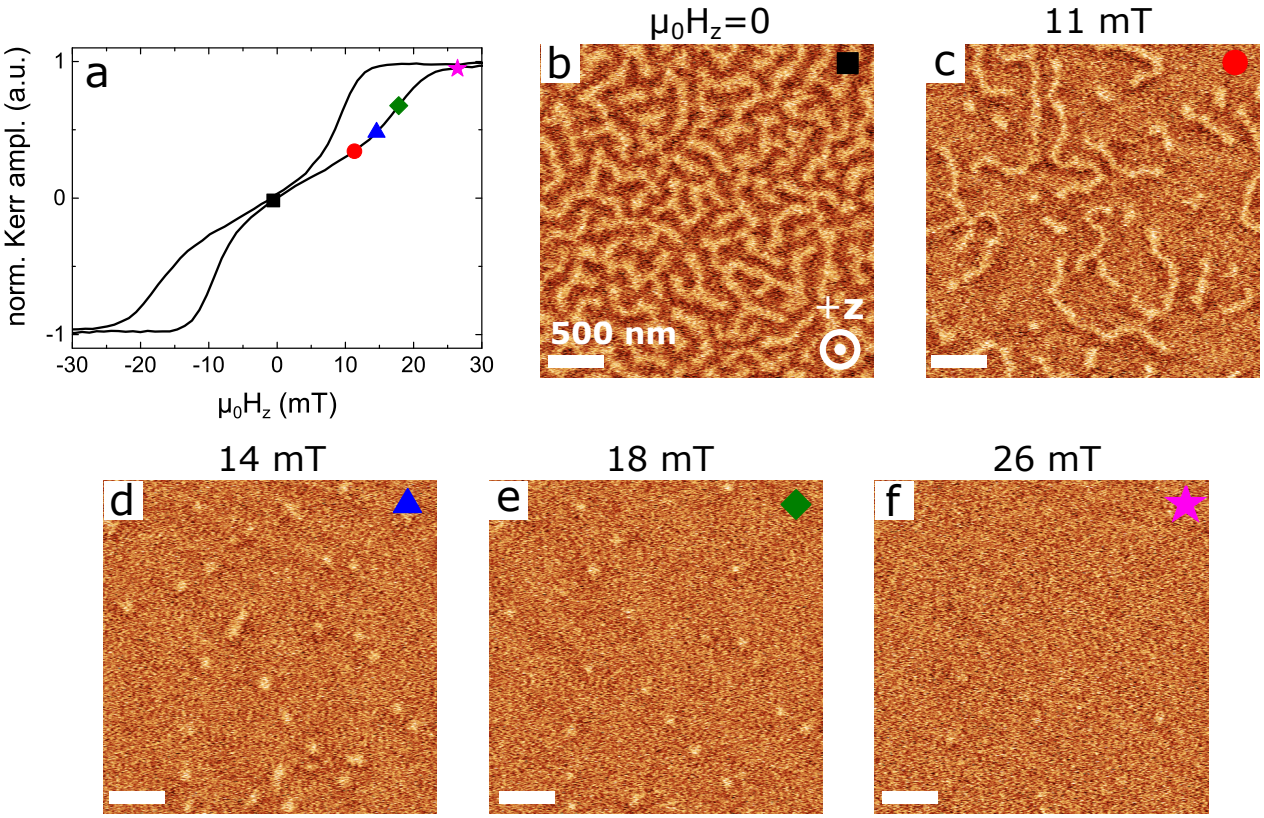

Fig. 4.3: Magnetic skyrmions in extended films | **a.** MOKE hysteresis loop measured on a Pt/Co(0.96nm)/MgO sample. **b-f.** MFM images showing the magnetic texture for different external magnetic fields $\mu_0 H_z$ indicated by the corresponding symbol on the hysteresis loop. Images dimensions: 3×3 µm^2.

In extended films, it is necessary to apply an OOP external magnetic field to stabilise magnetic skyrmions. Furthermore, the skyrmion position is not controlled. In the following sections, we explore different approaches to tune the skyrmion size and stability by confining them in nanostructures (§4.3), by inserting a bias layer (§4.4) and by light-ion irradiation (§4.5).

[1] This sample was deposited in another batch and the spin reorientation transition here was rather found at $t_{Co} \approx 1.02$ nm. The sample of Fig. 4.2 corresponds to the reference sample for the study of the skyrmion dynamics presented in Chapter 5.

4.3 Skyrmions in confined geometries

The stability of magnetic skyrmions in confined geometries is quite different from that in extended films. In finite geometries, the demagnetising field, which depends on the size and shape of the nansotructure, strongly influences the magnetic ground state [171,172]. In this section, we explore the effect of confinement on the skyrmion stability in the light of experiments and micromagnetic simulations performed during this thesis. First in circular dots, in which a skyrmion is confined in all directions, and then in tracks where a skyrmion is only confined along the width. Most of the results presented in this section (§4.3) can be found in ref. [173].

4.3.1 Dot geometry

The image of Fig. 4.4.a shows a magnetic skyrmion in a 630-nm-diameter circular dot at zero field with a diameter of 200 nm. Here the dimensions of the nanostructure play a major role in the skyrmion stability: in larger dots (1.2 µm), a worm-like pattern is rather observed and an external field is required to stabilise magnetic skyrmions [48], as in the extended film of Fig. 4.3. We also notice that the skyrmion is positioned near the edge of the dot, whereas the dipolar repulsion from the edges rather favours a skyrmion position in its centre. This suggests that the skyrmion is pinned by local defects. The application of a small perpendicular magnetic field does not modify substantially the skyrmion structure and size (Fig. 4.4.b), up to a critical field $\mu_0 H_z = 2.8$ mT (Fig. 4.4.c) where a sharp decrease of the skyrmion diameter to 90 nm is observed. This is visible on Fig. 4.4.e which shows the skyrmion diameter (star symbols) as a function of the external field.

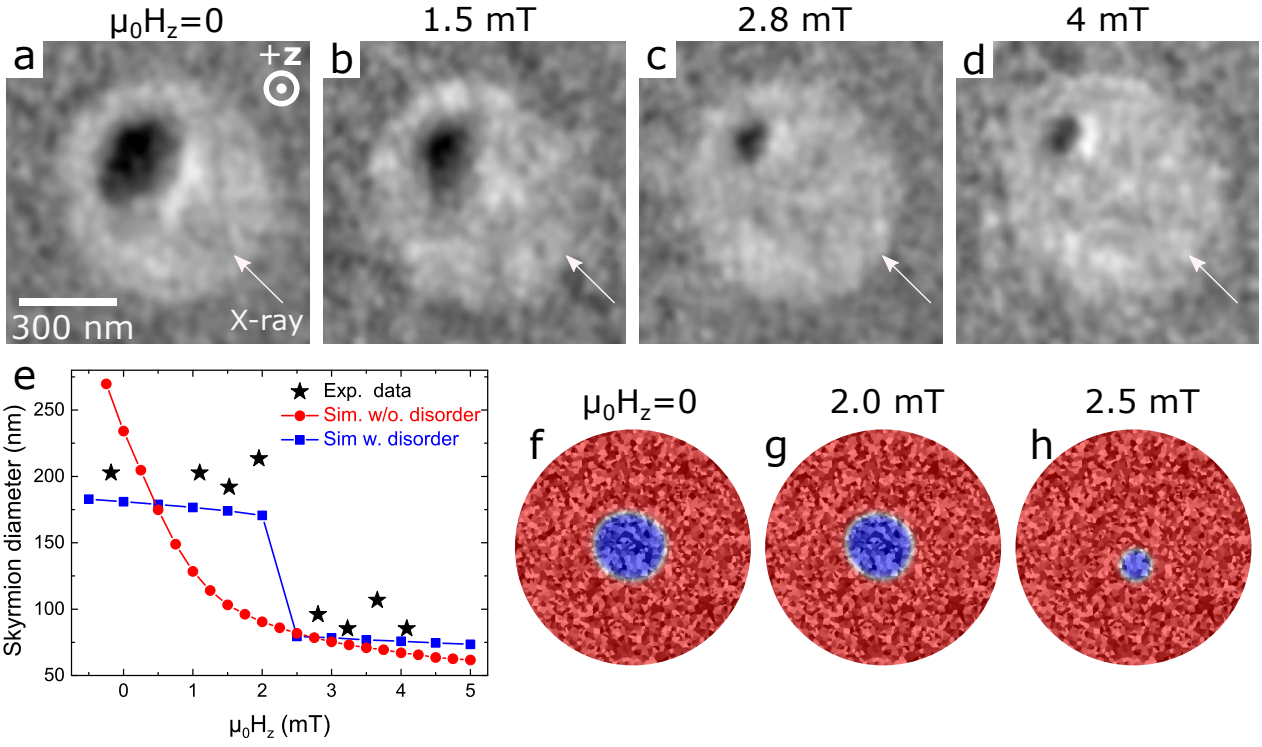

Fig. 4.4: Magnetic skyrmions in a dot | **a-d.** XMCD-PEEM images of a magnetic skyrmion in a 630-nm-diameter circular dot for different external magnetic fields $\mu_0 H_z$. **e.** Skyrmion diameter as a function of the external field. Experimental data (black stars), micromagnetic simulations without disorder (red dots) and with disorder (blue squares). In the simulations including disorder, the grain size is $g = 10$ nm and the anisotropy is varied randomly within $(1 \pm \delta K_u)K_u$ with $\delta K_u = 2.5\%$, K_u being the macroscopic, measured anisotropy. **f-h.** Micromagnetic simulations: skyrmion for different external fields corresponding to the blue squares in **e**. The red (blue) colour indicates a magnetisation pointing along $+\hat{\boldsymbol{z}}$ $(-\hat{\boldsymbol{z}})$. The bright (dark) grains indicate regions with stronger (weaker) anisotropy.

To better understand these experimental results, we carried out micromagnetic simulations with the open-source code Mumax3 [174]. The cell size is $1 \times 1 \times t$ nm^3 and the following parameters, taken from a previous study [48], were used: the exchange constant $A = 27.5$ pJ m^{-1}, the uniaxial anisotropy constant $K_u = 1.45 \times 10^6$ J m^{-3}, the DMI constant $D = 2.05$ mJ m^{-2}, the saturation magnetisation $M_s = 1.44$ MA m^{-1} and the FM film thickness $t = 1.06$ nm. The initial state is a 200-nm-diameter circular bubble positioned in the centre of the 630-nm-diameter circular dot. This configuration is then relaxed at zero field and the field is increased step by step. Upon increasing H_z, the skyrmion diameter decreases continuously and covers a wider range of sizes than the one observed (see Fig.4.4.e, red dots). Moreover, the contraction of the core is isotropic and the skyrmion remains in the centre of the dot (not shown), as expected notably from the symmetry of the demagnetising field.

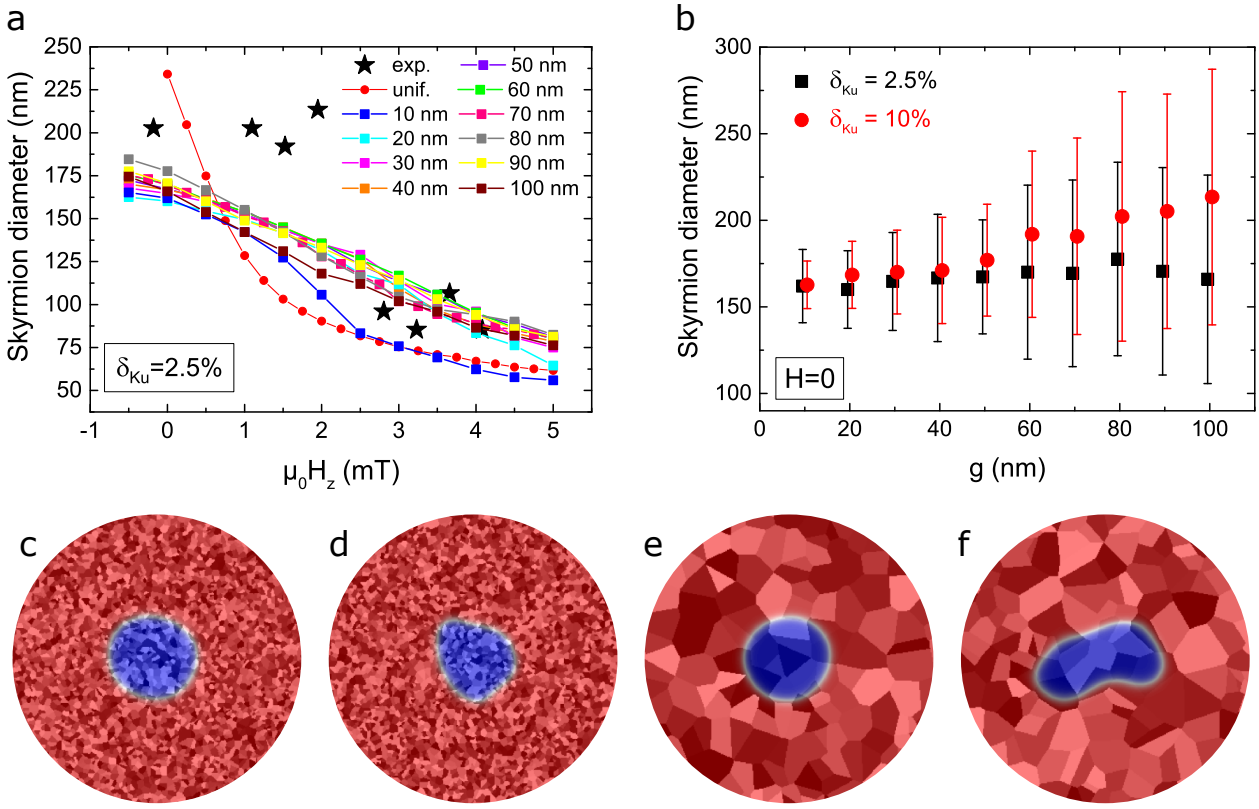

Fig. 4.5: Micromagnetic simulations: effect of the disorder on the skyrmion size | a. Average skyrmion diameter as a function of the external magnetic field in a 630-nm-diameter circular dot, for different grain sizes, $g = 10-100$ nm, and for a disorder parameter $\delta K_u = 2.5\%$. Black stars are experimental data and red dots simulations without disorder. **b.** Average zero-field skyrmion diameter as a function of the grain size, for $\delta K_u = 2.5\%$ (black squares) and $\delta K_u = 10\%$ (red dots). The curves are shifted along the x-axis for clarity. Error bars denote standard deviation. In all simulation with disorder, the diameter is averaged over 50 realisations. **c-f.** Zero-field skyrmion texture for different $\{g, \delta K_u\}$: **c.** {10 nm, 2.5%}, **d.** {10 nm, 10%}, **e.** {50 nm, 2.5%} and **f.** {50 nm, 10%}.

Let us now add disorder to the problem. Is it well known that the polycrystalline grain structure of sputtered magnetic films is a source of pinning for DWs [175–177]. Pinning centres may originate from any source of inhomogeneity in the film such as grain boundaries, roughness and fluctuations of Co thickness. To model it qualitatively, a grain distribution with local anisotropy fluctuations is introduced [137,178]. The average grain size is g and, from grain to grain, we assume that the anisotropy fluctuates randomly within $(1 \pm \delta K_u)K_u$ around the macroscopic, measured value K_u. We refer to δK_u as disorder parameter. The grain size and the anisotropy were varied respectively in the ranges $g = 10-100$ nm and $\delta K_u = 2.5\%-10\%$, with multiple realisations for each set of parameters

$\{g, \delta K_u\}$. The simulations reveal a behaviour very similar to the experimental case for different realisations of grains distributions. Fig. 4.4.e. shows the dependence of the skyrmion diameter on the perpendicular magnetic field for a specific realisation with $g = 10$ nm and $\delta Ku = 2.5\%$ (see Fig. 4.4.f-h). As observed experimentally, the skyrmion diameter decreases in a step-like fashion when the magnetic field reaches a certain critical value. In Fig. 4.4.f-h, the magnetisation texture (red/blue) is superimposed on the grain distribution where bright (dark) grains correspond to regions with stronger (weaker) anisotropy. For $\mu_0 H_z \leq 2.0$ mT, the skyrmion is trapped in its initial location and slightly stretched away from its initial circular shape by the local grain structure; the magnetic field affects little its shape and position. When the depinning field ($\mu_0 H_z = 2.5$ mT) is reached, the skyrmion prefers to 'jump' in a neighbouring region, despite the additional cost in dipolar energy far from the centre, and again shows a smaller susceptibility to the external field than in the disorder-free scenario. This characteristic step-like decrease of the skyrmion diameter is observed for various sets of parameters $\{g, \delta K_u\}$.

We now investigate the influence of the characteristic parameters of the disorder. For each $\{g, \delta K_u\}$, the diameter is averaged over multiple realisations. For deformed skyrmions, we calculate an effective diameter defined by $d_{sk} = 2\sqrt{\mathcal{A}_{sk}/\pi}$, where $\mathcal{A}_{sk}$ is the area defined by $m_z < 0$. Fig. 4.5.a shows the evolution of the average effective skyrmion diameter as a function of the external field for $g = 10 - 100$ nm and $\delta K_u = 2.5\%$. It appears that the susceptibility of the skyrmion size to the external field is reduced by the disorder. Furthermore, on average, the field-dependence of the skyrmion size is found to be almost independent of the grain size; except for the smallest one considered ($g = 10$ nm) where skyrmions are less sensitive to pinning at high field. In fact, this behaviour is observed for larger values of δK_u (up to 10%), which suggests lesser pinning effects when the skyrmion is large as compared to the grain size.

To complete the picture, Fig. 4.5.b shows the evolution of the skyrmion diameter with the grain size, at zero external field and for two disorder parameters: $\delta K_u = 2.5\%$ and 10%. Typical realisations corresponding to four different situations (strong/weak disorder and small/large grains) are shown in Fig. 4.5.c-f. We observe that for small disorder, the zero-field skyrmion size is approximately constant with the grain size, whereas it increases on average as the disorder increases. Note that this remains true at larger field. In fact, for strong disorder, the initial state is stretched out after relaxation and very often turns into a worm-shaped domain. This effect is much larger for large grains (see Fig. 4.5.c-f). On the contrary, for weaker disorder ($\delta K_u = 2.5\%$ and 5%), the skyrmion recovers its initial circular shape at large fields, as shown in Fig.4.4.h. An additional interesting feature is that the standard deviation (error bars in Fig. 4.5.b) increases with increasing grain size, for both disorder parameters. This suggests that for a strong anisotropy disorder and for a large film surface, one will be more likely to observe an important dispersion in the skyrmion size and shapes for large grains.

Furthermore, note that the simulations represent the system at $T = 0$ K. An increase in temperature is expected to lower the effect of pinning [179]. Indeed, the disorder introduces some energy barrier that needs to be overcome for the skyrmion size to follow the disorder-free field-dependence, which can be enabled by thermal fluctuations. This energy barrier has another consequence: the skyrmion size depends on the initial state since the path for the skyrmion to shrink from a large size and the path to expand from a small size are different [179]. This can result in a hysteresis in the field-dependence of the skymrion size [180]. Note that for the experiments of Fig. 4.4.a-d, the skyrmion recovers its initial size and position when switching off the external field.

4.3.2 Track geometry

The track geometry is of particular interest for applications based on skyrmion-shift operations such as racetrack memories. Fig. 4.6.a-c show XMCD-PEEM images of magnetic skyrmions in 500-nm-wide tracks for different applied fields, $\mu_0 H_z$. In this geometry, at remanence or in the presence of a small magnetic field ($\mu_0 H_z < 2$ mT), worm-like domains are observed. This configuration minimises the dipolar energy in the absence of confinement along the track length, allowing their expansion in this direction. These worms tend to align with the tracks, while they are randomly

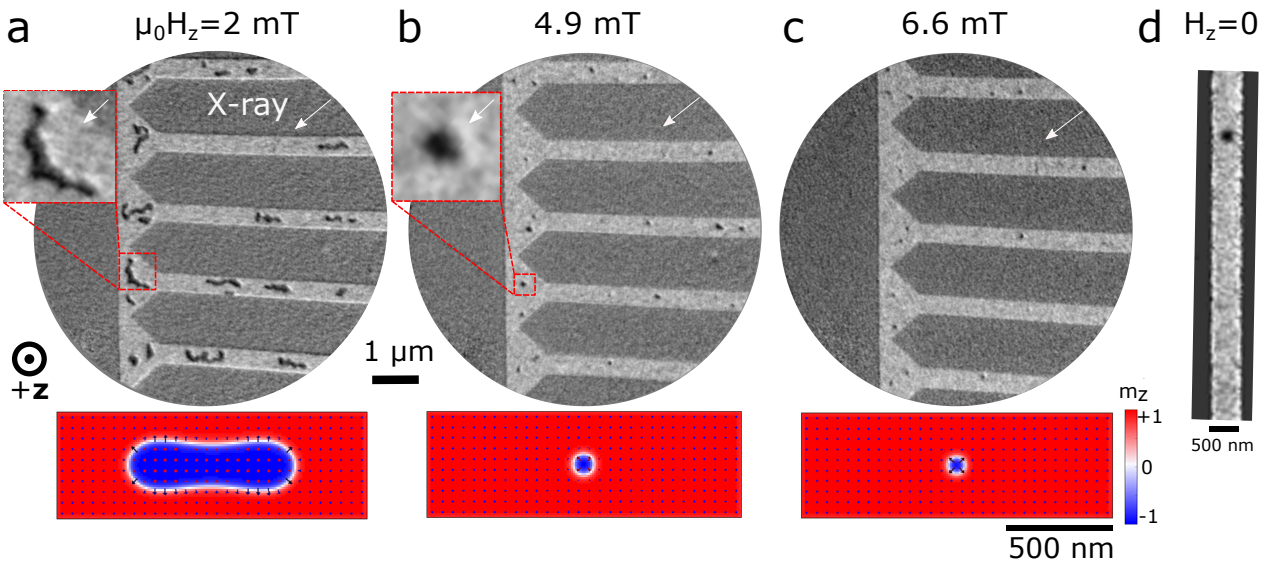

Fig. 4.6: Magnetic skyrmions in tracks | **a-c.** XMCD-PEEM images of the magnetic texture in 500-nm-wide tracks for different external magnetic fields, $\mu_0 H_z$. Insets dimensions: **a.** 800×800 nm^2 and **b.** 500×500 nm^2. Below each image is represented the simulated magnetisation texture in the absence of disorder. **d.** XMCD-PEEM image of a magnetic skyrmion in a 540-nm-wide track at zero field.

oriented in the largest areas of the nanostructures. We observe a strong white (black) contrast on the upper (bottom) DWs perpendicular to the X-ray beam (inset of Fig. 4.6.a), indicating their left-handed Néel character.

Upon applying a larger field, $\mu_0 H_z > 2$ mT, the initial worm-like domains shrink into isolated skyrmions (Fig. 4.6.b-c), as in extended films (Fig. 4.3).[1] Again, the white/black contrast in the direction perpendicular to the beam demonstrates that the homochiral Néel structure is preserved. Interestingly, stable skyrmions in racetracks are also observed in the absence of external field (see Fig. 4.6.d), most probably due to pinning effects preventing their expansion along the track length, as explained in the previous section.

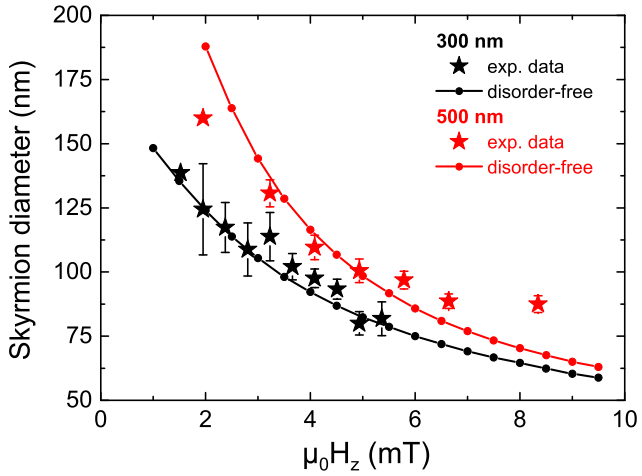

Fig. 4.7: Skyrmion size in tracks | Average skyrmion diameter as a function of the external magnetic field measured in 500-nm-wide tracks (red stars) and in 300 nm-wide tracks (black stars). The red (black) dots correspond to micromagnetic simulations.

[1] Note that some skyrmions are not visible anymore as the field is increased (Fig. 4.6.c) to $\mu_0 H_z = 8$ mT. In fact, they are probably too small to be observed since by decreasing the magnetic field down to ≈ 1 mT, the skyrmions expand and turn into worm-like domains at the same position where they were initially.

The average skyrmion diameter measured in the tracks is plotted as a function of the external field in Fig. 4.7. The same experiments were performed in 300-nm-tracks. For both track widths, a large decrease of the skyrmions size is observed in the range of applied field and reaches 80 nm in the 300-nm-wide tracks. In addition, we observe that the track width affects the skyrmions size, especially at low magnetic field: the narrower the track the smaller the skyrmions. This geometrical confinement effect can be explained by the dipolar interactions of the DWs delimiting the skyrmion with the magnetic charges on the track edges. As the magnetic field increases and the skyrmion diameter decreases, the influence of the track width on the skyrmion diminishes. This indicates that the skyrmion equilibrium size is governed by the Zeeman energy term and that the dipolar interactions with the track edges play a less significant role. These experiments suggest that the size of magnetic skyrmions can be easily tuned by narrowing down the tracks, as predicted by micromagnetic simulations [114,133], provided that the track edges do not compress the skyrmion down to a non-thermally stable size.

In Fig. 4.7, we also plotted the result of micromagnetic simulations obtained in 300- and 500-nm-wide tracks in the absence of disorder. It reproduces the confinement effect: skyrmions are smaller in narrower tracks and the size difference introduced by the confinement diminishes as the skyrmions are compressed by the field. Furthermore, it shows that the skyrmion size exhibits a larger susceptibility to the external field than in the experiments, which can be accounted for by pinning-related effects as explained in the previous section. We note that a better agreement is found in the 300 nm case. This may be due to the reduced susceptibility of the skyrmion size to the field in narrower tracks, even in the absence of disorder, which reduces the discrepancy between the two scenarios, with and without disorder.

4.4 Zero-field skyrmions in an extended exchange-biased film

The stabilisation of magnetic skyrmions in extended films (§4.2) and tracks (§4.3.2) requires the presence of an external field to prevent their expansion into worm domains. When confined in all directions, skyrmions can be stabilised in the absence of external field (§4.3.1) and their stability is strongly dependent on the nanostructure dimensions. This is quite restrictive for applications, which require stable zero-field skyrmions, as we would like to use other geometries than just dots. In the present section, we explore a different approach to stabilise magnetic skyrmions in extended films, in the absence of both external field and geometrical confinement. To achieve this, we exploit the internal exchange field arising from the RKKY coupling between a hard FM layer, referred to as bias layer (BL), and a FM layer hosting skyrmions [181].

The BL consists in our case of Pt(5)/$[$Pt(0.25)/Co(0.5)$]_7$ and the stack hosting skyrmions is Pt(0.75)/Co(1.1)/MgO(0.9) (thicknesses in nm). The RKKY coupling is obtained by inserting a Ru spacer between the BL and the Pt/Co/MgO stack [182]. The complete stack, BL/Ru(t_{Ru})/Pt/Co/MgO, is shown in Fig. 4.8.a. The BL exhibits a strong PMA leading to a uniform magnetisation at remanence with a coercive field $\mu_0 H_c = 43$ mT, as seen from Fig. 4.8.b. To tune the interlayer exchange field, the Ru layer is deposited as a wedge, hence exploiting the thickness-dependence of the RKKY interaction. Note that the top Co layer is also deposited as a wedge, perpendicular to the Ru wedge. We selected a position, hence a Co thickness, for which we observe the characteristic bended loops indicating a multi-domain configuration at remanence. Furthermore, the top Pt thickness is decreased to 0.75 nm in order to transmit an — attenuated — AF coupling [183].

The major (black) and minor (red) hysteresis loops measured at three locations on the Ru wedge are shown in Fig. 4.8.d. Let us first look at the loop for $t_{Ru} = 0.94$ nm. It exhibits four plateaus with three magnetisation reversals, characteristic of an AF RKKY coupling. Schematically, coming from negative saturation and increasing the field leads to the following reversals: $\begin{smallmatrix}\downarrow\\\downarrow\end{smallmatrix} \dashrightarrow \begin{smallmatrix}\uparrow\\\downarrow\end{smallmatrix} \dashrightarrow \begin{smallmatrix}\downarrow\\\uparrow\end{smallmatrix} \dashrightarrow \begin{smallmatrix}\uparrow\\\uparrow\end{smallmatrix}$, where the top (bottom) arrow represents the top Co layer (BL). The reversal of the BL occurs at $|H_z| = |H_c|$ and the minor loop (in red) corresponds to that of the top Co layer. This can be seen from its relative amplitude to the full loop. The minor loop is shifted by $\mu_0 H_{bias}$ with respect to $H_z = 0$, which we refer to as bias field. This bias field quantifies the strength of the RKKY coupling

between the BL and the top Co layer. In other words, it is the effective magnetic field exerted on the top Co layer by the BL. For $t_{Ru} = 0.94$ nm, $\mu_0 H_{bias}$ is larger than the saturation field of the top Co layer such that, at $H_z = 0$, the top Co layer is uniformly magnetised in a direction opposite to the BL uniform magnetisation. Then, increasing the Ru thickness leads to a decrease of $\mu_0 H_{bias}$. For $t_{Ru} = 1.04$ nm, the bias field is smaller than the coercive field of the BL, H_c, but larger than the saturation field of the top Co layer. As a result, the top Co layer is still uniformly magnetised at $H_z = 0$. Increasing further the Ru thickness to $t_{Ru} = 1.12$ nm leads to a cancellation of the bias field. We also note from Fig. 4.8.d that the coercive field of the central hysteresis increases with increasing RKKY coupling, *i.e.* with decreasing t_{Ru}. This can be attributed to the biasing effect of the top Co layer on the BL. Indeed, the coercive field of the BL measured independently (Fig. 4.8.b) is recovered in the limit of zero coupling ($t_{Ru} = 1.12$ nm in Fig. 4.8.d). The evolution of the bias field with the Ru thickness is shown in Fig. 4.8.c. It was measured from the minor loops at different locations, 0.5 mm apart on the wedge. It exhibits a variation consistent with the oscillatory behaviour expected on a wider range of Ru thicknesses [183,184], and the maximum AF coupling is obtained for $t_{Ru} = 0.82$ nm. Therefore, moving along the Ru wedge is equivalent to tuning the value of an effective field exerted on the top Co layer. Note that for $t_{Ru} > 1.12$ nm the RKKY coupling becomes FM ($\mu_0 H_{bias} < 0$).

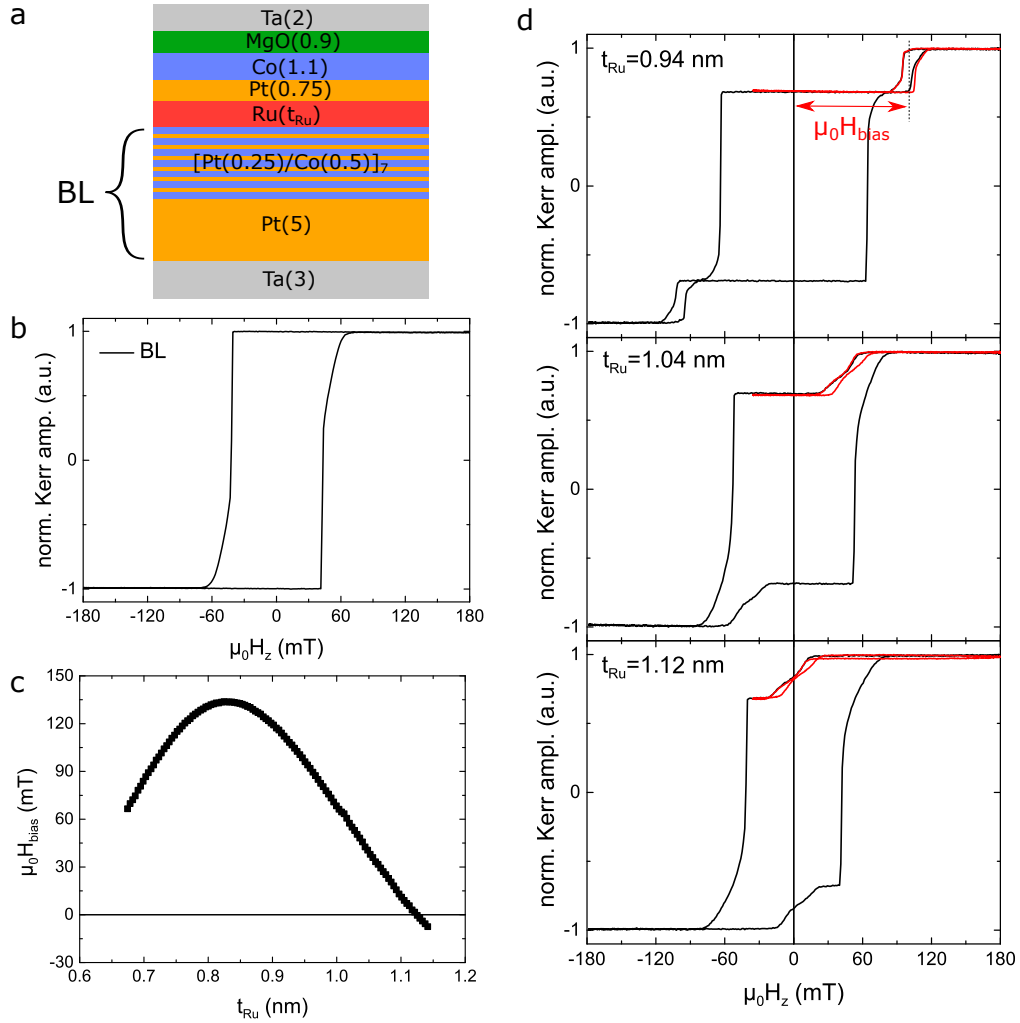

Fig. 4.8: Exchange-biased Pt/Co/MgO film | **a.** Schematics of the complete stack (BL = bias layer), thicknesses in nm. The Ru(t_{Ru}) layer is deposited as a wedge with $t_{Ru} = 0.67 - 1.14$ nm. **b.** OOP MOKE hysteresis loop for the BL, measured in Ta/BL/Ru/Pt. **c.** Bias field as a function of the Ru thickness. **d.** Major (black) and minor (red) loops measured for the complete stack (**a**) at three locations on the Ru wedge. For $t_{Ru} = 0.94$ nm, 1.04 nm and 1.12 nm, the bias field is respectively $\mu_0 H_{bias} = 100.6$ mT, 45.7 mT and 1.7 mT.

To stabilise magnetic skyrmions in the exchange-biased Pt/Co/MgO film, the bias field must be finely controlled. Fig. 4.9.a displays the minor loops measured at five different locations on the Ru wedge ≈ 1 mm apart, starting from $t_{Ru} = 1.12$ nm, for negligible RKKY coupling ($\mu_0 H_{bias} = 1.7$ mT). For 1.08 nm $\leq t_{Ru} \leq$ 1.12 nm, the bias field is smaller than the saturation field of the top Co layer, so one may expect a non-uniform magnetisation texture in the top Co layer.

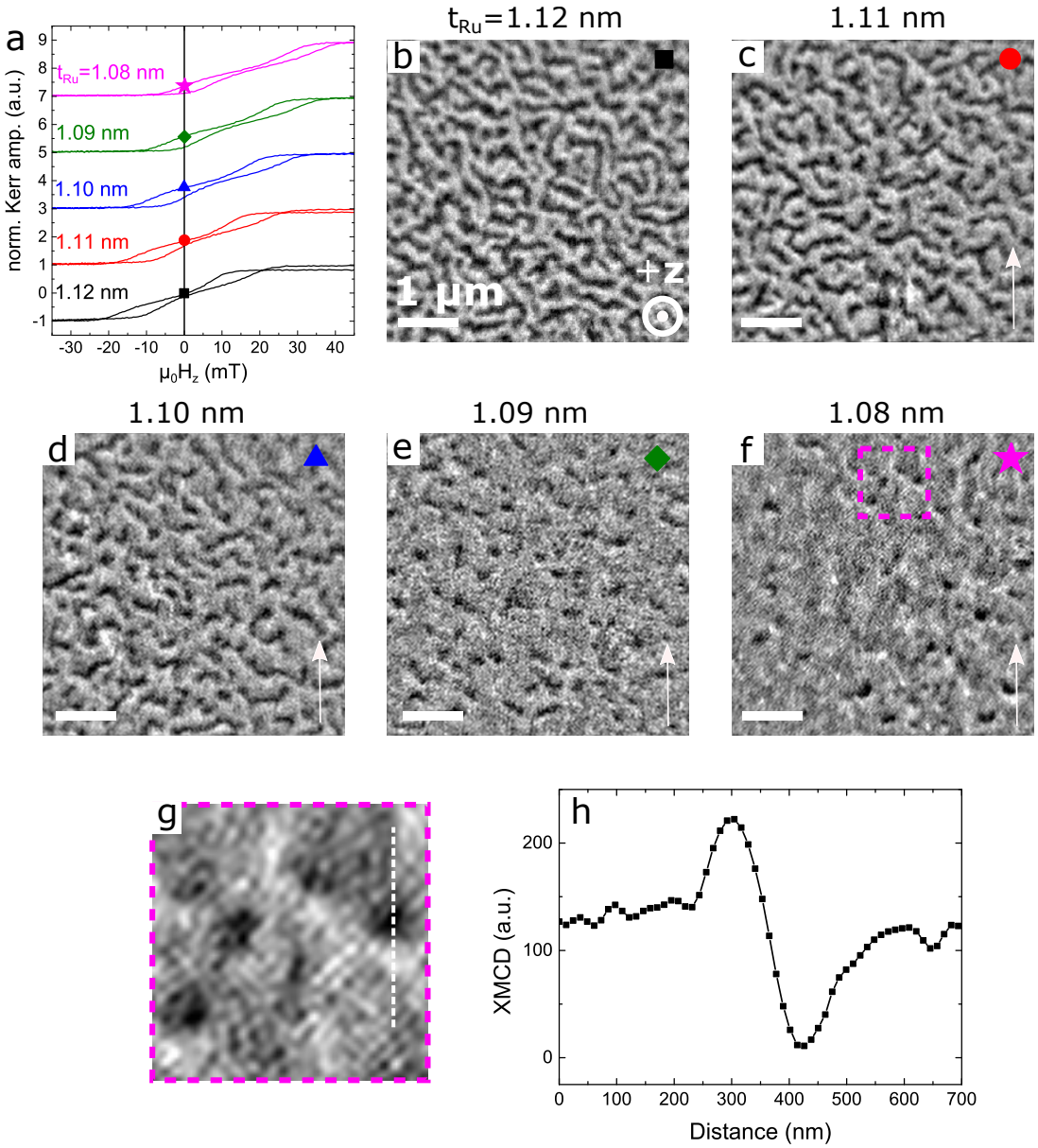

Fig. 4.9: Zero-field magnetic skyrmions in exchange-biased Pt/Co/MgO | **a.** Minor hysteresis loops measured at five locations, ≈ 1 mm apart on the Ru wedge, with nominal thickness t_{Ru}. For $t_{Ru} = 1.08$ nm, 1.09 nm, 1.10 nm, 1.11 nm and 1.12 nm, the bias field is respectively $\mu_0 H_{bias} = 18.1$ mT, 13.1 mT, 9.1 mT, 5.7 mT and 1.7 mT. **b-f.** XMCD-PEEM images of the the magnetic texture at these five locations and at zero external magnetic field. The white arrows indicate the X-ray beam direction. Images dimensions: 5×5 µm^2. **g.** Zoom in the region delimited by the dashed square in **f**. **h.** Line-scan of the XMCD contrast (squares) along the X-ray beam direction corresponding the the dotted line in **g**. The solid line is a guide for the eye.

To observe the magnetisation texture, we performed X-PEEM experiments. The sample was saturated beforehand with a positive OOP field, $\mu_0 H_z \approx 200$ mT. At $H_z = 0$, the magnetisation relaxes in the state indicated by the symbols on the hysteresis loops (Fig. 4.9.a). The images of Fig. 4.9.b-f display the XMCD-PEEM contrast observed at these 5 locations, all at zero field. For

t_{Ru} = 1.12 nm, owing to the negligible bias field, $\mu_0 H_{bias}$ = 1.7 mT, labyrinthine worm domains are observed. Then, gradually increasing $\mu_0 H_{bias}$, by decreasing t_{Ru}, lifts the degeneracy between up and down domains. The worms shorten and eventually shrink into isolated skyrmions, exactly mimicking an external field. In theses images, the light (dark) gray colour indicates a magnetisation pointing along $-\hat{\boldsymbol{z}}$ ($+\hat{\boldsymbol{z}}$). Since the BL is uniformly magnetised along $+\hat{\boldsymbol{z}}$, the AF coupling results in a uniform bias field in the $-\hat{\boldsymbol{z}}$ direction, *i.e.* promoting light gray contrast, hence leading to the stabilisation of skyrmions with core magnetisation along $+\hat{\boldsymbol{z}}$.

Note that within each 5×5 µm^2 image, the small Ru thickness variation corresponds to a bias field variation of ≈ 0.02 mT. Hence, in one image, the variation of $\mu_0 H_{bias}$ across the wedge can be neglected. Therefore, a clear parallel can be drawn between the application of an external field in a Pt/Co/MgO film (Fig. 4.3) and the tuning of the Ru thickness in the exchange-biased Pt/Co/MgO (Fig. 4.9). We notice however a certain dispersion in the skyrmion size and shape in Fig. 4.9.f, unlike the sample without BL (Fig. 4.3). As discussed earlier in §4.3.1, this can be attributed to material inhomogeneities. Furthermore, a larger roughness can also be expected for the Pt/Co/MgO stack grown on the BL as compared to that grown directly on Si. In addition, the roughness of the Ru layer may induce local fluctuations of the bias field.

Furthermore, the observed contrast in the direction of the X-ray beam is consistent with DWs and skyrmions exhibiting a left-handed Néel chirality, as expected from the sign of the interfacial DMI in Pt/Co/MgO. To emphasise this, Fig. 4.9.g shows a zoom in a region of Fig. 4.9.f that displays several skyrmions. The line-scan of the intensity along the beam (white dashed line) is plotted in Fig. 4.9.h. The maximum (minimum) corresponds to a magnetisation parallel (anti-parallel) to the X-ray beam and the plateaus to a magnetisation pointing along $-\hat{\boldsymbol{z}}$. The magnetisation hence rotates according to $\downarrow\rightarrow\uparrow\leftarrow\downarrow$. The distance between the two peaks then provides a measurement of the skyrmion diameter: d_{sk} = 124 nm.

To conclude, we saw that magnetic skyrmions can be nucleated in the absence of both geometrical confinement and external field by exploiting the RKKY interaction between a hard FM layer and a FM layer specifically designed to host skyrmions. Controlling the Ru spacer thickness allows to finely tune the internal field exerted on the top FM layer. This method, exactly mimicking an external field, allows to stabilise magnetic skyrmions in the absence of external excitations and patterning. Finally, note that a bias field can also be induced by exploiting the direct exchange arising at the interface between an AF and a FM, as it was recently demonstrated for 600-nm-diameter skyrmionic bubble in an IrMn/FeCoB/MgO film [185]. This was recently demonstrated at Spintec for small, sub-100 nm skyrmions, in Pt/Co/NiFe/IrMn films with a significant DMI [186].

4.5 Writing magnetic skyrmions using light-ion irradiation

In the above sections, we saw how the skyrmion size and stability can be tuned in confined geometries, which allows to compress them by reducing the nanostructure dimensions. In extended films, skyrmions can be nucleated in the presence of either an external magnetic field (§4.2) or an internal exchange-bias field (§4.4). Nonetheless, their precise nucleation position is hardly controllable. In the present section, we explore a novel approach to nucleate skyrmions and control their position, using light-ion-irradiation (He^+) in an ultra-thin Pt/Co/MgO film.

The first demonstration of the modification of magnetic properties by He^+ irradiation dates back to 1998. In their pioneering work, Chappert *et al.* [187] observed that the anisotropy of ultra-thin Pt/Co-based films was reduced upon increasing the irradiation dose (ID), defined as the number of incoming ions per unit area,[1] leading to a reorientation of the easy magnetisation axis from OOP to IP. They also explored the potential of patterning using He^+ ions to create DW arrays. The reduction of the anisotropy was later investigated in Pt/Co/Pt films and was attributed to irradiation-induced intermixing at the Pt/Co interfaces [188]. One particularly exciting feature of ion-irradiation is the possibility to pattern magnetic films using a focused ion beam (FIB), permitting a local tuning of magnetic properties [189]. In particular, Zhang *et al.* [190] investigated the effect

[1] also referred to as fluence

of local Ga^+ irradiation in perpendicularly magnetised $[Co/Pt]_8$ multilayers. In ≈ 500-nm-diameter disks, patterned with a Ga^+ FIB, the authors observed the formation of bubbles while the pristine — non-irradiated — area remained uniformly magnetised. However, these bubbles exhibited random helicities while chiral Néel DWs were observed in the pristine part. This was mainly attributed to an important irradiation-induced disorder and alloying, expected to be much larger for heavier ions [191]. Similarly, Balk *et al.* [192] recently showed that the DMI can be spatially tuned in Pt/Co/Pt by Ar^+ irradiation. They observed a reversal of the sign of the DMI, attributed to the etching of the top Pt layer and the subsequent oxidation of Co. One advantage of lighter ions like He^+, is that they induce much less intermixing and disorder at the interfaces and do not etch the film [191]; they rather stop in the substrate after passing through the stack and induce short-range atomic displacements.

The effect of He^+ irradiation has been extensively investigated in recent years in crystalline Ta/FeCoB/MgO films. More specifically, upon increasing the ID, a diminution of the effective anisotropy [193–195] and the saturation magnetisation [193] was reported in several papers. In addition, it was observed that increasing the ID also leads to an increase of the DMI, from $D = 0.01$ mJ m^{-2} in the pristine film to $D = 0.08$ mJ m^{-2} for ID = 16 ion nm^{-2} [194,195], leading to an enhancement of the field-driven DW velocity in the flow regime [194]. This increase in the DMI was attributed to a broadening of the Ta/FeCoB interface upon irradiation-induced intermixing [194]. Note that it is also possible that irradiation affects the Rashba-type DMI at the FeCoB/MgO interface.

Finally, in Pt/Co/Pt films, He^+ irradiation was shown to reduce the pinning of DWs. This effect was attributed to a homogenisation of pinning centres in the Co layer as a result of short-range irradiation-induced atomic displacements [196,197]. All the results mentioned above offer exciting perspectives to locally control magnetic properties.

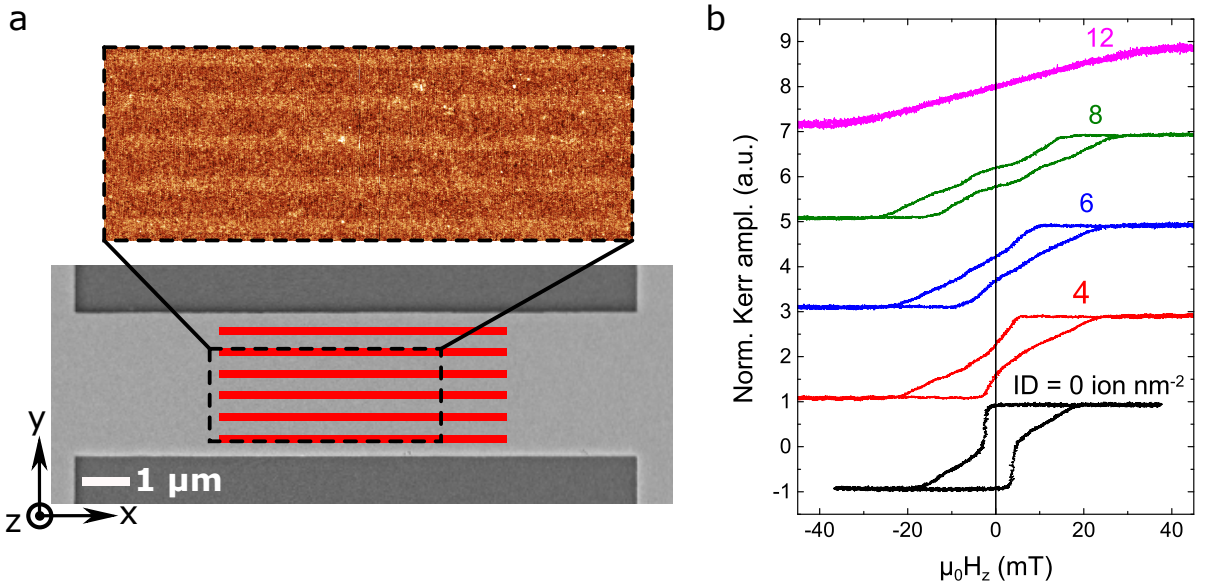

Fig. 4.10: Patterning using a He^+ focused ion beam | **a.** SEM image of a 3-µm-wide Pt/Co/MgO track. The red lines indicate the irradiated patterns, of dimensions 6000 × 150 nm^2, with a spacing of 300 nm. The image in the black dashed rectangle shows the topography acquired by AFM for ID = 6 ion nm^{-2}. **b.** OOP MOKE hysteresis loops for different ID, measured in 2 × 2 µm^2 irradiated areas using a sub-µm focused laser spot.

So far, the effect of He^+ irradiation in material stacks hosting skyrmions has not yet been reported. Here, I present some preliminary results obtained during my PhD. As mentioned above, we use our well-known Pt/Co/MgO stack. The film consists of Ta(3)/Pt(3)/Co(0.97)/MgO(0.9)/Ta(2) (thicknesses in nm), patterned into 3-µm-wide tracks using the process described in §3.4. The Pt/Co/MgO tracks were then irradiated with He^+ ions. The irradiation procedure was carried out

at RT using a FIB at constant ion energy (25 keV). The FIB allows us to control the geometry of the irradiated pattern with a high spatial resolution. Fig. 4.10.a displays a scanning electron microscopy (SEM) image of a Pt/Co/MgO track. The irradiated patterns, drawn in red, are 6000×150 nm^2 lines. These lines can be seen on the topography image (black dashed rectangle), acquired by AFM for ID = 6 ion nm^{-2}. The brighter colour corresponds to a slightly larger height, indicating that the film has swollen upon irradiation, most probably caused by He^+-ion implantation. Different IDs were realised: Fig. 4.10.b displays the OOP hysteresis loops measured for IDs ranging from 0 (pristine) to 12 ion nm^{-2}. These loops were measured by MOKE in 2×2 µm^2 irradiated areas on the same sample. To do so, we used a sub-µm focused laser spot, which allows us to measure local changes of the magnetisation as a function of the external field. Fig. 4.10.b reveals that, as the ID increases, the coercivity decreases, suggesting a decrease of the effective anisotropy. For ID = 12 ion nm^{-2} the hysteresis indicates an IP easy magnetisation axis. Note that XMCD-PEEM images confirmed that for this ID, the magnetisation has turned IP in the irradiated areas.

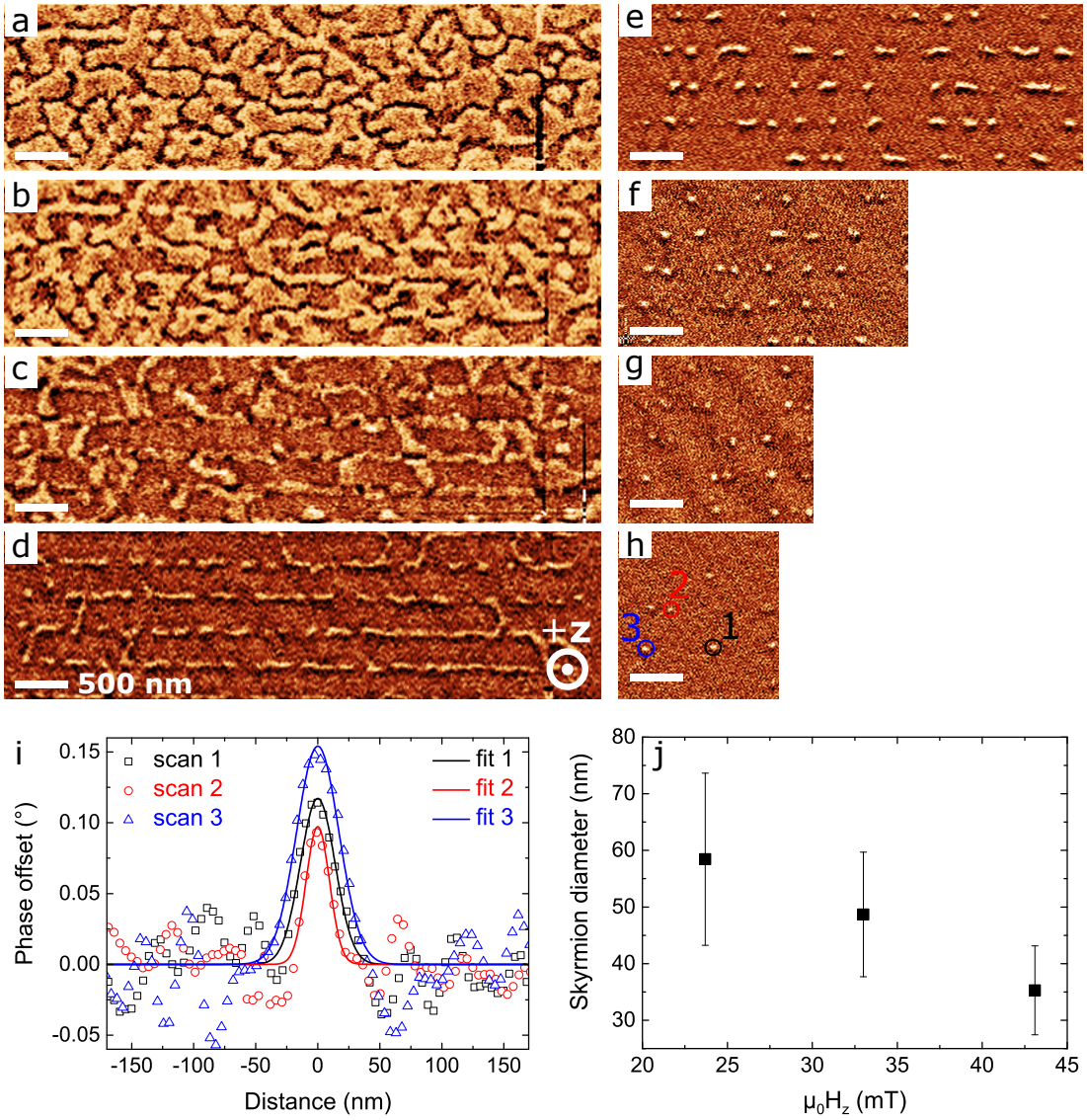

Fig. 4.11: Magnetic skyrmions in irradiated tracks | **a-h.** MFM images showing the magnetic texture in the irradiated lines of Fig. 4.10.a, with ID = 6 ion nm^{-2}, for different external OOP fields: **a.** $\mu_0 H_z = 0$ mT, **b.** 4 mT, **c.** 8 mT, **d.** 10 mT, **e.** 19 mT, **f.** 24 mT, **g.** 33 mT and **h.** 43 mT. Scale bar is 500 nm for all images. **i.** Line-scans of the MFM signal (symbols) acquired for the three skyrmions in **h**. Solid lines are Gaussian fits. **j.** Average skyrmion diameter as a function of the external field measured in the irradiated tracks from images **f-h**. The diameter is defined as the full width at half maximum of the Gaussian.

Let us now look at the magnetisation texture in the irradiated lines of Fig. 4.10.a. Fig. 4.11.a-h show MFM images acquired for different external fields $\mu_0 H_z$. The magnetisation was saturated beforehand with $\mu_0 H_z \approx -100$ mT. At $H_z = 0$ (Fig. 4.11.a), the image displays a labyrinthine worm domain pattern. We note an imbalance between up and down domains, which could be due to the small remanent magnetisation of the pristine area. Then, upon increasing the external field, the domains progressively shrink, up to a point where the pristine part is uniformly magnetised, at $\mu_0 H_z = 10$ mT (Fig. 4.11.d), revealing worm domains aligned in the irradiated lines. Increasing further the field (Fig. 4.11.e-h) leads to the separation of these worms into isolated skyrmions, which are then compressed towards smaller sizes. In the pristine area, no magnetic skyrmion are observed upon increasing the field, unlike for example the sample of §4.3. This can be explained by the larger anisotropy, visible from the non-zero remanence on the ID = 0 loop in Fig. 4.10.b.

In the irradiated lines however, the reduced anisotropy allows the nucleation of magnetic skyrmions, that reach very small sizes. Fig. 4.11.i shows line-scans of the MFM signal (symbols) acquired at $\mu_0 H_z = 43$ mT for the three skyrmions marked in Fig. 4.11.h. The skyrmion diameter can be estimated from the full width at half maximum of the Gaussian fit (solid lines), which gives: $d_{sk1} = 33$ nm, $d_{sk2} = 22$ nm and $d_{sk3} = 41$ nm. Using this definition, we plot in Fig. 4.11.j the skyrmion diameter as a function of the external field extracted from Fig. 4.11.f-h. The average skyrmion diameter reaches very small values, down to 35 nm for $\mu_0 H_z = 43$ mT.

Material characterisation is under way at Spintec, which shall allow to determine the precise impact of He^+ irradiation on magnetic properties such as D and M_s. We can expect the irradiation to introduce intermixing at the Pt/Co interface [188]. In Ta/FeCoB/MgO, the DMI was observed to increase upon He^+ irradiation [194,195]. In Pt/Co, *ab initio* calculations rather predict a slight decrease of the DMI upon increasing Pt-Co intermixing [198]. Further experimental investigation needs to be carried out to confirm the actual effect of He^+-irradiation on the DMI in Pt/Co/MgO.

To conclude, He^+ irradiation provides a method to locally write magnetic skyrmions in a film where they would not otherwise be stable. This external degree of control offers promising perspectives to tune the skyrmion stability in ultra-thin films, bringing them one step closer to applications.

This work was realised in collaboration with the Centre de Nanosciences et de Nanotechnologies (C2N), Palaiseau, with the support of Mamour Sall, Dominique Mailly and Dafiné Ravelosona. The MFM experiments were performed with the help of Kumari Gaurav Rana at the Institut Néel in Grenoble.

4.6 Conclusions

In this chapter, I presented different approaches investigated during my PhD to nucleate and stabilise magnetic skyrmions in ultra-thin Pt/Co/MgO films. This system, known to host left-handed Néel skyrmions, was used as a building block for the different studies. In extended films, optimising the Co thickness close to the spin reorientation transition allows to nucleate skyrmions from the labyrinthine worm domains on applying an external magnetic field. In confined geometries, the skyrmion size can be tuned by playing on the nanostructure dimensions. From these observations, we also saw that the field-dependence of the skyrmion size is greatly impacted by pinning, which can be qualitatively accounted in micromagnetic simulations by introducing a grain distribution with anisotropy disorder. Then, instead of using an external field or geometrical confinement, we demonstrated that skyrmions can also be stabilised by coupling the Co layer to a uniformly magnetised FM layer, via a Ru spacer, which produces an internal effective field. Tuning the Ru thickness is hence analogous to varying an external field. Finally, a novel approach to locally control skyrmion nucleation using a He^+ FIB was shown. In the next chapter, we will see more on the current-driven motion of magnetic skyrmions.

Chapter 5

Current-driven skyrmion dynamics in an ultra-thin film

5.1 Introduction

For the future development of skyrmion-based applications involving memory-shift operations such as racetrack memories [9] and logic devices [134], it is necessary to control and to characterise the motion of skyrmions induced by an electrical current. In the previous chapters, we saw that sputtered HM/FM/NM stacks combine several key features: the presence of stable skyrmions under ambient conditions combined with large SOTs enabling fast skyrmion motion. In recent years, mostly over the course of my PhD, significant progresses have been made in the observation of the current-driven skyrmion motion [109,110,121,146,152,155,162]. These studies notably revealed that the SkHE exhibits a pronounced dependence on the skyrmion velocity (or the current density) [146,155]. In particular, quite a few studies focused on $[\mathrm{HM/FM/NM}]_N$ multilayers with a large number of repetitions N. It is notably in $[\mathrm{Pt/CoFeB/MgO}]_{15}$ that the the largest skyrmion velocities ($\approx$ 100 m s^{-1}) were reported, for skyrmion in the range of 100 nm [110]. However, as explained previously in §2.4.2, the large dipolar fields in these stray-field-coupled multilayers may outweigh the DMI, leading to the stabilisation twisted spin structures with non-uniform chirality across the stack [141–143]. This results in a complex current-driven dynamics due to layer-dependent SOTs [144,145,164]. In particular, these hybrid-chirality textures may not conserve their topological charge during the motion, even at relatively low current density, and therefore not be skyrmions, which strongly impedes their motion [164]. Furthermore, for a given current density, a larger Joule dissipation is also expected in multilayers since the dissipated power scales with the total film thickness. For these reasons, single-layer films with homogeneous skyrmion chirality present a clear advantage for technological purposes.

This chapter presents the results obtained on the current-driven skyrmion motion in an ultra-thin Pt/Co/MgO film. In Chapter 4, we saw that this system hosts left-handed Néel skyrmions at RT with diameters in the range of 100 nm. First, a description of the experiments is provided and the main experimental results are exposed: the observation of the current-driven skyrmion motion, reaching velocities up to 100 m s^{-1}, and the observation of the SkHE which exhibits a marked drive-dependence. Then, in order to interpret as accurately as possible these results based on the Thiele model as well as micromagnetic simulations, a detailed characterisation of the magnetic film is carried out. After detailing the different measurements, the comparison with the predictions of the Thiele equation, in terms of velocity and skyrmion Hall angle (SkHA), is presented. These results are then complemented by real-scale micromagnetic simulations including material inhomogeneities. The simulations reveal the prominent role of pinning on the skyrmion motion and allow to reproduce the different regimes of the dynamics. Finally, the present experimental results are compared to previous experimental studies.

5.2 Experimental observation of the current-driven skyrmion motion

To study the current-driven motion of magnetic skyrmions, a Ta(3)/Pt(3)/Co(0.6-1.1)/MgO(0.9)/Ta(2) film was deposited by magnetron sputtering on a 100 mm high-resistivity Si wafer. The film was then patterned into 3-µm-wide tracks with contact pads consisting of Ti(10nm)/Au(100nm), using the nanofabrication process described in §3.4 (see Fig. 5.1). The skyrmion motion was observed by X-PEEM, at RT, at a position on the Co wedge corresponding to $t_{Co} = 0.9$ nm. To stabilise skyrmions from the initially demagnetised configuration, an OOP external magnetic field $\mu_0 H_z \approx -5$ mT is applied, hence stabilising skyrmions with a core magnetised along $+\hat{\boldsymbol{z}}$.

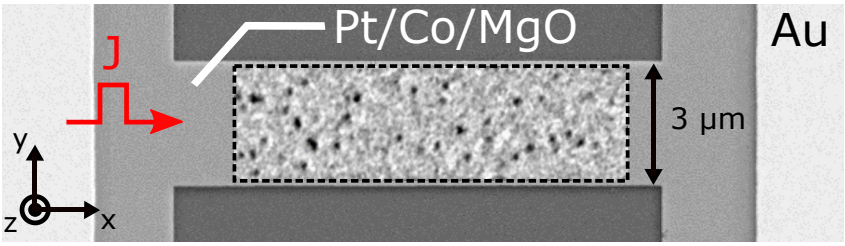

Fig. 5.1: Device for current-driven skyrmion motion experiments | SEM image showing a 3-µm-wide Pt/Co/MgO track with Ti/Au contact pad. A superimposed XCMD-PEEM image displays isolated skyrmions at $\mu_0 H_z \approx -5$ mT.

From XMCD-PEEM images, we can extract an average diameter for these skyrmions. For deformed skyrmion, we calculate an effective diameter assuming an elliptical shape: if a and b are the major and minor axes of the elliptical skyrmion, its diameter is approximated by $d_{sk} = 2\sqrt{ab}$. Fig. 5.2 displays a histogram of the effective diameter measured for a large number of skyrmions, at $\mu_0 H_z \approx -5$ mT. From a Gaussian fit (solid line), we extract an average $d_{sk} = 156 \pm 45$ nm, the error being the standard deviation. This dispersion is a consequence of the disorder and inhomogeneities inherent to granular films that affect the skyrmion size and morphology [173,179,180], as discussed in §4.3.1.

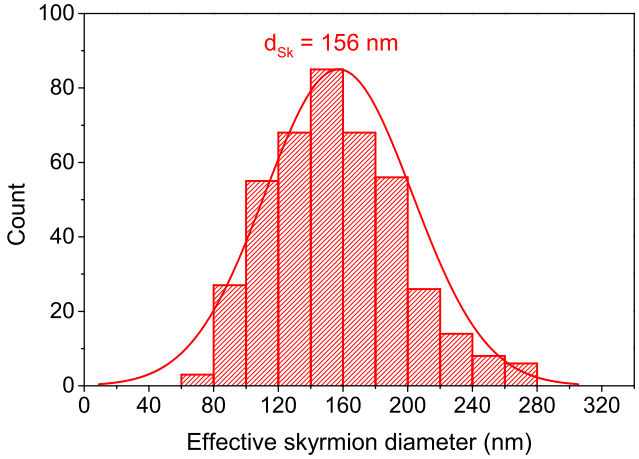

Fig. 5.2: Skyrmion diameter | Distribution of the measured effective skyrmion diameter at $\mu_0 H_z \approx -5$ mT. The solid line is a fit assuming a Gaussian distribution, with average 156 nm and standard deviation 45 nm.

To follow their current-driven motion, ns current pulses are injected in the track, and the skyrmion position is recorded before and after each pulse (static imaging). In Fig. 5.3.a-d and 5.3.e-i, two sequences of imagess show the characteristic skyrmion motion. Before each acquisition, a single 11 ns current pulse of amplitude $J = 5.6 \times 10^{11}$ A m^{-2} is injected along $+\hat{\boldsymbol{x}}$. Overall, some skyrmions exhibit a net motion of several hundreds of nm along the current, *i.e.* against the elec-

tron flow (yellow and orange circles). The same directionality is also observed for skyrmions with opposite core polarity, when $H_z > 0$. In addition, these skyrmions experience a net motion perpendicular to the current direction: this is the signature of the SkHE. This kind of motion is consistent with the current-driven dynamics of left-handed Néel skyrmions governed by the SHE and with the skyrmion core polarity, as explained in §2.5. Nevertheless, the skyrmion motion also exhibits a stochastic character, with events of nucleation (black circle) and annihilation (red and blue circles). In addition, the sequences of Fig. 5.3.a-d and 5.3.e-i reveal that the skyrmion displacement are not identical for each current pulse. Finally, some skyrmions appear distorted after a current pulse, and sometimes acquire an elongated shape. This stochastic behaviour can be attributed to the presence of pinning sites obstructing the skyrmion motion [121,178].

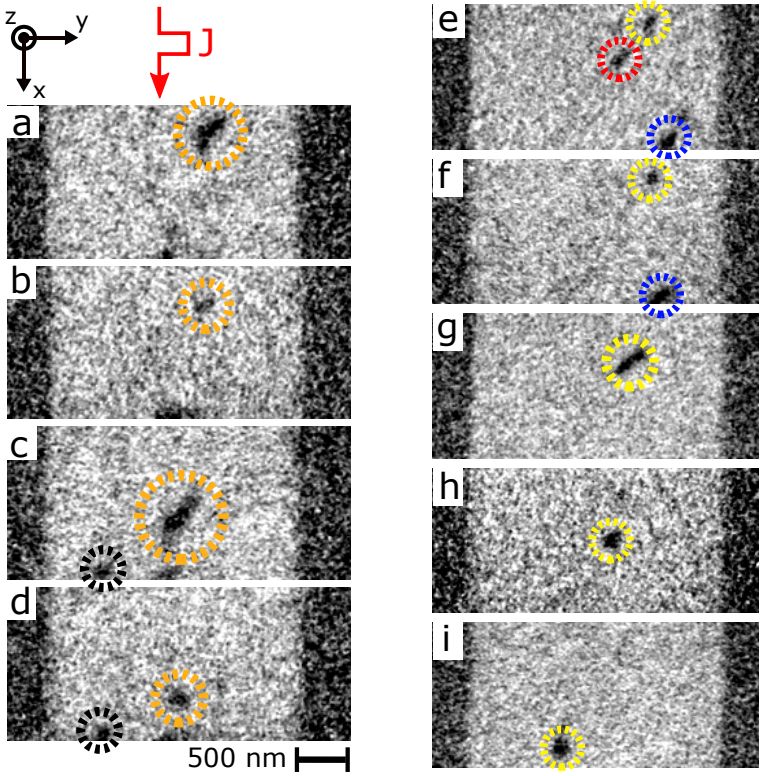

Fig. 5.3: Observation of the current-driven skyrmion motion | **a-d.** and **e-i.** Two distinct sequences of XMCD-PEEM images. Each image was acquired after a single 11 ns current pulse of amplitude $J = 5.6 \times 10^{11}$ A m^{-2}. In both cases, the charge current is flowing along $+\hat{\boldsymbol{x}}$. The external magnetic field is $\mu_0 H_z \approx -5$ mT.

Despite this irregular motion, systematic measurements of the current-induced displacements, averaged over a large number of skyrmions, allow to extract an average skyrmion velocity and an average SkHA, defined here as the angle Θ_{SkH} between the current and the skyrmion motion directions (see Fig. 5.4.a-c). Fig. 5.4.d displays the evolution of the skyrmion velocity with the current density. The velocity is calculated for each skyrmion as the total displacement divided by the measured pulse width (8 ns and 11 ns), and then averaged over multiple events for identical current density. The current density is calculated for each pulse from the measured current transmitted through the device, assuming that it flows uniformly in Pt(3)/Co(0.9), owing to the larger resistivity of the Ta(3) under-layer. The thermal drift between each acquisition is corrected from larger images using the right-angled corner of the track (see Fig. 5.1). Note that only the moving skyrmions, *i.e.* those for which a significant displacement was observed after injection of a single current pulse, were taken into account in the average.

Below a threshold current density, highlighted by the shaded area in Fig. 5.4.d, no significant displacement was observed after injection of a single current pulse. Above $J = 3.5 \times 10^{11}$ A m^{-2}, the skyrmion velocity increases monotonically with the current density, and reaches 100 m s^{-1} for

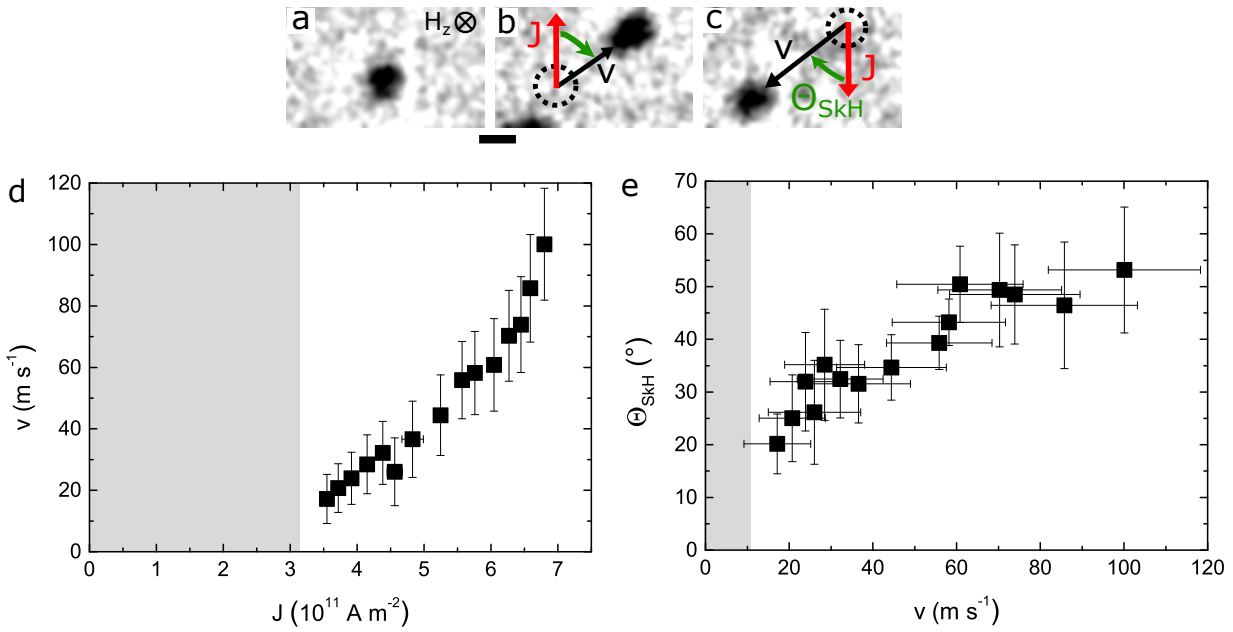

Fig. 5.4: Experimental skyrmion velocity and skyrmion Hall angle | **a-c.** Sequence of XMCD-PEEM images showing a skyrmion after 2 consecutive 8 ns current pulses with opposite polarities (scale bar is 200 nm). The SkHA, Θ_{SkH}, is defined as the angle between the current and the skyrmion motion directions. **d.** Skyrmion velocity as a function of the current density. **e.** SkHA as a function of the skyrmion velocity. The error bars denote the sum of the systematic measurement error and the standard deviation. The shaded areas highlight the regime for which no significant displacement was observed after injection of a single pulse.

$J = 6.8 \times 10^{11}$ A m^{-2}. Note that injecting larger current densities leads to skyrmion nucleation, most likely on defects, making it difficult to distinguish displacements from nucleation events. Furthermore, as previously mentioned, the current injection also leads to a motion perpendicular to the current direction. The direction of deflection with respect to the current direction is unchanged when reversing the current direction (see Fig. 5.4.a-c), which is a hallmark of the SkHE. The measurements (Fig. 5.4.e) reveal that the SkHA depends on the skyrmion velocity: it also exhibits a monotonic increase, up to about 50°.

In the following, these results are discussed and interpreted in the light of Thiele's model (§5.4) as well as micromagnetic simulations (§5.5). For this purpose, a complete characterisation of the static and transport properties of the Pt/Co/MgO stack was carried out. Details about the measurements of the different parameters are provided in the following section. A summary of all the parameters is given in §5.3.6 so the reader may jump directly to this section and the followings for the discussion.

5.3 Characterisation of the system for modelling the skyrmion dynamics

The different measurements were performed on a Ta(3)/Pt(3)/Co(0.6-1.1)/MgO(0.9)/Ta(2) full film sample — hereafter Pt/Co/MgO — that was deposited alongside the wafer where the skyrmion motion was studied (except for M_s measurements as detailed below in §5.3.1).

5.3.1 Saturation magnetisation and anisotropy

The saturation magnetisation and the anisotropy were measured by SQUID magnetometry. To measure M_s, different — non-wedged — Pt/Co(t_{Co})/MgO samples were deposited, with t_{Co} ranging from 0.6 nm to 3 nm. The total magnetic moment was measured at RT from the IP and OOP hysteresis loops on $\approx 5 \times 5$ mm^2 samples. The area of each sample was precisely extracted

from SEM images. Fig. 5.5.a displays the measured magnetic moment per unit area, $M_s t_{Co}$, as a function of the Co thickness, t_{Co}. The saturation magnetisation is extracted from a linear fit: we find $M_s = 1.42 \pm 0.05$ MA m^{-1}, that is the saturation magnetisation of the Co bulk. The intercept of the fit with the x-axis is found very close to $t_{Co} = 0$, indicating the absence of magnetically dead layer, in line with previous measurements [199].

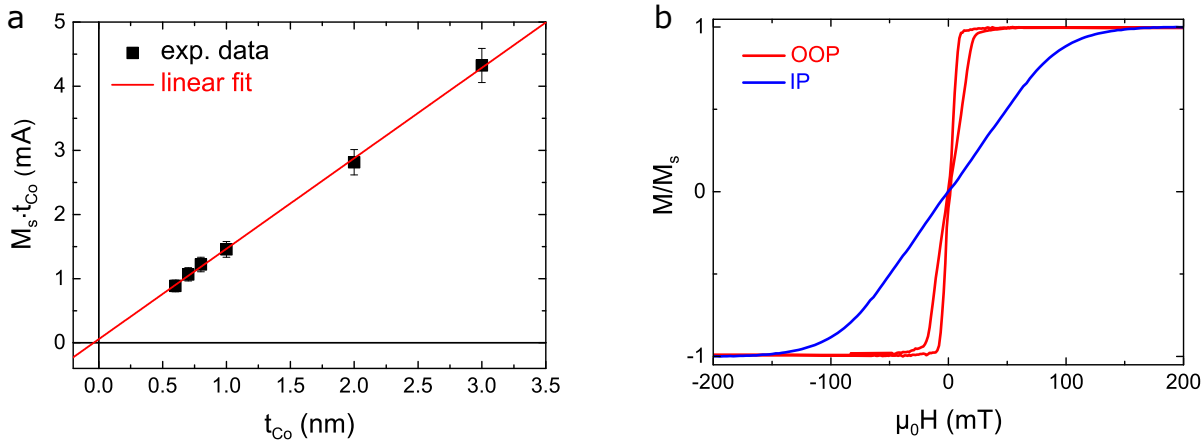

Fig. 5.5: Saturation magnetisation and effective anisotropy measurements | SQUID magnetometry measurements at RT. **a.** Magnetic moment per unit area measured on different Pt/Co(t_{Co})/MgO samples. **b.** IP and OOP hysteresis loops measured on a Pt/Co(0.9)/MgO sample.

The anisotropy field was measured from the hard-axis hysteresis loop on a Pt/Co(0.9)/MgO sample ($\approx 3 \times 3$ mm^2), at the position on the wedge where the skyrmion motion was observed. A value $K_{eff} = 7 \times 10^4$ J m^{-3} was found for the effective anisotropy, from which we deduce the uniaxial anisotropy constant, $K_u = K_{eff} + \mu_0 M_s^2/2 = (1.34 \pm 0.12) \times 10^6$ J m^{-3}.

5.3.2 Dzyaloshinskii-Moriya interaction

The DMI constant, D, was measured by Brillouin light scattering (BLS) spectroscopy on a Pt/Co(0.91nm)/MgO sample.

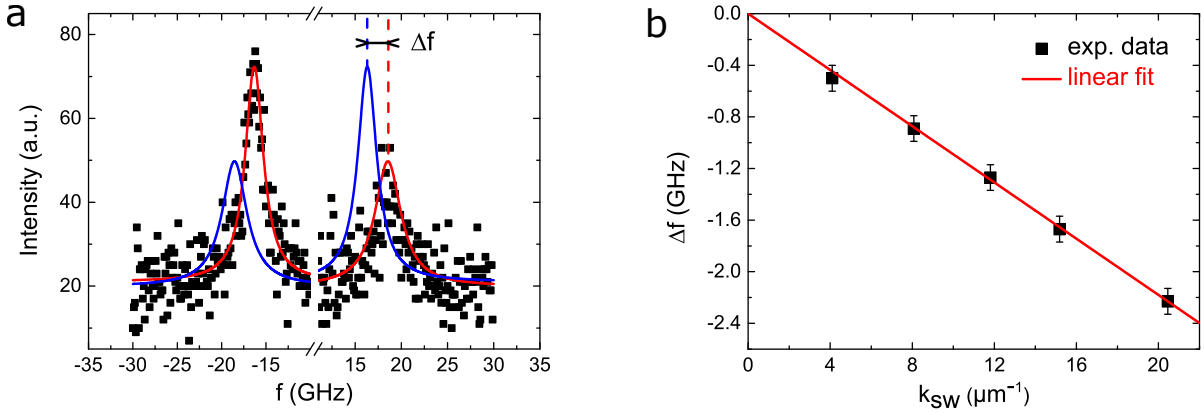

Fig. 5.6: Brillouin light scattering measurements | **a.** BLS spectrum measured for an IP field $\mu_0 H = 0.6$ T, and for $k_{SW} = 20.45$ µm^{-1}. The black squares are experimental data and the red line is a Lorentzian fit. The blue line is the Lorentzian inverted with respect to $f = 0$. Δf is the shift between the Stokes and anti-Stokes peak frequencies. **b.** Frequency shift as a function of the wave vector.

The principle of the technique is the following: the magnetisation is saturated in the film plane by an external field ($\mu_0 H = 0.6$ T), and spin waves (SW) propagating along the direction perpendicular to this field are probed by a laser with a well-defined wave vector, k_{SW}. The preferred handedness

introduced by the DMI leads to an energy difference between two SW propagating in opposite directions, *i.e.* with opposite wave vector. This energy difference corresponds to a frequency shift: $\Delta f\left(k_{SW}\right) = f_S\left(k_{SW}\right) - f_{AS}\left(k_{SW}\right)$, where f_S and f_{AS} are the Stokes (a SW is created) and anti-Stokes (a SW is absorbed) frequencies. This frequency shift is directly related to the DMI by the relation $\Delta f\left(k_{SW}\right) = 2\gamma k_{SW} D/\left(\pi M_s\right)$, with γ the gyromagnetic ratio [41].

Fig. 5.6.a shows a BLS spectrum measured for an IP field $\mu_0 H = 0.6$ T and for $k_{SW} = 20.45$ µm^{-1}. It displays the Stokes and anti-Stokes peaks, characterised respectively by $f_S > 0$ and $f_{AS} < 0$. The frequency shift, Δf, is obtained from a Lorentzian fit (red line). These measurements are performed for several wave vectors (see Fig. 5.6.b, black squares). The DMI is then extracted from the linear fit of $\Delta f\left(k_{SW}\right)$ (Fig. 5.6.b, red line). We find $D = -1.27 \pm 0.04$ mJ m^{-2}, using $M_s = 1.42$ MA m^{-1} (§5.3.1) and $\gamma/(2\pi) = 31$ GHz T^{-1}, extracted from FMR measurements. In these experiments, a negative D value indicates a left-handed chirality, in line with a previous study [48]. For consistency with the convention used in this work, we will consider the absolute value of D in the following. Note that to extract the DMI from BLS measurements, unlike with other methods based on asymmetric DW propagation [35,43,44], it is not required to know the DW width $\Delta = \sqrt{A/K_{eff}}$, and therefore the exchange and effective anisotropy constants, thus reducing the measurement error.

The BLS measurements were performed by Mohamed Belmeguenai and Yves Roussigné at the Laboratoire des Sciences des Procédés et des Matériaux (LSPM) in Villetaneuse, France.

5.3.3 Exchange constant

In order to estimate the exchange constant, A, two different methods were used. On the one hand, we compared the average domain width, measured at zero field in Pt/Co(0.91nm)/MgO using MFM,[1] to that extracted from micromagnetic simulations for different A values. On the other hand, we fitted the Stokes and anti-Stokes frequencies measured by BLS by their analytical expressions, which depends on A.

The simulations were performed with Mumax3 [174] using the following parameters: $M_s = 1.42$ MA m^{-1}, $D = 1.27$ mJ m^{-2}, $K_u = 1.33 \times 10^6$ J m^{-3} and $\alpha = 0.5$. Here the slightly lower anisotropy accounts for the slightly larger thickness of the sample used. Fig. 5.7.a displays the calculated domain width as a function of A. The insets of Fig. 5.7.a show the zero-field domain configuration observed by MFM and that obtained from micromagnetic simulations with $A = 15$ pJ m^{-1}. In the simulations, a 200-nm-diameter bubble is relaxed at zero field, resulting in this particular domain pattern. Note that the equilibrium domain size does not depend on the initial state. In addition, periodic boundary conditions are considered to mimic an infinite film. The red lines in Fig. 5.7.a indicate the domain size extracted from the MFM image: 120 ± 49 nm. We find $A = 16 \pm 6$ pJ m^{-1}. This value was chosen for the micromagnetic simulations.

We note the imprecision on the estimation of A given the uncertainty on the domain width measurement. To support these findings, this value is then compared to that extracted from BLS measurements, more precisely from the dependence of the Stokes and anti-Stokes frequencies on the SW wave vector, k_{SW}. These frequencies are given by [41]:

$$\begin{aligned} f(k_{SW}) &= f_0(k_{SW}) \pm \frac{1}{2}\Delta f(k_{SW}) \\ &= \frac{\gamma\mu_0}{2\pi}\sqrt{\left(H + J_0 k_{SW}^2 + P(k_{SW}t)M_s\right)\left(H + J_0 k_{SW}^2 - P(k_{SW}t)M_s - H_K\right)} \pm \frac{\gamma}{\pi M_s} D k_{SW} \end{aligned} \quad (5.1)$$

Here $J_0 = 2A/(\mu_0 M_s)$, $P(k_{SW}t) = 1 - \left(1 - e^{-|k_{SW}|t}\right)/\left(|k_{SW}|t\right)$, H_K is the anisotropy field and the $+$ $(-)$ sign corresponds to f_S (f_{AS}). Fig. 5.7.b displays the measured f_S and f_{AS} (symbols). Using eq. (5.1), we plot the analytical values for the two frequencies corresponding to $A = 16 \pm$

[1] Same sample as the one used for BLS measurements.

6 pJ m^{-1}. A very good agreement is found in the range of A values extracted from domain width measurements, and the best fit is found for $A \approx 18$ pJ m^{-1}, which falls within the previous estimation. This confirms the relevance of using $A = 16$ pJ m^{-1} in the simulations. Note that for modelling the skyrmion dynamics, A mainly impacts the DW width Δ, included in the calculation of the skyrmion velocity and the SkHA. Since $\Delta \propto \sqrt{A}$, a small change in A would have very little influence on these two quantities.

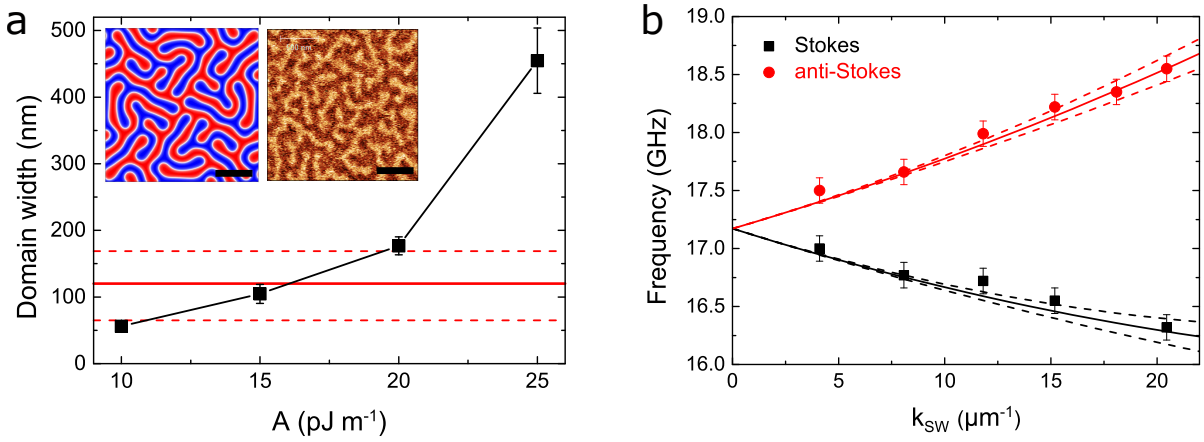

Fig. 5.7: Estimation of the exchange constant | **a.** Micromagnetic simulations: average domain width as a function of A. The error bars denote the standard deviation and the solid black line is a guide for the eye. The red lines indicate the average domain width measured from the zero-field MFM image: 120 ± 49 nm. The insets display the zero-field domain configuration observed by MFM and the one obtained from micromagnetic simulations with $A = 15$ pJ m^{-1} (scale bar is 500 nm). **b.** BLS measurements: measured Stokes (black squares) and anti-Stokes (red dots) frequencies as a function of the wave vector, k_{SW}. The lines represent the expressions given by eq. (5.1) with $A = 16 \pm 6$ pJ m^{-1}.

5.3.4 Magnetic damping

The magnetic damping, α, was extracted from field-driven DW dynamics experiments. The DW motion was followed by MOKE microscopy on the same Pt/Co(t_{Co})/MgO stack, at a position on the wedge corresponding to $t_{Co} = 0.63$ nm where larger domains are observed, owing to the larger effective anisotropy ($K_{eff} = 6.7 \times 10^5$ J m^{-3}). The external magnetic field is applied along the easy axis (OOP) to displace DWs.

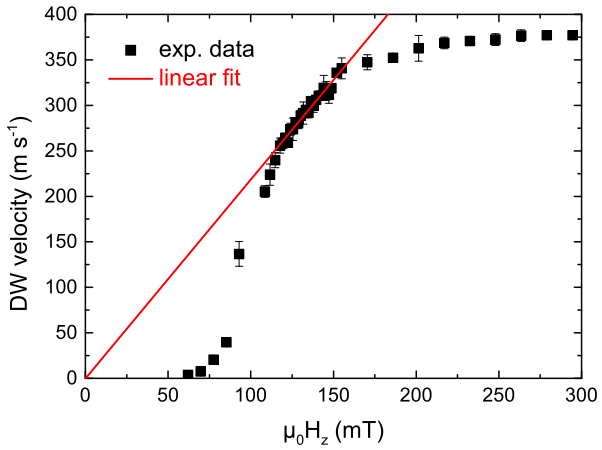

Fig. 5.8: Field-driven DW dynamics experiments | The DW velocity, measured from MOKE microscopy images on a Pt/Co(0.63nm)/MgO, as a function of the external OOP magnetic field. The red line is a linear fit in the flow regime.

Fig. 5.8 shows the measured DW velocity as a function of the external field. In the steady-state regime, the DW velocity can be expressed as follows: $v_{DW} = \mu_{DW}\mu_0 H_z$, with μ_{DW} the DW mobility. The mobility takes different values in the flow and precessional regimes, respectively $\mu_{DW} = \gamma\Delta/\alpha$ and $\mu_{DW} = \gamma\Delta/(\alpha + \alpha^{-1})$ [66]. Experimentally, we find $\mu_{DW} = 2.2$ m s^{-1} mT^{-1}. We extract $\Delta = 5$ nm from our material parameters using $A = 16$ pJ m^{-1} and $K_{eff} = 6.7 \times 10^5$ J m^{-3}. A fit in the flow regime yields $\alpha = 0.43 \pm 0.08$, taking into account the uncertainty on A and using $\gamma/(2\pi) = 31$ GHz T^{-1}. On the contrary, using the expression in the precessional regime would lead to a non-physical, complex value for the damping. This implies that the DW dynamics in the observed linear regime is in the flow regime, consistently with the large DMI (see §1.3.2).

The DW dynamics experiments were performed by José Peña-Garcia and Stefania Pizzini at the Institut Néel in Grenoble, France.

5.3.5 Spin-orbit torques

The DL-SOT and FL-SOT were extracted from RT quasi-static harmonic Hall voltage measurements [87,94] on a Pt/Co(0.9)/MgO film. The film was patterned into a 5-µm-wide cross, as represented in Fig. 5.9.a. An AC current of frequency $\omega/(2\pi) = 10$ Hz is injected along $\hat{\boldsymbol{x}}$ and the transverse resistance, along $\hat{\boldsymbol{y}}$, is measured. As introduced earlier (§1.3.3.2), the DL-SOT and FL-SOT, $\boldsymbol{T}_{DL(FL)} = -\gamma_0 \left(\boldsymbol{m} \times \boldsymbol{H}_{DL(FL)}\right)$, can be expressed in terms of their effective fields as follows: $\mu_0 \boldsymbol{H}_{DL} = C_{DL} J[(\hat{\boldsymbol{z}} \times \hat{\boldsymbol{j}}) \times \boldsymbol{m}] = C_{DL} J\,(\hat{\boldsymbol{y}} \times \boldsymbol{m})$ and $\mu_0 \mathbf{H}_{FL} = C_{FL} J(\hat{\boldsymbol{z}} \times \hat{\boldsymbol{j}}) = C_{FL} J \hat{\boldsymbol{y}}$, where $\hat{\boldsymbol{j}} = \hat{\boldsymbol{x}}$ is the unit vector in the current direction [87].

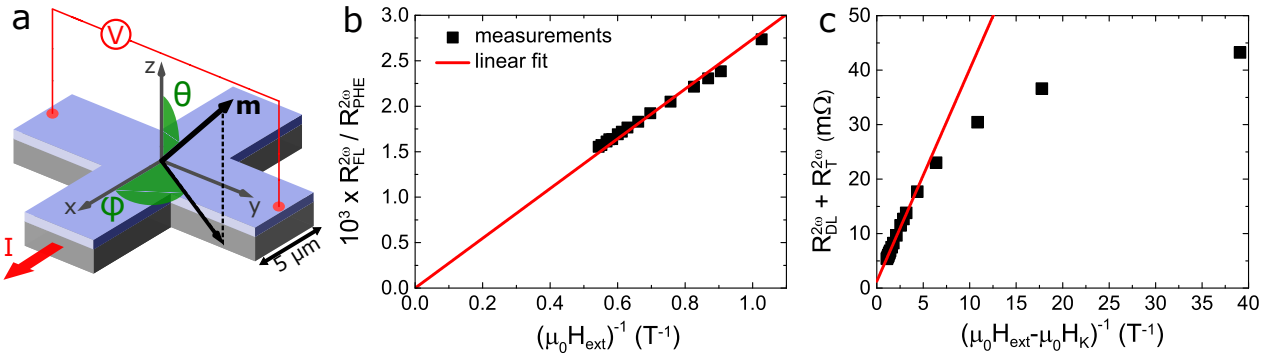

Fig. 5.9: Harmonic Hall voltage measurements | **a.** Schematics of the device consisting of a 5-µm-wide cross. **b.** Second harmonic FL component as a function of the external magnetic field. The red line is a linear fit with fixed zero intercept: for an infinitely large external field, the magnetisation is saturated in the field direction and the response to the SOTs vanishes. **c.** Second harmonic DL and thermal components as a function of the effective field exerted on the magnetisation. The red line is a linear fit in the regime $H_{ext} > H_K$. The DL-SOT effective field is obtained from the slope while the intercept provides the thermal component.

The principle of the measurement is the following: the amplitude of these effective fields is compared to that of an external field. The external field, $\boldsymbol{H}_{ext} = \cos(\varphi)\,\hat{\boldsymbol{x}} + \sin(\varphi)\,\hat{\boldsymbol{y}}$, is rotated in the sample plane and the transverse harmonic resistances are measured for $0 \leq \varphi \leq 2\pi$. Using a spherical coordinate system, as defined in Fig. 5.9.a, the first harmonic expression for the Hall resistance is given by: $R_H^{\omega} = R_{AHE}^{\omega} \cos(\theta) + R_{PHE}^{\omega} \sin^2(\theta) \sin(2\varphi)$ [200]. This expression provides the equilibrium position of the magnetisation, which depends on the first harmonic anomalous and planar Hall coefficients, R_{AHE}^{ω} and R_{PHE}^{ω} respectively. The second harmonic resistance $R_H^{2\omega}$ consists of the FL, DL and thermal components, $R_{FL}^{2\omega}$, $R_{DL}^{2\omega}$ and $R_{\nabla T}^{2\omega}$, such that $R_H^{2\omega} = R_{FL}^{2\omega} + R_{DL}^{2\omega} + R_{\nabla T}^{2\omega}$. The components $R_{FL}^{2\omega}$ and $R_{DL}^{2\omega} + R_{\nabla T}^{2\omega}$ can be separated based on their distinct φ-dependence. The FL-SOT and DL-SOT effective fields can be further obtained from these two terms by considering their dependence on the total magnetic field acting on the magnetisation. One the one hand, $\boldsymbol{H}_{FL}$ is equivalent to a homogeneous IP magnetic field, independent of the magnetisation direction, and

it can be shown that $R_{FL}^{2\omega} \propto 1/H_{ext}$. On the other hand, $\boldsymbol{H}_{DL}$ depends on the magnetisation orientation. Since the Co exhibits PMA, the action of both external and anisotropy fields needs to be taken into account to extract the DL component. Then, one can show that $R_{DL}^{2\omega} + R_{\nabla T}^{2\omega} \propto 1/\left(H_{ext} - H_K\right)$. Fig. 5.9.b and 5.9.c display the dependence of these two terms.

The DL and FL components are then extracted from the slope in the linear regime (red lines) and found to be $C_{DL} = 2.1 \times 10^{-14}$ and $C_{FL} = 0.9 \times 10^{-14}$ T A^{-1} m^2, that is $C_{DL} = 2.1$ and $C_{FL} = 0.9$ mT per 10^{11} A m^{-2}. To calculate these terms, $C_{DL(FL)} = H_{DL(FL)}/J$, we estimated the current density J with the same assumption as for the skyrmion motion experiments: all the current flows in the Pt(3)/Co(0.9) bilayer. Since the skyrmion velocity is proportional to C_{DL}, this approximation does not introduce any discrepancy between the experimental data and the analytical expression. Finally, note that the sign of the DL-SOT is consistent with the SHE in Pt (positive SHA) [7,79,86,87] while the sign of the FL-SOT is consistent with the Rashba effect [7,201].

These experiments provide a direct measurement of SOTs. Therefore, the value of the DL-SOT effective field can be used to calculate the skyrmion velocity predicted by the model and the measured ratio C_{FL}/C_{DL} can be implemented directly into the micromagnetic code. This way, it is not required to estimate the SHA, which would constitute an additional source of error.

I realised the fabrication of the device. The harmonic Hall voltage measurements were performed by Jayshankar Nath with the help of Ioan Mihai Miron at Spintec.

5.3.6 Summary

Below is a table that summarises the different parameter used to model the current-driven skyrmion dynamics in Pt/Co/MgO. The determination of the different parameters is given in the above sections. The DW width Δ was deduced from micromagnetic simulations (see §5.5 hereafter).

$\gamma/(2\pi)$ (GHz T^{-1})	31
M_s (MA m^{-1})	1.42 ± 0.05
K_u (10^6 J m^{-3})	1.34 ± 0.12
D (mJ m^{-2})	1.27 ± 0.04
α ($t_{Co} = 0.63$ nm)	0.43 ± 0.08
A (pJ m^{-1})	16 ± 6
Δ (nm)	11.5
R (nm)	78 ± 23
C_{DL} (10^{-14} T A^{-1} m^2)	2.1
C_{FL} (10^{-14} T A^{-1} m^2)	0.9

Table 5.1: Summary of the parameters for Pt/Co/MgO | Gyromagnetic ratio γ, saturation magnetisation M_s, uniaxial anisotropy constant K_u, DMI constant D, magnetic damping α, exchange constant A, DW width Δ, average skyrmion radius R at $\mu_0|H_z| \approx 5$ mT, effective magnetic fields associated with the DL-SOT and FL-SOT, C_{DL} and C_{FL} respectively. All parameters were measured for $t_{Co} = 0.9$ nm, except α, measured for $t_{Co} = 0.63$ nm.

5.4 Comparison with the Thiele model

The experimental results are first compared with the prediction of the Thiele equation, introduced in §2.5, and whose derivation is detailed in §A.1. Although simple, this equation captures most of the physical ingredients that drive the skyrmion dynamics and is particularly relevant in an ultra-thin film with homogeneous Néel chirality across its thickness. It reads:

$$\boldsymbol{F} + \boldsymbol{G} \times \boldsymbol{v} - \alpha \mathcal{D} \boldsymbol{v} = \boldsymbol{0} \tag{5.2}$$

with $\boldsymbol{F}$ the force due to the current. For a left-handed Néel skyrmion with $p = 1$, which corresponds to most of the experiments described in §5.2, $\boldsymbol{G} = G\hat{\boldsymbol{z}}$ with $G = -4\pi M_s t/\gamma$. Furthermore, $R \gg \Delta$ yields $\mathcal{D} = \frac{M_s t}{\gamma} 2\pi \frac{R}{\Delta}$. Upon injecting a current into the Pt/Co/MgO stack, a DL-SOT and a FL-SOT are exerted on the magnetisation, and an Oersted field is generated. These terms result in different forces on the skyrmion. Litzius *et al.* [146] notably claimed that the observed drive-dependence of the SkHA can be accounted for by the effect of a large FL-SOT on a deformed skyrmion, and Hrabec *et al.* [152] showed that the Oersted field can be translated into a force perpendicular to the current direction. Since the skyrmion is assumed rigid in the present model, the FL-SOT, equivalent to the action of a homogeneous IP magnetic field, does not generate any force. Its effect will be analysed with micromagnetic simulations in the next section. Therefore, only the forces due to DL-SOT and the Oersted field, $\boldsymbol{F}_{DL}$ and $\boldsymbol{F}_{Oe}$ respectively, are considered in the following. We can hence write $\boldsymbol{F} = \boldsymbol{F}_{DL} + \boldsymbol{F}_{Oe}$, with $\boldsymbol{F}_{DL} = F_{DL}\hat{\boldsymbol{x}}$ and $\boldsymbol{F}_{Oe} = F_{Oe}\hat{\boldsymbol{y}}$ (see §A.2 for their calculation). The longitudinal (v_x) and transverse (v_y) skyrmion velocity can further be expressed as:

$$v_x = \frac{\alpha \mathcal{D} F_{DL} - G F_{Oe}}{G^2 + \alpha^2 \mathcal{D}^2} \tag{5.3}$$

$$v_y = \frac{G F_{DL} + \alpha \mathcal{D} F_{Oe}}{G^2 + \alpha^2 \mathcal{D}^2} \tag{5.4}$$

The different forces exerted on the skyrmion are given in Fig. 5.10. Note that it represents a snapshot of the moving, rigid skyrmion in the steady-state regime. The DL-SOT drives the skyrmion along the current and the gyrotropic force $\boldsymbol{G} \times \boldsymbol{v}$ describes a deflection of the skyrmion in a transverse direction, consistent with that observed experimentally (see Fig. 5.3.a-c). The observed direction of motion is thus consistent with a dynamics governed by the SHE-induced DL-SOT. Then, the Oersted field force is opposite to the y component of the gyrotropic force. Hence, we can already point out that this term can only reduce the measured SkHA and therefore cannot account for the

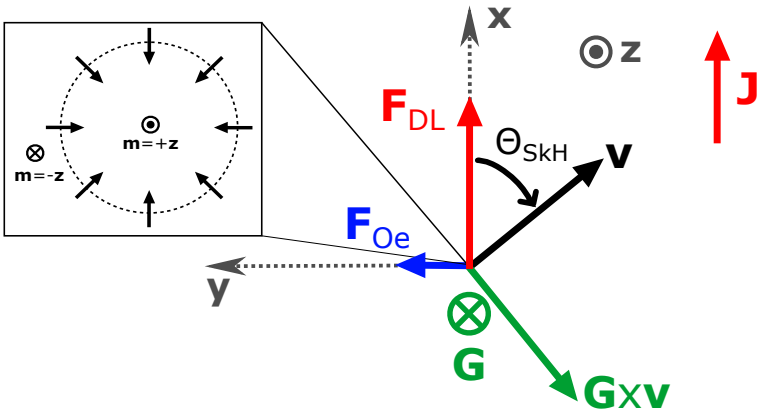

Fig. 5.10: Direction of the forces exerted on a moving rigid skyrmion | The skyrmion is of Néel type with a left-handed chirality and $p = 1$, *i.e.* $N_{sk} = 1$ (inset). $\boldsymbol{G}$ is the gyrotropic vector, $\boldsymbol{J}$ the charge current (opposite to the electron flow) and $\boldsymbol{F}_{DL}$ and $\boldsymbol{F}_{Oe}$ are respectively the forces due to the DL-SOT and the Oersted field.

observed drive-dependence of the SkHA. This remains true for a left-handed skyrmion with opposite core polarity, since upon reversing N_{sk}, both G and F_{Oe} change sign but not F_{DL} (see §A.2).

J (A m^{-2})	F_{DL}	$F_{G,y}$	F_{Oe}
4×10^{11}	8.26	−3.83	0.04
7×10^{11}	14.46	−6.71	0.07

Table 5.2: Amplitude of the forces exerted on a moving rigid skyrmion | The forces, given in pN, are calculated from the expressions given in §A.2 using the parameters of Table 5.1. $F_{G,y}$ denotes the y-component of the gyrotropic force, $\boldsymbol{F}_G = \boldsymbol{G} \times \boldsymbol{v}$.

To emphasise this, the different forces were evaluated numerically assuming that the skyrmion has a radial 360° Bloch DW profile, consistently with experimental observations [48,108], and using the experimental parameters of Table 5.1. The results are given in Table 5.2, with $F_{G,y}$ the y-component of the gyrotropic force, $\boldsymbol{F}_G = \boldsymbol{G} \times \boldsymbol{v}$. It reveals that F_{Oe} is negligible as compared to $F_{G,y}$. Therefore, the Oersted field cannot explain the drive-dependence of the SkHA observed experimentally and can be be neglected in the calculation of the skyrmion velocity and the SkHA. This remains true for narrower tracks where the Oersted field gradient is larger: typically, $F_{G,y}/F_{Oe} \approx 10$ for 300-nm-wide tracks.[1] Finally, neglecting the terms proportional to F_{Oe} in eq. (5.3) and eq. (5.4) yields:

$$v = \frac{\gamma\pi}{4} \frac{R}{\sqrt{\left(\frac{\alpha R}{2\Delta}\right)^2 + 1}} C_{DL} J \tag{5.5}$$

$$\tan \Theta_{SkH} = \frac{2\Delta}{\alpha R} \tag{5.6}$$

where Θ_{SkH} is taken positive for consistency with the convention of Fig. 5.4 and Fig. 5.10. Using the experimental parameters (Table 5.1), we plot the analytical solution on the experimental data in Fig. 5.11 (red solid lines).

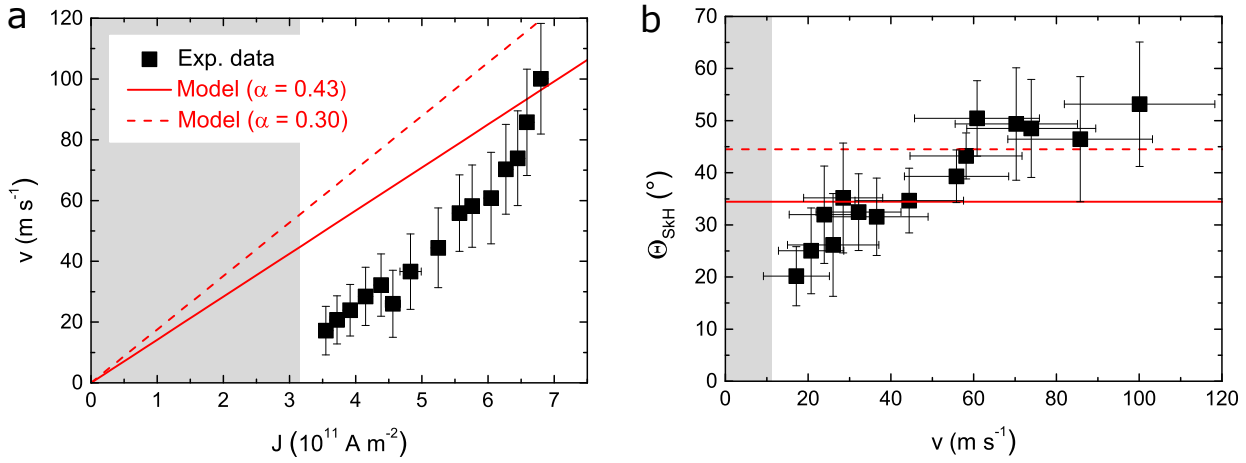

Fig. 5.11: Comparison of the experimental skyrmion velocity and SkHA with the analytical model | **a.** Skyrmion velocity as a function of the current density. **b.** SkHA as a function of the skyrmion velocity. The red lines are the analytical skyrmion velocity and SkHA, calculated from **a.** eq. (5.5) and **b.** eq. (5.6), using the experimental parameters given in Table 5.1 for $\alpha = 0.43$ (solid line) and $\alpha = 0.30$ (dashed line).

[1] Note that in such narrow tracks, edge repulsion may also contribute by opposing the transverse skyrmion motion.

For the velocity (Fig. 5.11.a), a relatively good agreement is found with the experimental data at high current density, considering that v depends critically on quite a few parameters (see eq. (5.5)). Nevertheless, the experimental velocity is smaller than the one predicted by the Thiele equation at low current density. A similar observation was pointed out for current-driven DW velocities measured in Pt/Co/AlO_x [64]. It can be accounted for by the effect of pinning on the skyrmion dynamics, not taken into account in this simple model. Pinning is expected to introduce a thermally activated regime at low driving current, characterised by smaller velocities. This indicates that the skyrmion dynamics in our experiments is in a depinning regime and points at the existence of a flow regime for the largest current densities injected.

Concerning the SkHA (Fig. 5.11.b), a value $\Theta_{SkH} = 34° \pm 8°$ is found, accounting for the dispersion in the skyrmion radius. This SkHA is independent of the skyrmion velocity or the applied current, in sharp contrast with our observations as well as previous experimental studies [146,155]. This discrepancy with the experiments can also be explained by the presence of pinning sites [121,178,202]. Moreover, the calculated — steady-flow — SkHA is found below the largest measured values. However, as it will be shown hereafter by simulations (§5.5), the SkHA is expected to tend towards the analytical value at large skyrmion velocity.

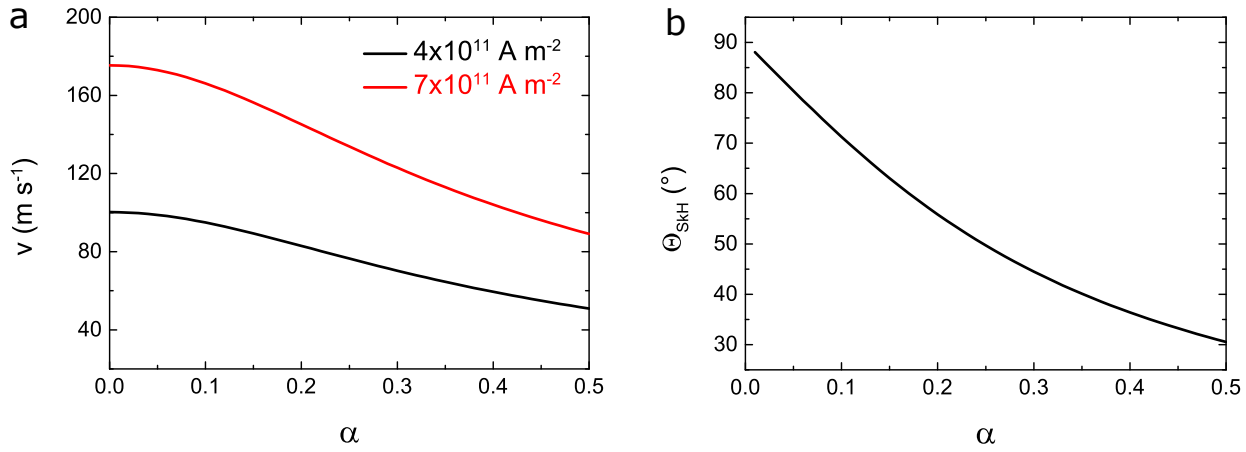

Fig. 5.12: Influence of the damping on the skyrmion velocity and the SkHA | a. Skyrmion velocity calculated from eq. (5.5) as a function of the magnetic damping α for two current densities, corresponding to the smallest and largest current densities used in the experiments (Fig. 5.11). **b.** SkHA as a function of α calculated from eq. (5.6).

It is noteworthy that the damping is a critical parameter in the calculation of the skyrmion velocity and the SkHA. This is emphasised in Fig. 5.12 which displays v and Θ_{SkH} as a function of α, calculated for the smallest and largest current densities used in the experiments. Here, we used $\alpha = 0.43$, measured in Pt/Co(0.63nm)/MgO from the DW mobility in the field-driven steady-flow regime (§5.3.4). Such a large damping is very often required to account for the measured DW mobility in ultra-thin films, for example Pt/Co/Pt [65,66], Pt/Co/AlO_x [64,65] and Pt/Co/GdO_x [65]. Different mechanisms have been proposed to explain these large α: roughness and material inhomogeneities [203,204], spin pumping into the Pt [205] and Rashba SOC [206].[1] These additional damping contributions can significantly impact the DW and skyrmion mobility [209]. Although the determination of the different dissipation mechanisms is beyond the scope of this work, one may argue that these terms are of interfacial origin (except for the material imperfections contribution). Hence, the damping is expected to be lower for thicker Co. In fact, the $\alpha = 0.43$ value was measured for thinner Co ($t_{Co} = 0.63$ nm), which is required to stabilise large domains and drive DWs with an external field. The simplest approximation to account for the increase in the Co thickness is to assume that $\alpha \propto 1/t$, leading to $\alpha = 0.30$ for $t_{Co} = 0.9$ nm. Accounting for

[1] An additional dissipation mechanism exists when large magnetisation gradients, *i.e.* DWs or skyrmions, are present: intra-layer spin pumping [207]. This was proposed to explain the difference between the damping extracted from field-driven DW dynamics and FMR experiments [208].

this correction leads to an enhancement of the calculated skyrmion velocity and SkHA: $\Theta_{SkH} = 45° \pm 8°$ (see Fig. 5.11, red dashed lines). This provides a better agreement with the experimental results, as it will be justified in the following section.

5.5 Micromagnetic simulations

To go beyond the assumptions and limitations of the analytical model, we carried out micromagnetic simulations using the micro3D code [210], with the parameters of Table 5.1.[1] The geometry consists of a $1040 \times 560 \times 0.9$ nm^3 track with a cell size of $3.2 \times 3.2 \times 0.45$ nm^3. Fig. 5.13.a displays the initial skyrmion state. The magnetic field was tuned to obtain the same skyrmion radius at rest as in the experiments: $R = 78.8$ nm at $\mu_0 H_z = -5.4$ mT, in quantitative agreement with the observations. In Fig. 5.13.b is plotted the OOP magnetisation profile (m_z) across the skyrmion. The radius as well as the DW width, $\Delta = 11.5$ nm, are extracted from a fit with a 360° Bloch DW profile.

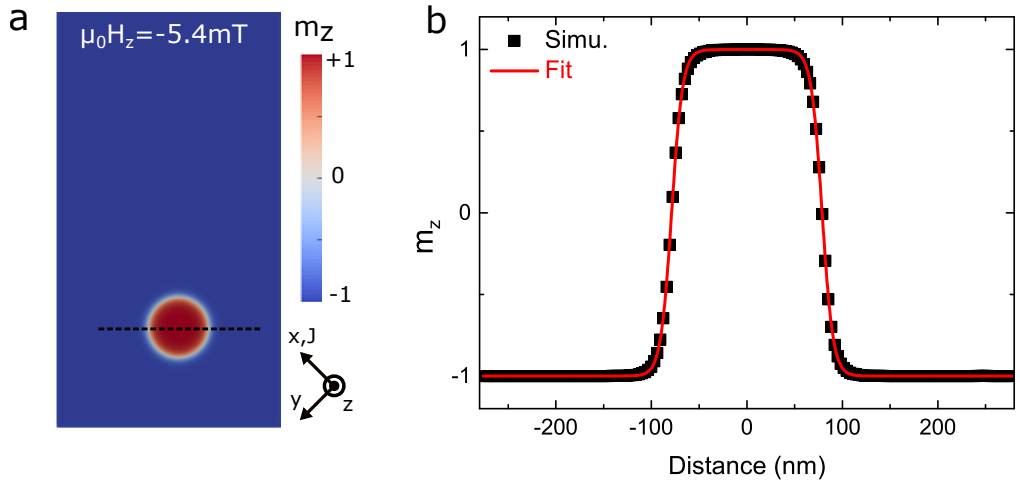

Fig. 5.13: Micromagnetic simulations: initial state | **a.** Skyrmion at rest, $\mu_0 H_z = -5.4$ mT. **b.** Skyrmion profile (dashed black line in **a**). The red solid line is a fit with a 360° Bloch DW profile from which are extracted the skyrmion radius ($R = 78.8$ nm) and the DW width ($\Delta = 11.5$ nm).

To study the current-driven dynamics of this skyrmion, both the DL-SOT and the FL-SOT were implemented into the micromagnetic code, using the measured ratio $C_{FL}/C_{DL} = 0.45$. Fig. 5.14.a and 5.14.b show snapshots of the skyrmion dynamics during the application of a current of amplitude $J = 2.9 \times 10^{11}$ A m^{-2} and 6.7×10^{11} A m^{-2} respectively. As indicated by the red arrow, the current is tilted by 45° so that the skyrmion roughly moves along the track. The simulations reveal that the skyrmion expands and deforms, an effect even more pronounced when the current is large. In addition, it is purely dynamical: when the current is switched off, the skyrmion shrinks back to its original size and recovers its rotational symmetry. To highlight this effect, we calculated the effective skyrmion size, defined as the area for which $m_z > 0$, normalised by the skyrmion area at rest, πR^2. Fig. 5.14.c displays its evolution with the current density. It shows that the skyrmion size increases significantly, in contradiction with the rigid-core assumption of Thiele's model. This effect is actually analogous to another well-known effect observed for DW: the asymmetric DW velocity relative to the current direction when driven by SOTs [211–213]. In short, different tilt angles, that is the angle between the DW internal magnetisation ($m_z = 0$) and the current, result in different DL-SOT-induced velocities [214]. In a skyrmion, enclosed by an initially circular DW, the tilt angle varies continuously from 0 to 360°. As a result, different sections of the skyrmion exhibit different DL-SOT-induced velocities, resulting in its deformation.

[1] The micromagnetic simulations were performed by Liliana Buda-Prejbeanu at Spintec.

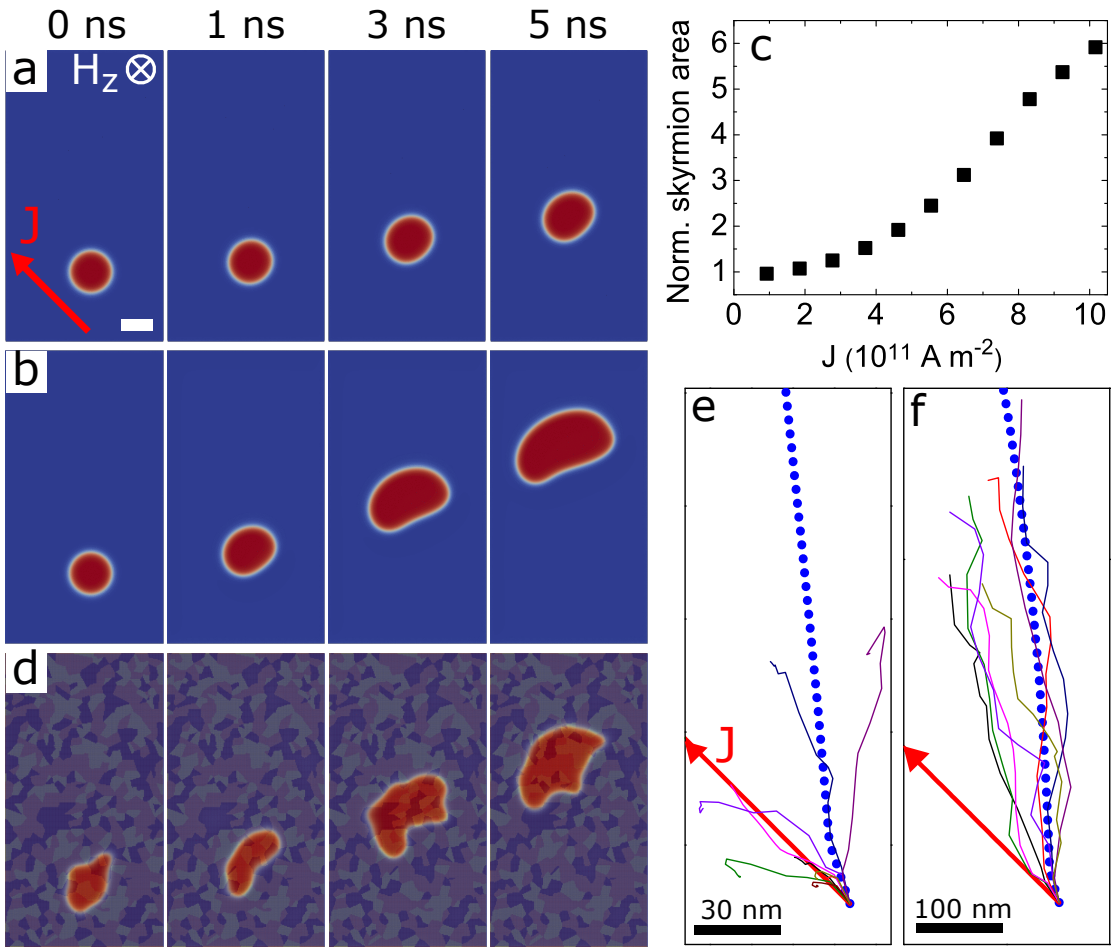

Fig. 5.14: Micromagnetic simulations: current-driven skyrmion dynamics | **a,b.** Sequences of snapshots showing the skyrmion motion in a disorder-free film with **a.** $J = 2.9 \times 10^{11}$ A m^{-2} and **b.** $J = 6.7 \times 10^{11}$ A m^{-2} (scale bar is 100 nm). **c.** Evolution of the skyrmion size with the current density (at 5 ns). The size is defined as the area for which $m_z > 0$ (in red) normalised by the area at rest πR^2. **d.** Sequence of snapshots in a disordered film for $J = 6.7 \times 10^{11}$ A m^{-2}. The dark (bright) grains are region with stronger (weaker) anisotropy. **e,f.** Trajectories recorded for different grain distributions for **e.** $J = 2.9 \times 10^{11}$ A m^{-2} and **f.** 6.7×10^{11} A m^{-2}. The blue dotted lines indicate the skyrmion trajectories in the absence of disorder. Deformed skyrmions are located by their barycentre.

To follow the dynamics of a non-circular skyrmion, we record the position of its barycentre. The skyrmion velocity and SkHA thus obtained are plotted as blue dots in Fig. 5.15.a and 5.15.b. Remarkably, the simulations are in excellent agreement with the simple prediction of the analytical model (red line), highlighting the relevance of discussing the experimental results in the light Thiele's model. Surprisingly, the DL-SOT-induced expansion/deformation does not alter significantly the skyrmion dynamics in the range of current density considered, in spite of the large expansion. Therefore, this effect cannot account for the evolution of the skyrmion velocity and SkHA observed experimentally.

Another explanation to account for the evolution of the skyrmion velocity and the SkHA is the presence of pinning sites in the material [121,178,202]. To include such an effect, we introduce disorder, modelled by a distribution of grains with different anisotropies [137,178], as already presented in §4.3.1. The average grain size is 30 nm and the anisotropy is varied randomly within $(1 \pm 0.05)\, K_u$. Fig. 5.14.d displays the motion of a skyrmion for a given disorder configuration and for $J = 6.7 \times 10^{11}$ A m^{-2}. It reveals that the skyrmion experiences an additional dynamical deformation due to the local variation of anisotropy creating minima for the DW energy. This makes it difficult to draw a distinction between the contributions of DL-SOT and disorder to the skyrmion

deformation. The skyrmion at rest is also distorted since it relaxes on an inhomogeneous energy landscape (§4.3.1). Fig. 5.14.e and 5.14.f display the skyrmion trajectories recorded for different grain distributions and for $J = 2.9 \times 10^{11}$ A m^{-2} and $J = 6.7 \times 10^{11}$ A m^{-2}, respectively. The blue dotted lines represent the trajectories in the absence of disorder. The first plot reveals a stochastic dynamics, with a large dispersion in the direction of motion. In some cases, the skyrmions are stopped on a strong pinning site, preventing further motion. For larger current densities, the number of such events decreases and the trajectories approach that of the ideal case. This is emphasised in Fig. 5.15.a, which shows the skyrmion velocity as a function of the current density with and without disorder.

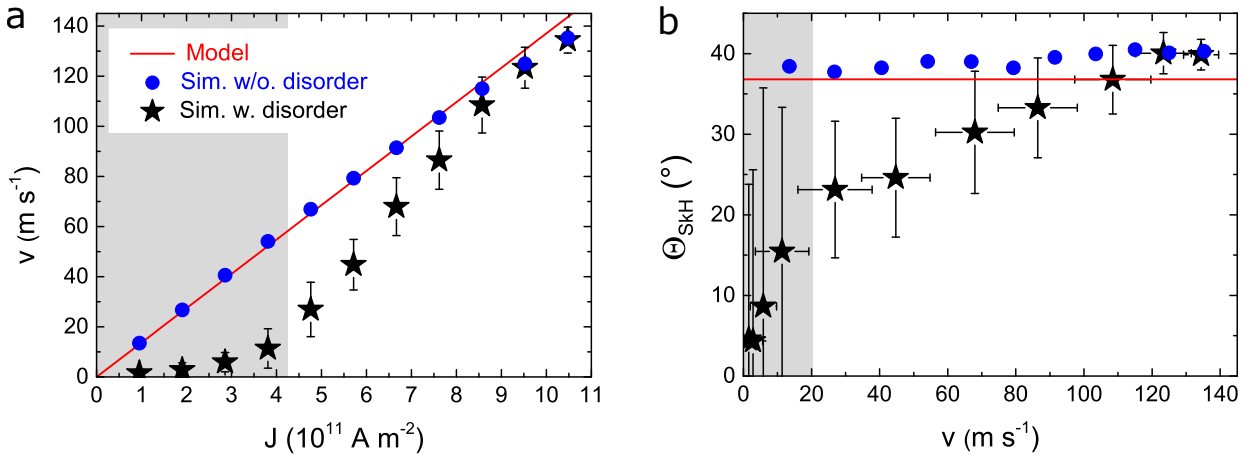

Fig. 5.15: Micromagnetic simulations: skyrmion velocity and SkHA | **a.** Skyrmion velocity as a function of the current density in a disorder-free film (blue circles) and in a disordered film (black stars). **b.** SkHA as a function of the skyrmion velocity. The analytical solutions (red solid lines) are calculated from **a.** eq. (5.5) and **b.** eq. (5.6). The error bars denote the standard deviation. The shaded areas highlight the pinning regime.

The disorder introduces different regimes in the dynamics: at low driving current, the average velocity, calculated from the total displacement after 8 ns computation time, is close to zero. This pinning regime is highlighted by the shaded area in Fig. 5.15.a. At higher current density, the driving force becomes large as compared to the pinning force, resulting in an increased mobility. Eventually, the skyrmion velocity catches up with the disorder-free velocity, which can be identified as the flow regime. This behaviour is completely analogous to that of current-driven DWs [64] and points out that care should be taken when interpreting the regime of the skyrmion dynamics. In the pinning regime, a reduction in the average SkHA is observed (Fig. 5.15.b). Upon increasing the driving force, the SkHA increases monotonically and converges towards the disorder-free SkHA in the flow regime. These results can be understood as follows: pinning can be pictured as a force opposite to the ideal skyrmion motion direction [215], thus lowering its velocity. The gyrotropic response to this force will deviate the skyrmion from its initial trajectory, in a direction transverse to this pinning force, according to $\boldsymbol{G} \times \boldsymbol{v}$. This effect, sometimes referred to as extrinsic SkHE [178], prevails at low current density and becomes negligible as the driving forces gradually outweighs the pinning force.

Furthermore, the influence of the FL-SOT on such distorted skyrmions was also investigated. In a recent study, the effect of a sizeable FL-SOT coupled to a skyrmion deformation was put forward to explain the drive-dependence of the SkHA [146]. We considered different values of the ratio C_{FL}/C_{DL}: 0, 0.45 and 1, 0.45 being the measured value (§5.3.5). The corresponding skyrmion velocity and SkHA, obtained from disorder-free simulations, are plotted in Fig. 5.16.a and 5.16.b respectively. It reveals that, even for FL-SOT amplitudes twice as large as the measured value, its effect on the skyrmion dynamics is largely negligible in the range of current density considered. Moreover, increasing the FL-SOT leads to a (small) decrease of the SkHA rather than an increase. Therefore, the FL-SOT cannot account for the velocity-dependence of the SkHA observed

experimentally. Lastly, as highlighted in Fig. 5.16.c and 5.16.d, the FL-SOT has very little influence on the dynamical skyrmion deformation/expansion. Hence, for realistic relative SOTs amplitudes (up to $C_{FL} = C_{DL}$), the effect of the FL-SOT on the current-driven skyrmion dynamics can safely be neglected.

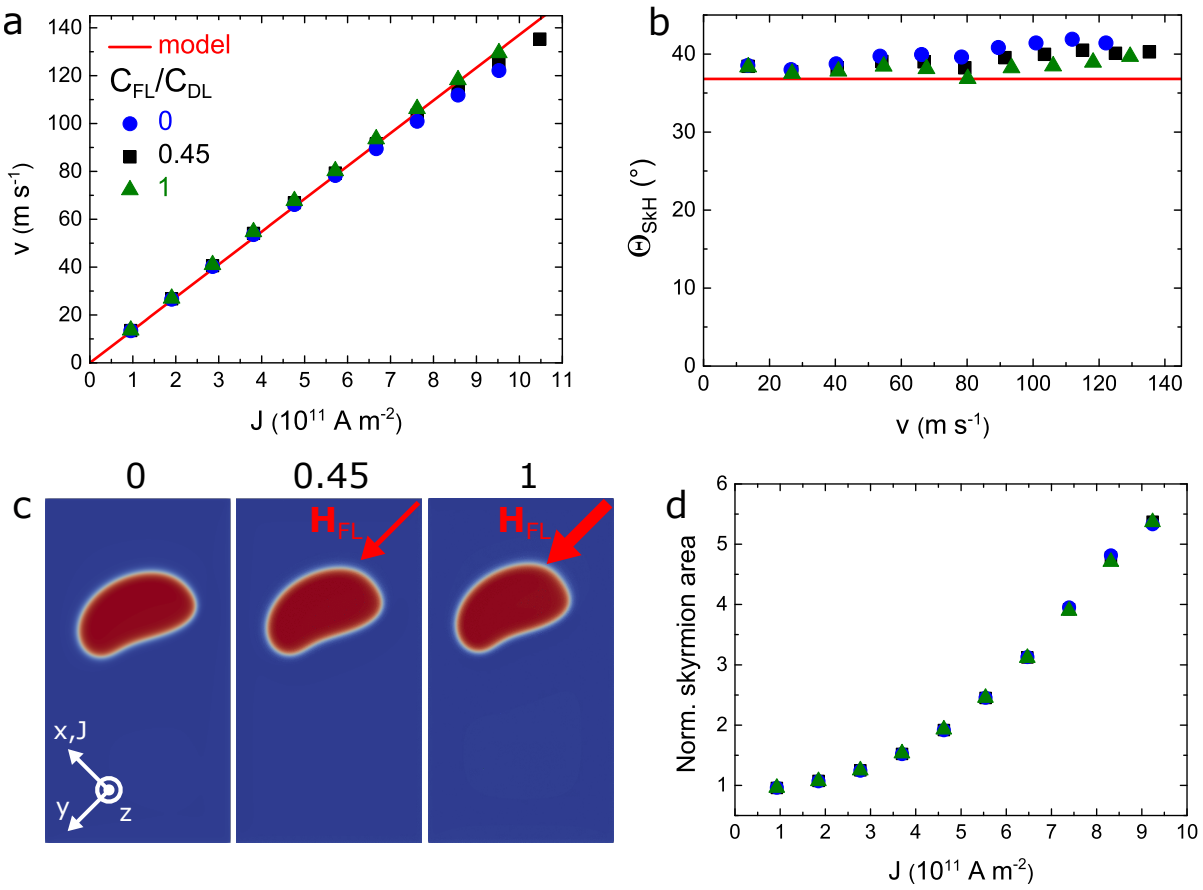

Fig. 5.16: Micromagnetic simulations: influence of the FL-SOT | **a.** Skyrmion velocity and **b.** SkHA obtained from micromagnetic simulations in a disorder-free film for different C_{FL}/C_{DL}; 0.45 is the measured value. **c.** Snapshots of a skyrmion after 5 ns at $J = 6.7 \times 10^{11}$ A m^{-2} and for different C_{FL}/C_{DL}. **d.** Evolution of the skyrmion size with the current density (at 5 ns). The size is defined as the total area for which $m_z > 0$ (in red in **c**) normalised by the area at rest.

By comparing Fig. 5.11 and Fig. 5.15, we see that the simulations are in excellent agreement with the observations. This strongly supports that the observed drive-dependence of the skyrmion velocity and that of the SkHA are due to pinning effects. Note that only the non-shaded areas are to be compared as the pinning regime is not observed in the experiments. Although the critical current densities and skyrmion velocities at which the depinning and flow regimes are reached depend on the choice of disorder parameters [121,178], this approach constitutes a good qualitative description of the pinning effect on the current-driven skyrmion motion. Indeed, the same three-regime behaviour is obtained for DMI, exchange and saturation magnetisation disorder [121]. Qualitatively, the simulations show reveal that the disorder-free velocity and SkHA constitute upper bounds for the velocity and SkHA in disordered systems. This supports the aforementioned assumption of a lower damping in Pt/Co(0.9nm)/MgO film. Now we see that considering $\alpha = 0.30$ instead of $\alpha = 0.43$, measured for Pt/Co(0.63nm)/MgO, enhances the disorder-free velocity and SkHA (Fig. 5.15, red dashed lines), leading to an excellent agreement with the simulations. Therefore, it points out that the observed skyrmion dynamics is in a depinning regime, and suggests that the flow regime is reached for the largest current densities.

5.6 Comparison with other experiments

5.6.1 Skyrmion velocity

To date, several groups have reported the current-driven motion of magnetic skyrmions in HM/FM/NM films (single- and multi-layers). The main results are presented in Table 5.3. Overall, similar results were obtained for Pt/FM-based systems, with skyrmion sizes and velocities of the same order of magnitude. Note that weaker pinning effects were reported in some amorphous materials such as Ta/FeCoB/TaO_x [155] and $[Pt/CoFeB/MgO]_{15}$ [110,146].

Material	d_{sk} (nm)	v (m s^{-1})	J (10^{11} A m^{-2})	Ref.
$[Pt/Co/Ta]_{15}$	$\sim$ 150 (estim.)	50	3.5	[110]
$[Pt/Co_{60}Fe_{20}B_{20}/MgO]_{15}$	$\sim$ 150 (estim.)	115	5	[110]
$Ta/Fe_{60}Co_{20}B_{20}/TaO_x$	800-1100	0.8	0.6	[155]
Pt/Ni/Co/Ni/Au/Ni/Co/Ni/Pt	160	65	4.5	[152]
$[Pt/Fe_{65.6}Gd_{25}Co_{9.4}/MgO]_{20}$	180	50	3.5	[162]
Pt/Co/MgO	160	100	7	This work
$Pt/Co_{60}Fe_{20}B_{20}/MgO$	170	110	7.5	This work

Table 5.3: Skyrmion velocity: comparison between different systems | Material stack, average skyrmion diameter d_{sk} (estimated from the data when not mentioned explicitly), maximum skyrmion velocity v and current density J at which v was measured.

During this thesis, we also studied the skyrmion motion in Pt/CoFeB/MgO, and performances similar to Pt/Co/MgO were observed (see Fig. 5.17). We measured velocities up to 110 m s^{-1} for skyrmions of the same size. However, no reduction of pinning was noted, which could be due to inhomogeneous material growth or annealing-related effects during the nanofabrication process. Nevertheless, the maximum velocities measured in the ultra-thin films studied during this thesis

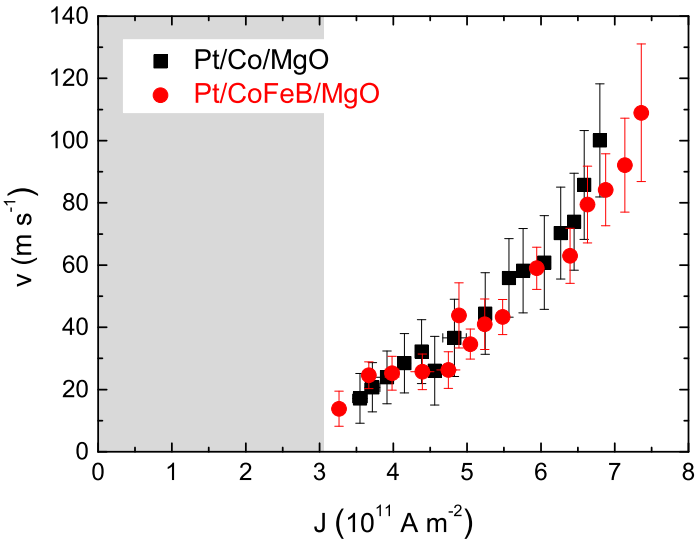

Fig. 5.17: Skyrmion velocity: Pt/Co/MgO vs Pt/CoFeB/MgO | Skyrmion velocity as a function of the current density measured in Ta(3)/Pt(3)/Co(0.9)/MgO(0.9)/Ta(2) and in Ta(3)/Pt(3)/$Co_{60}Fe_{20}B_{20}$(0.95)/MgO(0.9)/Ta(2 films (thicknesses in nm) at room temperature.

(Co and CoFeB) are comparable to those measured in stray-field-coupled multilayers for skyrmions of similar size (see Table 5.3). And using single-layers allows to lower power dissipation by a factor of the number of repetitions, *i.e.* by one order of magnitude. Moreover, it allows to prevent stray-field-related effects, detrimental for the motion of skyrmions [144,145,164].

5.6.2 Skyrmion Hall effect

Two other studies showed the drive-dependence of the SkHE: Jiang *et al.* [155] in Ta/FeCoB/TaO_x, for $d_{sk} \approx 1$ µm and $v \approx 1$ m s^{-1}; and Litzius *et al.* [146] in $[Pt/CoFeB/MgO]_{15}$, for $d_{sk} \approx 100$ nm and $v \approx 100$ m s^{-1}. Note that another study by Woo *et al.* [162] reported on the drive-dependence of the SkHA in a ferrimagnetic multilayer composed of $[Pt/FeGdCo/MgO]_{20}$. To exploit the dipolar coupling between each layer, in order to stabilise worm domains that can be shrunk into isolated skyrmions by an external field, the GdFeCo thickness was optimised so that the magnetic moment compensation temperature (450 K) was sufficiently far from RT. Hence, the conclusions remain essentially the same as those for FM multilayers.[1]

In the first study, the SkHA was observed to increase with the current density and to saturate (see Fig. 5.18.a). This is in agreement with the behaviour dictated by pinning effects, similarly to our observations in Pt/Co/MgO. A steady-flow SkHA $\Theta_{SkH} = 28°$ was measured for a skyrmion radius $R = 550$ nm, leading to $\Delta/\alpha = 146$ nm using eq. (5.6). In this study, the authors assumed that $\alpha \sim 0.02$ which would imply $\Theta_{SkH} = 75°$ using their estimation of $\Delta = 21$ nm. However, using α as a fitting parameter rather yields $\alpha = 0.14$, highlighting the crucial importance of a proper evaluation of the damping in skyrmion dynamics experiments.

In the second study, a monotonic increase was observed in the same skyrmion velocity range as in our experiments (see Fig. 5.18.b). Here, a ratio $\Delta/\alpha = 7.6$ nm was extracted from the dependence of Θ_{SkH} on R. The authors claimed that the effect of a sizeable FL-SOT ($C_{FL}/C_{DL} = 5$), coupled to skyrmion deformations, could be responsible for both the small Δ/α ratio and the velocity-dependence of the SkHA. However, the assumed FL-SOT values were much larger than those reported for Pt/CoFeB/MgO [216] and for Pt/FM/MgO stacks in general [7]. For realistic relative SOTs amplitudes, in these systems, the FL-SOT has actually very little effect on the skyrmion dynamics (see Fig. 5.16). Pinning effects could account for the measured Δ/α ratio: if the flow regime is not reached, the measured SkHA would be smaller than the flow SkHA predicted by eq. (5.6). Furthermore, the inter-layer stray fields in these multilayers can lead to a complex dynamics and a drive-dependent SkHA even in the absence of disorder or FL-SOT due to layer-dependent chiralities [145,164]. These effects, specific to multilayers and not taken into account in 2D micromagnetic simulations, may also contribute to the drive-dependence of the SkHE.[2]

In the present work (Fig. 5.18.c), although stronger pinning effects are observed, we combine several interesting features of the two previous studies: the fast motion and small skyrmion sizes measured in multilayers and the homogeneous through-thickness skyrmion chirality of single-layers. This allows to interpret part of the experimental results based on the simple Thiele model. We go a step further by performing a detailed characterisation of the film properties, in particular by measuring to crucial parameters of the dynamics: the SOTs and the damping. The different effects that may impact the SkHE in our system can so be sorted out, which notably enables to rule out the influence of the FL-SOT. This allows in turn to conclude on the predominant role of pinning on the current-driven skyrmion dynamics.

The present study also highlights the importance of evaluating the damping in ultra-thin films hosting skyrmions. During the last months of this thesis, FMR measurements were performed by Kyongmo An and Olivier Klein at Spintec in $Pt/Co(t_{Co})/MgO$, for $t_{Co} = 0.63$ nm and $t_{Co} = 0.9$ nm. The following values were extracted: $\alpha_{FMR}\,(0.63\text{nm}) = 0.16$ and $\alpha_{FMR}\,(0.9\text{nm}) = 0.10$. As

[1] Although stray-field-related effects (hybrid chirality) are expected to be less prominent in ferrimagnetic multilayers, owing to the much smaller net magnetisation.

[2] Actually, in a very recent study published a few weeks before the final submission of the present manuscript, the same group showed that skyrmions in $[Pt/CoFeB/MgO]_{15}$ do exhibit a uniform, left-handed Néel chirality across the stack [217]; so pinning may be the only one to blame for this drive-dependent SkHE...

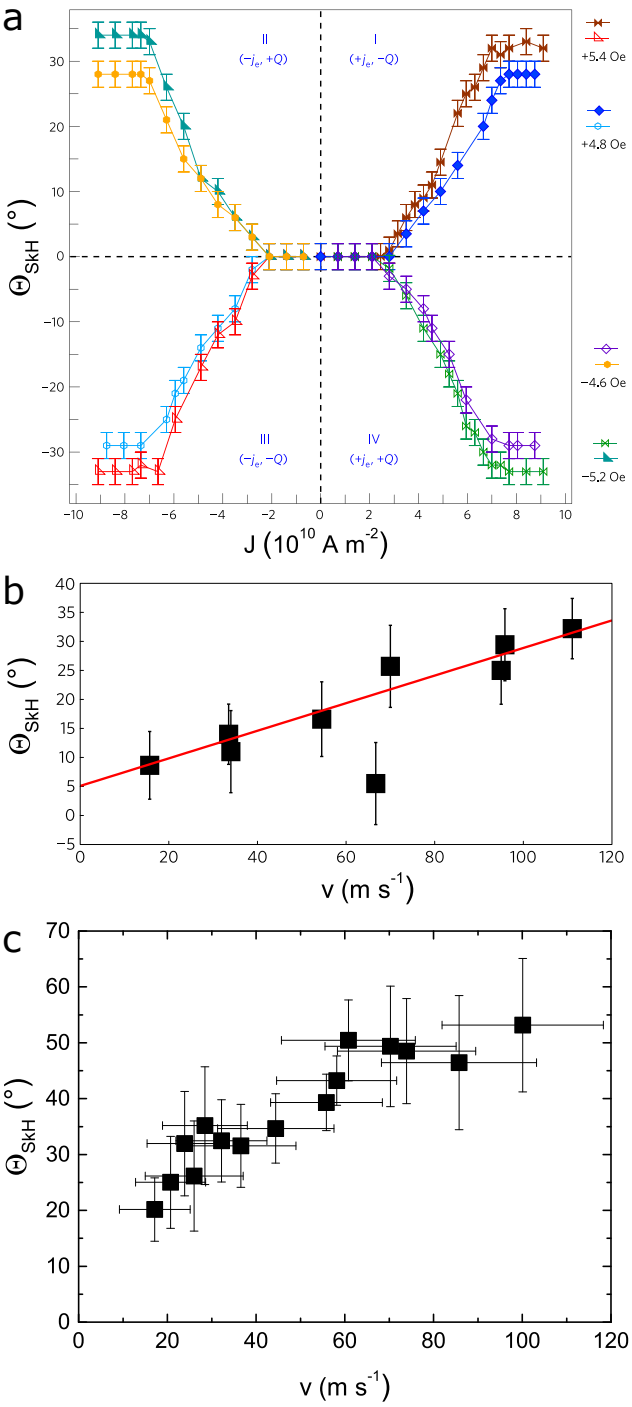

Fig. 5.18: Drive-dependent SkHE: comparison with other experiments | **a.** SkHA as a function of the current density in $Ta/Fe_{60}Co_{20}B_{20}/TaO_x$ for a skyrmion diameter $d_{sk} \approx 1$ µm and a velocity $v \approx 1$ m s^{-1}. Adapted from ref. [155]. **b.** SkHA as a function of the skyrmion velocity in $[Pt/Co_{60}Fe_{20}B_{20}/MgO]_{15}$ for $d_{sk} \approx 100$ nm. Adapted from ref. [146]. **c.** This study: SkHA as a function of the skyrmion velocity in Pt/Co/MgO for $d_{sk} \approx 100$ nm.

expected, a smaller damping is measured for thicker, and the damping ratio approximately follows an inverse Co thickness dependence. This supports the aforementioned assumption of a lower damping for $t_{Co} = 0.9$ nm (§5.4). Nonetheless, the damping extracted from the DW mobility in the field-driven steady-flow regime, $\alpha_{DW}\,(0.63\text{nm}) = 0.43$, is about three times larger than the FMR value. In a previous experimental report [208], this discrepancy was attributed to intra-layer spin-pumping effects, expected to come into play when large magnetisation gradients are present, *i.e.* DWs. Note that using the value $\alpha_{FMR}\,(0.9\text{nm}) = 0.10$ in eq. (5.5) and (5.6) would enhance the skyrmion

mobility as well as the SkHA, thus shifting the flow regime to much higher current densities/ skyrmion velocities. Assuming that a larger damping is involved in the calculation of the skyrmion velocity and the SkHA, as for DWs, provides a better agreement with the experimental result. Further experiments shall allow to test this assumption, preferentially in a low-pinning material with a clear saturation of the SkHA; for example Ta/FeCoB/TaO_x which also hosts larger skyrmions and hence does not require high-resolution microscopy. In this system, a value $\alpha_{sk} = 0.14$ can be extracted from the steady-flow SkHA [155]. For consistency, a thorough material characterisation, similar to the one presented in this chapter, must also be performed to extract an α from the dependence of the skyrmion velocity on the current density. Finally, FMR measurements performed on the same sample shall allow to compare the two values, namely α_{sk} and α_{FMR}.

5.7 Conclusions

To conclude, we studied the current-driven dynamics of 160 nm skyrmions, at RT, in a model system composed of a single-layer of Pt/Co/MgO. Velocities up to 100 m s^{-1} were obtained, which correspond to the state-of-the-art velocities measured in stray-field-coupled multilayers for skyrmions of similar size. Using a single-layer allows to lower power dissipation by one order of magnitude and to ensure a homochiral Néel skyrmion configuration, thus preventing additional complexity inherent to multilayers. Furthermore, a detailed characterisation of the film properties enables to discuss in detail the experimental results in the light of a simple analytical model based on the Thiele equation. Completing these results by micromagnetic simulations including material inhomogeneities allows to reproduce the different regimes of the dynamics, and to sort out the different effects impacting the skyrmion motion. Finally, we can conclude on the origin of the observed drive-dependence of the SkHE, that is pinning. Pinning hence appears to be the main difficulty to be overcome for the development of skyrmion-based applications.

Chapter 6

Skyrmions in synthetic antiferromagnets

6.1 Introduction: why SAFs?

Magnetic skyrmions in FM materials are by nature subject to the SkHE, which deflects them in a direction perpendicular to the driving force, *e.g.* the current direction for SOT-driven left-handed Néel skyrmions. This effect is a downside for applications such as racetrack memories since the a skyrmion will always move towards the edge of the device, which impedes their motion and can result in their annihilation. To overcome this issue, antiferromagnetic (AF) skyrmions could be utilised. An AF skyrmion can be pictured as the superimposition of two AF-coupled FM skyrmions, exhibiting the same chirality but opposite core polarity, and hence opposite topological charge. Such an AF skyrmion has a vanishing net magnetic moment, a zero topological charge and is expected to be driven along the current direction, without SkHE [157,218]. Furthermore, cancelling the dipolar interactions contribution is also predicted to be beneficial for the thermal stability of small skyrmions [117].

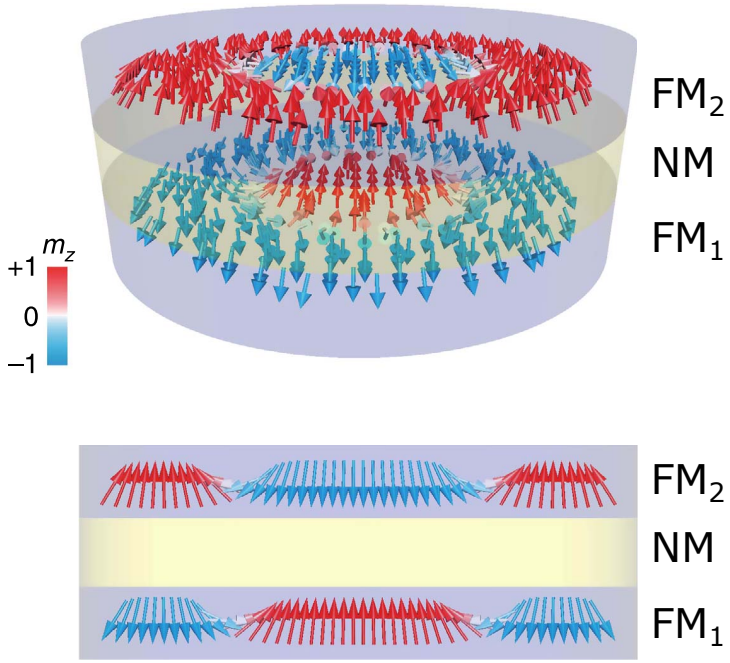

Fig. 6.1: Illustration of a SAF skyrmion | Schematics of a SAF bilayer composed of two FM layers, FM_1 and FM_2, and a NM spacer mediating an AF coupling. Both FM layers host a Néel magnetic skyrmion. The two AF-coupled skyrmions exhibit the same left-handed Néel chirality but opposite topological charge: $N_{sk} = +1$ (-1) in FM_1 (FM_2). Adapted from ref. [218].

AF skyrmions may be realised in AF materials [157] but have not been observed so far. Optimising AF materials to obtain the desired magnetic properties for their stabilisation still remains a very challenging task. In particular, the DMI has not yet been reported in AF films. Additionally, spin textures in fully compensated AFs are difficult to detect [219].

Another possibility is to employ ferrimagnets. Ferrimagnets are partially compensated AFs in which two sub-lattices carry magnetic moments aligned in opposite directions; for example Co and Gd in a Co_xGd_{1-x} alloy. Recently, magnetic skyrmions were evidenced in non-compensated ferrimagnets consisting of $[Pt/Fe_{25}Gd_{65.6}Co_{9.4}/MgO]_{20}$ [162] and $Pt/Co_{44}Gd_{56}/TaO_x$ [220]. Optimising ferrimagnetic materials to obtain the desired properties is also a challenging enterprise: the magnetisation ratio of the two sub-lattices depends critically on the temperature as well as on the alloy composition. Even if the composition is finely adjusted to reach magnetic moment compensation at room temperature, it can still be perturbed by current-induced heating.

Finally, another approach, investigated during this thesis, relies on synthetic AF (SAF) [218]. A SAF is composed of two FM layers antiferromagnetically coupled via a NM spacer, mediating a RKKY-type interlayer exchange interaction. It is typically composed of one or several repetitions of the $FM_1/NM/FM_2$ stack. In such a system, we call SAF skyrmion the spin texture represented in Fig. 6.1. It consists of two AF-coupled FM skyrmions, sharing the same chirality, here left-handed Néel type, but with opposite topological charge: $N_{sk} = +1$ (-1) for the skyrmion in FM_1 (FM_2). As a result, the gyrotropic vectors $\boldsymbol{G} \propto -M_s t N_{sk} \hat{\boldsymbol{z}}$ are opposite for each skyrmion. If the SAF is fully compensated, *i.e.* if $M_s t$ is equal for FM_1 and FM_2, the net gyrotropic vector vanishes for the bilayer skyrmion, resulting in a cancellation of the SkHE. Furthermore, theoretical studies predict that SAF skyrmions can be driven efficiently by SOTs [117] and, because the two constituent FM skyrmions are tightly bound, a moving SAF skyrmion is also expected to benefit from an enhanced thermal stability [221]. Lastly, SAF skyrmions, such as AF skyrmions in general, are expected to be insensitive to moderate external fields. This advantage for technological purposes also constitutes a challenge when it comes to their nucleation. In this chapter, we demonstrate a method to nucleate and annihilate SAF skyrmions at zero field, by using only current injection.

6.2 Design of SAF multilayers and observation of SAF skyrmions

In order to stabilise skyrmions in SAFs, different requirements must be met for the two constituent FM layers: (i) PMA; (ii) a large DMI; (iii) a strong AF coupling; (iv) the same total magnetic moment, $M_s t$, to obtain a fully compensated SAF; (v) SOTs. In addition, the DMI and the DL-SOT must have the same sign for the two skyrmion to be driven in the same direction.[1] Note that the two constituent FM layers can be composed either of the same or different materials. Here, we chose to use different materials. This was motivated by the use of X-ray microscopy that allows to probe a specific element by tuning the X-ray energy on a specific absorption edge, as explained in §3.3. Therefore, even if the net magnetisation vanishes in a compensated SAF, it is possible to image the magnetisation texture in only one constituent FM.

We designed SAFs with the following structure: $Pt(0.5)/FM_1/Ru(0.85)/Pt(0.5)/FM_2/Ru(0.85)$, where $FM_1 = Co(0.3)/Ni_{80}Fe_{20}(t_{NiFe})/Co(0.3)$ and $FM_2 = Co(t_{Co})$ (thicknesses in nm). Both FM_1 and FM_2 are deposited on Pt to exploit the PMA and DMI originating from the Pt/Co interface. The Ru spacer is inserted to induce an RKKY coupling between FM_1 and FM_2 [182]. We chose $t_{Ru} = 0.85$ nm to reach the maximum AF coupling, according to the optimisation performed on exchange-biased films (see §4.4). The Co/Ru interfaces in turn enhance the PMA. As suggested by recent studies, they may also contribute to the net DMI by adding to that of Pt/Co [37,38].

The material stacks for the two constituent FM layers, $Pt/FM_2/Ru$ and $Pt/FM_1/Ru$, are represented in Fig. 6.2.a and 6.2.b respectively. In Fig. 6.2.c the material stack for the SAF with $t_{Co} = 1.35$ nm is represented. For each sample, the buffer layer (Buff.) consists of Ta(3)/Pt(2.5). Each FM was tuned close to the spin reorientation transition. Fig. 6.2.d-f show the OOP hysteresis

[1] For example, if $D > 0$ and $\Theta_{SH} > 0$ (as in Pt/Co), both FM skyrmion exhibit a left-handed Néel chirality and are driven along the current direction.

loops measured by MOKE in these three samples. In Fig. 6.2.d, t_{Co} is varied between 1.25 nm and 1.40 nm on different (non-wedged) samples and the loops display the gradual transition from PMA to IP anisotropy. In Fig. 6.2.e, the $Ni_{80}Fe_{20}$ layer (hereafter NiFe) is deposited as a wedge with $t_{NiFe} = 0.76 - 1.55$ nm. Here also, the loops display the gradual transition from PMA to IP anisotropy and, for $t_{NiFe} = 1.32$ nm, a reversal characteristic of a multi-domain state is observed.

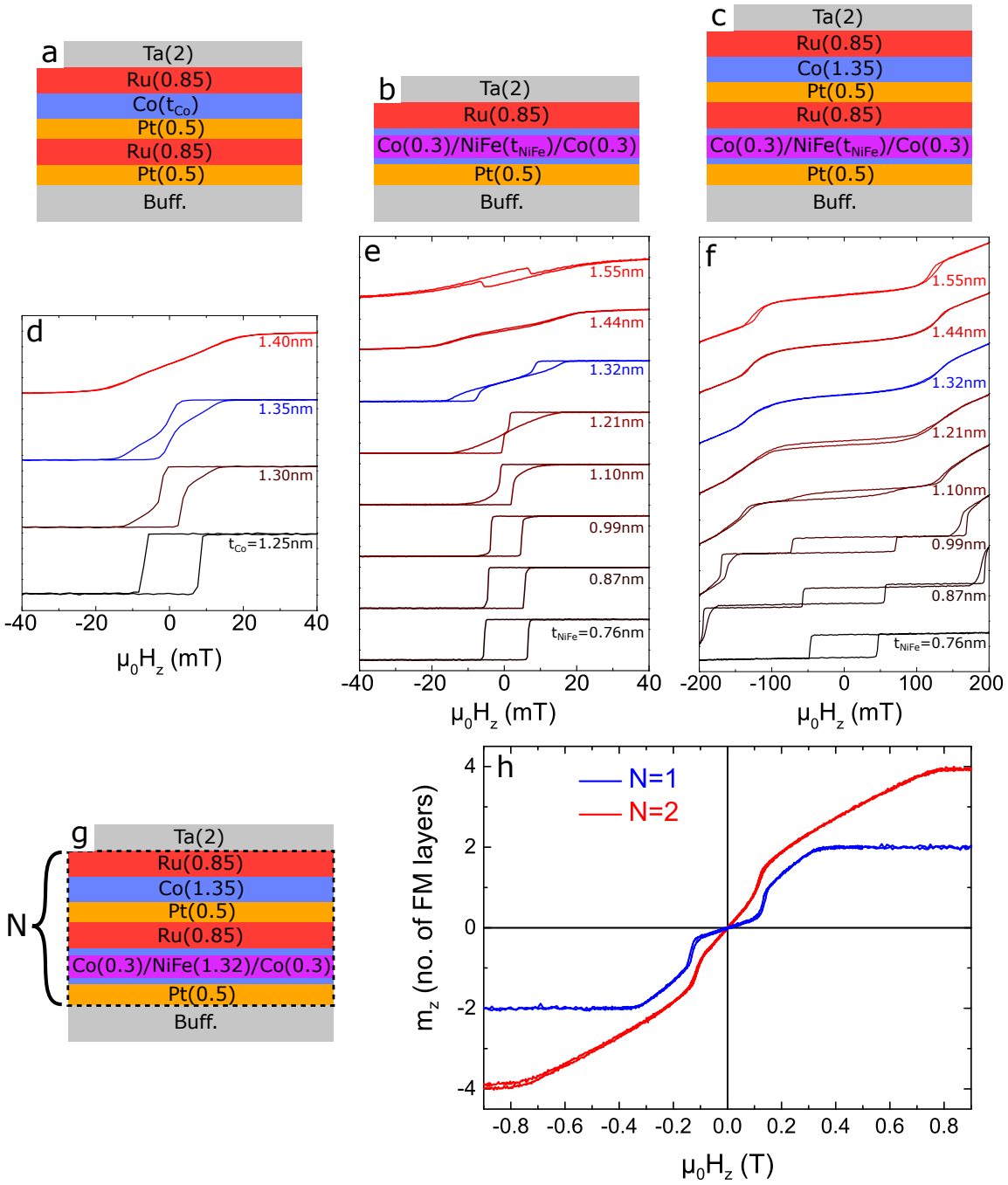

Fig. 6.2: Optimisation of compensated SAF multilayers | **a,b.** Material stacks for the constituent FM layers, **a.** $Pt/FM_2/Ru$ and **b.** $Pt/FM_1/Ru$, with $FM_2 = Co(t_{Co})$ and $FM_1 = Co(0.3)/Ni_{80}Fe_{20}(t_{NiFe})/Co(0.3)$ (thicknesses in nm). **c.** Material stack for the SAF, $Pt/FM_1/Ru/Pt/FM_2/Ru$, with $t_{Co} = 1.35$ nm. Buff. denotes Ta(3)/Pt(2.5). The NiFe layer in **b** and **c** is deposited as a wedge. **d-f.** OOP MOKE hysteresis loops measured in the above stacks. The loops in **d** correspond to different (non-wedged) samples. In **e** and **f**, each loop is measured at positions 10 mm apart on the wedge. **g.** Material stack for the multi-layered SAF, $[Pt/FM_1/Ru/Pt/FM_2/Ru]_N$, with $t_{NiFe} = 1.32$ nm and $t_{Co} = 1.35$ nm. **h.** VSM hysteresis loop measured in **g** for different N. The signal is normalised and multiplied by the total number of constituent FM layers ($2N$).

Fig. 6.2.f shows the loops for the SAF with $t_{Co} = 1.35$ nm at different locations on the NiFe wedge. These loops exhibit two reversals, characteristic of AF RKKY coupling of perpendicularly magnetised layers. The amplitude of the central hysteresis, clearly visible for $t_{NiFe} \leq 1.10$ nm, is proportional to the net magnetic moment. Upon increasing the NiFe thickness, this amplitude decreases and eventually vanishes for $t_{NiFe} = 1.32$ nm, indicating magnetic moment compensation. This is accompanied by a widening of the central hysteresis, consistently with the diminution of the net magnetic moment. Note that the thickness of the Co layers surrounding the NiFe (0.3 nm) was chosen so that the spin reorientation transition of FM_1 matches that of FM_2. It also allows to increase the magnetisation of FM_1 to match that of FM_2, since M_s (NiFe) $< M_s$ (Co). The second reversal is followed by a constant-susceptibility region, corresponding to spin-flop processes, characteristic of SAFs with weak anisotropy [182,222]. Note that the OOP saturation is not reached due to the limited applicable field with the MOKE set up. It will appear on the VSM loop as detailed below. The field at which this spin-flop transition occurs decreases with increasing NiFe thickness, as a result of the weakening of the anisotropy and of the RKKY coupling [222].

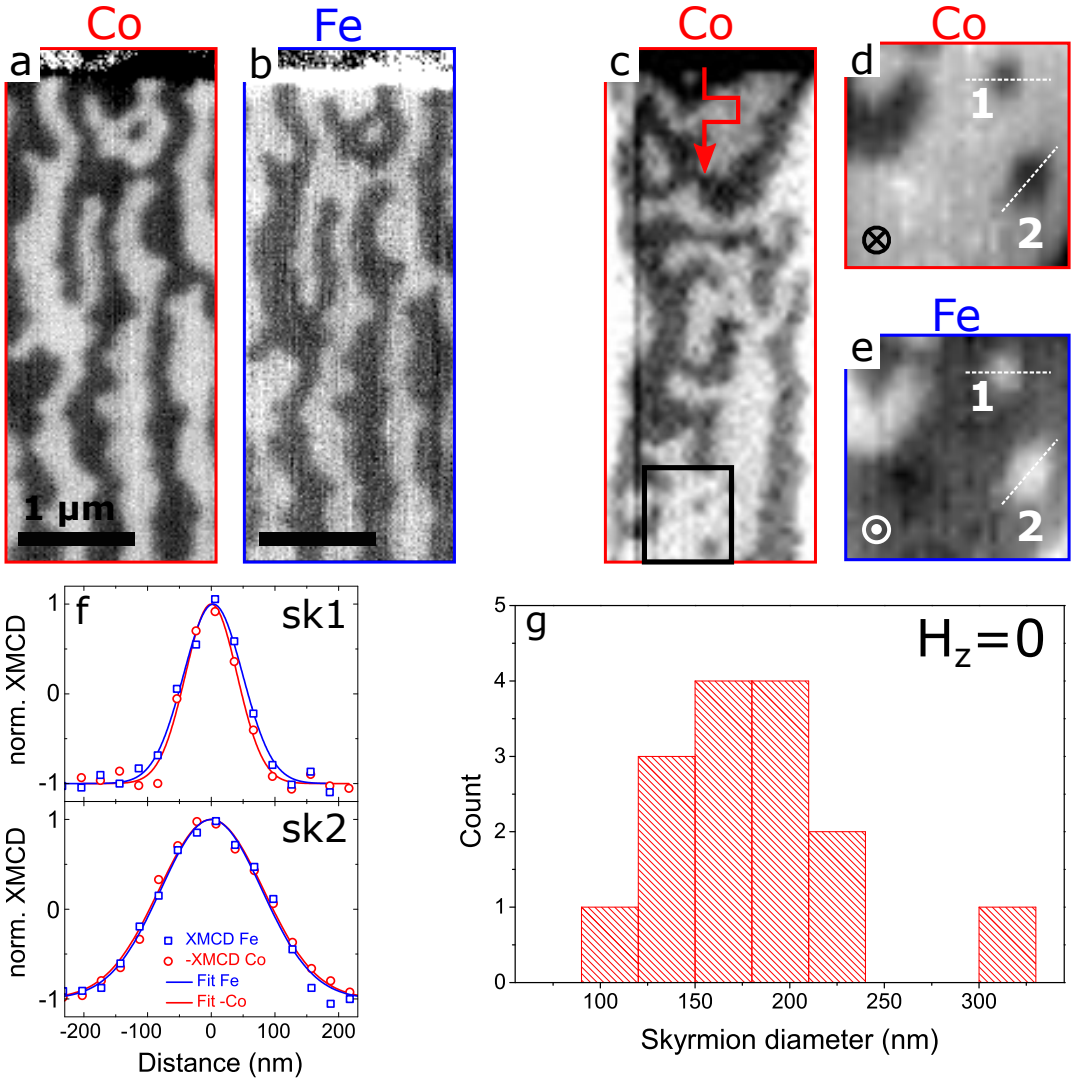

Fig. 6.3: Observation of SAF skyrmions | **a,b.** XMCD-STXM images acquired at **a.** the Co L_3 and **b.** the Fe L_3 absorption edges after OOP demagnetisation. **c.** XMCD-STXM image after injection of a 1 ns current pulse of amplitude $J = 5.8 \times 10^{11}$ A m^{-2}. **d,e.** XMCD-STXM images acquired at **d.** the Co and **e.** the Fe edge in the area of **c** delimited by a black rectangle. **f.** Normalised XMCD signal obtained from line-scans along the white dashed line in **d** and **e**. The signal for Co is inverted. The solid lines are Gaussian fits. **g.** Distribution of skyrmion diameters. All images were acquired at RT and at zero field.

As mentioned above, we used X-ray microscopy to probe a specific constituent FM layer. More precisely, we used STXM, which measures the absorption of X-ray light transmitted through the entire stack (see §3.3.3). A larger amount of magnetic material results in a larger X-ray absorption and therefore in an enhanced contrast. For this reason, we deposited a multi-layered SAF, consisting of $[\mathrm{Pt/FM_1/Ru/Pt/FM_2/Ru}]_N$ with $t_{NiFe} = 1.32$ nm and $t_{Co} = 1.35$ nm, as represented in Fig. 6.2.g. Fig. 6.2.h displays the OOP hysteresis loops measured by VSM for $N = 1$ and $N = 2$. The signal was normalised then multiplied by the total number of constituent FM layers ($2N$). For $N = 1$, the saturation is now clearly visible at $\mu_0|H_z| = 340$ mT. The loop for $N = 2$ also exhibits a vanishing magnetic moment at zero field, characteristic of compensated SAFs. Here, while the spin-flop transition occurs at the same field for all N, the saturation field is larger for $N = 2$ than for $N = 1$, as expected for multi-layered SAFs with weak anisotropy [222].

We now look at the magnetisation texture in these compensated SAFs, using STXM for its element-sensitivity. The stack of Fig. 6.6.g with $N = 2$ was deposited on both a Si substrate (reference sample of Fig. 6.2.h) and on a 100-nm-thick Si_3N_4 membrane for STXM experiments (see §3.3.3). The film deposited on the membrane was then patterned into 2-µm-wide tracks contacted by Ti(10nm)/Au(100nm) pads using the process described in §3.4. Fig. 6.3.a and 6.3.b. show two XMCD-STXM images acquired at the Co L_3 and Fe L_3 absorption edges. They were recorded at zero external magnetic field after demagnetisation performed by the application of a decaying, alternating OOP field. For reminder, an XMCD-STXM image is calculated as the difference between two STXM images acquired with circular left and circular right X-ray polarisations (§3.3.1). It hence displays only the magnetic contrast, which is proportional to m_z since the beam is normal to the sample surface.

The images of Fig. 6.3.a and 6.3.b display worm-like domains as well as a magnetic skyrmion. They further reveal that the magnetic contrast is opposite at the Co and Fe edges. At the Fe edge, the magnetic contrast originates purely from $\mathrm{FM_1}$. At the Co edge, it originates from $\mathrm{FM_1}$ and $\mathrm{FM_2}$ as both layers contain Co. However, the Co thickness is larger in $\mathrm{FM_2}$ (1.35 nm) than in $\mathrm{FM_1}$ (0.6 nm) (see Fig. 6.2.g). Consequently, the absorption — hence the XMCD — at the Co edge is larger in $\mathrm{FM_2}$. The magnetic contrast observed at the Co edge therefore provides the magnetic state in $\mathrm{FM_2}$, confirming that the domains in $\mathrm{FM_1}$ and $\mathrm{FM_2}$ are AF coupled.

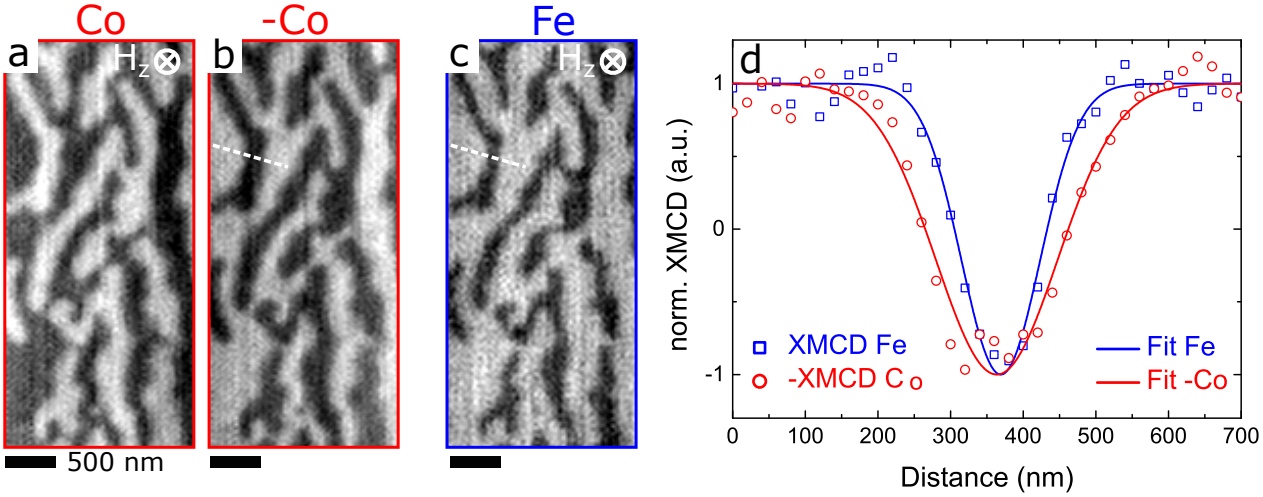

Fig. 6.4: Effect of the external field | **a.** XMCD-STXM image acquired at the Co edge in the presence of an external magnetic field $\mu_0 H_z = -50$ mT. **b.** Same image with inverted contrast. **c.** Same image at the Fe edge. **d.** Normalised XMCD signal obtained from the line-scans along the white dashed lines in **b** and **c**. The solid lines are Gaussian fits.

Fig. 6.3.c shows the same track (at the Co edge) after injection of a 1 ns current pulse of amplitude $J = 5.8 \times 10^{11}$ A m^{-2}. The current injection leads to domain and skyrmion nucleation, most probably caused by the heating of the track. Fig. 6.3.d and 6.3.e show two XMCD-STXM images acquired respectively at the Co L_3 and Fe L_3 absorption edges in the area of Fig. 6.3.c

displaying two skyrmions. To emphasise this AF coupling, we plot in Fig. 6.3.f the XMCD contrast acquired along the white dashed lines (open symbols). Due to the small skyrmion sizes and the limited resolution of the instrument, the XMCD, proportional to m_z, is best fitted by a Gaussian (solid lines). For comparison purposes, the signal for Co is inverted and both signals are normalised using the maximum and minimum obtained from the fit. Note that the drift between the two acquisitions was corrected from larger images using a structural (*i.e.* non-magnetic) defect. Fig. 6.3.f reveals that both signals superimpose accurately, within the resolution limit of the instrument, confirming that these magnetic textures are SAF skyrmions. These plots allow in turn to extract their diameter, from the full width at half maximum: $d_{sk1} = 90$ nm and $d_{sk2} = 160$ nm. By repeating the same procedure, several skyrmions were nucleated. The histogram of Fig. 6.3.g shows the diameter distribution, with average $d_{sk} = 180 \pm 49$ nm, the error being the standard deviation. This falls within the typical size range of FM skyrmions in Pt/Co-based systems.

It is noteworthy that, unlike FM materials, the external field cannot be used to nucleate skyrmions in SAFs. Applying a field results in non-compensated magnetic moments, as it can be seen from the non-zero susceptibility in the hysteresis around $H_z = 0$ (see Fig. 6.2.h). To emphasise this, Fig. 6.4.a shows a XMCD-STXM image acquired at the Co edge in the presence of an external field $\mu_0 H_z = -50$ mT, which promotes white contrast. Fig. 6.4.b shows the same image with inverted contrast and Fig. 6.4.c the image acquired at the Fe edge. By comparing Fig. 6.4.b and 6.4.c, we clearly see that the ratio of up and down domains is different in FM_1 and FM_2. This is highlighted in Fig. 6.4.d which displays the XMCD contrast acquired along the white dashed lines in Fig. 6.4.b and 6.4.c. The width of the domain scanned is found to be 197 nm in FM_2 (Co) and 128 nm in FM_1 (Fe). The SAF is therefore not compensated any more, in contrast with the zero-field situation.

To conclude, these experiments demonstrate the existence of stable, zero-field, room-temperature skyrmions in compensated SAFs.

6.3 Chiral DWs and skyrmions in a compensated SAF

In STXM experiments, only the OOP component of the magnetisation is accessible. To determine the chirality of the observed spin textures, we performed X-PEEM experiments on a compensated SAF bilayer deposited on a high-resistivity Si wafer. Fig. 6.5.a shows the OOP hysteresis loop measured by VSM, which exhibits a very similar trend as the sample of Fig. 6.2.h ($N = 1$). Fig. 6.5.b shows an XMCD-PEEM image acquired at the Co L_3 absorption edge and at zero external field. It displays alternate up/down domains as well as an isolated skyrmion of diameter $d_{sk} \approx 160$ nm. In Fig. 6.5.c, we plot the XMCD contrast measured along the X-ray beam along the white dashed line in Fig. 6.5.b. Since the contrast is proportional to the projection of the X-ray

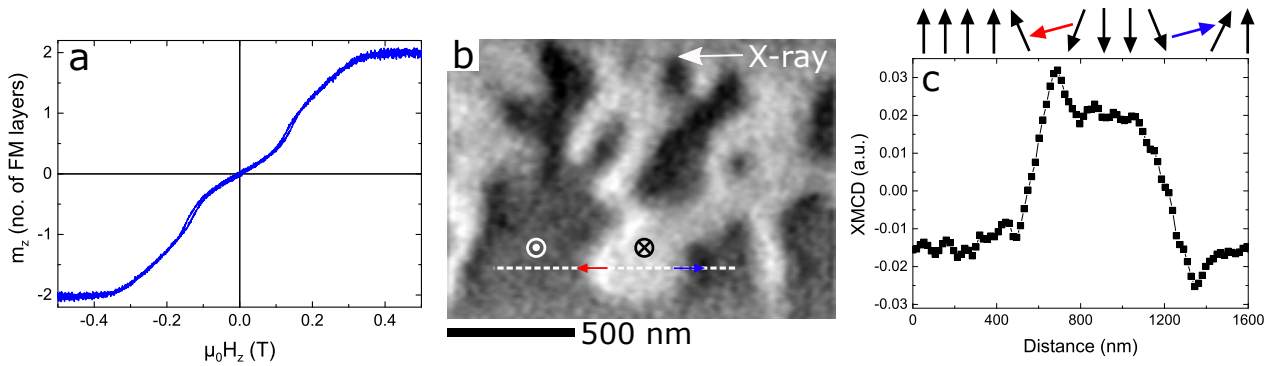

Fig. 6.5: Chiral DWs and skyrmion in a compensated SAF | **a.** OOP hysteresis loop measured by VSM on a compensated SAF with two constituent FM layers. **b.** XMCD-PEEM image acquired at the Co L_3 absorption edge and at zero external magnetic field. **c.** Line-scan of the XMCD contrast along the X-ray beam direction indicated by the white dashed line in **a**.

beam direction on the magnetisation (§3.3.2), we choose DWs perpendicular to the X-ray beam. The XMCD contrast exhibits the typical maximum and minimum corresponding respectively to a magnetisation parallel and anti-parallel to the beam. Hence, the magnetisation rotates according to ↑←↓→↑, which is the signature of a left-handed Néel DW. This strong white/black contrast is not observed for DWs perpendicular to the beam direction, which further supports that the DWs are of Néel type. This left-handed Néel character is consistent with the sign of the DMI in both constituent FM layers, as dictated by the Pt/Co interfaces. Note that the photo-emission at the Fe or Ni edge was too weak to allow imaging the spin texture in FM_1. The NiFe layer is actually buried under ≈ 6 nm of material, which prevents the photo-electrons from being extracted, further motivating the choice of STXM to image SAF spin textures. Nevertheless, the AF coupling, clearly visible from the hysteresis loop (Fig. 6.5.a), promotes DWs of the same chirality in both constituent FM layers so one can reasonably expect left-handed Néel spin textures in the NiFe layer as well.

6.4 Controlled current-induced nucleation/annihilation of SAF skyrmions

In the experiments presented in the above, we saw that the high density of domains makes difficult the nucleation of isolated skyrmions, especially because the external field cannot be utilised. In the present section, we explore another approach to locally nucleate skyrmions using ns current pulses. For this purpose, we optimised SAF multilayers with larger anisotropy, in order to obtain a uniformly magnetised state at zero field.

The material stacks for the two constituent FM layers and for the SAF bilayer are shown in Fig. 6.6.a, 6.6.b and 6.6.c respectively. Fig. 6.6.d-f display the OOP hysteresis loops measured by MOKE in these three samples. Here, $Pt/FM_2/Ru$ exhibits full remanence due to the smaller Co thickness (0.9 nm), while $Pt/FM_1/Ru$ is kept close to the spin reorientation transition by reducing the thickness of the Co layers in contact with the NiFe to 0.2 nm. Fig. 6.6.f shows the loop for the SAF bilayer ($N = 1$). Note that here also, the NiFe layer is deposited as a wedge. Only the loops measured at a position corresponding to $t_{NiFe} = 0.95$ nm, for which the compensation is reached, are shown.[1] Fig. 6.6.f reveals that the magnetisation reversals are sharper, owing to the larger anisotropy.

For STXM experiments, we deposited SAF multilayers consisting of $[Pt/FM_1/Ru/Pt/FM_2/Ru]_N$ (Fig. 6.6.g). The OOP hysteresis loops measured by VSM for different N are shown in Fig. 6.6.h, wherein the signal is again expressed in units of the total number of constituent FM layers ($2N$). These loops exhibit a vanishing magnetic moment and zero susceptibility to the field in the central plateau region, which is characteristic of uniformly magnetised, compensated SAFs. For $N = 1$, only one reversal exists, which defines the interlayer exchange field $\mu_0|H_{RKKY}| = 200$ mT. For $N > 1$, an additional reversal appears at $|H_z| = 2H_{RKKY}$. It corresponds to the reversal of the internal FM layers, *i.e.* all but the top-most and bottom-most FM layers: since each internal FM layer is AF-coupled on both sides (below and above), twice the external field is required to switch their magnetisation [223]. This can be seen from the amplitude of the different plateaus in Fig. 6.6.h: for $H_{RKKY} < |H_z| < 2H_{RKKY}$, the net magnetisation is $|m_z| = 2$, independently of N, while $|m_z| = 2N$ at saturation ($|H_z| \gg 2H_{RKKY}$). This means that $(N - 1)$ layers have switched between the two plateaus.

We then performed STXM experiments on this compensated SAF. The stack of Fig. 6.6.g with $N = 12$ was deposited on both a Si substrate (reference sample) and a Si_3N_4 membrane. The loop of Fig. 6.6.h ($N = 12$) was measured by VSM on the reference sample at the location of the membrane. The sample deposited on the membrane was then patterned into 2-µm-wide tracks with Ti(10nm)/Au(100nm) contact pads. In addition, a triangular-shaped injection tip, consisting of Ti(10nm)/Au(100nm), was patterned at one end of the track for skyrmion nucleation (§3.3.3).

[1] The apparent net magnetic moment in Fig. 6.6.f is probably an artefact due to the depth-sensitivity of the MOKE or because the maximum applicable field does not suffice to fully saturate the SAF. The VSM loop (Fig. 6.6.h, $N = 1$), which provides a measurement of the total moment, confirms that the SAF is compensated.

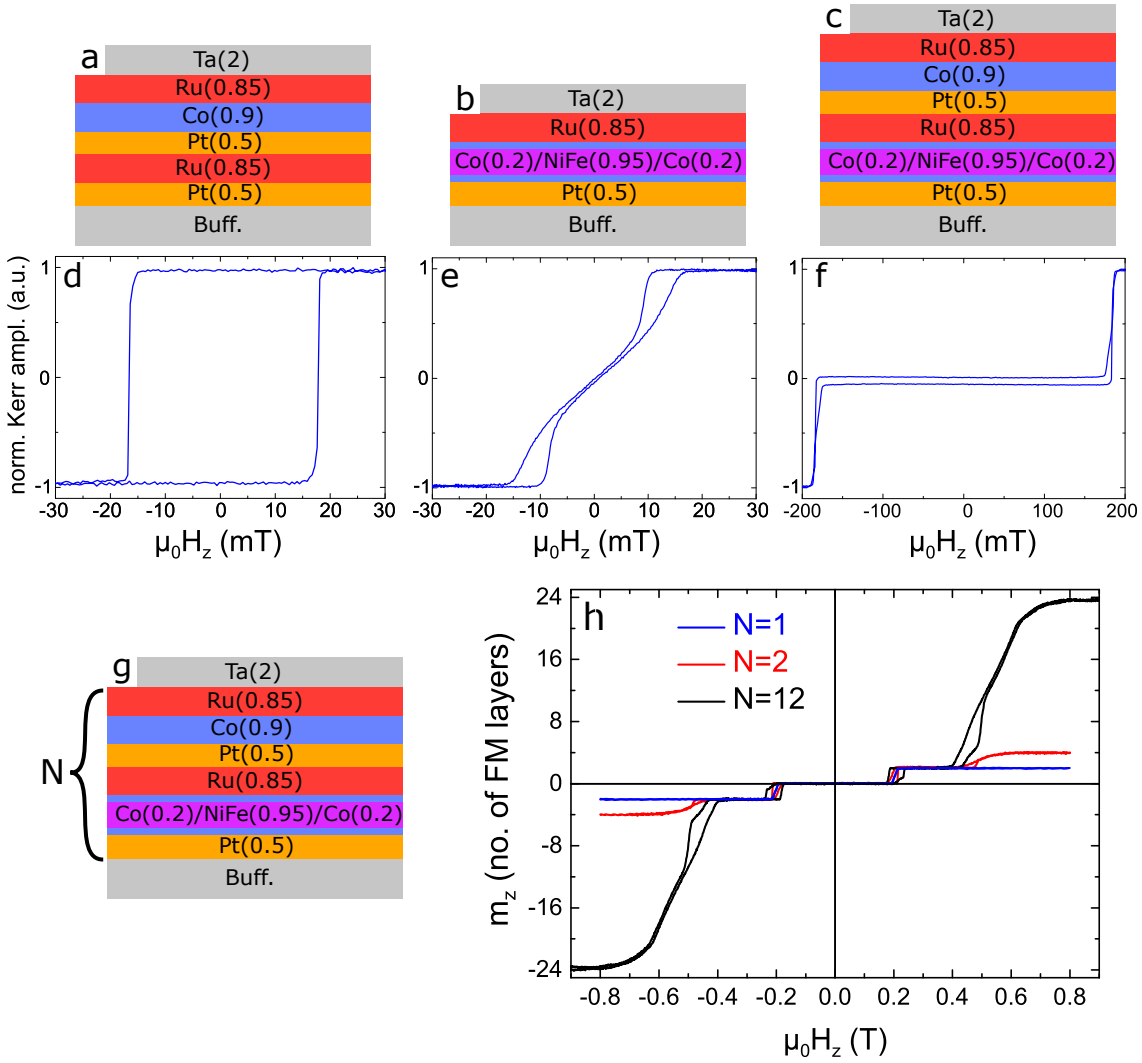

Fig. 6.6: Compensated SAF multilayers with large PMA | **a,b.** Material stacks for the constituent FM layers, **a.** Pt/FM_2/Ru and **b.** Pt/FM_1/Ru, with FM_2 = Co(0.9) and FM_1 = Co(0.2)/$Ni_{80}Fe_{20}$(0.95)/Co(0.2) (thicknesses in nm). **c.** Material stack for the SAF, Pt/FM_1/Ru/Pt/FM_2/Ru. Buff. denotes Ta(3)/Pt(2.5). **d-f.** OOP MOKE hysteresis loops measured in the above stacks. **g.** Material stack for the multi-layered SAF. **h.** VSM hysteresis loops measured for different N. The signal is normalised and multiplied by the total number of constituent FM layers ($2N$).

Firstly, we image the magnetisation texture. Fig. 6.7.a shows a STXM image of a track acquired at the Co edge and at zero external field, that displays a uniformly magnetised state. Fig. 6.7.b shows the same track after injection of multiple 10 ns current pulses with $J \approx 10^{12}$ A m^{-2}, leading to random nucleation of domains, most likely caused by the heating of the track. Fig. 6.7.c and 6.7.d show two XMCD-STXM images of a skyrmion acquired respectively at the Co and Fe absorption edges in the area marked with a rectangle in Fig. 6.7.b. It points out the AF coupling between FM_1 and FM_2 as explained previously, which is emphasised in the plot of the XMCD contrast in Fig. 6.7.e (open symbols). Here, due to the larger size of the skyrmion, the signal, proportional to m_z, is best fitted by a 360° Bloch DW profile (solid lines). Both signals superimpose very accurately, confirming the SAF character of the nucleated spin textures. Note that the effects observed in stray-field-coupled FM multilayers such as hybrid chiralities [141–143] are not expected is SAFs since the stray fields emanating from two adjacent FM layers compensate.

Starting from a uniformly magnetised track, after OOP saturation with an external field ($\mu_0 H_z \approx$ 400 mT), we now look closely at the local current injection through the tip. In Fig. 6.8.a-g, a sequence of images acquired at zero field shows the skyrmion nucleation/annihilation process.

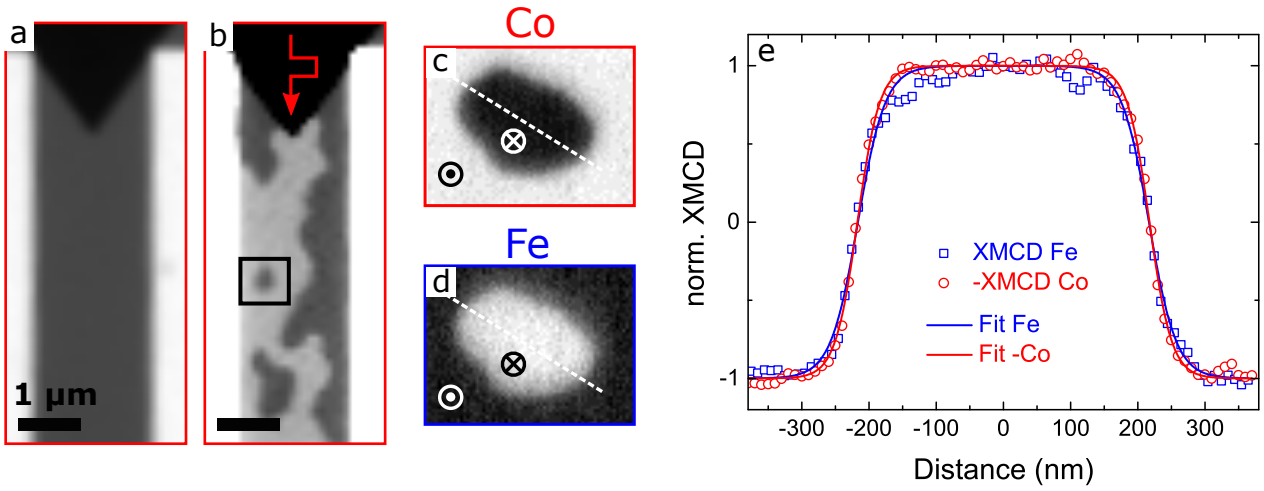

Fig. 6.7: Observation of SAF skyrmions (large PMA) | **a.** STXM image of a 2-µm-wide at the Co edge.**b.** Same image after injection of multiple 10 ns current pulses of amplitude $J \approx 10^{12}$ A m^{-2}. **c,d.** XMCD-STXM images acquired at **c.** the Co and **d.** the Fe edges in the area of **b** delimited by a rectangle. **e.** Normalised XMCD signal obtained from the line-scans along the white dashed lines in **c** and **d**. The signal for Co is inverted. The solid lines are fit with a 360° Bloch DW profile. All images were acquired at RT and at zero field.

Before each image, a single 5 ns current pulse of amplitude $J = 6.2 \times 10^{11}$ A m^{-2} is injected. Here, $\boldsymbol{J} = J\hat{\boldsymbol{x}}$ denotes the direction of the current, that is opposite to the electron flow. For $J > 0$, a skyrmion is injected in the track below the gold tip. Upon reversing the current direction ($J < 0$), the skyrmion is annihilated. This is highlighted in Fig. 6.8.h which displays the skyrmion diameter measured in the images above: $d_{sk} \approx 420$ nm. This process was found to be quite reproducible. In addition, it was found to be independent of the initial direction of the magnetisation, in line with recent experiments in FM multilayers [224]. Note that below this current density, no nucleation was observed, regardless of the current direction. However, increasing the pulse length to 10 ns leads to the nucleation of a multi-domain state similar to the one shown in Fig. 6.7.b, most likely caused by

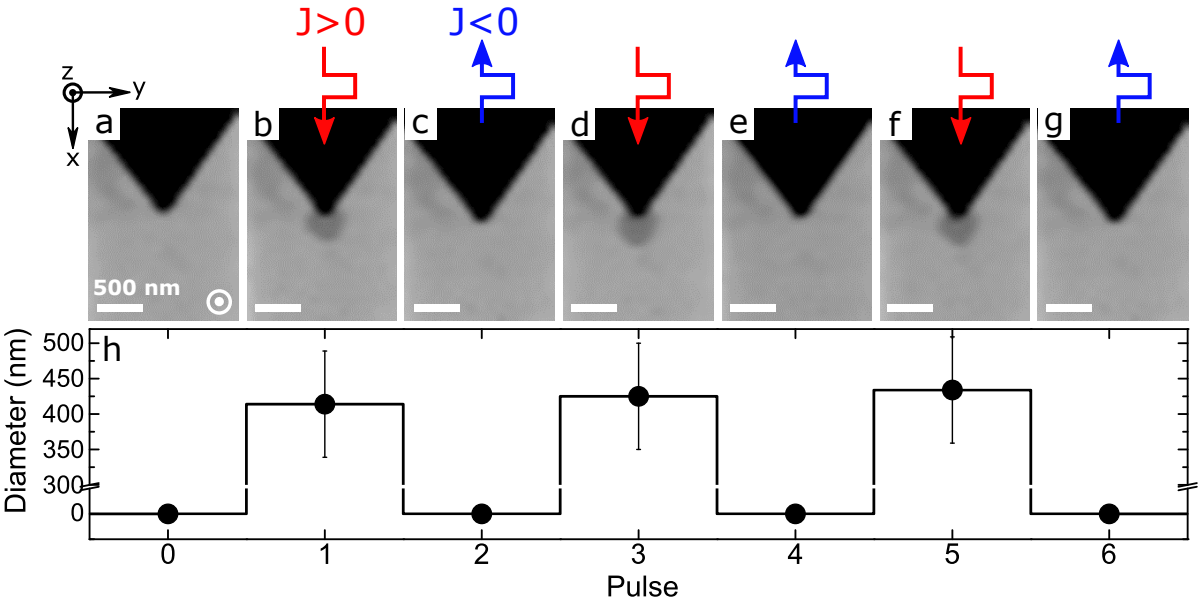

Fig. 6.8: Current-induced nucleation/annihilation of SAF skyrmions | **a-g.** Sequence of STXM images acquired at the Co edge. Before each acquisition, a single 5 ns current pulse with $J = 6.2 \times 10^{11}$ A m^{-2} is injected in the direction indicated by the red and blue arrows. **h.** Skyrmion diameter measured in the above images. The solid line is a guide for the eye.

the heating of the track. Note that, starting from a nucleated skyrmion, the injection of another pulse with $J > 0$ does not result in its annihilation but rather in its expansion as it is driven by the diverging current lines. On the contrary, when injecting a current pulse with $J < 0$, the skyrmion is pushed towards the tip, eventually resulting in its annihilation.

These experiments demonstrate that local current injection through patterned tips can be used to nucleate skyrmions in compensated SAFs.

6.5 Conclusions and perspectives

In this chapter, we saw the foreseen advantages of SAF skyrmions, in particular the cancellation of the SkHE. By designing compensated SAFs composed of two different FM materials, Co and $Ni_{80}Fe_{20}$, we observed SAF spin textures using element-sensitive STXM. These experiments revealed SAF skyrmions with diameters in the range of 100 nm at zero field. Further, X-PEEM experiments confirmed the left-handed Néel character of these SAF spin textures. As the skyrmion nucleation in SAFs is challenging, particularly because external fields cannot be employed, we then studied the potential of local current injection. By designing injection tips, we showed the controlled nucleation and annihilation of skyrmions in an otherwise uniformly magnetised track. The possibility to nucleate skyrmions by using purely current injection in compensated SAFs offers very promising perspectives for future applications.

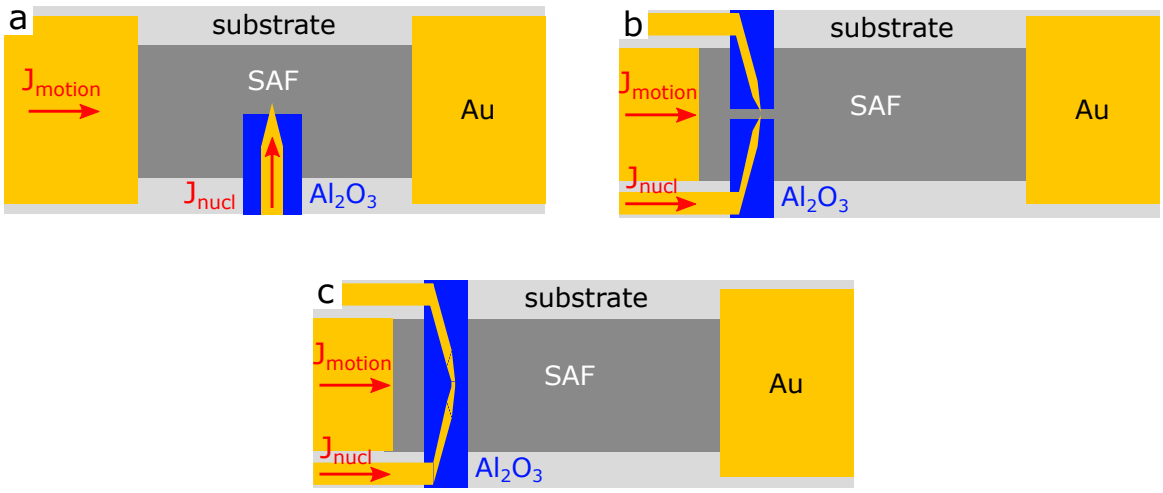

Fig. 6.9: Proposed designs for SAF tracks with integrated skyrmion injector | **a.** Device with two contact pads for the motion and an injection tip. **b.** Here, two injection tips converge in a small area. **c.** Same as **b** but the injection tips are connected and isolated from the track to exploit only the heating effect when a current flows through the narrow constriction.

Nevertheless, the geometry employed was not optimised to study the skyrmion motion. Because the current flows perpendicular to the film plane through the injector, one edge of the nucleated skyrmion remained tied to the tip. To overcome this issue and to achieve both skyrmion nucleation and motion in the same device, we propose different designs: in Fig. 6.9.a, a relatively simple 3-contact device combines the injection tip employed in the experiments presented above with two contact pads for the skyrmion motion. The injector must be isolated from the SAF track by an insulator (*e.g.* Al_2O_3) to ensure that the current flows through the tip, perpendicular to the film. In Fig. 6.9.b, another geometry is shown. Here, two injection tips converge in a small area, which may allow a better control of the skyrmion size by preventing the current lines from diverging. It would also allow to reduce the writing power, as the resistance for the writing path is significantly lower than in the previous device. Lastly, Fig. 6.9.c shows an alternative design to that of Fig. 6.9.b. Here, two injection tips are connected and isolated from the SAF track by an insulator. This would generate a 'hot spot' to nucleate skyrmions by pure heating, without passing current through the magnetic stack.

Finally, note that Legrand *et al.* [225] very recently reported the observation of SAF skyrmions in Pt/Co/Ru/Pt/Co/Ru, using a different approach. In their experiments, a SAF with vanishing anisotropy was deposited on a bias layer (BL), similar to the one used in §4.4, to bias one constituent FM. Although this method allows to nucleate isolated skyrmions in compensated SAFs, it does not seem suitable for their current-driven motion, because a significant part of the current would flow in the BL. Exploiting the exchange at the interface between one constituent FM and an insulating AF [186] such as NiO [219] may allow to overcome this limitation.

Chapter 7

Summary and perspectives

7.1 Summary

Here is a brief summary of some of the important concepts and results of this thesis. We have seen that magnetic skyrmions offer promising perspectives for future memory and logic applications and that trilayer systems with SIA consisting of HM/FM/NM combine several key features for the manipulation of magnetic skyrmions at RT. In particular, Pt/Co-based systems, that have been used throughout this work, combine PMA, a large DMI and SOTs, which constitute some of the essential ingredients to achieve stable, RT skyrmions and for their efficient current-induced manipulation. At the beginning of this work, magnetic skyrmion had just been observed at RT both in single- and multi-layered HM/FM/NM systems [48,109–111], and notably in Pt/Co/MgO at Spintec [48]. At that time, the primary objective was to study their current-driven dynamics as it is one crucial functionality for future skyrmion-based devices. In parallel, several studies were conducted to engineer magnetic skyrmions in ultra-thin films.

In Chapter 4, I presented different experimental approaches to realise magnetic skyrmions in ultra-thin Pt/Co/MgO films at RT. First in extended films, lowering the effective anisotropy close to the spin reorientation transition by tuning the Co thickness allows to nucleate labyrinthine worm domains, which can be shrunk into isolated magnetic skyrmions upon applying an external, OOP magnetic field. We then saw that the skyrmion stability can be tuned by confining them in different geometries: dots (confined in all directions) and tracks (confined in one direction only). The study of the skyrmion size in dots notably unveiled the intricate role of pinning in determining its field-dependence, which can be well accounted for by considering a granular film with local anisotropy fluctuations [173]. When not confined in all directions, as in dots, the stabilisation of isolated skyrmions almost always requires the presence of an external field, which constitutes an evident limitation for applications. In this context, we investigated an alternative approach to integrate the field within the magnetic stack, by exploiting the AF coupling between a Pt/Co/MgO stack designed to host and a bias layer, via a Ru spacer. By gradually changing the Ru thickness, we observed the transition from worm domains to isolated skyrmions, as in extended films, only without assistance from an external field. Lastly, we explored the potential of ion-patterning to induce skyrmion stability. In all the aforementioned experiments, the position of magnetic skyrmions was hardly controllable. Using a focused He^+ ion beam to locally modify the anisotropy, we showed that skyrmion arrays can be nucleated and their position finely controlled in a film where they were not originally stable.

In Chapter 5, I presented a detailed study of the current-driven skyrmion dynamics in an ultra-thin Pt/Co/Co film. We measured velocities up to 100 m s^{-1} for skyrmion sizes in the range of 100 nm and observed that the SkHE, a signature of the skyrmion topology, is markedly dependent on the velocity, in contrast with the prediction of analytical models. This study combines the homogeneous chiral spin texture and low power dissipation of single-layer films with small skyrmion sizes and large velocities. This constitutes a step forward compared to multilayers by limiting power consumption and by preventing stray-field-related effects that may lead to the stabilisation

of hybrid-chirality spin textures with complex motion. Supported by a complete characterisation of the film properties, including the measurement of the SOTs governing the dynamics as well as the magnetic damping, the experimental results were accurately compared to the predictions of the Thiele model, revealing a good agreement at large skyrmion velocities. Finally, micromagnetic simulations including notably material inhomogeneities allowed to sort out the different effects that may impact the skyrmion dynamics and in particular to rule out the effect of the FL-SOT, thus clearly identifying pinning as sole responsible for the velocity-dependence of the SkHE [226].

In Chapter 6, the conception of SAF skyrmions, foreseen to exhibit SkHE-free motion, was investigated experimentally. We designed compensated SAF multilayers comprising different FM materials and, using element-sensitive STXM, we observed SAF skyrmions with diameter in the range of 100 nm. The left-handed Néel character of these SAF spin textures was further revealed by X-PEEM. While the first experiments relied on random current-assisted nucleation, we then explored another approach to nucleate skyrmions in a controlled fashion using local current injection through patterned tips. Starting from a uniformly magnetised state in a compensated SAF at RT, we showed that magnetic skyrmions can be reproducibly nucleated and annihilated, in the absence of external field. These last results open up new prospects for achieving RT skyrmion-based devices beyond the conventional FM skyrmions.

7.2 Perspectives

In the continuity of this work, different possibilities for future developments and improvements can be foreseen.

Regarding pinning, which is one current show-stopper for the development of skyrmion-based technologies, different directions can be envisaged. Firstly, amorphous materials can be used. In some studies, it was shown to mitigate pinning effects: in a single-layer Ta/FeCoB/TaO_x for skyrmion diameters $d_{sk} \approx 1$ µm and velocities $v \approx 1$ m s^{-1} [109,155] and in a multilayer [Pt/CoFeB/MgO]$_{15}$ for $d_{sk} \approx 100$ nm and $v \approx 100$ m s^{-1} [110,146]. Nevertheless, pinning-free motion has not yet been reported for small skyrmions with large velocities in single-layer films, a prerequisite to reduce power consumption and to prevent stray-field-related effects. During this thesis, current-driven skyrmion dynamics experiments were conducted in a single-layer Pt/CoFeB/MgO and performances similar to multilayers were measured ($d_{sk} \approx 100$ nm and $v \approx 100$ m s^{-1}). However, no reduction of pinning was observed as compared to Pt/Co/MgO. Note in addition that using amorphous FMs greatly reduces the choice of materials. Other approaches shall be investigated to improve the material quality to be closer to epitaxial films such as substrate heating during the sputtering deposition and post-deposition annealing. Finally, He^+-ion irradiation is also expected to reduce pinning effects [196,197].

On another note, the demonstration of skyrmion nucleation induced by ion-irradiation (§4.5) offers an exciting additional degree of freedom to further control magnetic skyrmions. Beyond these preliminary experiments, the next step is to study their dynamics. In Fig. 7.1.a-f, two sequences of XMCD-PEEM images show the current-driven motion of a couple skyrmions in irradiated lines at two different angles with respect to the current direction: 0° (Fig. 7.1.a-c) and 22.5° (Fig. 7.1.d-f). Remarkably, the skyrmions are moved back and forth within the irradiated lines, at velocities of $v(0°) \approx 35$ m s^{-1} and $v(22.5°) \approx 60$ m s^{-1}, while a significant skyrmion Hall angle is expected at these velocities (§5.2). He^+-patterning could hence offer the confinement effect to guide magnetic skyrmions. Combined with the expected reduction of pinning in irradiated films, these results offer promising perspectives to achieve reliable current-driven skyrmion motion. Note that for this skyrmion core polarity, the SkHA is in the direction of the irradiated line of Fig. 7.1.d-f. This may explain the difference in velocities measured: because the SkHE induces a motion at a finite angle, a stronger confinement effect is observed when the irradiated line is parallel to the current direction (Fig. 7.1.a-c). This may result in a reduction of the skyrmion velocity as it was observed for skyrmions sliding along the physical edge of a patterned track [155].

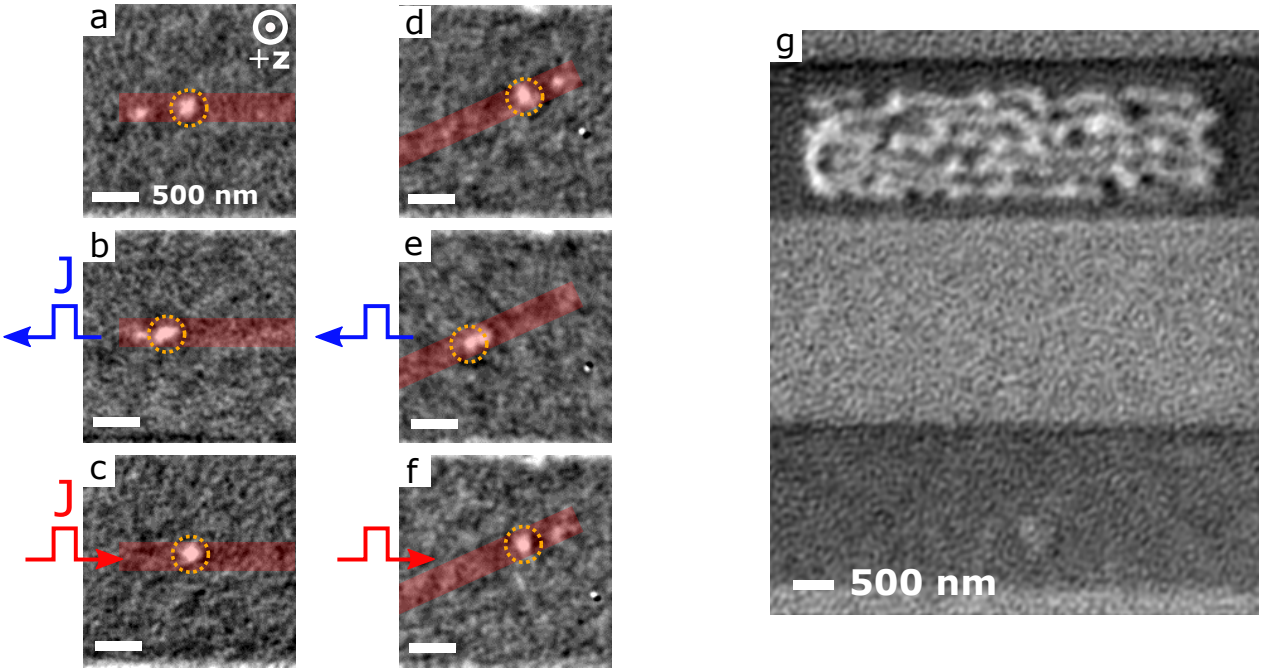

Fig. 7.1: Future prospects for ion-patterned films | **a-f.** Sequence of XMCD-PEEM images showing the current-driven skyrmion motion in irradiated Pt/Co/MgO tracks. The irradiated patterns (in red) are 300-nm-wide lines at an angle **a-c.** 0° and **d-f.** 22.5° with respect to the current direction. The external field is $\mu_0 H_z \approx +10$ mT. The current density is $J = 6.6 \times 10^{11}$ A m^{-2} and the pulse length 11 ns. **g.** XMCD-PEEM image of a compensated SAF composed of Pt/Co/Ru/Pt/Co/MgO. The top track was irradiated using a He^+ FIB while the bottom track is pristine. Image acquired at zero field.

Finally, we have seen that the nucleation of skyrmions in compensated SAFs is somewhat challenging and different directions shall be explored.

He^+-irradiation can also be employed for this purpose. A preliminary result is shown in Fig. 7.1.g. This XMCD-PEEM image was acquired at zero field in a compensated SAF composed of Pt/Co/Ru/Pt/Co/MgO. Here, only the top track was irradiated with a He^+ FIB. While the pristine (bottom) track is uniformly magnetised, the irradiated area in the top track exhibits stripe-like domains, presumably caused by the diminution of the anisotropy. This shows the potential of using ion-irradiation in compensated SAFs. Different patterns shall be investigated such as nanodots to serve as nucleation centres upon passing a current in the track, as proposed theoretically [227]. Note further that a large contrast — at the Co absorption edge — is observed even if the SAF is compensated and contains only Co. Indeed, since more photo-electrons originate from the top than from the bottom FM layer, the magnetic state of the top layer is clearly visible. The image of Fig. 7.1.g shows in turn the potential of using X-PEEM to image compensated SAFs.

For the current-induced skyrmion nucleation in SAFs, we proposed different designs (§6.5) which are being investigated to achieve both skyrmion nucleation and motion in the same device. This shall allow in turn to investigate the SkHE in compensated SAFs.

Another approach to nucleate SAF skyrmions relies on exchange-biased SAF multilayers, whether with a bias layer via RKKY coupling (§4.4) [225] or by exploiting the direct exchange at the interface between an AF and one constituent FM layer [185,186]. The latter option, if realised with an insulating AF such as NiO, offers the advantage of limiting short-circuits when passing a current in the stack, hence limiting power dissipation.

Finally, in the long run, other stimuli already proven effective to nucleate FM skyrmions shall be investigated in SAFs such as an electric field by application of a gate voltage [49,150] or ultra-fast laser pulses [228]. To study the electric field effect, Pt/Co/Ru/Pt/Co/MgO (Fig. 7.1.g) would typically be a good candidate as it is capped with an oxide.

Appendix Forces of the Thiele equation

This appendix contains the detailed steps to calculate the different forces of the Thiele equation. First, the Thiele procedure is applied to the LLG equation in order to obtain the general Thiele equation. Then the expressions of the forces are derived.

A.1 From the LLG equation to the Thiele equation

We first write the LLG equation [59,60] including the damping-like spin-orbit torque (DL-SOT):

$$\frac{\partial \boldsymbol{m}}{\partial t} = -\gamma_0 \left(\boldsymbol{m} \times \boldsymbol{H}_{eff}\right) + \alpha \left(\boldsymbol{m} \times \frac{\partial \boldsymbol{m}}{\partial t}\right) - \gamma_0 \left(\boldsymbol{m} \times \boldsymbol{H}_{DL}\right) \tag{A.1}$$

where $\boldsymbol{H}_{eff} = \boldsymbol{H}_{ex} + \boldsymbol{H}_K + \boldsymbol{H}_d + \boldsymbol{H}_{DMI} + \boldsymbol{H}_{ext}$ (exchange, anisotropy, dipolar, DMI and external fields). The Thiele procedure is the following: the right-hand side of eq. (A.1) is factorised into a total effective magnetic field, $\boldsymbol{H}_{tot}$, such that:

$$\frac{\partial \boldsymbol{m}}{\partial t} = -\gamma_0 \boldsymbol{m} \times \boldsymbol{H}_{tot} = -\gamma_0 \boldsymbol{m} \times \left(\boldsymbol{H}_{eff} - \frac{\alpha}{\gamma_0}\frac{\partial \boldsymbol{m}}{\partial t} + \boldsymbol{H}_{DL}\right) \tag{A.2}$$

Then, both sides of the above equation is cross-multiplied by $\boldsymbol{m}$ and the different terms rearranged to express $\boldsymbol{H}_{eff}$ as follows:

$$\boldsymbol{H}_{eff} = -\frac{1}{\gamma_0}\frac{\partial \boldsymbol{m}}{\partial t} \times \boldsymbol{m} + \frac{\alpha}{\gamma_0}\frac{\partial \boldsymbol{m}}{\partial t} - \boldsymbol{H}_{DL} + \lambda \boldsymbol{m} \tag{A.3}$$

where $\lambda = \boldsymbol{m} \cdot \boldsymbol{H}_{tot}$. The fundamental assumption in Thiele's approach is to consider a magnetisation texture in rigid motion [151], which can be written $\boldsymbol{m}(\boldsymbol{r}, t) = \boldsymbol{m}(\boldsymbol{r} - \boldsymbol{v}t)$, $\boldsymbol{v}$ being the skyrmion velocity. The time derivative can then be translated into a space derivative:

$$\frac{\partial \boldsymbol{m}}{\partial t} = -\left(\boldsymbol{v} \cdot \boldsymbol{\nabla}\right)\boldsymbol{m} = -\sum_i v_i \frac{\partial \boldsymbol{m}}{\partial x_i} \tag{A.4}$$

The total force acting on the rigid magnetisation texture is [151]:

$$\boldsymbol{F} = \begin{pmatrix} F_x \\ F_y \\ F_z \end{pmatrix}, \; F_i = -\mu_0 M_s \iiint d^3 r \boldsymbol{H}_{eff} \cdot \frac{\partial \boldsymbol{m}}{\partial x_i} \tag{A.5}$$

with $i = x, y, z$ and $d^3 r = dxdydz$ an infinitesimal volume element. Let us first consider the scenario without DL-SOT ($\boldsymbol{H}_{DL} = \boldsymbol{0}$) and calculate the different forces exerted on the spin texture. The procedure is the following: we inject eq. (A.4) into eq. (A.3) and then apply eq. (A.5) to the terms on the right-hand side of eq. (A.3). Doing so, we obtain the following expression:

$$F_i = -\frac{\mu_0 M_s}{\gamma_0} \iiint d^3 r \left[\sum_j v_j \left(\boldsymbol{m} \times \frac{\partial \boldsymbol{m}}{\partial x_j} + \alpha \frac{\partial \boldsymbol{m}}{\partial x_j}\right) + \gamma_0 \lambda \boldsymbol{m}\right] \cdot \frac{\partial \boldsymbol{m}}{\partial x_i} \tag{A.6}$$

For a thin FM film of thickness t with homogeneous magnetisation across its thickness (*i.e.* along $\hat{\boldsymbol{z}}$), one has $\iiint d^3r = \iiint dxdydz = t \iint dxdy$. Moreover, $\boldsymbol{m} \cdot (\partial \boldsymbol{m}/\partial x_i) = 0$ so the term proportional to λ vanishes. Finally, $\boldsymbol{H}_{eff}$ does not generate a force on the skyrmion,[1] hence one can write $F_i = 0$ in eq. (A.6), which yields (using $\gamma_0 = \mu_0\gamma$):

$$0 = -\sum_j \left[\frac{M_s t}{\gamma} \iint dxdy \left(\frac{\partial \boldsymbol{m}}{\partial x_i} \times \frac{\partial \boldsymbol{m}}{\partial x_j} \right) \cdot \boldsymbol{m} \right] v_j + \alpha \sum_j \left[\frac{M_s t}{\gamma} \iint dxdy \left(\frac{\partial \boldsymbol{m}}{\partial x_i} \cdot \frac{\partial \boldsymbol{m}}{\partial x_j} \right) \right] v_j \quad \text{(A.7)}$$

The two term of the right-hand side can further be written with their vectorial form:

$$\boldsymbol{G} \times \boldsymbol{v} - \alpha \boldsymbol{\mathcal{D}} \cdot \boldsymbol{v} = \boldsymbol{0} \quad \text{(A.8)}$$

with

$$\boldsymbol{G} = \begin{pmatrix} 0 \\ 0 \\ G \end{pmatrix}, \; G = -\frac{M_s t}{\gamma} \iint dxdy \, \boldsymbol{m} \cdot \left(\frac{\partial \boldsymbol{m}}{\partial x} \times \frac{\partial \boldsymbol{m}}{\partial y} \right) \quad \text{(A.9)}$$

$$\boldsymbol{\mathcal{D}} = \begin{pmatrix} \mathcal{D}_{xx} & \mathcal{D}_{xy} \\ \mathcal{D}_{yx} & \mathcal{D}_{yy} \end{pmatrix}, \; \mathcal{D}_{ij} = \frac{M_s t}{\gamma} \iint dxdy \left(\frac{\partial \boldsymbol{m}}{\partial x_i} \cdot \frac{\partial \boldsymbol{m}}{\partial x_j} \right) \quad \text{(A.10)}$$

$$\boldsymbol{v} = \begin{pmatrix} v_x \\ v_y \\ 0 \end{pmatrix} \quad \text{(A.11)}$$

Eq. (A.8) constitutes the so-called Thiele equation. $\boldsymbol{G} = G\hat{\boldsymbol{z}}$ is the gyrotropic vector with $G = -(M_s t/\gamma) \cdot 4\pi N_{sk}$, N_{sk} being the topological charge. Since for a skyrmion $N_{sk} = p = \pm 1$, the direction of $\boldsymbol{G}$ only depends on the skyrmion core polarity p. Finally, $\boldsymbol{\mathcal{D}}$ is the dissipation matrix.

A.2 Calculation of the forces acting on a moving skyrmion

A.2.1 Thiele equation with the force due to the DL-SOT

We can now calculate the force due to the DL-SOT using the same procedure. The effective field associated is $\boldsymbol{H}_{DL} = H_{DL}^0 \left(\boldsymbol{m} \times \left(\hat{\boldsymbol{j}} \times \hat{\boldsymbol{z}} \right) \right)$, where $\boldsymbol{J} = J\hat{\boldsymbol{j}}$ is the charge current (*i.e.* opposite to the electron flow). We consider $H_{DL}^0 > 0$, consistently with the sign in Pt/Co/MgO (§5.3.5). Furthermore, we write $\mu_0 H_{DL}^0 = C_{DL} J$, where C_{DL} is the effective magnetic field per unit current density (in T A^{-1} m^2). Defining $\hat{\boldsymbol{j}} = \hat{\boldsymbol{x}}$ leads to:

$$\boldsymbol{H}_{DL} = H_{DL}^0 \left(\hat{\boldsymbol{y}} \times \hat{\boldsymbol{m}} \right) \quad \text{(A.12)}$$

The Thiele equation thus becomes

$$\boldsymbol{F}_{DL} + \boldsymbol{G} \times \boldsymbol{v} - \alpha \boldsymbol{\mathcal{D}} \cdot \boldsymbol{v} = \boldsymbol{0} \quad \text{(A.13)}$$

The DL-SOT-induced force, $\boldsymbol{F}_{DL}$, is obtained by repeating the procedure described above:

$$F_{DL,i} = -\mu_0 M_s t H_{DL}^0 \iint dxdy \left(m_x \frac{\partial m_z}{\partial x_i} - m_z \frac{\partial m_x}{\partial x_i} \right) \quad \text{(A.14)}$$

Let us now assume a skyrmion with a rotational (cylindrical) symmetry. We can write $\partial \boldsymbol{m}/\partial x = \partial \boldsymbol{m}/\partial y$ and $\partial \boldsymbol{m}/\partial x \cdot \partial \boldsymbol{m}/\partial y = 0$, and then $\mathcal{D}_{xy} = \mathcal{D}_{yx} = 0$ and $\mathcal{D}_{xx} = \mathcal{D}_{yy} = \mathcal{D}$.

[1] The external field $\boldsymbol{H}_{ext}$ is assumed spatially homogeneous and applied in the OOP direction.

The expressions of the longitudinal (v_x) and transverse (v_y) skyrmion velocities are then given by:

$$v_x = \frac{\alpha\mathcal{D}F_{DL,x} - GF_{DL,y}}{G^2 + \alpha^2\mathcal{D}^2} \tag{A.15}$$

$$v_y = \frac{GF_{DL,x} + \alpha\mathcal{D}F_{DL,y}}{G^2 + \alpha^2\mathcal{D}^2} \tag{A.16}$$

Finally, the skyrmion Hall angle (SkHA), that is the angle Θ_{SkH} between $\boldsymbol{F}_{DL}$ and $\boldsymbol{v}$, can be derived:

$$\tan\Theta_{SkH} = \frac{G}{\alpha\mathcal{D}} \tag{A.17}$$

We now wish to calculate the different terms composing eq. (A.15) to (A.17). To do so, we consider the geometry of Fig. A.2: a circular, left-handed Néel skyrmion with radius R and core $m_z = 1$ is placed in a uniform FM background with $m_z = -1$ ($p = 1$). This situation corresponds to the experiments presented in Chapter 5. For a Néel skyrmion, $F_{DL,y} = 0$ and we write $F_{DL,x} = F_{DL} \neq 0$. It is suitable to use a polar coordinate system (r, φ) such that $x = r\cos\varphi$, $y = r\sin\varphi$ and $\boldsymbol{m} = (m_r, m_\varphi, m_z)$ (see Fig. A.2). For a Néel skyrmion, the orthoradial component of the magnetisation vanishes ($m_\varphi = 0$), therefore the reduced magnetisation vector at position (r, φ) can be written as

$$\boldsymbol{m}(r,\varphi) = \begin{pmatrix} m_x(r,\varphi) \\ m_y(r,\varphi) \\ m_z(r) \end{pmatrix} = \begin{pmatrix} \sin\theta(r)\cos\varphi \\ \sin\theta(r)\sin\varphi \\ \cos\theta(r) \end{pmatrix} = \begin{pmatrix} m_r(r)\cos\varphi \\ m_r(r)\sin\varphi \\ m_z(r) \end{pmatrix} \tag{A.18}$$

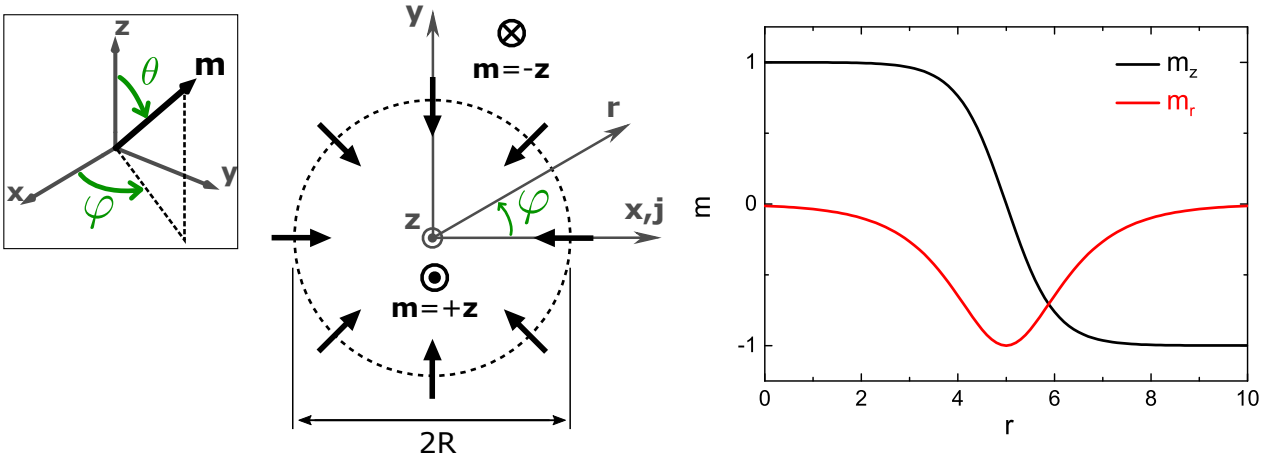

Fig. A.2: Skyrmion schematics for the calculations of the forces | (Left) Top view of a left-handed Néel skyrmion with core polarity $p = 1$. The thick black arrows represent the magnetisation $\boldsymbol{m}$ at the perimeter of the skyrmion ($m_z = 0$). R is the skyrmion radius. The charge current flows in the $+\hat{\boldsymbol{x}}$ direction. The inset defines the polar and azimuthal angles, θ and φ respectively. (Right) Magnetisation profiles for a 180° DW profile (eq. (A.29)) for $R/\Delta = 5$.

The partial derivatives $\partial\boldsymbol{m}/\partial x$ and $\partial\boldsymbol{m}/\partial y$ as well as their cross and scalar products are needed to calculate the different forces. They read:

$$\frac{\partial \boldsymbol{m}}{\partial x} = \begin{pmatrix} \cos^2\varphi \frac{dm_r}{dr} + \sin^2\varphi \frac{m_r}{r} \\ \sin\varphi\cos\varphi\left(\frac{dm_r}{dr} - \frac{m_r}{r}\right) \\ \cos\varphi \frac{dm_z}{dr} \end{pmatrix} \tag{A.19}$$

$$\frac{\partial \boldsymbol{m}}{\partial y} = \begin{pmatrix} \sin\varphi\cos\varphi\left(\frac{dm_r}{dr} - \frac{m_r}{r}\right) \\ \sin^2\varphi \frac{dm_r}{dr} + \cos^2\varphi \frac{m_r}{r} \\ \sin\varphi \frac{dm_z}{dr} \end{pmatrix} \tag{A.20}$$

$$\frac{\partial \boldsymbol{m}}{\partial x} \times \frac{\partial \boldsymbol{m}}{\partial y} = \begin{pmatrix} -\frac{m_x}{r}\frac{dm_z}{dr} \\ -\frac{m_y}{r}\frac{dm_z}{dr} \\ -\frac{m_z}{r}\frac{dm_z}{dr} \end{pmatrix} \tag{A.21}$$

$$\frac{\partial \boldsymbol{m}}{\partial x} \cdot \frac{\partial \boldsymbol{m}}{\partial x} = \frac{\partial \boldsymbol{m}}{\partial y} \cdot \frac{\partial \boldsymbol{m}}{\partial y} = \cos^2\varphi \left(\frac{dm_r}{dr}\right)^2 + \sin^2\varphi \left(\frac{m_r}{r}\right)^2 + \cos^2\varphi \left(\frac{dm_z}{dr}\right)^2 \tag{A.22}$$

The different terms composing the Thiele equation can hence be expressed as follows:

$$\boldsymbol{G} = \begin{pmatrix} 0 \\ 0 \\ G \end{pmatrix}, G = -4\pi \frac{M_s t}{\gamma} p \tag{A.23}$$

$$\boldsymbol{\mathcal{D}} = \begin{pmatrix} \mathcal{D} & 0 \\ 0 & \mathcal{D} \end{pmatrix}, \ \mathcal{D} = \pi \frac{M_s t}{\gamma} \int_0^{+\infty} dr \left(r \left(\frac{dm_r}{dr}\right)^2 + \left(\frac{m_r}{r}\right)^2 + \left(\frac{dm_z}{dr}\right)^2 \right) \tag{A.24}$$

$$\boldsymbol{F}_{DL} = \begin{pmatrix} F_{DL} \\ 0 \\ 0 \end{pmatrix}, \ F_{DL} = -\mu_0 M_s t \pi H_{DL}^0 \int_0^{+\infty} dr \left(r m_z \frac{dm_r}{dr} + m_z m_r - r m_r \frac{dm_z}{dr} \right) \tag{A.25}$$

At this point, note that for a left-handed Néel skyrmion with $p = 1$ (Fig. A.2), $F_{DL} > 0$ and $G < 0$. Hence, the skyrmion is driven along the current direction ($+\hat{\boldsymbol{x}}$) and the SkHE is along $-\hat{\boldsymbol{y}}$. For $p = -1$, $F_{DL} > 0$ and $G > 0$ hence the skyrmion is still driven along the current but deflected along along $+\hat{\boldsymbol{y}}$ (opposite SkHA). Similarly, for a right-handed Néel skyrmion with $p = 1$ ($p = -1$), $F_{DL} < 0$ and $G < 0$ ($G < 0$). It is therefore driven against the current direction and deflected in the $+\hat{\boldsymbol{y}}$ ($-\hat{\boldsymbol{y}}$) direction. In the following, we only consider the situations of Fig. A.2. Using $m_z = \cos\theta$ and $m_r = \sin\theta$, eq. (A.23) to (A.25) become:

$$\boldsymbol{G} = \begin{pmatrix} 0 \\ 0 \\ G \end{pmatrix}, \ G = -4\pi \frac{M_s t}{\gamma} \tag{A.26}$$

$$\boldsymbol{\mathcal{D}} = \begin{pmatrix} \mathcal{D} & 0 \\ 0 & \mathcal{D} \end{pmatrix}, \ \mathcal{D} = \pi \frac{M_s t}{\gamma} \int_0^{+\infty} dr \left(r \left(\frac{d\theta}{dr}\right)^2 + \frac{\sin^2\theta}{r} \right) \tag{A.27}$$

$$\boldsymbol{F}_{DL} = \begin{pmatrix} F_{DL} \\ 0 \\ 0 \end{pmatrix}, \ F_{DL} = -\mu_0 M_s t \pi H_{DL}^0 \int_0^{+\infty} dr \left(r \frac{d\theta}{dr} + \cos\theta \sin\theta \right) \tag{A.28}$$

In order to evaluate the different terms given by eq. (A.26) to (A.28), we assume that the skyrmion has a radial 180° Bloch DW profile (see Fig. A.2), consistently with experimental observations [48,108]:

$$\theta(r) = -2\arctan\left(\exp\left(\frac{r - R}{\Delta}\right)\right) \tag{A.29}$$

Then, by injecting eq. (A.29) into eq. (A.27) and (A.28), the different forces can be evaluated.[1] Furthermore, if $R \gg \Delta$, the expressions of $\mathcal{D}$ and F_{DL} simplify [70,152]:

[1] By noticing that $d\theta/dr = (\sin\theta)/\Delta$.

$$\boldsymbol{\mathcal{D}} = \begin{pmatrix} \mathcal{D} & 0 \\ 0 & \mathcal{D} \end{pmatrix}, \; \mathcal{D} \approx \frac{M_s t}{\gamma} 2\pi \left(\frac{R}{\Delta} + \frac{\Delta}{R} \right) \approx \frac{M_s t}{\gamma} 2\pi \frac{R}{\Delta} \tag{A.30}$$

$$\boldsymbol{F}_{DL} = \begin{pmatrix} F_{DL} \\ 0 \\ 0 \end{pmatrix}, \; F_{DL} \approx \mu_0 M_s t \pi^2 H_{DL}^0 R \tag{A.31}$$

A numerical integration of eq. (A.27) and eq. (A.28) allows to verify the consistency of the above expressions for the parameters of our experiments (§5.3.6). Finally, injecting eq. (A.26), (A.30) and (A.31) into eq. (A.15) and (A.16) yields (using $\mu_0 H_{DL}^0 = C_{DL} J$):

$$v = \sqrt{v_x^2 + v_y^2} = \frac{\gamma \pi}{4} \frac{R}{\sqrt{\left(\frac{\alpha R}{2\Delta}\right)^2 + 1}} C_{DL} J \tag{A.32}$$

$$\tan \Theta_{SkH} = -\frac{2\Delta}{\alpha R} \tag{A.33}$$

A.2.2 Inclusion of the Oersted field

When a current flows in the stack, it generates an Oersted field. As proposed by Hrabec *et al.* [152], this field exerts a force on the skyrmion. I borrow their calculation for the present section. For the skyrmion dynamics experiments presented in Chapter 5, the skyrmions were displaced in 3-µm-wide tracks consisting of Ta(3)/Pt(3)/Co(0.9)/MgO(0.9)/Ta(2) (thicknesses in nm).

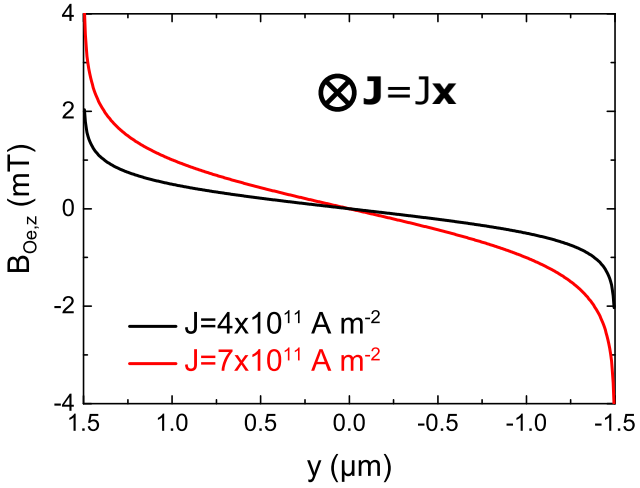

Fig. A.3: Oersted field in a 3-µm-wide track | OOP component of the Oersted field, $B_{Oe,z}$, calculated from eq. (A.34) using the parameters of a 3-µm-wide, Ta(3)/Pt(3)/Co(0.9)/MgO(0.9)/Ta(2) track: $h = 3.9$ nm and $w = 3$ µm.

In such an ultra-thin film, the Oersted field, $\boldsymbol{B}_{Oe}$, is essentially perpendicular to the film plane and takes the following form [152]:

$$B_{Oe,z}(y) = \frac{\mu_0 J h}{4\pi} \left[\ln \left(\frac{(h/2)^2 + (w/2+y)^2}{(h/2)^2 + (w/2-y)^2} \right) + 8 \frac{w/2+y}{h/2} \arctan \left(\frac{h/2}{w/2+y} \right) - 8 \frac{w/2-y}{h/2} \arctan \left(\frac{h/2}{w/2-y} \right) \right] \tag{A.34}$$

where $h = 3.9$ nm is the total thickness of the conductive layers and $w = 3$ µm is the track width. The variation of the Oersted field as a function of the position in the track is given in Fig. A.3 for

two current densities, $J = 4 \times 10^{11}$ A m^{-2} and $J = 7 \times 10^{11}$ A m^{-2}, corresponding to the smallest and the largest current density injected during the experiments.

In the central region of the track, this expression simplifies into:

$$B_{Oe,z}(y) = \frac{2\mu_0 Jh}{\pi w} y \tag{A.35}$$

Thus, from eq. (A.5), applying the same procedure as for the other forces, the force due to the Oersted field can be derived for a skyrmion in the centre of the track:

$$\boldsymbol{F}_{Oe} = \begin{pmatrix} 0 \\ F_{Oe} \\ 0 \end{pmatrix}, F_{Oe} = \frac{2Jh}{w} \mu_0 M_s t \int_0^{+\infty} dr \left(r^2 \sin\theta \frac{d\theta}{dr} \right) \tag{A.36}$$

The expression for the skyrmion velocity components hence become:

$$v_x = \frac{\alpha \mathcal{D} F_{DL} - G F_{Oe}}{G^2 + \alpha^2 \mathcal{D}^2} \tag{A.37}$$

$$v_y = \frac{G F_{DL} + \alpha \mathcal{D} F_{Oe}}{G^2 + \alpha^2 \mathcal{D}^2} \tag{A.38}$$

Here, we see that $F_{Oe} > 0$ for a left-handed Néel skyrmion with $p = 1$, that is opposite to the gyrotropic force. Similarly, upon reversing the skyrmion core polarity, both F_{Oe} and G change sign so the Oersted field always act against the gyrotropic force. Since it turns out that F_{Oe} is negligible, adding the Oersted field to the problem does not modify the calculated velocity and SkHA. Therefore, the expressions (A.32) and (A.33) remain valid for the experiments described in Chapter 5.

References

[1] Baibich M. N., Broto J. M., Fert A., Van Dau F. N., Petroff F., Etienne P., Creuzet G., Friederich A. & Chazelas J., *Giant Magnetoresistance of (001)Fe/(001)Cr Magnetic Superlattices*, Phys. Rev. Lett. **61**, 2472 (1988). [p. 1]

[2] Binasch G., Grünberg P., Saurenbach F. & Zinn W., *Enhanced magnetoresistance in layered magnetic structures with antiferromagnetic interlayer exchange*, Phys. Rev. B **39**, 4828 (1989). [p. 1]

[3] Julliere M., *Tunneling between ferromagnetic films*, Phys. Lett. A **54**, 225 (1975). [p. 1]

[4] Moodera J. S., Kinder L. R., Wong T. M. & Meservey R., *Large Magnetoresistance at Room Temperature in Ferromagnetic Thin Film Tunnel Junctions*, Phys. Rev. Lett. **74**, 3273 (1995). [p. 1]

[5] Slonczewski J. C., *Current-driven excitation of magnetic multilayers*, J. Magn. Magn. Mater. **159**, L1 (1996). [p. 1]

[6] Myers E. B., Ralph D. C., Katine J. A., Louie R. N. & Buhrman R. A., *Current-Induced Switching of Domains in Magnetic Multilayer Devices*, Science **285**, 867 (1999). [p. 1]

[7] Manchon A., Železný J., Miron I. M., Jungwirth T., Sinova J., Thiaville A., Garello K. & Gambardella P., *Current-induced spin-orbit torques in ferromagnetic and antiferromagnetic systems*, Rev. Mod. Phys. **91**, 035004 (2019). [pp. 1, 17, 19, 20, 69, 78]

[8] Parkin S. S. P., Hayashi M. & Thomas L., *Magnetic Domain-Wall Racetrack Memory*, Science **320**, 190 (2008). [pp. 1, 19, 28]

[9] Fert A., Cros V. & Sampaio J., *Skyrmions on the track*, Nat. Nanotech. **8**, 152 (2013). [pp. 2, 11, 27, 61]

[10] Brown W. F., *Micromagnetics*, Wiley J. (ed.), Interscience Publishers, New York, London (1963). [p. 5]

[11] Coey J. M. D., *Magnetism and Magnetic Materials*, Cambridge University Press, New York (2009). [p. 6]

[12] Aharoni A., *Demagnetizing factors for rectangular ferromagnetic prisms*, J. Appl. Phys. **83**, 3432 (1998). [p. 7]

[13] Soumyanarayanan A., Reyren N., Fert A. & Panagopoulos C., *Emergent phenomena induced by spin–orbit coupling at surfaces and interfaces*, Nature **539**, 509 (2016). [p. 7]

[14] Blundell S., *Magnetism in Condensed Matter*, Oxford University Press, New York (2001). [p. 8]

[15] Bychkov Y. A. & Rashba É. I., *Properties of a 2D electron gas with lifted spectral degeneracy*, Sov. J. Exper. Theor. Phys. Lett. **39**, 78 (1984). [p. 8]

[16] Bychkov Y. A. & Rashba E. I., *Oscillatory effects and the magnetic susceptibility of carriers in inversion layers*, J. Phys. C: Sol. State. Phys. **17**, 6039 (1984). [p. 8]

[17] Gambardella P. & Miron I. M., *Current-induced spin–orbit torques*, Phil. Trans. R. Soc. A **369**, 3175 (2011). [pp. 8, 19, 21]

[18] Néel L., *Anisotropie magnétique superficielle et surstructures d'orientation*, J. Phys. Radium **15**, 225 (1954). [p. 9]

[19] Hubert A. & Schäfer R., *Magnetic Domains: The Analysis of Magnetic Microstructures*, Springer-Verlag, Berlin Heidelberg (1998). [p. 9]

[20] Zeper W. B., Greidanus F. J. a. M., Carcia P. F. & Fincher C. R., *Perpendicular magnetic anisotropy and magneto-optical Kerr effect of vapor-deposited Co/Pt-layered structures*, J. Appl. Phys. **65**, 4971 (1989). [p. 9]

[21] Weller D., Wu Y., Stöhr J., Samant M. G., Hermsmeier B. D. & Chappert C., *Orbital magnetic moments of Co in multilayers with perpendicular magnetic anisotropy*, Phys. Rev. B **49**, 12888 (1994). [p. 10]

[22] Nakajima N., Koide T., Shidara T., Miyauchi H., Fukutani H., Fujimori A., Iio K., Katayama T., Nývlt M. & Suzuki Y., *Perpendicular Magnetic Anisotropy Caused by Interfacial Hybridization via Enhanced Orbital Moment in Co/Pt Multilayers: Magnetic Circular X-Ray Dichroism Study*, Phys. Rev. Lett. **81**, 5229 (1998). [p. 10]

[23] Dieny B. & Chshiev M., *Perpendicular magnetic anisotropy at transition metal/oxide interfaces and applications*, Rev. Mod. Phys. **89**, 025008 (2017). [p. 10]

[24] Yang H. X., Chshiev M., Dieny B., Lee J. H., Manchon A. & Shin K. H., *First-principles investigation of the very large perpendicular magnetic anisotropy at Fe/MgO and Co/MgO interfaces*, Phys. Rev. B **84**, 054401 (2011). [p. 10]

[25] Rodmacq B., Manchon A., Ducruet C., Auffret S. & Dieny B., *Influence of thermal annealing on the perpendicular magnetic anisotropy of Pt/Co/AlO_x trilayers*, Phys. Rev. B **79**, 024423 (2009). [p. 10]

[26] Gweon H. K., Yun S. J. & Lim S. H., *A very large perpendicular magnetic anisotropy in Pt/Co/MgO trilayers fabricated by controlling the MgO sputtering power and its thickness*, Sci. Rep. **8**, 1266 (2018). [p. 10]

[27] Dzyaloshinsky I., *A thermodynamic theory of "weak" ferromagnetism of antiferromagnetics*, J. Phys. Chem. Solids **4**, 241 (1958). [p. 11]

[28] Moriya T., *New Mechanism of Anisotropic Superexchange Interaction*, Phys. Rev. Lett. **4**, 228 (1960). [p. 11]

[29] Moriya T., *Anisotropic Superexchange Interaction and Weak Ferromagnetism*, Phys. Rev. **120**, 91 (1960). [p. 11]

[30] Fert A. & Levy P. M., *Role of Anisotropic Exchange Interactions in Determining the Properties of Spin-Glasses*, Phys. Rev. Lett. **44**, 1538 (1980). [p. 11]

[31] Fert A., *Magnetic and Transport Properties of Metallic Multilayers*, Mater. Sci. Forum **59**, 439 (1991). [p. 11]

[32] Mühlbauer S., Binz B., Jonietz F., Pfleiderer C., Rosch A., Neubauer A., Georgii R. & Böni P., *Skyrmion Lattice in a Chiral Magnet*, Science **323**, 915 (2009). [pp. 11, 25, 27]

[33] Crépieux A. & Lacroix C., *Dzyaloshinsky–Moriya interactions induced by symmetry breaking at a surface*, J. Magn. Magn. Mater. **182**, 341 (1998). [p. 11]

[34] Bode M., Heide M., von Bergmann K., Ferriani P., Heinze S., Bihlmayer G., Kubetzka A., Pietzsch O., Blügel S. & Wiesendanger R., *Chiral magnetic order at surfaces driven by inversion asymmetry*, Nature **447**, 190 (2007). [p. 11]

[35] Hrabec A., Porter N. A., Wells A., Benitez M. J., Burnell G., McVitie S., McGrouther D., Moore T. A. & Marrows C. H., *Measuring and tailoring the Dzyaloshinskii-Moriya interaction in perpendicularly magnetized thin films*, Phys. Rev. B **90**, 020402 (2014). [pp. 12, 66]

[36] Yang H., Boulle O., Cros V., Fert A. & Chshiev M., *Controlling Dzyaloshinskii-Moriya Interaction via Chirality Dependent Atomic-Layer Stacking, Insulator Capping and Electric Field*, Sci. Rep. **8**, 12356 (2018). [p. 12]

[37] Yang H., Chen G., Cotta A. A. C., N'Diaye A. T., Nikolaev S. A., Soares E. A., Macedo W. A. A., Liu K., Schmid A. K., Fert A. & Chshiev M., *Significant Dzyaloshinskii–Moriya interaction at graphene–ferromagnet interfaces due to the Rashba effect*, Nat. Mater. **17**, 605 (2018). [pp. 12, 82]

[38] Khadka D., Karayev S. & Huang S. X., *Dzyaloshinskii–Moriya interaction in Pt/Co/Ir and Pt/Co/Ru multilayer films*, J. Appl. Phys. **123**, 123905 (2018). [pp. 12, 82]

[39] Bogdanov A. & Hubert A., *Thermodynamically stable magnetic vortex states in magnetic crystals*, J. Magn. Magn. Mater. **138**, 255 (1994). [pp. 12, 23, 25]

[40] Yang H., Thiaville A., Rohart S., Fert A. & Chshiev M., *Anatomy of Dzyaloshinskii-Moriya Interaction at Co/Pt Interfaces*, Phys. Rev. Lett. **115**, 267210 (2015). [p. 12]

[41] Belmeguenai M., Adam J.-P., Roussigné Y., Eimer S., Devolder T., Kim J.-V., Cherif S. M., Stashkevich A. & Thiaville A., *Interfacial Dzyaloshinskii-Moriya interaction in perpendicularly magnetized Pt/Co/AlO$_x$ ultrathin films measured by Brillouin light spectroscopy*, Phys. Rev. B **91**, 180405 (2015). [pp. 12, 66]

[42] Rohart S. & Thiaville A., *Skyrmion confinement in ultrathin film nanostructures in the presence of Dzyaloshinskii-Moriya interaction*, Phys. Rev. B **88**, 184422 (2013). [p. 12]

[43] Je S.-G., Kim D.-H., Yoo S.-C., Min B.-C., Lee K.-J. & Choe S.-B., *Asymmetric magnetic domain-wall motion by the Dzyaloshinskii-Moriya interaction*, Phys. Rev. B **88**, 214401 (2013). [pp. 12, 66]

[44] Pizzini S., Vogel J., Rohart S., Buda-Prejbeanu L. D., Jué E., Boulle O., Miron I. M., Safeer C. K., Auffret S., Gaudin G. & Thiaville A., *Chirality-Induced Asymmetric Magnetic Nucleation in Pt/Co/AlO$_x$ Ultrathin Microstructures*, Phys. Rev. Lett. **113**, 047203 (2014). [pp. 12, 66]

[45] Moon J.-H., Seo S.-M., Lee K.-J., Kim K.-W., Ryu J., Lee H.-W., McMichael R. D. & Stiles M. D., *Spin-wave propagation in the presence of interfacial Dzyaloshinskii-Moriya interaction*, Phys. Rev. B **88**, 184404 (2013). [p. 12]

[46] Di K., Zhang V. L., Lim H. S., Ng S. C., Kuok M. H., Yu J., Yoon J., Qiu X. & Yang H., *Direct Observation of the Dzyaloshinskii-Moriya Interaction in a Pt/Co/Ni Film*, Phys. Rev. Lett. **114**, 047201 (2015). [p. 12]

[47] Kim K.-W., Lee H.-W., Lee K.-J. & Stiles M. D., *Chirality from Interfacial Spin-Orbit Coupling Effects in Magnetic Bilayers*, Phys. Rev. Lett. **111**, 216601 (2013). [p. 12]

[48] Boulle O., Vogel J., Yang H., Pizzini S., de Souza Chaves D., Locatelli A., Menteş T. O., Sala A., Buda-Prejbeanu L. D., Klein O., Belmeguenai M., Roussigné Y., Stashkevich A., Chérif S. M., Aballe L., Foerster M., Chshiev M., Auffret S., Miron I. M. & Gaudin G., *Room-temperature chiral magnetic skyrmions in ultrathin magnetic nanostructures*, Nat. Nanotech. **11**, 449 (2016). [pp. 12, 26, 27, 42, 43, 47, 48, 50, 51, 66, 71, 93, 100]

[49] Srivastava T., Schott M., Juge R., Křižáková V., Belmeguenai M., Roussigné Y., Bernand-Mantel A., Ranno L., Pizzini S., Chérif S.-M., Stashkevich A., Auffret S., Boulle O., Gaudin G., Chshiev M., Baraduc C. & Béa H., *Large-Voltage Tuning of Dzyaloshinskii–Moriya Interactions: A Route toward Dynamic Control of Skyrmion Chirality*, Nano Lett. **18**, 4871 (2018). [pp. 12, 32, 95]

[50] Cho J., Kim N.-H., Lee S., Kim J.-S., Lavrijsen R., Solignac A., Yin Y., Han D.-S., van Hoof N. J. J., Swagten H. J. M., Koopmans B. & You C.-Y., *Thickness dependence of the interfacial Dzyaloshinskii–Moriya interaction in inversion symmetry broken systems*, Nat. Comm. **6**, 7635 (2015). [p. 12]

[51] Kim N.-H., Han D.-S., Jung J., Park K., Swagten H. J. M., Kim J.-S. & You C.-Y., *Dependence of interfacial Dzyaloshinskii–Moriya interaction and perpendicular magnetic anisotropy on the thickness of the heavy-metal layer*, Appl. Phys. Express **10**, 103003 (2017). [p. 12]

[52] Tacchi S., Troncoso R. E., Ahlberg M., Gubbiotti G., Madami M., Åkerman J. & Landeros P., *Interfacial Dzyaloshinskii-Moriya Interaction in Pt/CoFeB Films: Effect of the Heavy-Metal Thickness*, Phys. Rev. Lett. **118**, 147201 (2017). [p. 12]

[53] Bruno P. & Chappert C., *Oscillatory coupling between ferromagnetic layers separated by a non-magnetic metal spacer*, Phys. Rev. Lett. **67**, 1602 (1991). [p. 13]

[54] Bruno P. & Chappert C., *Ruderman-Kittel theory of oscillatory interlayer exchange coupling*, Phys. Rev. B **46**, 261 (1992). [p. 13]

[55] Parkin S. S. P. & Mauri D., *Spin engineering: Direct determination of the Ruderman-Kittel-Kasuya-Yosida far-field range function in ruthenium*, Phys. Rev. B **44**, 7131 (1991). [p. 13]

[56] DeJong M. D. & Livesey K. L., *Analytic theory for the switch from Bloch to N\'eel domain wall in nanowires with perpendicular anisotropy*, Phys. Rev. B **92**, 214420 (2015). [p. 14]

[57] Malozemoff A. P. & Slonczewski J. C., *Magnetic Domain Walls in Bubble Materials*, Wolfe R. (ed.), Academic Press, London (1979). [pp. 14, 27]

[58] Thiaville A., Rohart S., Jué É., Cros V. & Fert A., *Dynamics of Dzyaloshinskii domain walls in ultrathin magnetic films*, Europhys. Lett. **100**, 57002 (2012). [pp. 14, 15, 16, 17, 21, 47]

[59] Landau L. & Lifshitz E. *3 - On the theory of the dispersion of magnetic permeability in ferromagnetic bodies, Reprinted from Physikalische Zeitschrift der Sowjetunion 8, Part 2, 153, (1935)*, in *Perspectives in Theoretical Physics*, Pitaevski L. P. (ed.), Pergamon, Amsterdam (1992). [pp. 15, 97]

[60] Gilbert T. L., *A phenomenological theory of damping in ferromagnetic materials*, IEEE Trans. Magn. **40**, 3443 (2004). [pp. 15, 97]

[61] Azzawi S., Hindmarch A. T. & Atkinson D., *Magnetic damping phenomena in ferromagnetic thin-films and multilayers*, J. Phys. D: Appl. Phys. **50**, 473001 (2017). [p. 16]

[62] Schryer N. L. & Walker L. R., *The motion of 180° domain walls in uniform dc magnetic fields*, J. Appl. Phys. **45**, 5406 (1974). [p. 16]

[63] Mougin A., Cormier M., Adam J. P., Metaxas P. J. & Ferré J., *Domain wall mobility, stability and Walker breakdown in magnetic nanowires*, Europhys. Lett. **78**, 57007 (2007). [p. 16]

[64] Miron I. M., Moore T., Szambolics H., Buda-Prejbeanu L. D., Auffret S., Rodmacq B., Pizzini S., Vogel J., Bonfim M., Schuhl A. & Gaudin G., *Fast current-induced domain-wall motion controlled by the Rashba effect*, Nat. Mater. **10**, 419 (2011). [pp. 16, 18, 19, 21, 72, 75]

[65] Pham T. H., Vogel J., Sampaio J., Vaňatka M., Rojas-Sánchez J.-C., Bonfim M., Chaves D. S., Choueikani F., Ohresser P., Otero E., Thiaville A. & Pizzini S., *Very large domain wall velocities in Pt/Co/GdO$_x$ and Pt/Co/Gd trilayers with Dzyaloshinskii-Moriya interaction*, Europhys. Lett. **113**, 67001 (2016). [pp. 16, 72]

[66] Metaxas P. J., Jamet J. P., Mougin A., Cormier M., Ferré J., Baltz V., Rodmacq B., Dieny B. & Stamps R. L., *Creep and Flow Regimes of Magnetic Domain-Wall Motion in Ultrathin Pt/Co/Pt Films with Perpendicular Anisotropy*, Phys. Rev. Lett. **99**, 217208 (2007). [pp. 16, 17, 68, 72]

[67] Lemerle S., Ferré J., Chappert C., Mathet V., Giamarchi T. & Le Doussal P., *Domain Wall Creep in an Ising Ultrathin Magnetic Film*, Phys. Rev. Lett. **80**, 849 (1998). [p. 17]

[68] Chauve P., Giamarchi T. & Le Doussal P., *Creep and depinning in disordered media*, Phys. Rev. B **62**, 6241 (2000). [p. 17]

[69] Brataas A., Kent A. D. & Ohno H., *Current-induced torques in magnetic materials*, Nat. Mater. **11**, 372 (2012). [p. 17]

[70] Sampaio J., Cros V., Rohart S., Thiaville A. & Fert A., *Nucleation, stability and current-induced motion of isolated magnetic skyrmions in nanostructures*, Nat. Nanotech. **8**, 839 (2013). [pp. 18, 27, 28, 32, 35, 100]

[71] Tomasello R., Martinez E., Zivieri R., Torres L., Carpentieri M. & Finocchio G., *A strategy for the design of skyrmion racetrack memories*, Sci. Rep. **4**, 6784 (2014). [pp. 18, 27, 32]

[72] Boulle O., Malinowski G. & Kläui M., *Current-induced domain wall motion in nanoscale ferromagnetic elements*, Mater. Sci. Eng. R **72**, 159 (2011). [pp. 18, 19]

[73] Zhang S. & Li Z., *Roles of Nonequilibrium Conduction Electrons on the Magnetization Dynamics of Ferromagnets*, Phys. Rev. Lett. **93**, 127204 (2004). [p. 18]

[74] Zhang J., Levy P. M., Zhang S. & Antropov V., *Identification of Transverse Spin Currents in Noncollinear Magnetic Structures*, Phys. Rev. Lett. **93**, 256602 (2004). [p. 18]

[75] Kläui M., Vaz C. A. F., Bland J. A. C., Wernsdorfer W., Faini G., Cambril E. & Heyderman L. J., *Domain wall motion induced by spin polarized currents in ferromagnetic ring structures*, Appl. Phys. Lett. **83**, 105 (2003). [p. 18]

[76] Thiaville A., Nakatani Y., Miltat J. & Vernier N., *Domain wall motion by spin-polarized current: A micromagnetic study*, J. Appl. Phys. **95**, 7049 (2004). [p. 18]

[77] Garate I., Gilmore K., Stiles M. D. & MacDonald A. H., *Nonadiabatic spin-transfer torque in real materials*, Phys. Rev. B **79**, 104416 (2009). [p. 18]

[78] Hayashi M., Thomas L., Rettner C., Moriya R., Bazaliy Y. B. & Parkin S. S. P., *Current Driven Domain Wall Velocities Exceeding the Spin Angular Momentum Transfer Rate in Permalloy Nanowires*, Phys. Rev. Lett. **98**, 037204 (2007). [p. 19]

[79] Emori S., Bauer U., Ahn S.-M., Martinez E. & Beach G. S. D., *Current-driven dynamics of chiral ferromagnetic domain walls*, Nat. Mater. **12**, 611 (2013). [pp. 19, 20, 21, 69]

[80] Ryu K.-S., Thomas L., Yang S.-H. & Parkin S., *Chiral spin torque at magnetic domain walls*, Nat. Nanotech. **8**, 527 (2013). [pp. 19, 21]

[81] Dyakonov M. I. & Perel V. I., *Current-induced spin orientation of electrons in semiconductors*, Phys. Lett. A **35**, 459 (1971). [p. 19]

[82] Hirsch J. E., *Spin Hall Effect*, Phys. Rev. Lett. **83**, 1834 (1999). [p. 19]

[83] Sinova J., Culcer D., Niu Q., Sinitsyn N. A., Jungwirth T. & MacDonald A. H., *Universal Intrinsic Spin Hall Effect*, Phys. Rev. Lett. **92**, 126603 (2004). [p. 19]

[84] Edelstein V. M., *Spin polarization of conduction electrons induced by electric current in two-dimensional asymmetric electron systems*, Solid State Comm. **73**, 233 (1990). [p. 19]

[85] Khvalkovskiy A. V., Cros V., Apalkov D., Nikitin V., Krounbi M., Zvezdin K. A., Anane A., Grollier J. & Fert A., *Matching domain-wall configuration and spin-orbit torques for efficient domain-wall motion*, Phys. Rev. B **87**, 020402 (2013). [p. 20]

[86] Liu L., Lee O. J., Gudmundsen T. J., Ralph D. C. & Buhrman R. A., *Current-Induced Switching of Perpendicularly Magnetized Magnetic Layers Using Spin Torque from the Spin Hall Effect*, Phys. Rev. Lett. **109**, 096602 (2012). [pp. 20, 69]

[87] Garello K., Miron I. M., Avci C. O., Freimuth F., Mokrousov Y., Blügel S., Auffret S., Boulle O., Gaudin G. & Gambardella P., *Symmetry and magnitude of spin-orbit torques in ferromagnetic heterostructures*, Nat. Nanotech. **8**, 587 (2013). [pp. 20, 21, 68, 69]

[88] Liu L., Pai C.-F., Li Y., Tseng H. W., Ralph D. C. & Buhrman R. A., *Spin-Torque Switching with the Giant Spin Hall Effect of Tantalum*, Science **336**, 555 (2012). [p. 20]

[89] Pai C.-F., Liu L., Li Y., Tseng H. W., Ralph D. C. & Buhrman R. A., *Spin transfer torque devices utilizing the giant spin Hall effect of tungsten*, Appl. Phys. Lett. **101**, 122404 (2012). [p. 20]

[90] Manchon A. & Zhang S., *Theory of nonequilibrium intrinsic spin torque in a single nanomagnet*, Phys. Rev. B **78**, 212405 (2008). [p. 21]

[91] Manchon A. & Zhang S., *Theory of spin torque due to spin-orbit coupling*, Phys. Rev. B **79**, 094422 (2009). [p. 21]

[92] Liu L., Moriyama T., Ralph D. C. & Buhrman R. A., *Spin-Torque Ferromagnetic Resonance Induced by the Spin Hall Effect*, Phys. Rev. Lett. **106**, 036601 (2011). [p. 21]

[93] Montazeri M., Upadhyaya P., Onbasli M. C., Yu G., Wong K. L., Lang M., Fan Y., Li X., Khalili Amiri P., Schwartz R. N., Ross C. A. & Wang K. L., *Magneto-optical investigation of spin–orbit torques in metallic and insulating magnetic heterostructures*, Nat. Comm. **6**, 8958 (2015). [p. 21]

[94] Hayashi M., Kim J., Yamanouchi M. & Ohno H., *Quantitative characterization of the spin-orbit torque using harmonic Hall voltage measurements*, Phys. Rev. B **89**, 144425 (2014). [pp. 21, 68]

[95] Ivanov B. A., Stephanovich V. A. & Zhmudskii A. A., *Magnetic vortices: The microscopic analogs of magnetic bubbles*, J. Magn. Magn. Mater. **88**, 116 (1990). [pp. 23, 25]

[96] Bogdanov A. & Hubert A., *The Properties of Isolated Magnetic Vortices*, phys. status solidi (b) **186**, 527 (1994). [pp. 23, 25]

[97] Skyrme T. H. R., *A unified field theory of mesons and baryons*, Nucl. Phys. **31**, 556 (1962). [p. 23]

[98] Braun H.-B., *Topological effects in nanomagnetism: From superparamagnetism to chiral quantum solitons*, Adv. Phy. **61**, 1 (2012). [p. 23]

[99] Nagaosa N. & Tokura Y., *Topological properties and dynamics of magnetic skyrmions*, Nat. Nanotech. **8**, 899 (2013). [pp. 23, 24]

[100] Kézsmárki I., Bordács S., Milde P., Neuber E., Eng L. M., White J. S., Rønnow H. M., Dewhurst C. D., Mochizuki M., Yanai K., Nakamura H., Ehlers D., Tsurkan V. & Loidl A., *Néel-type skyrmion lattice with confined orientation in the polar magnetic semiconductor GaV_4S_8*, Nat. Mater. **14**, 1116 (2015). [p. 23]

[101] Nayak A. K., Kumar V., Ma T., Werner P., Pippel E., Sahoo R., Damay F., Rößler U. K., Felser C. & Parkin S. S. P., *Magnetic antiskyrmions above room temperature in tetragonal Heusler materials*, Nature **548**, 561 (2017). [pp. 25, 35]

[102] Münzer W., Neubauer A., Adams T., Mühlbauer S., Franz C., Jonietz F., Georgii R., Böni P., Pedersen B., Schmidt M., Rosch A. & Pfleiderer C., *Skyrmion lattice in the doped semiconductor $Fe_{1-x}Co_xSi$*, Phys. Rev. B **81**, 041203 (2010). [pp. 25, 27]

[103] Yu X. Z., Onose Y., Kanazawa N., Park J. H., Han J. H., Matsui Y., Nagaosa N. & Tokura Y., *Real-space observation of a two-dimensional skyrmion crystal*, Nature **465**, 901 (2010). [pp. 25, 27]

[104] Yu X. Z., Kanazawa N., Onose Y., Kimoto K., Zhang W. Z., Ishiwata S., Matsui Y. & Tokura Y., *Near room-temperature formation of a skyrmion crystal in thin-films of the helimagnet FeGe*, Nat. Mater. **10**, 106 (2011). [pp. 25, 26, 27]

[105] Seki S., Yu X. Z., Ishiwata S. & Tokura Y., *Observation of Skyrmions in a Multiferroic Material*, Science **336**, 198 (2012). [pp. 25, 27]

[106] Heinze S., von Bergmann K., Menzel M., Brede J., Kubetzka A., Wiesendanger R., Bihlmayer G. & Blügel S., *Spontaneous atomic-scale magnetic skyrmion lattice in two dimensions*, Nat. Phys. **7**, 713 (2011). [pp. 26, 27]

[107] Romming N., Hanneken C., Menzel M., Bickel J. E., Wolter B., von Bergmann K., Kubetzka A. & Wiesendanger R., *Writing and Deleting Single Magnetic Skyrmions*, Science **341**, 636 (2013). [pp. 26, 27]

[108] Romming N., Kubetzka A., Hanneken C., von Bergmann K. & Wiesendanger R., *Field-Dependent Size and Shape of Single Magnetic Skyrmions*, Phys. Rev. Lett. **114**, 177203 (2015). [pp. 26, 27, 47, 71, 100]

[109] Jiang W., Upadhyaya P., Zhang W., Yu G., Jungfleisch M. B., Fradin F. Y., Pearson J. E., Tserkovnyak Y., Wang K. L., Heinonen O., te Velthuis S. G. E. & Hoffmann A., *Blowing magnetic skyrmion bubbles*, Science **349**, 283 (2015). [pp. 26, 27, 32, 61, 93, 94]

[110] Woo S., Litzius K., Krüger B., Im M.-Y., Caretta L., Richter K., Mann M., Krone A., Reeve R. M., Weigand M., Agrawal P., Lemesh I., Mawass M.-A., Fischer P., Kläui M. & Beach G. S. D., *Observation of room-temperature magnetic skyrmions and their current-driven dynamics in ultrathin metallic ferromagnets*, Nat. Mater. **15**, 501 (2016). [pp. 26, 27, 31, 35, 36, 61, 77, 93, 94]

[111] Moreau-Luchaire C., Moutafis C., Reyren N., Sampaio J., Vaz C. a. F., Horne N. V., Bouzehouane K., Garcia K., Deranlot C., Warnicke P., Wohlhüter P., George J.-M., Weigand M., Raabe J., Cros V. & Fert A., *Additive interfacial chiral interaction in multilayers for stabilization of small individual skyrmions at room temperature*, Nat. Nanotech. **11**, 444 (2016). [pp. 26, 27, 31, 93]

[112] Soumyanarayanan A., Raju M., Oyarce A. L. G., Tan A. K. C., Im M.-Y., Petrović A. P., Ho P., Khoo K. H., Tran M., Gan C. K., Ernult F. & Panagopoulos C., *Tunable room-temperature magnetic skyrmions in Ir/Fe/Co/Pt multilayers*, Nat. Mater. **16**, 898 (2017). [pp. 26, 31, 32]

[113] Jaiswal S., Litzius K., Lemesh I., Büttner F., Finizio S., Raabe J., Weigand M., Lee K., Langer J., Ocker B., Jakob G., Beach G. S. D. & Kläui M., *Investigation of the Dzyaloshinskii-Moriya interaction and room temperature skyrmions in W/CoFeB/MgO thin films and microwires*, Appl. Phys. Lett. **111**, 022409 (2017). [pp. 26, 31]

[114] Fert A., Reyren N. & Cros V., *Magnetic skyrmions: Advances in physics and potential applications*, Nat. Rev. Mater. **2**, 17031 (2017). [pp. 26, 28, 54]

[115] Jiang W., Chen G., Liu K., Zang J., te Velthuis S. G. E. & Hoffmann A., *Skyrmions in magnetic multilayers*, Phys. Rep. **704**, 1 (2017). [pp. 26, 28]

[116] Everschor-Sitte K., Masell J., Reeve R. M. & Kläui M., *Perspective: Magnetic skyrmions—Overview of recent progress in an active research field*, J. Appl. Phys. **124**, 240901 (2018). [pp. 26, 28]

[117] Büttner F., Lemesh I. & Beach G. S. D., *Theory of isolated magnetic skyrmions: From fundamentals to room temperature applications*, Sci. Rep. **8**, 4464 (2018). [pp. 27, 30, 31, 81, 82]

[118] Bernand-Mantel A., Camosi L., Wartelle A., Rougemaille N., Darques M. & Ranno L., *The skyrmion-bubble transition in a ferromagnetic thin film*, SciPost Phys. **4**, 027 (2018). [pp. 27, 28, 29, 31]

[119] Nagaosa N., Yu X. Z. & Tokura Y., *Gauge fields in real and momentum spaces in magnets: Monopoles and skyrmions*, Phil. Trans. R. Soc. A **370**, 5806 (2012). [p. 27]

[120] Yu X., Mostovoy M., Tokunaga Y., Zhang W., Kimoto K., Matsui Y., Kaneko Y., Nagaosa N. & Tokura Y., *Magnetic stripes and skyrmions with helicity reversals*, Proc. Natl. Acad. Sci. USA **109**, 8856 (2012). [p. 27]

[121] Legrand W., Maccariello D., Reyren N., Garcia K., Moutafis C., Moreau-Luchaire C., Collin S., Bouzehouane K., Cros V. & Fert A., *Room-Temperature Current-Induced Generation and Motion of sub-100 nm Skyrmions*, Nano Lett. **17**, 2703 (2017). [pp. 27, 31, 32, 61, 63, 72, 74, 76]

[122] Pollard S. D., Garlow J. A., Yu J., Wang Z., Zhu Y. & Yang H., *Observation of stable Néel skyrmions in cobalt/palladium multilayers with Lorentz transmission electron microscopy*, Nat. Comm. **8**, 14761 (2017). [pp. 27, 31]

[123] Maccariello D., Legrand W., Reyren N., Garcia K., Bouzehouane K., Collin S., Cros V. & Fert A., *Electrical detection of single magnetic skyrmions in metallic multilayers at room temperature*, Nat. Nanotech. **13**, 233 (2018). [p. 27]

[124] Hanneken C., Otte F., Kubetzka A., Dupé B., Romming N., von Bergmann K., Wiesendanger R. & Heinze S., *Electrical detection of magnetic skyrmions by tunnelling non-collinear magnetoresistance*, Nat. Nanotech. **10**, 1039 (2015). [p. 27]

[125] Penthorn N. E., Hao X., Wang Z., Huai Y. & Jiang H. W., *Experimental Observation of Single Skyrmion Signatures in a Magnetic Tunnel Junction*, Phys. Rev. Lett. **122**, 257201 (2019). [p. 27]

[126] Jonietz F., Mühlbauer S., Pfleiderer C., Neubauer A., Münzer W., Bauer A., Adams T., Georgii R., Böni P., Duine R. A., Everschor K., Garst M. & Rosch A., *Spin Transfer Torques in MnSi at Ultralow Current Densities*, Science **330**, 1648 (2010). [p. 27]

[127] Yu X. Z., Kanazawa N., Zhang W. Z., Nagai T., Hara T., Kimoto K., Matsui Y., Onose Y. & Tokura Y., *Skyrmion flow near room temperature in an ultralow current density*, Nat. Comm. **3**, 988 (2012). [p. 27]

[128] Kang W., Huang Y., Zheng C., Lv W., Lei N., Zhang Y., Zhang X., Zhou Y. & Zhao W., *Voltage Controlled Magnetic Skyrmion Motion for Racetrack Memory*, Sci. Rep. **6**, 23164 (2016). [p. 27]

[129] Tokunaga Y., Yu X. Z., White J. S., Rønnow H. M., Morikawa D., Taguchi Y. & Tokura Y., *A new class of chiral materials hosting magnetic skyrmions beyond room temperature*, Nat. Comm. **6**, 7638 (2015). [p. 27]

[130] Karube K., White J. S., Reynolds N., Gavilano J. L., Oike H., Kikkawa A., Kagawa F., Tokunaga Y., Rønnow H. M., Tokura Y. & Taguchi Y., *Robust metastable skyrmions and their triangular–square lattice structural transition in a high-temperature chiral magnet*, Nat. Mater. **15**, 1237 (2016). [p. 27]

[131] Karube K., White J. S., Morikawa D., Bartkowiak M., Kikkawa A., Tokunaga Y., Arima T., Rønnow H. M., Tokura Y. & Taguchi Y., *Skyrmion formation in a bulk chiral magnet at zero magnetic field and above room temperature*, Phys. Rev. Mater. **1**, 074405 (2017). [p. 27]

[132] Parkin S. & Yang S.-H., *Memory on the racetrack*, Nat. Nanotech. **10**, 195 (2015). [p. 28]

[133] Zhang X., Zhao G. P., Fangohr H., Liu J. P., Xia W. X., Xia J. & Morvan F. J., *Skyrmion-skyrmion and skyrmion-edge repulsions in skyrmion-based racetrack memory*, Sci. Rep. **5**, 7643 (2015). [pp. 28, 35, 54]

[134] Zhang X., Ezawa M. & Zhou Y., *Magnetic skyrmion logic gates: Conversion, duplication and merging of skyrmions*, Sci. Rep. **5**, 9400 (2015). [pp. 28, 61]

[135] Kim J.-V., Garcia-Sanchez F., Sampaio J., Moreau-Luchaire C., Cros V. & Fert A., *Breathing modes of confined skyrmions in ultrathin magnetic dots*, Phys. Rev. B **90**, 064410 (2014). [p. 28]

[136] Finocchio G., Ricci M., Tomasello R., Giordano A., Lanuzza M., Puliafito V., Burrascano P., Azzerboni B. & Carpentieri M., *Skyrmion based microwave detectors and harvesting*, Appl. Phys. Lett. **107**, 262401 (2015). [p. 28]

[137] Garcia-Sanchez F., Sampaio J., Reyren N., Cros V. & Kim J.-V., *A skyrmion-based spin-torque nano-oscillator*, New J. Phys. **18**, 075011 (2016). [pp. 28, 51, 74]

[138] Huang Y., Kang W., Zhang X., Zhou Y. & Zhao W., *Magnetic skyrmion-based synaptic devices*, Nanotechnology **28**, 08LT02 (2017). [p. 28]

[139] Pinna D., Abreu Araujo F., Kim J.-V., Cros V., Querlioz D., Bessiere P., Droulez J. & Grollier J., *Skyrmion Gas Manipulation for Probabilistic Computing*, Phys. Rev. Appl. **9**, 064018 (2018). [p. 28]

[140] Kang W., Huang Y., Zhang X., Zhou Y. & Zhao W., *Skyrmion-Electronics: An Overview and Outlook*, Proc. IEEE **104**, 2040 (2016). [p. 28]

[141] Dovzhenko Y., Casola F., Schlotter S., Zhou T. X., Büttner F., Walsworth R. L., Beach G. S. D. & Yacoby A., *Magnetostatic twists in room-temperature skyrmions explored by nitrogen-vacancy center spin texture reconstruction*, Nat. Comm. **9**, 2712 (2018). [pp. 31, 61, 88]

[142] Legrand W., Chauleau J.-Y., Maccariello D., Reyren N., Collin S., Bouzehouane K., Jaouen N., Cros V. & Fert A., *Hybrid chiral domain walls and skyrmions in magnetic multilayers*, Sci. Adv. **4**, eaat0415 (2018). [pp. 31, 61, 88]

[143] Li W., Bykova I., Zhang S., Yu G., Tomasello R., Carpentieri M., Liu Y., Guang Y., Gräfe J., Weigand M., Burn D. M., van der Laan G., Hesjedal T., Yan Z., Feng J., Wan C., Wei J., Wang X., Zhang X., Xu H., Guo C., Wei H., Finocchio G., Han X. & Schütz G., *Anatomy of Skyrmionic Textures in Magnetic Multilayers*, Adv. Mat. **31**, 1807683 (2019). [pp. 31, 61, 88]

[144] Legrand W., Ronceray N., Reyren N., Maccariello D., Cros V. & Fert A., *Modeling the Shape of Axisymmetric Skyrmions in Magnetic Multilayers*, Phys. Rev. Appl. **10**, 064042 (2018). [pp. 31, 36, 61, 78]

[145] Lemesh I. & Beach G. S. D., *Twisted domain walls and skyrmions in perpendicularly magnetized multilayers*, Phys. Rev. B **98**, 104402 (2018). [pp. 31, 36, 61, 78]

[146] Litzius K., Lemesh I., Krüger B., Bassirian P., Caretta L., Richter K., Büttner F., Sato K., Tretiakov O. A., Förster J., Reeve R. M., Weigand M., Bykova I., Stoll H., Schütz G., Beach G. S. D. & Kläui M., *Skyrmion Hall effect revealed by direct time-resolved X-ray microscopy*, Nat. Phys. **13**, 170 (2017). [pp. 31, 35, 61, 70, 72, 75, 77, 78, 79, 94]

[147] Siemens A., Zhang Y., Hagemeister J., Vedmedenko E. Y. & Wiesendanger R., *Minimal radius of magnetic skyrmions: Statics and dynamics*, New J. Phys. **18**, 045021 (2016). [p. 32]

[148] Lemesh I., Litzius K., Böttcher M., Bassirian P., Kerber N., Heinze D., Zázvorka J., Büttner F., Caretta L., Mann M., Weigand M., Finizio S., Raabe J., Im M.-Y., Stoll H., Schütz G., Dupé B., Kläui M. & Beach G. S. D., *Current-Induced Skyrmion Generation through Morphological Thermal Transitions in Chiral Ferromagnetic Heterostructures*, Adv. Mat. **30**, 1805461 (2018). [p. 32]

[149] Hsu P.-J., Kubetzka A., Finco A., Romming N., von Bergmann K. & Wiesendanger R., *Electric-field-driven switching of individual magnetic skyrmions*, Nat. Nanotech. **12**, 123 (2017). [p. 32]

[150] Schott M., Bernand-Mantel A., Ranno L., Pizzini S., Vogel J., Béa H., Baraduc C., Auffret S., Gaudin G. & Givord D., *The Skyrmion Switch: Turning Magnetic Skyrmion Bubbles on and off with an Electric Field*, Nano Lett. **17**, 3006 (2017). [pp. 32, 95]

[151] Thiele A. A., *Steady-State Motion of Magnetic Domains*, Phys. Rev. Lett. **30**, 230 (1973). [pp. 32, 97]

[152] Hrabec A., Sampaio J., Belmeguenai M., Gross I., Weil R., Chérif S. M., Stashkevich A., Jacques V., Thiaville A. & Rohart S., *Current-induced skyrmion generation and dynamics in symmetric bilayers*, Nat. Comm. **8**, 15765 (2017). [pp. 35, 36, 61, 70, 77, 100, 101]

[153] Iwasaki J., Koshibae W. & Nagaosa N., *Colossal Spin Transfer Torque Effect on Skyrmion along the Edge*, Nano Lett. **14**, 4432 (2014). [p. 35]

[154] Yoo M.-W., Cros V. & Kim J.-V., *Current-driven skyrmion expulsion from magnetic nanostrips*, Phys. Rev. B **95**, 184423 (2017). [p. 35]

[155] Jiang W., Zhang X., Yu G., Zhang W., Wang X., Benjamin Jungfleisch M., Pearson J. E., Cheng X., Heinonen O., Wang K. L., Zhou Y., Hoffmann A. & te Velthuis S. G. E., *Direct observation of the skyrmion Hall effect*, Nat. Phys. **13**, 162 (2017). [pp. 35, 36, 61, 72, 77, 78, 79, 80, 94]

[156] Huang S., Zhou C., Chen G., Shen H., Schmid A. K., Liu K. & Wu Y., *Stabilization and current-induced motion of antiskyrmion in the presence of anisotropic Dzyaloshinskii-Moriya interaction*, Phys. Rev. B **96**, 144412 (2017). [p. 35]

[157] Barker J. & Tretiakov O. A., *Static and Dynamical Properties of Antiferromagnetic Skyrmions in the Presence of Applied Current and Temperature*, Phys. Rev. Lett. **116**, 147203 (2016). [pp. 35, 81, 82]

[158] Zhang X., Xia J., Zhou Y., Wang D., Liu X., Zhao W. & Ezawa M., *Control and manipulation of a magnetic skyrmionium in nanostructures*, Phys. Rev. B **94**, 094420 (2016). [p. 35]

[159] Kolesnikov A. G., Stebliy M. E., Samardak A. S. & Ognev A. V., *Skyrmionium – high velocity without the skyrmion Hall effect*, Sci. Rep. **8**, 16966 (2018). [p. 35]

[160] Camosi L., Rohart S., Fruchart O., Pizzini S., Belmeguenai M., Roussigné Y., Stashkevich A., Cherif S. M., Ranno L., de Santis M. & Vogel J., *Anisotropic Dzyaloshinskii-Moriya interaction in ultrathin epitaxial Au/Co/W(110)*, Phys. Rev. B **95**, 214422 (2017). [p. 35]

[161] Camosi L., Rougemaille N., Fruchart O., Vogel J. & Rohart S., *Micromagnetics of antiskyrmions in ultrathin films*, Phys. Rev. B **97**, 134404 (2018). [p. 35]

[162] Woo S., Song K. M., Zhang X., Zhou Y., Ezawa M., Liu X., Finizio S., Raabe J., Lee N. J., Kim S.-I., Park S.-Y., Kim Y., Kim J.-Y., Lee D., Lee O., Choi J. W., Min B.-C., Koo H. C. & Chang J., *Current-driven dynamics and inhibition of the skyrmion Hall effect of ferrimagnetic skyrmions in GdFeCo films*, Nat. Comm. **9**, 959 (2018). [pp. 36, 61, 77, 78, 82]

[163] Schulz T., Ritz R., Bauer A., Halder M., Wagner M., Franz C., Pfleiderer C., Everschor K., Garst M. & Rosch A., *Emergent electrodynamics of skyrmions in a chiral magnet*, Nat. Phys. **8**, 301 (2012). [p. 35]

[164] Lemesh I. & Beach G. S., *Walker Breakdown with a Twist: Dynamics of Multilayer Domain Walls and Skyrmions Driven by Spin-Orbit Torque*, Phys. Rev. Appl. **12**, 044031 (2019). [pp. 36, 61, 78]

[165] Parker M. R., *The Kerr magneto-optic effect (1876–1976)*, Physica B+C **86-88**, 1171 (1977). [p. 38]

[166] Srivastava T. *Engineering and dynamical control of interfacial properties in ultra-thin films to tune magnetic spin textures*. PhD thesis, Univ. Grenoble Alpes (2019). [p. 39]

[167] Stöhr J., Padmore H. A., Anders S., Stammler T. & Scheinfein M. R., *Principles of X-Ray Magnetic Dichroism Spectromicroscopy*, Surf. Rev. Lett. **05**, 1297 (1998). [p. 41]

[168] Pizzini S. *Structure, magnétisme local et dynamique de l'aimantation de couches minces couplées étudiés par Spectroscopie d'Absoption X et effet Kerr magnéto-optique*. HDR, Univ. Grenoble Alpes (2006). [p. 41]

[169] Cao A., Zhang X., Koopmans B., Peng S., Zhang Y., Wang Z., Yan S., Yang H. & Zhao W., *Tuning the Dzyaloshinskii–Moriya interaction in Pt/Co/MgO heterostructures through the MgO thickness*, Nanoscale **10**, 12062 (2018). [p. 48]

[170] Parakkat V. M., Ganesh K. R. & Anil Kumar P. S., *Tailoring Curie temperature and magnetic anisotropy in ultrathin Pt/Co/Pt films*, AIP Adv. **6**, 056118 (2016). [p. 48]

[171] Behera A. K., Mishra S. S., Mallick S., Singh B. B. & Bedanta S., *Size and shape of skyrmions for variable Dzyaloshinskii–Moriya interaction and uniaxial anisotropy*, J. Phys. D: Appl. Phys. **51**, 285001 (2018). [p. 50]

[172] Ho P., Tan A. K., Goolaup S., Oyarce A. G., Raju M., Huang L., Soumyanarayanan A. & Panagopoulos C., *Geometrically Tailored Skyrmions at Zero Magnetic Field in Multilayered Nanostructures*, Phys. Rev. Appl. **11**, 024064 (2019). [p. 50]

[173] Juge R., Je S.-G., de Souza Chaves D., Pizzini S., Buda-Prejbeanu L. D., Aballe L., Foerster M., Locatelli A., Menteş T. O., Sala A., Maccherozzi F., Dhesi S. S., Auffret S., Gautier E., Gaudin G., Vogel J. & Boulle O., *Magnetic skyrmions in confined geometries: Effect of the magnetic field and the disorder*, J. Magn. Magn. Mater. **455**, 3 (2018). [pp. 50, 62, 93]

[174] Vansteenkiste A., Leliaert J., Dvornik M., Helsen M., Garcia-Sanchez F. & Waeyenberge B. V., *The design and verification of MuMax3*, AIP Adv. **4**, 107133 (2014). [pp. 51, 66]

[175] Ranjan R., Jiles D. C., Buck O. & Thompson R. B., *Grain size measurement using magnetic and acoustic Barkhausen noise*, J. Appl. Phys. **61**, 3199 (1987). [p. 51]

[176] Yu R. H., Basu S., Zhang Y., Parvizi-Majidi A. & Xiao J. Q., *Pinning effect of the grain boundaries on magnetic domain wall in FeCo-based magnetic alloys*, J. Appl. Phys. **85**, 6655 (1999). [p. 51]

[177] Voto M., Lopez-Diaz L. & Torres L., *Effects of grain size and disorder on domain wall propagation in CoFeB thin films*, J. Phys. D: Appl. Phys. **49**, 185001 (2016). [p. 51]

[178] Kim J.-V. & Yoo M.-W., *Current-driven skyrmion dynamics in disordered films*, Appl. Phys. Lett. **110**, 132404 (2017). [pp. 51, 63, 72, 74, 75, 76]

[179] Gross I., Akhtar W., Hrabec A., Sampaio J., Martínez L. J., Chouaieb S., Shields B. J., Maletinsky P., Thiaville A., Rohart S. & Jacques V., *Skyrmion morphology in ultrathin magnetic films*, Phys. Rev. Mater. **2**, 024406 (2018). [pp. 52, 62]

[180] Zeissler K., Mruczkiewicz M., Finizio S., Raabe J., Shepley P. M., Sadovnikov A. V., Nikitov S. A., Fallon K., McFadzean S., McVitie S., Moore T. A., Burnell G. & Marrows C. H., *Pinning and hysteresis in the field dependent diameter evolution of skyrmions in Pt/Co/Ir superlattice stacks*, Sci. Rep. **7**, 15125 (2017). [pp. 52, 62]

[181] Chen G., Mascaraque A., N'Diaye A. T. & Schmid A. K., *Room temperature skyrmion ground state stabilized through interlayer exchange coupling*, Appl. Phys. Lett. **106**, 242404 (2015). [p. 54]

[182] Bloemen P. J. H., van Kesteren H. W., Swagten H. J. M. & de Jonge W. J. M., *Oscillatory interlayer exchange coupling in Co/Ru multilayers and bilayers*, Phys. Rev. B **50**, 13505 (1994). [pp. 54, 82, 84]

[183] Bandiera S., Sousa R. C., Auffret S., Rodmacq B. & Dieny B., *Enhancement of perpendicular magnetic anisotropy thanks to Pt insertions in synthetic antiferromagnets*, Appl. Phys. Lett. **101**, 072410 (2012). [pp. 54, 55]

[184] Parkin S. S. P., More N. & Roche K. P., *Oscillations in exchange coupling and magnetoresistance in metallic superlattice structures: Co/Ru, Co/Cr, and Fe/Cr*, Phys. Rev. Lett. **64**, 2304 (1990). [p. 55]

[185] Yu G., Jenkins A., Ma X., Razavi S. A., He C., Yin G., Shao Q., lin He Q., Wu H., Li W., Jiang W., Han X., Li X., Bleszynski Jayich A. C., Amiri P. K. & Wang K. L., *Room-Temperature Skyrmions in an Antiferromagnet-Based Heterostructure*, Nano Lett. **18**, 980 (2018). [pp. 57, 95]

[186] Rana K. G., Finco A., Fabre F., Chouaieb S., Haykal A., Buda-Prejbeanu L. D., Fruchart O., Denmat S. L., David P., Belmeguenai M., Denneulin T., Dunin-Borkowski R. E., Gaudin G., Jacques V. & Boulle O., *Room temperature skyrmions at zero field in exchange-biased ultrathin films*, arXiv:2001.00912 [cond-mat] (2020). [pp. 57, 91, 95]

[187] Chappert C., Bernas H., Ferré J., Kottler V., Jamet J.-P., Chen Y., Cambril E., Devolder T., Rousseaux F., Mathet V. & Launois H., *Planar Patterned Magnetic Media Obtained by Ion Irradiation*, Science **280**, 1919 (1998). [p. 57]

[188] Devolder T., *Light ion irradiation of Co/Pt systems: Structural origin of the decrease in magnetic anisotropy*, Phys. Rev. B **62**, 5794 (2000). [pp. 57, 60]

[189] Fassbender J. & McCord J., *Magnetic patterning by means of ion irradiation and implantation*, J. Magn. Magn. Mater. **320**, 579 (2008). [p. 57]

[190] Zhang S., Petford-Long A. K. & Phatak C., *Creation of artificial skyrmions and antiskyrmions by anisotropy engineering*, Sci. Rep. **6**, 31248 (2016). [p. 57]

[191] Rettner C. T., Anders S., Baglin J. E. E., Thomson T. & Terris B. D., *Characterization of the magnetic modification of Co/Pt multilayer films by He+, Ar+, and Ga+ ion irradiation*, Appl. Phys. Lett. **80**, 279 (2002). [p. 58]

[192] Balk A. L., Kim K.-W., Pierce D. T., Stiles M. D., Unguris J. & Stavis S. M., *Simultaneous control of the Dzyaloshinskii-Moriya interaction and magnetic anisotropy in nanomagnetic trilayers*, Phys. Rev. Lett. **119**, 077205 (2017). [p. 58]

[193] Diez L. H., García-Sánchez F., Adam J.-P., Devolder T., Eimer S., Hadri M. S. E., Lamperti A., Mantovan R., Ocker B. & Ravelosona D., *Controlling magnetic domain wall motion in the creep regime in He+-irradiated CoFeB/MgO films with perpendicular anisotropy*, Appl. Phys. Lett. **107**, 032401 (2015). [p. 58]

[194] Diez L. H., Voto M., Casiraghi A., Belmeguenai M., Roussigné Y., Durin G., Lamperti A., Mantovan R., Sluka V., Jeudy V., Liu Y. T., Stashkevich A., Chérif S. M., Langer J., Ocker B., Lopez-Diaz L. & Ravelosona D., *Enhancement of the Dzyaloshinskii-Moriya interaction and domain wall velocity through interface intermixing in Ta/CoFeB/MgO*, Phys. Rev. B **99**, 054431 (2019). [pp. 58, 60]

[195] Casiraghi A., Magni A., Diez L. H., Langer J., Ocker B., Pasquale M., Ravelosona D. & Durin G., *Bloch-to-Néel domain wall transition evinced through morphology of magnetic bubble expansion in Ta/CoFeB/MgO layers*, arXiv:1907.03708 [cond-mat] (2019). [pp. 58, 60]

[196] Devolder T., Ferré J., Chappert C., Bernas H., Jamet J.-P. & Mathet V., *Magnetic properties of He+ irradiated Pt/Co/Pt ultrathin films*, Phys. Rev. B **64**, 064415 (2001). [pp. 58, 94]

[197] Cayssol F., Menéndez J. L., Ravelosona D., Chappert C., Jamet J.-P., Ferré J. & Bernas H., *Enhancing domain wall motion in magnetic wires by ion irradiation*, Appl. Phys. Lett. **86**, 022503 (2005). [pp. 58, 94]

[198] Zimmermann B., Legrand W., Maccariello D., Reyren N., Cros V., Blügel S. & Fert A., *Dzyaloshinskii-Moriya interaction at disordered interfaces from ab initio theory: Robustness against intermixing and tunability through dusting*, Appl. Phys. Lett. **113**, 232403 (2018). [p. 60]

[199] Bandiera S., Sousa R. C., Rodmacq B. & Dieny B., *Asymmetric Interfacial Perpendicular Magnetic Anisotropy in Pt/Co/Pt Trilayers*, IEEE Mag. Lett. **2**, 3000504 (2011). [p. 65]

[200] Avci C. O., Garello K., Gabureac M., Ghosh A., Fuhrer A., Alvarado S. F. & Gambardella P., *Interplay of spin-orbit torque and thermoelectric effects in ferromagnet/normal-metal bilayers*, Phys. Rev. B **90**, 224427 (2014). [p. 68]

[201] Mihai Miron I., Gaudin G., Auffret S., Rodmacq B., Schuhl A., Pizzini S., Vogel J. & Gambardella P., *Current-driven spin torque induced by the Rashba effect in a ferromagnetic metal layer*, Nat. Mater. **9**, 230 (2010). [p. 69]

[202] Reichhardt C. & Reichhardt C. J. O., *Noise fluctuations and drive dependence of the skyrmion Hall effect in disordered systems*, New J. Phys. **18**, 095005 (2016). [pp. 72, 74]

[203] Min H., McMichael R. D., Donahue M. J., Miltat J. & Stiles M. D., *Effects of Disorder and Internal Dynamics on Vortex Wall Propagation*, Phys. Rev. Lett. **104**, 217201 (2010). [p. 72]

[204] Van de Wiele B., Laurson L. & Durin G., *The role of disorder in the domain wall dynamics of magnetic nanostrips*, Eur. Phys. J. B **86**, 86 (2013). [p. 72]

[205] Beaujour J.-M. L., Lee J. H., Kent A. D., Krycka K. & Kao C.-C., *Magnetization damping in ultrathin polycrystalline Co films: Evidence for nonlocal effects*, Phys. Rev. B **74**, 214405 (2006). [p. 72]

[206] Kim K.-W., Moon J.-H., Lee K.-J. & Lee H.-W., *Prediction of Giant Spin Motive Force due to Rashba Spin-Orbit Coupling*, Phys. Rev. Lett. **108**, 217202 (2012). [p. 72]

[207] Zhang S. & Zhang S. S.-L., *Generalization of the Landau-Lifshitz-Gilbert Equation for Conducting Ferromagnets*, Phys. Rev. Lett. **102**, 086601 (2009). [p. 72]

[208] Weindler T., Bauer H. G., Islinger R., Boehm B., Chauleau J.-Y. & Back C. H., *Magnetic Damping: Domain Wall Dynamics versus Local Ferromagnetic Resonance*, Phys. Rev. Lett. **113**, 237204 (2014). [pp. 72, 79]

[209] Kim J.-V., *Role of nonlinear anisotropic damping in the magnetization dynamics of topological solitons*, Phys. Rev. B **92**, 014418 (2015). [p. 72]

[210] Buda L. D., Prejbeanu I. L., Ebels U. & Ounadjela K., *Micromagnetic simulations of magnetisation in circular cobalt dots*, Comput. Mater. Sci. **24**, 181 (2002). [p. 73]

[211] Safeer C. K., Jué E., Lopez A., Buda-Prejbeanu L., Auffret S., Pizzini S., Boulle O., Miron I. M. & Gaudin G., *Spin–orbit torque magnetization switching controlled by geometry*, Nat. Nanotech. **11**, 143 (2016). [p. 73]

[212] Martinez E., Alejos O., Hernandez M. A., Raposo V., Sanchez-Tejerina L. & Moretti S., *Angular dependence of current-driven chiral walls*, Appl. Phys. Express **9**, 063008 (2016). [p. 73]

[213] Garg C., Pushp A., Yang S.-H., Phung T., Hughes B. P., Rettner C. & Parkin S. S. P., *Highly Asymmetric Chiral Domain-Wall Velocities in Y-Shaped Junctions*, Nano Lett. **18**, 1826–1830 (2018). [p. 73]

[214] Baumgartner M. & Gambardella P., *Asymmetric velocity and tilt angle of domain walls induced by spin-orbit torques*, Appl. Phys. Lett. **113**, 242402 (2018). [p. 73]

[215] Iwasaki J., Mochizuki M. & Nagaosa N., *Universal current-velocity relation of skyrmion motion in chiral magnets*, Nat. Comm. **4**, 1463 (2013). [p. 75]

[216] Lee H.-Y., Kim S., Park J.-Y., Oh Y.-W., Park S.-Y., Ham W., Kotani Y., Nakamura T., Suzuki M., Ono T., Lee K.-J. & Park B.-G., *Enhanced spin–orbit torque via interface engineering in Pt/CoFeB/MgO heterostructures*, APL Mat. **7**, 031110 (2019). [p. 78]

[217] Litzius K., Leliaert J., Bassirian P., Rodrigues D., Kromin S., Lemesh I., Zazvorka J., Lee K.-J., Mulkers J., Kerber N., Heinze D., Keil N., Reeve R. M., Weigand M., Waeyenberge B. V., Schütz G., Everschor-Sitte K., Beach G. S. D. & Kläui M., *The role of temperature and drive current in skyrmion dynamics*, Nat. Electron. **3**, 30 (2020). [p. 78]

[218] Zhang X., Zhou Y. & Ezawa M., *Magnetic bilayer-skyrmions without skyrmion Hall effect*, Nat. Comm. **7**, 10293 (2016). [pp. 81, 82]

[219] Baltz V., Manchon A., Tsoi M., Moriyama T., Ono T. & Tserkovnyak Y., *Antiferromagnetic spintronics*, Rev. Mod. Phys. **90**, 015005 (2018). [pp. 82, 91]

[220] Caretta L., Mann M., Büttner F., Ueda K., Pfau B., Günther C. M., Hessing P., Churikova A., Klose C., Schneider M., Engel D., Marcus C., Bono D., Bagschik K., Eisebitt S. & Beach G. S. D., *Fast current-driven domain walls and small skyrmions in a compensated ferrimagnet*, Nat. Nanotech. **13**, 1154 (2018). [p. 82]

[221] Zhang X., Ezawa M. & Zhou Y., *Thermally stable magnetic skyrmions in multilayer synthetic antiferromagnetic racetracks*, Phys. Rev. B **94**, 064406 (2016). [p. 82]

[222] Dieny B., Gavigan J. P. & Rebouillat J. P., *Magnetisation processes, hysteresis and finite-size effects in model multilayer systems of cubic or uniaxial anisotropy with antiferromagnetic coupling between adjacent ferromagnetic layers*, J. Phys.: Cond. Mat. **2**, 159 (1990). [pp. 84, 85]

[223] Hellwig O., Berger A., Kortright J. B. & Fullerton E. E., *Domain structure and magnetization reversal of antiferromagnetically coupled perpendicular anisotropy films*, J. Magn. Magn. Mater. **319**, 13 (2007). [p. 87]

[224] Finizio S., Zeissler K., Wintz S., Mayr S., Weßels T., Huxtable A. J., Burnell G., Marrows C. H. & Raabe J., *Deterministic Field-Free Skyrmion Nucleation at a Nanoengineered Injector Device*, Nano Lett. **19**, 7246 (2019). [p. 89]

[225] Legrand W., Maccariello D., Ajejas F., Collin S., Vecchiola A., Bouzehouane K., Reyren N., Cros V. & Fert A., *Room-temperature stabilization of antiferromagnetic skyrmions in synthetic antiferromagnets*, Nat. Mater. **19**, 34 (2019). [pp. 91, 95]

[226] Juge R., Je S.-G., Chaves D. d. S., Buda-Prejbeanu L. D., Peña-Garcia J., Nath J., Miron I. M., Rana K. G., Aballe L., Foerster M., Genuzio F., Menteş T. O., Locatelli A., Maccherozzi F., Dhesi S. S., Belmeguenai M., Roussigné Y., Auffret S., Pizzini S., Gaudin G., Vogel J. & Boulle O., *Current-Driven Skyrmion Dynamics and Drive-Dependent Skyrmion Hall Effect in an Ultrathin Film*, Phys. Rev. Appl. **12**, 044007 (2019). [p. 94]

[227] Büttner F., Lemesh I., Schneider M., Pfau B., Günther C. M., Hessing P., Geilhufe J., Caretta L., Engel D., Krüger B., Viefhaus J., Eisebitt S. & Beach G. S. D., *Field-free deterministic ultrafast creation of magnetic skyrmions by spin–orbit torques*, Nat. Nanotech. **12**, 1040 (2017). [p. 95]

[228] Je S.-G., Vallobra P., Srivastava T., Rojas-Sánchez J.-C., Pham T. H., Hehn M., Malinowski G., Baraduc C., Auffret S., Gaudin G., Mangin S., Béa H. & Boulle O., *Creation of Magnetic Skyrmion Bubble Lattices by Ultrafast Laser in Ultrathin Films*, Nano Lett. **18**, 7362 (2018). [p. 95]

Titre: Nucléation et dynamique de skyrmions magnétiques dans des films ultra-minces

Résumé: Les skyrmions magnétiques sont des enroulements chiraux de l'aimantation que l'on peut visualiser comme de minuscules domaines magnétiques circulaires délimités par des parois de domaine chirales. En raison de leur taille potentiellement nanométrique et car on leur prédit un déplacement efficace sous courant, les skyrmions magnétiques sont devenus des candidats prometteurs pour transporter l'information dans des mémoires et des dispositifs logiques non-volatiles et à forte densité de stockage. Ils ont récemment été observés à température ambiante dans des empilements du type métal lourd/ferromagnétique/non-magnétique, franchissant une étape importante en vue de développer des dispositifs utilisant des skyrmions. Suivant ces premières observations, l'objectif de cette thèse est d'étudier certaines propriétés clés des skyrmions que sont leur nucléation, leur stabilité et leur déplacement sous courant ; toutes à température ambiante. Les premiers résultats présentés portent sur la nucléation de skyrmions dans des films ultra-minces (pour une épaisseur de ferromagnétique de l'ordre de 1 nm) réalisée par ingénierie des propriétés magnétiques aux interfaces ainsi que de la géométrie des échantillons. La nucléation de skyrmions dans des films ultra-minces étendus, en géométrie confinée, dans des films polarisés par échange inter-couche puis dans des motifs définis par irradiation d'ions est présentée. La deuxième partie de ce travail concerne l'étude de la dynamique des skyrmions magnétiques sous courant. Dans un film ultra-mince de composition Pt/Co/MgO, on mesure des vitesses atteignant 100 m s^{-1}, pour des skyrmions de l'ordre de 100 nm. Cette étude met également en lumière l'effet Hall de skyrmion, signature de leur topologie, qui décrit la déviation de la trajectoire d'un skyrmion par rapport à celle dictée par le courant. Nous trouvons que cette déviation dépend nettement de la vitesse des skyrmions, contrairement à ce que prédisent les modèles existants. En combinant modèle analytique et simulations micromagnétiques, s'appuyant sur une caractérisation poussée des propriétés du film, nous trouvons que cette dépendance avec la vitesse peut être entièrement attribuée à des effets de piégeage qui entravent le déplacement des skyrmions. Enfin, la dernière partie de ce travail porte sur l'étude expérimentale de multi-couches antiferromagnétiques synthétiques, caractérisées par un moment magnétique net nul. Dans ces systèmes, on s'attend à ce que le déplacement des skyrmions s'effectue dans la direction du courant — sans effet Hall de skyrmion, une condition requise pour les applications. L'optimisation de multi-couches spécifiques permet l'observation, en microscopie à rayons X, de skyrmions antiferromagnétiques synthétiques de l'ordre de 100 nm. Puisque leur nucléation est délicate, un dispositif est par la suite conçu pour injecter localement du courant électrique à travers des pointes lithographiées. Ce dispositif permet de créer et de supprimer des skyrmions de manière contrôlée, en utilisant uniquement du courant, rapprochant ces skyrmions un peu plus des applications.

Title: Exploring different facets of magnetic skyrmion nucleation and dynamics in ultra-thin films

Abstract: Magnetic skyrmions are chiral magnetisation windings that can be pictured as minuscule, circular magnetic domains bounded by chiral domain walls. Owing to their potential nanometre size and predicted efficient current-driven motion, magnetic skyrmions hold great promise as future information carriers in high-density, non-volatile memory and logic applications. Their recent observation at room temperature in material stacks consisting of heavy metal/ferromagnet/non-magnet has lifted an important bottleneck towards the practical realisation of skyrmion-based devices. Following these early observations, the objective of this work is to tackle certain key attributes of magnetic skyrmions that are their nucleation, stability and current-driven motion; all at room temperature. The first results presented in this thesis deal with the stabilisation and nucleation of skyrmions in ultra-thin films (for a ferromagnet thickness around 1 nm) by engineering of the interfacial magnetic properties and the geometry. The nucleation of skyrmions in extended films, confined geometries, exchange-biased films and ion-irradiated films are presented. The second part of this work concerns the current-driven dynamics of magnetic skyrmions. In an ultra-thin Pt/Co/MgO film, we measure velocities up to 100 m s^{-1} for skyrmion sizes in the range of 100 nm. This study further highlights the skyrmion Hall effect, a hallmark of the skyrmion topology, which describes the deflection of a skyrmion trajectory from that imposed by the current. The angle of deflection is found to be dependent on the skyrmion velocity, in contrast with existing models. Combining analytical modelling and micromagnetic simulations, based on a thorough characterisation of the film properties, we find that this dependence on the velocity can be entirely attributed to pinning effects hindering the skyrmion motion. Finally, in the last part of this work, we investigate experimentally synthetic antiferromagnetic multilayers with vanishing magnetic moment. In such systems, magnetic skyrmions are expected to be driven along the current direction — without skyrmion Hall effect, a prerequisite for applications. By optimising specific multilayers and using element-sensitive X-ray microscopy, we observe synthetic antiferromagnetic skyrmions at room temperature with sizes in the range of 100 nm. As their nucleation is somewhat challenging, a device is then designed to locally inject current through patterned tips. This allows to create and delete skyrmions in a controlled fashion using solely current, bringing them one step closer to applications.